

# Two Particle Correlations with Direct Photon and $\pi^0$ Triggers in 200 GeV p+p and Au+Au Collisions

A Dissertation Presented

by

Matthew Nguyen

to

The Graduate School

in Partial Fulfillment of the

Requirements

for the Degree of

Doctor of Philosophy

in

Physics

Stony Brook University

May 2009

Copyright by  
Matthew Nguyen  
2009

Stony Brook University  
The Graduate School

Matthew Nguyen

We, the dissertation committee for the above candidate for the Doctor of Philosophy degree, hereby recommend acceptance of this dissertation.

Barbara Jacak  
Relativistic Heavy Ion Group, Stony Brook University  
Dissertation Director

Axel Drees  
Department of Physics and Astronomy, Stony Brook University  
Chairman of Dissertation

George Sterman  
C.N. Yang Institute for Theoretical Physics, Stony Brook University

Michael Tannenbaum  
Department of Physics, Brookhaven National Laboratory  
Outside Member

This dissertation is accepted by the Graduate School.

Lawrence Martin  
Dean of the Graduate School

Abstract of the Dissertation

# Two Particle Correlations with Direct Photon and $\pi^0$ Triggers in 200 GeV p+p and Au+Au Collisions

by

Matthew Nguyen

Doctor of Philosophy

in

Physics

Stony Brook University

2009

Measurements of the associated production of charged hadrons of  $1 < p_T < 5$  GeV are performed using leading  $\pi^0$  and direct photon triggers of  $5 < p_T < 15$  GeV. In this kinematic range the dominant mechanism of particle production opposite direct photons is quark jet fragmentation while  $\pi^0$  triggered correlations sample quark and gluon jet fragmentation in roughly equal proportion. The data are compared to a model which includes Leading Order pQCD calculations and a Gaussian  $k_T$  smearing. Evidence for a significant  $k_T$  effect is demonstrated in the photon+jet comparable to previous PHENIX measurements in the di-jet channel. In p + p collisions at mid-rapidity direct photon production is dominated by Quark-Gluon Compton scattering. A charge asymmetry in particle production associated with direct photons is expected based on the flavor composition of the valence quarks with a proton. The measured charge asymmetry confirms the dominance of

Compton scattering and constrains the possible Next-to-Leading Order contribution from photon bremsstrahlung. The sensitivity of two-particle correlations to the fragmentation function is investigated by comparing measurements of quantities such as the fragmentation variable  $x_E$  to several parameterizations of quark and gluon fragmentation functions in the same  $k_T$  smeared model. Finally, measurements of associated hadron production are performed with identified pions and protons in order to study the flavor dependence of hadron production at lower values of  $z$  than are sampled by single particle spectra.

To Mom, Dad and Jess: Sun, Moon and Star

# Contents

<b>List of Figures</b>	<b>xv</b>
<b>List of Tables</b>	<b>xv</b>
<b>Acknowledgements</b>	<b>xvi</b>
<b>1 Introduction</b>	<b>1</b>
1.1 QCD . . . . .	1
1.2 Relativistic Heavy-Ion Collisions and the Quark-Gluon Plasma . . . . .	5
1.3 Properties and Signatures of the Quark-Gluon Plasma . . . . .	6
1.3.1 Thermalization and Elliptic Flow . . . . .	8
1.3.2 High $p_T$ Suppression and Jet Energy Loss . . . . .	10
1.4 Jets and Two-Particle Correlations . . . . .	16
1.4.1 Elementary Collisions . . . . .	16
1.4.2 Heavy-Ion Collisions . . . . .	18
1.5 Direct Photons . . . . .	22
1.5.1 Direct Photons at Leading Order . . . . .	23
1.6 Correlations Using Direct Photons . . . . .	24
1.6.1 Beyond Leading Order . . . . .	26
1.7 Initial State Radiation and the $k_T$ Effect . . . . .	28
1.8 Direct Photons in Nuclear Collisions . . . . .	31
1.9 $\gamma + jet$ : The Golden Channel . . . . .	33
1.10 Statement of Purpose . . . . .	37
<b>2 Experimental Apparatus</b>	<b>39</b>
2.1 Overview . . . . .	39
2.1.1 RHIC . . . . .	39
2.1.2 PHENIX . . . . .	40
2.2 Global Detectors . . . . .	41
2.2.1 Beam-Beam Counters . . . . .	41
2.2.2 Zero Degree Calorimeters . . . . .	43

2.3	Centrality Determination . . . . .	44
2.4	Central Tracking . . . . .	45
2.4.1	Drift Chambers . . . . .	45
2.4.2	Pad Chambers . . . . .	46
2.5	Electromagnetic Calorimeters . . . . .	47
2.6	Particle Identification Detectors . . . . .	50
2.6.1	Ring Imaging Cherenkov Counters . . . . .	50
2.6.2	Time of Flight Detector . . . . .	51
2.7	Summary of PHENIX Data Set . . . . .	52
<b>3</b>	<b>Data Analysis</b>	<b>53</b>
3.1	Direct Photons and $R_\gamma$ . . . . .	53
3.1.1	Photon Sources . . . . .	53
3.1.2	$R_\gamma$ . . . . .	54
3.2	Particle Identification . . . . .	56
3.2.1	Photon Identification . . . . .	56
3.2.2	$\pi^0$ and $\eta$ Identification . . . . .	60
3.2.3	Charged Hadron Identification . . . . .	61
3.2.4	Proton and Pion Identification . . . . .	62
3.3	Two Particle Correlations . . . . .	64
3.3.1	Background Normalization . . . . .	64
3.3.2	Acceptance Corrections . . . . .	68
3.3.3	Charged Hadron Efficiency Corrections . . . . .	68
3.3.4	Elliptic Flow . . . . .	72
3.4	Statistical Subtraction Method . . . . .	73
3.4.1	Parent to Daughter Mapping . . . . .	75
3.4.2	Pair-by-pair weighting . . . . .	76
3.4.3	Decay Photon Estimate from Monte Carlo . . . . .	79
3.4.4	$\pi^0$ Reconstruction Efficiency . . . . .	84
3.4.5	Cutoff Correction for Decay Yields . . . . .	84
3.4.6	$\eta$ -hadron Correlations . . . . .	86
3.5	Isolation Cut Method . . . . .	89
<b>4</b>	<b>Cross Checks and Systematic Errors</b>	<b>96</b>
4.1	$R_\gamma$ . . . . .	96
4.2	Inclusive Photons . . . . .	97
4.3	$\pi^0$ Combinatorics . . . . .	97
4.4	Two-Body Decay Kinematics and the Opening Angle Effect .	99
4.5	PYTHIA studies . . . . .	101
4.6	Cluster Merging . . . . .	103
4.7	PISA Studies . . . . .	106

4.8	Isolation Method: $R_\gamma'$	110
4.9	Summary of Systematic Uncertainties	112
4.9.1	$p + p$	112
4.9.2	Au + Au	112
4.9.3	A Note on Correlated Errors	114
<b>5</b>	<b>Measurements of Nuclear Effects via Direct Photon Correlations</b>	<b>116</b>
5.1	Direct Photon Correlations in $p+p$	116
5.2	$\eta$ Correlations	118
5.3	Comparison to Au + Au Collisions	120
5.4	Near-Side Correlations: Implications for Induced Radiation and the Ridge	123
5.5	Energy Loss via $\gamma+Jets$	124
<b>6</b>	<b>Insights into Vacuum QCD Processes Using Isolated Direct Photon and <math>\pi^0</math> Correlations</b>	<b>129</b>
6.1	Correlation Functions	130
6.2	Isolating the Effects of Photon Fragmentation	131
6.3	Leading Order Monte Carlo Event Generator	136
6.4	Hard Scattering Kinematics: $x_E$ and $p_{OUT}$	138
6.5	Cross Checks on the Monte Carlo	142
6.6	Measuring the $k_T$ Effect	147
6.7	Sensitivity of $x_E$ Distributions to the Fragmentation Functions	149
6.8	Jet Multiplicity	154
6.9	Charge Asymmetry	154
6.10	Identified Hadron Partner Results	156
<b>7</b>	<b>Conclusions and Outlook</b>	<b>159</b>
7.1	Overview	159
7.2	Methodology	160
7.3	Interpretation	160
7.4	Outlook	163
	<b>Bibliography</b>	<b>171</b>
	<b>Appendix: Data Tables</b>	<b>172</b>

# List of Figures

1.1	Running of the Coupling Constant in QCD . . . . .	2
1.2	Lattice Predictions for a Phase Transition . . . . .	6
1.3	Bjorken Picture of Colliding Nuclei. . . . .	7
1.4	Cartoon illustrating the concept of elliptic flow . . . . .	9
1.5	Elliptic flow data compared to prediction using ideal hydrodynamics . . . . .	9
1.6	Constituent quark scaling of $v_2$ in PHENIX data . . . . .	10
1.7	Nuclear modification factor of hadrons and neutral pions in Au + Au collisions . . . . .	12
1.8	PHENIX $\pi^0 R_{AA}$ compared to predictions from an energy loss model . . . . .	13
1.9	Gluon contribution of different particle species for AKK fragmentation functions . . . . .	14
1.10	$R_{CP}$ of identified hadrons . . . . .	15
1.11	Cartoon illustrating a measurement of two-particle correlations from jets . . . . .	17
1.12	Hadron-hadron correlations from STAR demonstrating the disappearance of the away-side jet in Au + Au collisions. . . . .	18
1.13	PHENIX hadron-hadron correlations in Au + Au showing an opposite-side correlation displaced from $\pi$ . . . . .	19
1.14	Hadron-hadron correlations from STAR demonstrating the re-appearance of the away-side jet at large $p_T$ . . . . .	20
1.15	Example of fits to modified jet shapes observed in azimuthal correlations of central Au + Au collisions. . . . .	20
1.16	$I_{AA}$ for the head and head+shoulder regions from PHENIX . .	21
1.17	Ridge structure in $\Delta\eta$ correlations in Au + Au from STAR data	22
1.18	Feynman diagrams representing LO direct photon production	23
1.19	$x_E$ distributions with $\pi^0$ triggers and their insensitivity to the fragmentation function . . . . .	24
1.20	Ratio of positive to negative charge opposite direct photons . .	25

1.21	Examples of Feynman diagrams of photon bremsstrahlung processes at NLO. . . . .	26
1.22	NLO calculations of the direct photon cross section with and without an isolation cut . . . . .	27
1.23	Compilation of the world data on the $k_T$ effect . . . . .	28
1.24	Comparison of NLO calculations to the world data on direct photon cross sections . . . . .	29
1.25	Comparison of PHENIX $\pi^0$ and direct photon cross sections to pQCD calculations . . . . .	30
1.26	Nuclear modification factor for photons and $\pi^0$ 's and $\eta$ 's as a function of $p_T$ for central Au + Au collisions . . . . .	31
1.27	PHENIX Direct photon $R_{AA}$ compared to an energy loss calculation . . . . .	32
1.28	Calculation of the direct photon cross section in central Au + Au events . . . . .	33
1.29	Calculation of effective modification of the fragmentation function for direct photon-hadron correlations . . . . .	34
1.30	Model calculation of the dependence of hadron $R_{AA}$ and direct photon $I_{AA}$ on the medium profile. . . . .	35
1.31	Spatial distribution of vertices sample by hadron $R_{AA}$ , $\pi^0$ $I_{AA}$ and direct photon $I_{AA}$ in the ZOWW model . . . . .	35
1.32	Prediction of direct photon associated yield in Au + Au using AMY . . . . .	36
2.1	Aerial view of the RHIC complex. . . . .	39
2.2	Overhead view of the PHENIX detector. . . . .	40
2.3	The PHENIX central arm configuration during Run 6. . . . .	42
2.4	The Beam-Beam Counters . . . . .	42
2.5	Diagram of the beam line near the interaction region showing the position of the ZDC detectors and the dipole magnets . . . . .	43
2.6	Centrality determination in Run 4 Au + Au collisions . . . . .	44
2.7	The Drift Chambers . . . . .	45
2.8	The Pad Chambers . . . . .	46
2.9	The Electromagnetic Calorimeters . . . . .	47
2.10	The $\chi^2$ per degree of freedom distribution for electrons and pions in the PbSc detector. . . . .	48
2.11	The timing resolution of the Electromagnetic Calorimeter (PbSc) . . . . .	49
2.12	Cut-away view of the Ring Imaging Cherenkov Detector . . . . .	50
2.13	A section of slats in the Time-of-Flight Detector . . . . .	51
2.14	Timing resolution for hadrons in the TOF . . . . .	51

3.1	p + p $R_\gamma$ values determined from the Run 5 data . . . . .	54
3.2	Au + Au $R_\gamma$ values determined from the Run 4 data . . . . .	55
3.3	Hit distribution in the EMC in Run 6 p + p data . . . . .	56
3.4	The distribution of hit frequencies for each sector in Run 6 p + p data . . . . .	57
3.5	Hit distributions in the EMC after hot tower removal . . . . .	58
3.6	$\phi$ distribution of clusters from a bad run in the Run 4 data . .	59
3.7	$\Delta\phi$ distribution of cluster-track pairs for tracks with no near PC3 hit . . . . .	59
3.8	Distance cluster and tracks for a charged hadron veto cut . . .	60
3.9	Invariant mass distribution of photon pairs in p + p collisions .	61
3.10	$m^2$ distributions for hadrons in the EMC . . . . .	62
3.11	$m^2$ distributions for hadrons in the TOF . . . . .	63
3.12	Number of triggers and partners as a function of $N_{part}$ (left) and $N_{coll}$ for the multiplicity resolution correction ( $\xi$ ) . . . . .	66
3.13	Multiplicity resolution correction . . . . .	67
3.14	Demonstration of the acceptance correction for pair analyses .	69
3.15	Fit to the published non-identified hadron yields for a charged hadron efficiency correction in p + p collisions . . . . .	69
3.16	Fit to the published non-identified hadron yields for a charged hadron efficiency correction in Au + Au collisions . . . . .	69
3.17	Variation of raw yields as a function of track matching in p + p collisions for a charge hadron background study . . . . .	70
3.18	Variation of raw yields as a function of track matching in Au + Au collisions for a charge hadron background study . . . . .	71
3.19	Hadron efficiency correction functions for p + p collisions . .	71
3.20	Hadron efficiency correction functions for Au + Au collisions .	73
3.21	The magnitude of the elliptic flow ( $v_2$ ) for inclusive photons and $\pi^0$ 's . . . . .	74
3.22	The magnitude of the elliptic flow ( $v_2$ ) for charged hadrons . .	74
3.23	Decay probability function from Monte Carlo . . . . .	77
3.24	Diagram of decay photon associated yield estimation procedure	78
3.25	Hit distribution in the EMC in simulation . . . . .	79
3.26	Hit distribution in the EMC in data . . . . .	79
3.27	$\pi^0$ peak widths in data and simulation . . . . .	80
3.28	z distribution of reconstructed $\pi^0$ 's . . . . .	81
3.29	Decay probability function variation with z . . . . .	82
3.30	Comparison of decay probability function in data and estimated analytically and in simulation . . . . .	83
3.31	$\pi^0$ reconstruction efficiency in Run 6 p + p collisions . . . . .	84

3.32	Power law fits to associated yields as a function of $p_T^\pi$ in different ranges of $p_T^{hadron}$ for the cutoff corrections. . . . .	85
3.33	Invariant mass distributions for $\eta$ reconstruction in p + p collisions	87
3.34	$\Delta\phi$ distributions of raw, sideband and corrected $\eta$ associated yields . . . . .	88
3.35	Subtracted $\eta$ $p_T$ distribution . . . . .	89
3.36	$\eta$ reconstruction efficiency correction function . . . . .	90
3.37	Invariant mass of reconstructed $\eta$ 's binned by daughter $p_T$ . . . . .	90
3.38	$\Delta\phi$ distribution for $\eta$ daughter correlations . . . . .	91
3.39	Venn diagram illustrating the various quantities in the isolation method . . . . .	92
3.40	Decay probability functions in isolation method . . . . .	93
3.41	$p_T$ distributions of inclusive, tagged and non-isolated photons	95
4.1	Fits to the $\pi^0$ invariant mass distributions and signal-to-background in 0-20% central Au + Au. . . . .	97
4.2	Signal-to-background for $\pi^0$ and $\gamma(\pi^0)$ in 0-20% central Au + Au.	98
4.3	Peak divided by high-end sideband per-trigger yields for different $p_T$ combinations. . . . .	98
4.4	Peak divided by low-end sideband per-trigger yields for different $p_T$ combinations. . . . .	99
4.5	$\pi^0 \rightarrow 2\gamma$ decay in the parent rest frame and the lab frame. . . . .	99
4.6	The opening angle as a function of decay photon momentum . . . . .	100
4.7	$R_\gamma$ and similar quantities in PYTHIA . . . . .	101
4.8	Examples of the two photon invariant mass distribution and decay photon probability function from PYTHIA with resolution smearing . . . . .	102
4.9	Ratio of input to observed decay associated yields in PYTHIA	103
4.10	Comparison of total decay photon hadron yield to the yield from $\pi^0$ and $\eta$ only in PYTHIA . . . . .	104
4.11	Separation efficiency from a GEANT simulation using input from the test beam data . . . . .	105
4.12	Mapping of merging effect to daughter $p_T$ . . . . .	106
4.13	Separation efficiency as a function of photon $p_T$ . . . . .	106
4.14	Single photon efficiency correction function from PISA . . . . .	108
4.15	PISA decay probability function for $\eta$ 's . . . . .	109
4.16	Effect of conversion photons in PISA . . . . .	109
4.17	Invariant mass distribution of tagged photons . . . . .	111
4.18	Purity of photon pairs in the tagging method . . . . .	111
4.19	Invariant mass distributions for non-isolated pairs . . . . .	111
4.20	Purity of non-isolated decay photon pairs . . . . .	111

4.21	Systematic error breakdown for p + p data . . . . .	113
4.22	Systematic error breakdown for Au + Au data . . . . .	114
5.1	Per-trigger yields of charged hadrons with inclusive, decay and direct photon triggers using the statistical subtraction method.	116
5.2	Comparison of direct photon and $\pi^0$ associated yields as a function of $p_{T,t}$ on the near ( $-\pi < \Delta\phi < \pi$ radians) and away-sides ( $\pi < \Delta\phi < 3\pi/2$ radians) . . . . .	117
5.3	The effect of $\eta$ correlations compared to PYTHIA predictions	119
5.4	Inclusive, decay and direct photon associated yields in 0-20% Au + Au collisions. . . . .	120
5.5	Direct photon and $\pi^0$ associated yields in central (0-20%) Au + Au collisions and $\pi^0$ associated yields from p + p collisions. . . . .	121
5.6	Jet functions for all of the ingredients in the direct photon subtraction method . . . . .	122
5.7	The ratio of the near-side ( $ \Delta\phi  < 0.5$ radians) direct photon associated yield to that of $\pi^0$ in central (0-20%) Au+Au collisions. . . . .	123
5.8	Away-side ( $4/5\pi < \Delta\phi < 6/5\pi$ radians) direct photon and $\pi^0$ associated yields as a function of $p_{T,a}$ in p + p and central (0-20%) Au + Au collisions. . . . .	125
5.9	Cartoon depicting several different types of two-particle observables in the presence of a black core medium and diffuse medium	126
5.10	Direct photon $I_{AA}$ $\pi^0 I_{AA}$ and $\pi^0 R_{AA}$ as a function of $p_{T,a}$ in central Au + Au collisions . . . . .	127
5.11	Comparison to NLO predictions from ZOWW . . . . .	128
5.12	Demonstration of improved theory comparison using fixed associated $p_T$ range . . . . .	128
6.1	Per-trigger yields of charged hadrons with inclusive, decay and direct photon triggers using the isolation method. . . . .	130
6.2	Per-trigger yields of charged hadrons for isolated direct photon, direct photon and $\pi^0$ triggers. . . . .	131
6.3	The ratio of inclusive direct photon to $\pi^0$ associated yields on the near-side for several $p_{T,t}$ selections as a function of $p_{T,a}$ . . . . .	133
6.4	Away-side fragmentation photon associated yields in p+p collisions. . . . .	134
6.5	Comparison of away-side isolated direct photon associated yields to an NLO calculation . . . . .	135
6.6	Up and Gluon CTEQ6 PDFs evaluated at $Q^2 = 49$ GeV $^2$ . . . . .	137

6.7	Examples of several parameterizations of gluon to proton fragmentation function evaluated at $Q^2 = 49 \text{ GeV}^2$ . . . . .	138
6.8	A diagram showing the kinematics underlying the measurement of jet correlations between back-to-back particles . . . . .	139
6.9	Comparison of $\pi^0$ $x_E$ and $z_T$ distributions . . . . .	140
6.10	$x_E$ distributions for $\pi^0$ triggers (open) and isolated direct photon triggers (solid) with exponential fits . . . . .	141
6.11	Example of $x_E$ distributions from Monte Carlo . . . . .	142
6.12	$p_{\text{OUT}}$ distributions for $\pi^0$ triggers and isolated direct photon triggers . . . . .	143
6.13	Comparison of the Gaussian fits to $p_{\text{OUT}}$ for $\pi^0$ and isolated direct photons . . . . .	144
6.14	Inclusive $\pi^0$ and isolated direct photon spectra from Monte Carlo with and without $k_T$ smearing including power law fits.	145
6.15	The fractional contribution of the different $2 \rightarrow 2$ processes to the $\pi^0$ cross-section as determined by Monte Carlo calculation using the AKK fragmentation functions . . . . .	145
6.16	The gluon contribution to protons and pions for the AKK05 and AKK08 fragmentation functions as calculated in a leading order + $k_T$ Monte Carlo program. . . . .	146
6.17	$\langle  p_{\text{OUT}} ^2 \rangle$ for isolated direct photon triggers compared to Monte Carlo calculations . . . . .	148
6.18	$\langle  p_{\text{OUT}} ^2 \rangle$ for $\pi^0$ triggers compared to Monte Carlo calculations . . . . .	149
6.19	$\chi^2$ between $\langle  p_{\text{OUT}} ^2 \rangle$ as measured in data and Monte Carlo calculations for $\pi^0$ . . . . .	150
6.20	$\chi^2$ between $\langle  p_{\text{OUT}} ^2 \rangle$ as measured in data and Monte Carlo calculations for isolated direct photons . . . . .	151
6.21	$\sqrt{\langle  k_T ^2 \rangle}$ for $\pi^0$ triggers compared to previous results . . . . .	151
6.22	$\sqrt{\langle  k_T ^2 \rangle}$ for $\pi^0$ and isolated photon triggers . . . . .	152
6.23	Slope parameters for exponential fits to the isolated direct photon $x_E$ distributions compared to Monte Carlo calculations . . . . .	152
6.24	Slope parameters for exponential fits to the $\pi^0$ $x_E$ distributions compared to Monte Carlo calculations . . . . .	153
6.25	Ratio of isolated direct photon to $\pi^0$ per-trigger yields on the away-side compared to Monte Carlo calculations . . . . .	155
6.26	Charge asymmetry on the away-side compared to Monte Carlo calculations . . . . .	156
6.27	Identified hadron correlations . . . . .	157
6.28	Proton to pion ratio for isolated direct photon recoil jets . . . . .	158
6.29	Proton to pion ratio for isolated $\pi^0$ recoil jets . . . . .	158

# List of Tables

2.1	Summary of the PHENIX recorded data sets . . . . .	52
3.1	Resolution Corrections to $R_\gamma$ . . . . .	55
3.2	Cutoff corrections for $\pi^0$ and reconstruction . . . . .	86
3.3	Effective $R_\gamma$ for isolation method and the quantities used to calculate it . . . . .	95
4.1	Values of fit parameters for single photon efficiency correction function evaluated in PISA . . . . .	108
4.2	Separation Efficiency for photon pairs from $\pi^0$ decay estimated according to the two assumptions . . . . .	109
4.3	$R_\gamma$ and $R_\gamma'$ values and uncertainties on $R_\gamma'$ . . . . .	112
5.1	The ratio of the direct photon to $\pi^0$ associated yields on the near-side in Au + Au collisions . . . . .	124
6.1	The ratio of the inclusive direct photon to $\pi^0$ associated yields on the near-side . . . . .	132
6.2	Widths ( $\sigma$ ) of Gaussian fits to $p_{OUT}$ distributions for $\pi^0$ triggers .	142
6.3	Widths ( $\sigma$ ) of Gaussian fits to $p_{OUT}$ distributions for isolated direct triggers . . . . .	143
1	Near-side direct $\gamma$ -h yields for p + p collisions . . . . .	172
2	Away-side direct $\gamma$ -h yields for p + p collisions . . . . .	173
3	Near-side direct $\gamma$ -h yields for Au + Au collisions . . . . .	173
4	Away-side direct $\gamma$ -h yields for Au + Au collisions . . . . .	174
5	Away-side direct $\gamma$ -h yields for p + p collisions in the isolation method . . . . .	174
6	$\pi^0 x_E$ distributions from p + p collisions . . . . .	175
7	Isolated direct photon $x_E$ distributions from p + p collisions .	176
8	$\pi^0 p_{OUT}$ distributions from p + p collisions . . . . .	177
9	$\pi^0 p_{OUT}$ distributions from p + p collisions (continued) . . . . .	178
10	Isolated direct photon $p_{OUT}$ distributions from p + p collisions	179

# Acknowledgements

I owe a debt of gratitude to everyone to all those who believed in me and helped me out along the way.

In particular, I'm like to acknowledge to my original office-mates who taught me how to program and all smoked too many cigarettes: Felix Matathias, Sean Leckey and Sergey Butsyk and the subsequent generation of office-mates who I hope learned as much from me as I did from them: Anne Sickles, Kieran Boyle, Torsten Dahms and particularly Mike McCumber, without whose coffee machine this work could not have been completed. Also the newer generation of gamma-jetters who suffered my incoherent, rambling derivations and frequent name mis-spellings: Meghan Conners and Jon Chen.

I'd like to also acknowledge Swadhin Taneja for his ontological approach to Monte Carlo. Now we can rest assured without fear of logarithms. For his complicity in building the monstrous piece of code that produced these results, I am immensely indebted to Justin Frantz whose capacity for all-nighters belies his advanced age.

A higher tier of acknowledgement is reserved as a *mordida* for my defense next week. George Sterman for making field theory transparent and giving me a better grade than I deserved. Mike Tannenbaum for encouraging me to make the data sing. Axel Dress for telling me I should have finished long ago. And Barbara for not letting the theorists have all the fun.

# Chapter 1

## Introduction

### 1.1 QCD

Quantum Chromo-Dynamics is the fundamental field theory which describes the strong nuclear interaction. The QCD Lagrangian is

$$\mathcal{L} = \bar{\psi}_i (i\gamma^\mu \partial_\mu - m_i) \psi_i - g G_\mu^\alpha \bar{\psi}_i \gamma^\mu T_{ij}^\alpha \psi_j - \frac{1}{4} G_{\mu\nu}^\alpha G_\alpha^{\mu\nu} \quad (1.1)$$

which is closely analogous to the Lagrangian of QED, the theory which governs atomic interactions. In both cases the field  $\Psi$  represents a spin 1/2 fermion which for QCD is the *quark*. The field  $G$  is the massless spin 1 boson field of the *gluon* which is coupled to the fermion field with strength  $g$ . The gluon field tensor is expressed in terms of the gluon field a

$$G_{\mu\nu}^\alpha = \partial_\mu G_\nu^\alpha - \partial_\nu G_\mu^\alpha + C_{\beta\gamma}^\alpha G_\mu^\beta G_\nu^\gamma \quad (1.2)$$

The final term, absent in QED, represents the interaction of the gluon field with itself. This term is responsible for the qualitatively different nature of matter at the sub-nuclear scale than at the atomic one.

The fundamental symmetries of QCD are described mathematically by the SU(3) group. In the language of group theory, the  $T_{ij}^\alpha$  are the generators of the group which, in this case, are a set of eight 3x3 matrices.  $C_{\beta\gamma}^\alpha$  are a set of constants which satisfy the commutation relations of the generators. Physically, this group corresponds to a theory in which there is a quantum number which can take three values, called color, the QCD analog to electric charge. Flavor, another quantum number of the theory, gives rise to six different known quark states (labeled by the subscript  $i$  in the Lagrangian) each with a mass and (fractional) electric charge. The three lightest quarks, up, down and strange, also obey approximate SU(3) symmetry. This is responsible for the particular

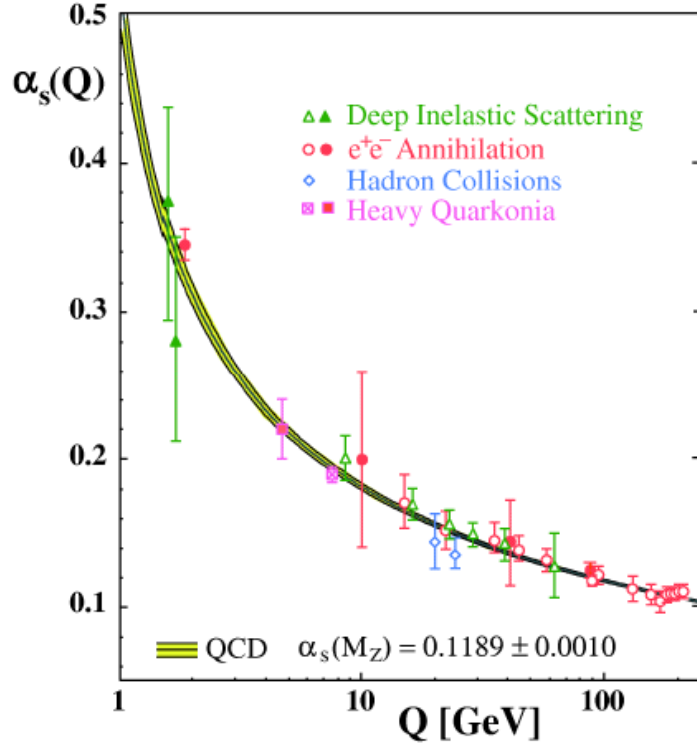


Figure 1.1: The QCD coupling,  $\alpha_s$  as a function of the momentum scale,  $Q$ . The data is extracted from data from different observables at two different orders in perturbation theory (open and closed symbols) and compared to a purely perturbative calculation. [1]

pattern of hadronic bound states, termed the Eight-Fold Way by Gell-Mann, which inspired the parton model in which the fundamental particles are no longer the hadrons but the partons inside them.

QCD and QED are characterized by a scale dependent coupling, meaning that the strength of the interaction depends on the momentum exchange. This dependence is encoded in the beta function which can be expanded as a perturbative series in  $\alpha_s$  ( $\equiv g^2/4\pi$ ).

$$\beta(\alpha_s) = b\alpha_s^2 + \mathcal{O}(\alpha_s^3) \quad (1.3)$$

The  $\beta$  function was famously evaluated at leading order by Gross, Wilczek and Politzer in 1973. They found that

$$b = -\frac{33 - 2n_f}{12\pi} \quad (1.4)$$

where  $n_f$  is the number of quark flavors. The dependence on the momentum scale of the interaction,  $Q$ , is

$$\alpha_s(Q^2) = \frac{1}{b \log(Q^2/\Lambda^2)} \quad (1.5)$$

where  $\Lambda$ , which defines the coupling at which perturbation theory breaks down, must be determined experimentally, and is known to be  $\approx 200$  MeV [2].

Figure 1.1 shows the dependence of the coupling on  $Q$  [1]. In contrast to QED, the  $\beta$  function is negative, at least for small  $n_f$  (only six flavors are known). This means that the strength of the coupling decreases with the momentum scale. This property, known as asymptotic freedom, implies that at large energy the interaction between quarks is small.

As the coupling approaches unity, for example when the distance between two quarks grows large, the energy carried by the fields exceeds the threshold for creation of new matter. The result is the phenomenon known as confinement whereby free quarks are not observed in nature, but rather, they are trapped in bound states for which the net color is zero. Two such types of states are known to exist: mesons, which consist of a quark and an anti-quark, and baryons, which consist of three quarks or three anti-quarks. Properties of these bound states, such as their masses, are generated dynamically and rely on the long range and hence, not perturbatively calculable, behavior of QCD. Fortunately, there exists a method due to Wilson wherein QCD may be calculated computationally at large scales by replacing continuous space by a finite lattice [3]. Lattice QCD, as it is known, is limited in its domain of applicability and must be accepted with a host of caveats. Nevertheless, it has been quite successful, as we shall see, in predicting the behavior of QCD at large temperature and small baryon density.

Before discussing the novel behavior of QCD in this regime, which is the focus of this thesis, it will be useful to discuss how partonic interactions are related to experimental observables such as the data in figure 1.1. Typically the perturbative regime of QCD is explored by high energy collisions of elementary particles, the simplest of which are electron-positron collisions. In such a collision one may obtain quarks in the final state by the reaction  $e^+ + e^- \rightarrow q + \bar{q}$ . Due to confinement however, quarks are not observed at the detector level, but rather hadronize into groups of mesons and baryons, which are correlated in phase space and collectively referred to as jets. The inclusive cross section for hadron production ( $\sigma$ ) may be written as the product of the partonic cross section ( $\hat{\sigma}$ ) and a parametrization of the non-calculable long-range behavior called the fragmentation function (FF), denoted  $D_c^h(z)$ , which is defined as the probability for a parton of flavor  $c$  to fragment into a hadron

taking a fraction  $z$  of its momentum:

$$d\sigma = \sum_c \int dz \ d\hat{\sigma}(p_a, p_b, p_c) \ D_c^h(z) \quad (1.6)$$

This property, known as factorization, is generally taken to hold for a wide variety of observables, although it is only provable in a limited number of cases.

A slightly more complex observable is the semi-inclusive cross section in Deeply Inelastic Scattering, in which an electron and a proton are collided. In this case, there is an additional non-perturbative function term the Parton Distribution Function (PDF) which describes the momentum distribution of the partons inside the proton. The differential cross section is then

$$d\sigma = \sum_{a,c} \int dx_a \ dz \ f_a(x_a) d\hat{\sigma}(p_a, p_b, p_c) \ D_c^h(z) \quad (1.7)$$

where (Bjorken)  $x$  is the fraction of the proton's momentum carried by the parton. On the surface, this seems somewhat troubling since the observed hadronic cross section would not uniquely determine the parton distribution and fragmentation functions. Fortunately, the long range behavior of these functions is generally believed to be independent of the collision process, a property known as universality. Hence, the same fragmentation functions apply regardless of the species of particle collided. Analogously, the parton distribution is only a property of the objects being collided and can be factorized from the collision process and subsequent fragmentation.

The cross section for hadro-production from proton-proton collisions can then be expressed as a similar form with the addition of a second integral over the additional parton:

$$d\sigma = \sum_{a,b,c} \int dx_a \ dx_b \ dz \ f_a(x_a) \ f_b(x_b) \ d\hat{\sigma}(p_a, p_b, p_c) \ D_c^h(z) \quad (1.8)$$

In a somewhat simplified picture this leads to a progression in which FF's are determined in  $e^+ + e^-$  collisions and used in DIS data. In turn, the DIS data are used to determine the PDF's which can then be applied in p+p collisions.

p+p collisions are important baseline data for collisions of heavy nuclei because, naively, one might expect a nuclear collisions to be a simply the sum of many independent p + p collisions. As it turns out, expectations for hadronic observables must be modified in nuclear collisions. Such departures provide a window into physics beyond the vacuum behavior of QCD accessed via elementary particles collisions. In the next section, the motivation for such studies is elucidated by providing some historical context.

## 1.2 Relativistic Heavy-Ion Collisions and the Quark-Gluon Plasma

The study of nuclear collisions is not a new endeavor and, in fact, predates the parton model. The history of the field can be traced back to the HILAC (Heavy Ion Linear Accelerator) at Berkeley, the first dedicated heavy-ion accelerator, which began operation in 1957. The objectives of the field at the time were the creation of new elements by nuclear transmutation and the investigation of radiation damage to human tissue for space travel [4]. During the 1970's a new paradigm began to emerge in which heavy-ion collisions were viewed as a tool to study the equation of state of matter at high temperature and density, conditions thought to govern the behavior of matter inside neutron stars. The accelerators of this era, the BEVALAC at Berkeley and the UNILAC at GSI, introduced much of the conceptual framework that is used to understand heavy-ion collisions today, an noteworthy example being the notion of collective flow [5].

By this time, the parton model of the nucleon elucidated by Feynman and Gell-Mann had already been verified by the Deeply Inelastic Scattering experiments at SLAC in the late 1960's, but it was not until the 1970's that the underlying theory QCD was developed in earnest. The field of heavy-ion physics would be profoundly influenced by the concept of asymptotic freedom. Based on this idea, Collins and Perry predicted that at sufficiently high densities long-range interactions would be effectively screened and nuclear matter would behave as an ideal gas of quarks and gluons [6]. These ideas were further developed by Shuryak and others who applied the machinery of finite temperature field theory to hot, dense matter [7–11]. It was shown that at high temperature gluons screen the color charge analogously to Debye screening in QED plasmas. The creation of this fundamentally new state of matter, the so-called Quark-Gluon Plasma (QGP), became one of the primary goals of nuclear physicists over the course of the following few decades and helped to motivate the construction of several colliders: the AGS, SPS, RHIC and the LHC.

### 1.3 Properties and Signatures of the Quark-Gluon Plasma

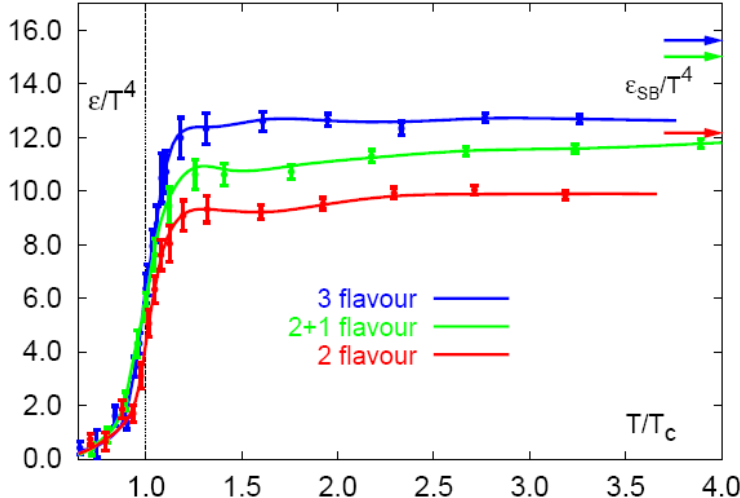


Figure 1.2: Lattice predictions for  $\epsilon/T^4$  as a function of  $T/T_c$  [12].

Although the prediction of a QGP state is based on perturbative ideas, its properties, most importantly the transition temperature, cannot be estimated perturbatively [13]. Although it was not recognized as such at the time, one estimate of the transition temperature actually pre-dates the advent of QCD. In the 1960's Hagedorn developed an effective theory to explain the number of resonance states. He found that the number of states in his model diverged at a temperature of 160 MeV, which is surprisingly close to modern estimates for the phase transition to a QGP [14].

With the advent of lattice QCD in the late 1970's a new tool became available to perform calculations at large coupling and high temperature. Figure 1.2 shows lattice predictions of the energy density ( $\epsilon$ ) divided by the fourth power of the temperature ( $T$ ), which for a thermodynamic system, is proportional to the number of degrees of freedom. The  $T$  axis has been scaled by the critical temperature,  $T_c$ , which is calculated to be 170 MeV.  $\epsilon/T^4$  exhibits a sharp rise at  $T_c$ , suggesting a phase transition from hadronic to partonic degrees of freedom. The value of  $\epsilon/T^4$  is shown to reach a plateau at approximately 80% of the Stephan-Boltzmann limit (indicated by arrows) which would describe an ideal gas of partons. The deviation from this limit has important ramifications in regards to the description of the QGP near  $T_c$ . Foremost among them, is the observation that the matter is thought to be strongly coupled [15], in

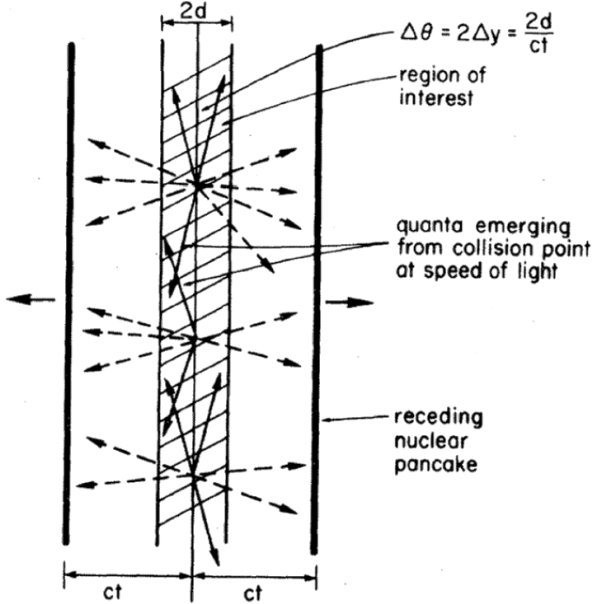


Figure 1.3: Schematic diagram illustrating particle production from the overlap zone of relativistic, colliding nuclei [17].

distinction to the original weakly coupled expectation of Collins and Perry. Lattice calculations are to be taken with a number of caveats, the discussion of which is not in the scope of this work. Nevertheless, a mounting body of experimental evidence supports the existence of the phase transition suggested by these results [16].

Lattice calculations, as well as estimates based on dimensional analysis [16], indicate that the transition to partonic degrees of freedom occurs at an energy density  $\epsilon \sim 1$  GeV. In order to connect the energy density in heavy-ion collisions to a physical observable and, moreover, to obtain a physical picture of nuclear collisions, I introduce the Bjorken picture [17], following closely the discussion in [16]. As depicted in figure 1.3, the nuclei are taken to be thin disks, contracted in the longitudinal (beam) direction due to their relativistic velocities, which pass through each other and produce particles in their wake. If one considers a longitudinal slice of thickness  $dz$  then the velocity of produced particles will be constrained to the interval  $0 \leq \beta_{||} \leq dz/\tau_{Form}$  where  $\tau_{Form}$  is the time-scale on which parton production takes place. The number of particles in the slice is then  $dN = (dz/\tau_{Form}) \frac{dN}{d\beta_{||}}$  which can be expressed in the boost-invariant form  $dN = (dz/\tau_{Form}) \frac{dN}{dy}$ . If  $\langle m_T \rangle$  is transverse mass of a particle (which is equivalent to the energy in the center of mass frame) then the energy density at the formation time is

$$\langle \epsilon(\tau_{Form}) \rangle = \frac{dN\langle m_T \rangle}{dzA} = \frac{dN(\tau_{Form})}{dy} \frac{\langle m_T \rangle}{\tau_{Form} A} = \frac{1}{\tau_{Form} A} \frac{dE_T(\tau_{Form})}{dy} \quad (1.9)$$

where  $A$  is the cross-sectional area of the nucleus, approximately 10 fm for Au, and the total transverse energy  $E_T$  is taken to be well approximated by  $\langle m_T \rangle N$ . The formation time can be roughly estimated via the uncertainty principle as  $\langle m_T \rangle / \hbar$ . In the limit that the particles are non-interacting after formation then  $\frac{dE_T(\tau_{Form})}{dy}$  can be equated with the measured  $\frac{dE_T}{d\eta}$ , which is similarly true for the number density. PHENIX has measured  $dE_T/dy$  to be  $\sim 600$  GeV in the most central collisions which, combined with the observed number density, implies  $\langle m_T \rangle \sim 0.57$  GeV. This yields an energy density of 15 GeV, well in excess of the phase transition boundary predicted by lattice QCD.

### 1.3.1 Thermalization and Elliptic Flow

In discussing the temperature of the matter produced in nuclear collisions, we have implicitly assumed that the concept of temperature is appropriate, i.e., that the matter is thermalized. Thermalization requires rescattering of the produced particles on a short time scale, such that they can adequately be described by hydrodynamics (*i.e.* as an expansion in the mean-free path). Such rescattering is manifest in collective motion of the matter in the radial direction due to the outward pressure generated by the expansion of the matter. This radial flow, as it is known, is evidenced by the violation of transverse kinetic energy ( $m_T - m$ ) scaling for central nuclear collisions, which would describe a purely thermal distribution [18]. An excess of yield at high  $p_T$ , with respect to the scaling expectation, is understood to be the radial boost imparted by the expanding matter. Radial flow alone however, does not establish whether collective motion was generated at early time, in the partonic phase, or later in the hadronic phase. To answer this question one considers variations in particle production as a function of azimuthal angle relative to the reaction plane ( $\phi_R$ ), the plane formed by the impact parameter and the beam axis. Canonically, this variation is expressed as a Fourier series.

$$\frac{dN}{d(\phi - \phi_R)} \propto A (1 + 2v_1 \cos(\phi - \phi_R) + 2v_2 \cos(2(\phi - \phi_R)) + \dots) \quad (1.10)$$

If one considers the oblong shape of the overlap region of slightly non-central collisions, the nucleon density is larger in the direction of the reaction

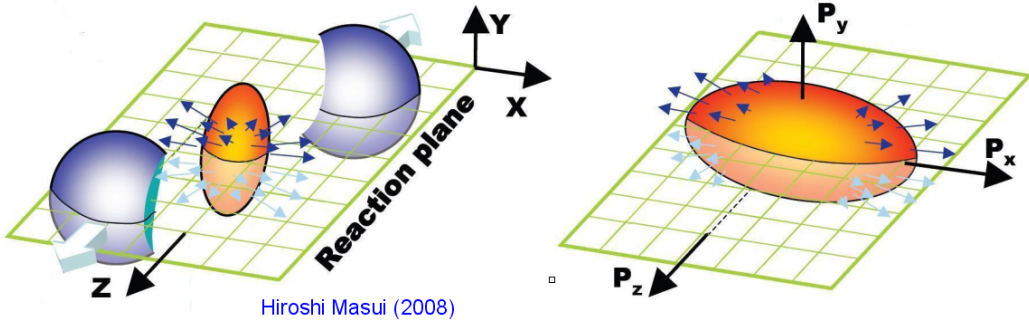


Figure 1.4: Cartoon illustrating the concept of elliptic flow. An asymmetry in the collision geometry of nuclei at finite impact parameter (left) results in a momentum anisotropy of produced particles (right) given sufficiently rapid thermalization.

plane than in the orthogonal direction. If the matter thermalizes quickly enough, this asymmetry of the collision zone would result in anisotropic particle production as demonstrated in the cartoon shown in figure 1.4. The dominant term in the Fourier expansion corresponding to this effect is  $v_2$ . Since such a term corresponds to an ellipse in momentum space, the mechanism which generates the effect is referred to as elliptic flow<sup>1</sup>.

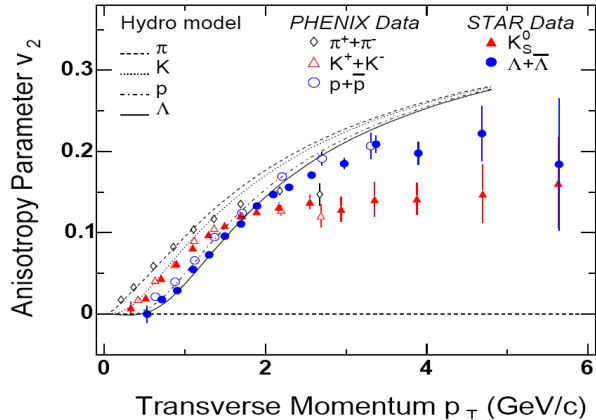


Figure 1.5:  $v_2$  as a function of transverse momentum for various species of charged hadrons compared to predictions for ideal hydrodynamics from [19].

Figure 1.5 shows elliptic flow data for several hadron species compared to predictions from an ideal hydrodynamic model. The data appear to agree quite

---

<sup>1</sup>Note that non-collective effects which are correlated to the reaction plane, such as jet quenching, can also give rise to a  $v_2$  modulation.

well with a hydrodynamic description until  $\sim 2$  GeV where other mechanisms of particle production are thought to become the dominant. Although this agreement is encouraging, the question of thermalization is not from a closed issue. For example, it has been pointed out that choosing different initial conditions (which are input into hydrodynamic calculations) results in larger elliptic flow when coupled with ideal hydrodynamics, overshooting the data [20].

A more explicit demonstration of the partonic nature of the elliptic flow is the observation of constituent quark scaling. Figure 1.6 shows that baryon and meson data lie nearly perfectly on the same curve when the  $v_2$  values are scaled by the number of quarks and plotted as function of the, similarly scaled, transverse kinetic energy. This indicated that the relevant degrees of freedom at the time of elliptic flow generation are partonic [21].

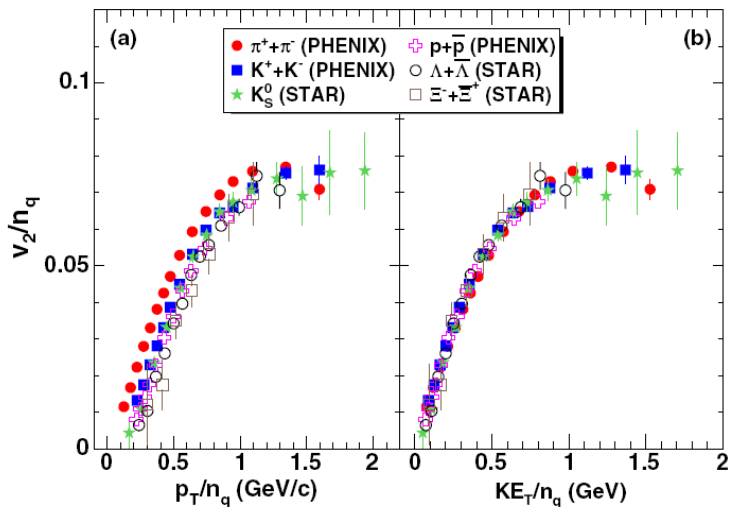


Figure 1.6:  $v_2$  as a function of  $p_T$  (left) and  $KE_T$  (right) scaled by the number of constituent quarks in minimum bias Au + Au collisions. [21].

### 1.3.2 High $p_T$ Suppression and Jet Energy Loss

Elliptic flow is only one of the pieces of evidence that support the picture of QGP formation in heavy-ion collisions. I will not attempt to give an inclusive overview of these results, as there are many. Instead, I will focus on what is arguably the most important result from the RHIC program: the observed depletion in the yield of high transverse momentum hadrons.

Nuclear effects on single particle observables are quantified by the nuclear modification factor,  $R_{AA}$ .

$$R_{AA} = \left( \frac{1}{N_{evt}} \frac{d^2 N^{AA}}{dp_T dy} \right) / \left( \frac{\langle N_{coll} \rangle}{\sigma_{inel}^{pp}} \frac{d^2 \sigma^{pp}}{dp_T dy} \right) \quad (1.11)$$

This quantity is the ratio of the observed per-event yield in nuclear collisions to the expected yield. The latter is the product of the p + p cross section,  $d^2 \sigma^{pp} / dp_T dy$ , and a scale factor  $\frac{\langle N_{coll} \rangle}{\sigma_{inel}^{pp}}$ , which is explained as follows. If the Au + Au collisions were simply a collection of superimposed p + p collisions, the cross section for a given inelastic process would be simply be product of the total number of nucleons participating in the collision ( $N_{part}$ ) and the inelastic nucleon-nucleon cross section ( $\sigma_{inel}^{pp}$ ). The cross section for soft production can reasonably be expected to scale in such a way.

For hard particle production, on the other hand,  $N_{part}$  scaling is known to be violated [22]. In the majority of the collisions only a small amount of momentum is exchanged. This means that a struck nucleon may suffer additional collisions. Since each of these subsequent collisions are equally as likely to result in a hard scattering, the cross section should instead, scale with the number of collisions ( $N_{coll}$ ).

$N_{coll}$  can be estimated using a simple set of assumptions collectively referred to as the Glauber model [23]. Using the Woods-Saxon parametrization of the nuclear density one can determine the relationship between  $N_{coll}$  and the impact parameter. Often,  $R_{AA}$  is expressed in terms of so-called nuclear thickness function  $\langle T_{AB} \rangle = \langle N_{coll} \sigma^{pp} \rangle$ .

$$R_{AA} = \left( \frac{1}{N_{evt}} \frac{d^2 N^{AA}}{dp_T dy} \right) / \left( \langle T_{AB} \rangle \frac{d^2 \sigma^{pp}}{dp_T dy} \right) \quad (1.12)$$

$R_{AA}$  results for Au + Au collisions are shown in figure 1.7. For central collisions the yield of light hadrons is suppressed by nearly a factor of 5. The absence of a similar effect in d + Au collisions demonstrates that the suppression is final state effect [25]. It is now generally accepted that the mechanism underlying high  $p_T$  suppression is rapid energy loss of the hard-scattered partons as they traverse the nuclear medium. Bjorken was the first to predict such an effect [26]. He assumed energy loss would proceed by elastic scattering of quarks off partons in the QGP. Gyulassy and Wang realized however, that induced gluon bremsstrahlung should be the dominant mode of energy loss <sup>2</sup> [27]. They also recognized that the characteristic time of gluon emission was long enough that one needed to consider coherence, the so-called Landau-

---

<sup>2</sup>Heavy quarks are an interesting exception in which collisional energy loss may in fact dominate.

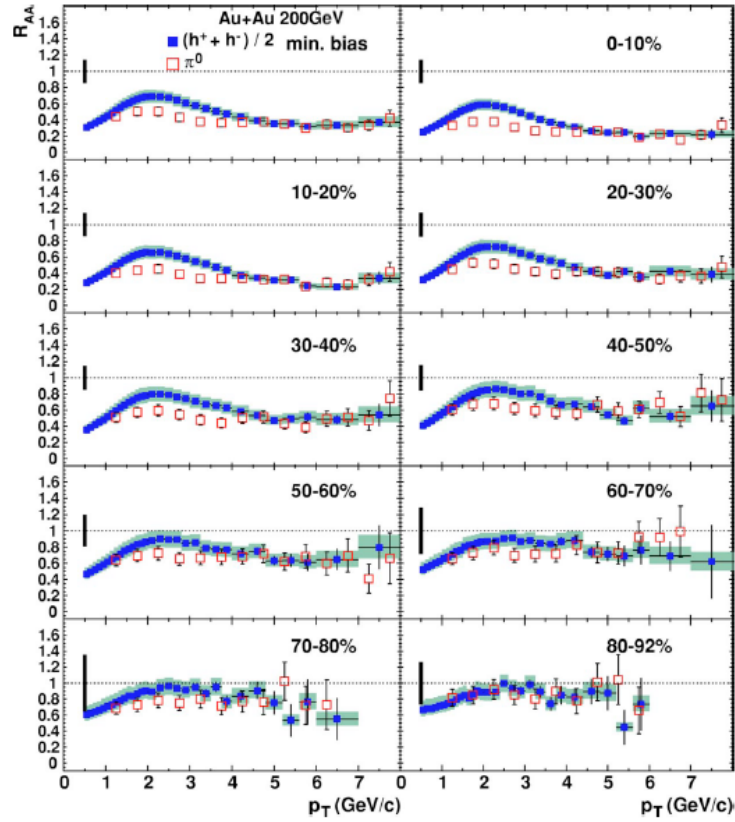


Figure 1.7: Nuclear modification factor for charged hadrons and neutral pions as a function of  $p_T$  for different centrality selections from PHENIX. [24]

Pomeranchuk-Migdal (LPM) effect, which was a previously unsolved problem in QCD [28], [29]. On the basis of the LPM effect, the energy loss is predicted to depend on the path-length squared,  $\Delta E \propto \hat{q}L^2$ , for a static medium [30], although for an expanding medium, the dependence may reduce to linear [31].

Over the course of the last decade a number of competing models of energy loss have been developed. We shall not attempt to detail the latest development in this rapidly developing field and instead refer the reader to the recent studies in [32–34]. Two of the early models, GLV [31] and BDMPS [30] are often considered as limits. In the former, the parton experiences a finite number of scatterings and the energy loss is evaluated as an expansion in the opacity. In the latter type of model the energy loss of the parton is continuous. These two limits can lead to qualitatively different observations. In all cases, the strength of the energy loss is quantified in terms of a single parameter which, for GLV-type models is the gluon density ( $dN_g/dy$ ) and for BDMPS-type models is the transport parameter  $\hat{q}$ , which represents the average momentum transfer

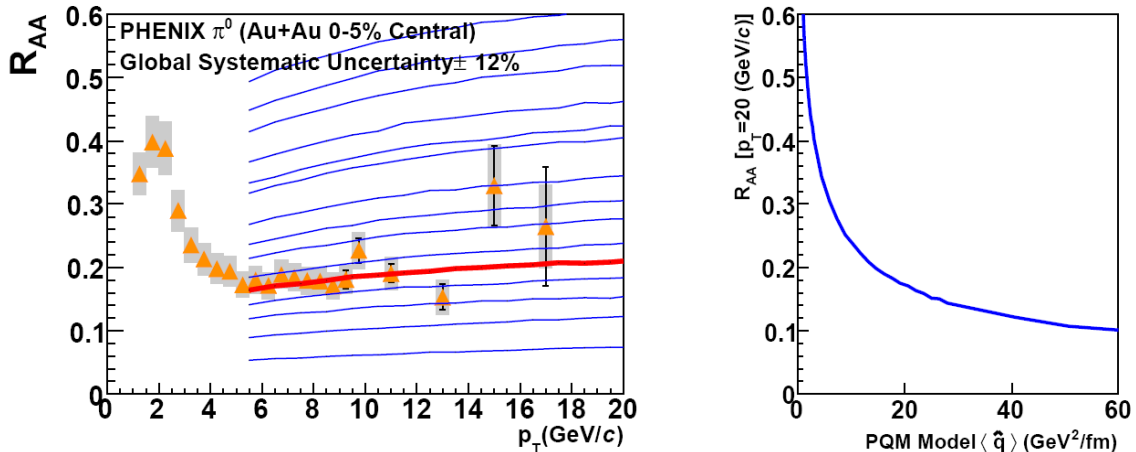


Figure 1.8: Left:  $\pi^0 R_{AA}$  compared to predictions from the PQM model for various values of  $\hat{q}$ . Right: The dependence of  $\hat{q}$  on  $R_{AA}$ . [35]

squared per-unit path-length.

As the RHIC data demonstrating large high  $p_T$  suppression emerged, the field began to shift its focus from searching for signatures of QGP formation to measurements of its properties. Since it can be directly related to medium properties, the determination of the energy loss strength, including its full space-time dependence, has become central to the field. Often such measurements are referred to as jet tomography. In contrast to conventional medical tomography in which an X-ray beam of known energy and intensity is used, in this case the probe is a sample of hard scattered partons, emanating from within the medium itself. The observed attenuation pattern can then be used to infer the opacity of the medium to color charged objects, a dynamical property of QCD matter that is neither calculable in pQCD or computable on the lattice.

Despite much progress over the last decade, there still remain a number of nagging open issues with regard to jet quenching models. The relationship between measurement and medium properties remains highly model dependent [36, 37] even in the case of a static, uniform medium, the so-called QGP brick problem. Worse, there is no general agreement on how to incorporate the space-time evolution and collective flow of the system. The values of the path-averaged transport coefficient  $\langle \hat{q} \rangle$  extracted from the different models span an uncomfortably large range of  $1 - 15 \text{ GeV/fm}$  [38, 39]. Recently, a collaboration of experimentalists and theorists called TECHQM was formed to address these issues systematically. Their progress can be tracked via their web-page [40].

Difficulties in extracting the transport parameter are not necessarily limited

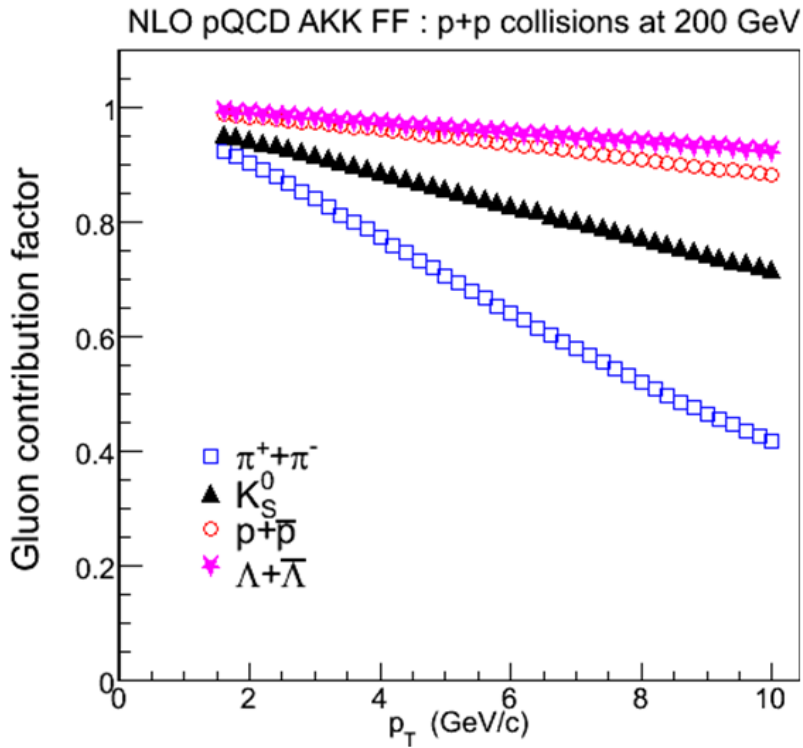


Figure 1.9: The fraction of various species of particles that come from gluon jets as a function of their  $p_T$  as parameterized by the AKK05 fragmentation functions [43]

to ambiguities in the theoretical description but may also arise from inherent limitations in the measurements performed. For example, one model found that for a sufficiently opaque medium,  $R_{AA}$  becomes saturated, i.e., the parton loses essentially all of its energy. The resulting hadron spectrum comes entirely from the surface of the collisions zone and is insensitive to any further increase in the opacity [41]. PHENIX performed a statistical analysis of the sensitivity of the various models to its  $\pi^0 R_{AA}$  data. The left panel of figure 1.8 shows the PHENIX  $\pi^0 R_{AA}$  data compared to predictions from the PQM model [41] for different values of  $\langle \hat{q} \rangle$ . On the right the dependence of  $\langle \hat{q} \rangle$  on  $R_{AA}$  is shown. The calculation does indeed flatten towards smaller values of  $R_{AA}$  demonstrating a reduced sensitivity. However, the path-averaged  $\langle \hat{q} \rangle$  is constrained to be within about 25% of its value of demonstrating a fair degree of sensitivity is preserved. [35, 42]

One of the predicted features of partonic jet energy loss that remains unobserved is stronger energy loss for gluons compared to quarks due to the presence of the color factor in the QCD coupling ( $C_F = 9/4$  for quarks vs 3

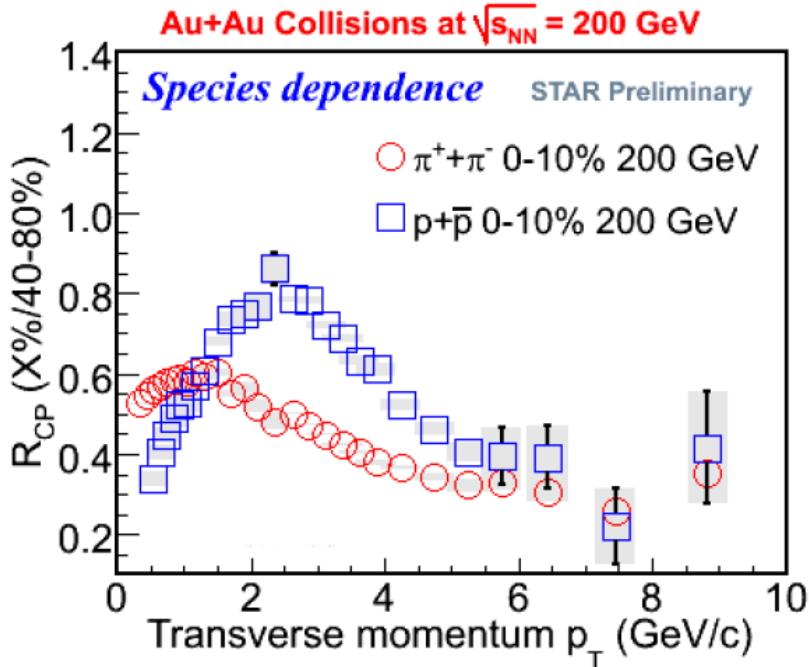


Figure 1.10:  $R_{CP}$  as a function of  $p_T$  for baryons and mesons from the STAR collaboration [45].

for gluons). It is often claimed that identified baryon and meson  $R_{AA}$  measurements should be sensitive to this factor [44]. The basis for this claim is the AKK05 set of fragmentation functions which indicate that at large  $z$  nearly all protons come from gluon jets as shown in figure 1.9 [43]. Figure 1.10 shows the STAR results for  $R_{CP}$  (similar to  $R_{AA}$  but peripheral events are substituted for p + p collisions) of identified baryons and mesons [45]. Above 5 GeV, where energy loss effects are expected to dominate,  $R_{CP}$  for baryons and mesons is similar to within the uncertainties. It has been suggested that this may signify energy loss saturation as discussed above, i.e., both quarks and gluons lose nearly all of their energy [46]. In the present work I will address the model dependence underlying the proton-gluon jet correspondence and propose that the color charge effect may be better studied using direct photon and  $\pi^0$  correlations.

The saturation argument suggests a fundamental limitation to the use of single particle yields as a probe of energy loss. Because the initial energy of the parton is not known, one has little ability to distinguish between a scenario in which a high  $p_T$  parton loses a large fraction of its energy and emerges as a small  $p_T$  jet as compared to the case in which a small  $p_T$  jet

simply emerges from the surface of the collision zone unaltered. Increased sensitivity can be achieved by more measurements in which the average path-length can be varied in a controlled way by tuning an experimental parameter or by better determining the initial energy of the parton. The former objective was accomplished by measuring  $R_{AA}$  as a function of angle with respect to the reaction plane [47]. The data appear to be at odds with a simple  $L$  or  $L^2$  dependence of the energy loss predicted by the LPM effect, a puzzle that has not yet been definitively resolved. The motivation for  $\gamma + jet$  measurements in nuclear collisions is that they fulfill the latter objective, since the initial energy of the away-side parton is easily determinable. Before describing these measurements, it will be useful to introduce jet and photon measurements in both elementary and heavy-ion collisions.

## 1.4 Jets and Two-Particle Correlations

### 1.4.1 Elementary Collisions

Evidence for hard scattering was first observed by the CERN-ISR experiments in the early 1970's as an excess in the single particle yield at high  $p_T$  [48]. As  $\sqrt{s}$  increases the data show an increasingly power-law-like behavior in contrast to the exponential behavior observed at lower energies. The definitive measurement of jet production came from evidence of back-to-back correlations from the SPEAR storage ring [49]. Contemporary jet measurements, for example at the Tevatron, invoke jet reconstruction algorithms to determine the full energy of the jet event-by-event. These methods are difficult to apply in heavy-ion collisions due to the overwhelming background from soft collisions. Instead, a very useful approach has been to measure correlations between particles.

The idea behind two-particle correlation measurements is to find a sample of high  $p_T$  particles, referred to as *triggers*, in order to obtain a sample dominated by jet events. Then one studies the yield of *partners*, i.e., particles associated with the trigger (also referred to as the conditional yield, associated yield or per-trigger yield). The most common example of such a measurement is to fix a window in trigger and associated  $p_T$  (denoted  $p_{T,t}$  and  $p_{T,a}$ ) and then to count the associated yield per trigger as a function of  $\Delta\phi$ , the azimuthal angle separating the two particles. We will often use the following shorthand to express such a per-trigger yield, where  $N$  is understood to be the number of pairs.

$$Y(\Delta\phi) \equiv \frac{1}{n^{triggers}} \frac{dN}{d\Delta\phi} \quad (1.13)$$

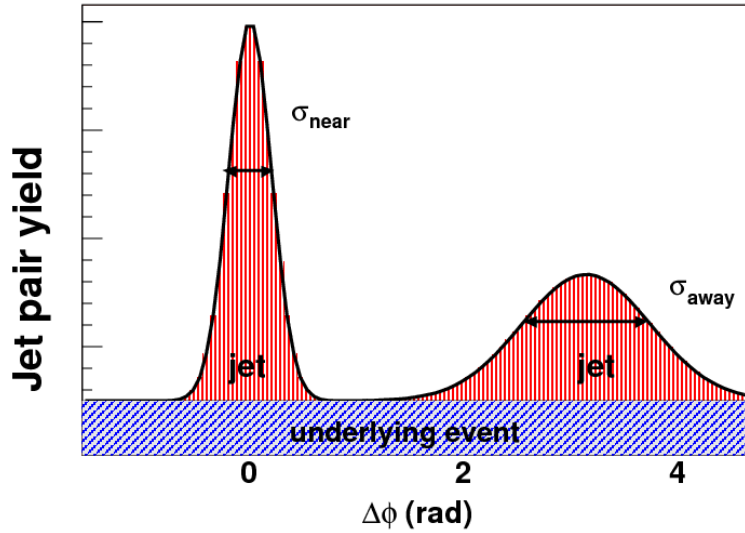


Figure 1.11: Cartoon illustrating a measurement of two-particle correlations from jets. Adapted from [50].

An example of a per-trigger yield measurement using  $\pi^0$  triggers and charged hadrons partners ( $\pi^0$ -h) in p + p collisions is shown in figure 1.11. The two-peak structure characteristic of such measurements shows that the event sample is dominated by di-jets, i.e., hard  $2 \rightarrow 2$  parton scattering. The peaks sit on top of a pedestal which is due to initial and final state interactions amongst the beam remnants and the hard-scattered partons [51]. In the PHENIX data this "underlying event" is usually subtracted away in both p + p and A + A collisions as discussed in section 3.3.1. In the case of A+A collisions there is a much larger underlying event resulting from the multitude of nucleon-nucleon interactions which occur. Moreover, the elliptic flow of the underlying event must be properly accounted for in order to study the jet correlations exclusively.

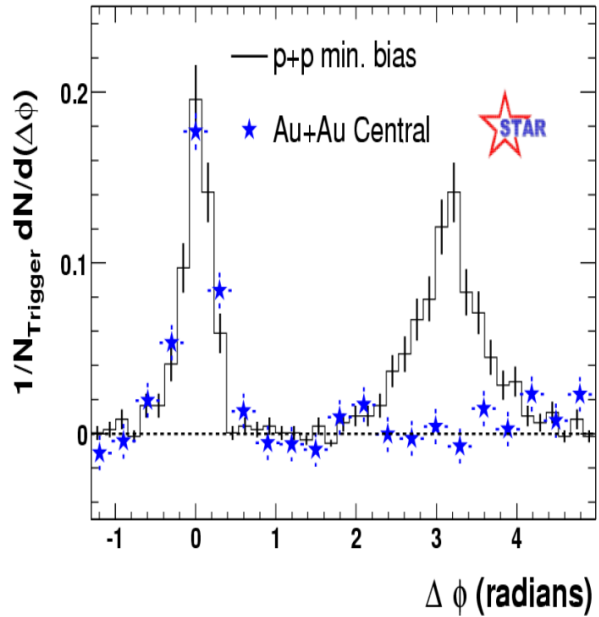


Figure 1.12: Per-trigger yield for hadron-hadron pairs in  $\sqrt{s_{NN}} = 200$  GeV p + p and Au + Au collisions. [52]

### 1.4.2 Heavy-Ion Collisions

A number of very interesting measurements of two particle correlations have been made in heavy-ion collisions. The STAR experiment performed a hadron-hadron ( $h - h$ ) correlation measurement with triggers of  $p_{T,t} > 4$  GeV and partners of  $2 \text{ GeV} < p_{T,a} < p_{T,t}$ . The result, shown in figure 1.12, demonstrates that for central Au + Au collisions the near-side jet looks very similar to p + p but the away-side jet completely disappears. This is consistent with a picture in which the near-side jet is usually produced near the surface and the away-side jet is completely absorbed by the medium.

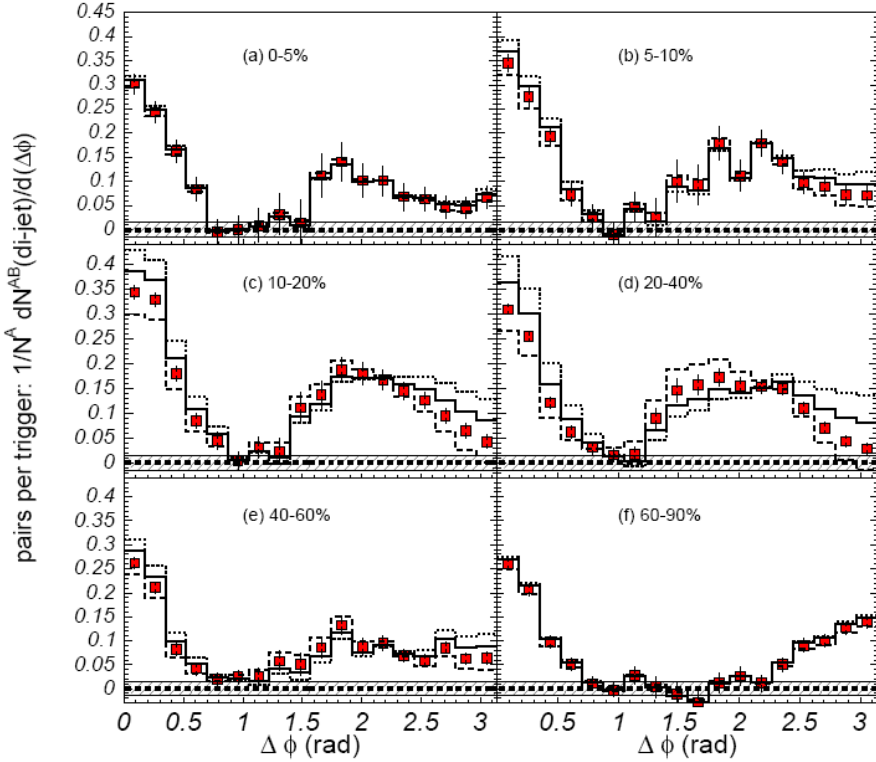


Figure 1.13: Per-trigger yield for hadron-hadron pairs in  $\sqrt{s_{NN}} = 200$  GeV p + p and Au + Au collisions. [53]

PHENIX found that by performing measurements at lower values of partner  $p_T$  one was able to observe the medium response to the deposited energy. Figure 1.13 shows a similar  $h - h$  correlation measurement but now for  $2.5 < p_{T,t} < 4$  GeV and  $1 < p_{T,a} < 2.5$  GeV for several centrality selections. For this lower  $p_T$  selection one finds that opposite side correlations are no longer backward peaked, but rather peaked more than one radian away from  $\pi$ . On the other hand, at large enough values of  $p_T$  STAR showed that the away-side jet returns to its standard shape, as shown in figure 1.14.

An in-depth study of the  $p_T$  evolution reveals that the data may be fairly well described by assuming that the shape of the correlation is the sum of two contributions: a Gaussian peak centered at  $\pi$  as is observed in p + p collisions and another Gaussian peak offset from  $\pi$  by about 1.1 radians [50]. Figure 1.15 shows a fit to a  $\Delta\phi$  distribution using such an ansatz. Rather than performing a fit, which is somewhat dependent on the functional form chosen one often defines a "head" region around  $\pi$  which is sensitive to the so-called punch-through jet and less so to medium response and a "shoulder" region

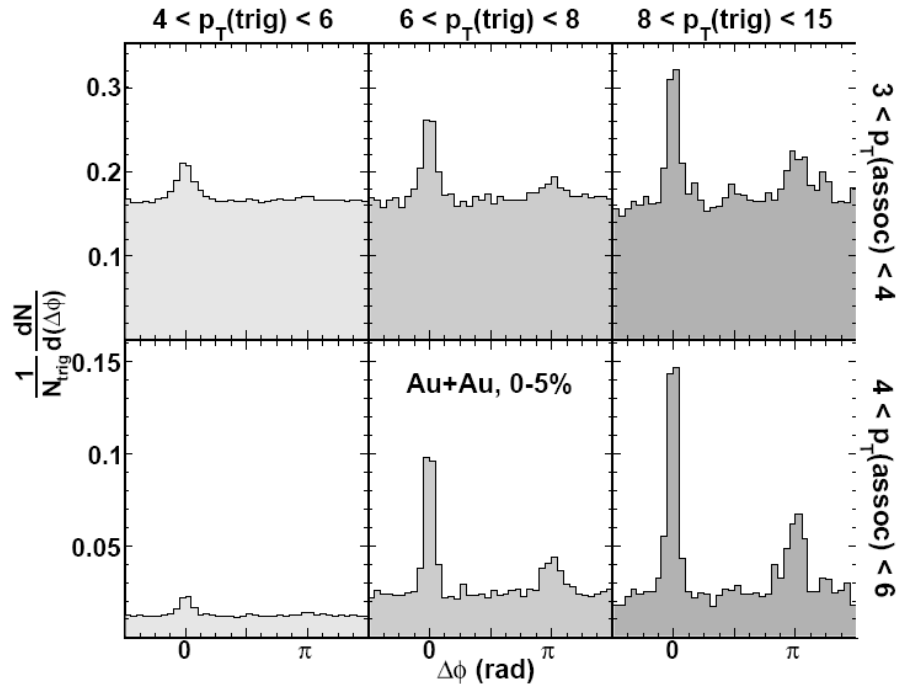


Figure 1.14: Per-trigger yield for hadron-hadron pairs in  $\sqrt{s_{NN}} = 200$  GeV Au + Au collisions. [54]

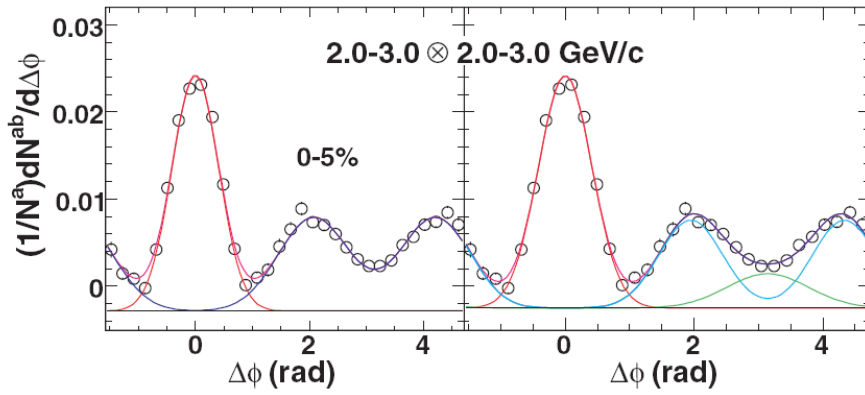


Figure 1.15: Example of fits to the Au + Au per-trigger yield in central collisions. The right panel shows a three Gaussian fit also shown separated into its head and shoulder components [50].

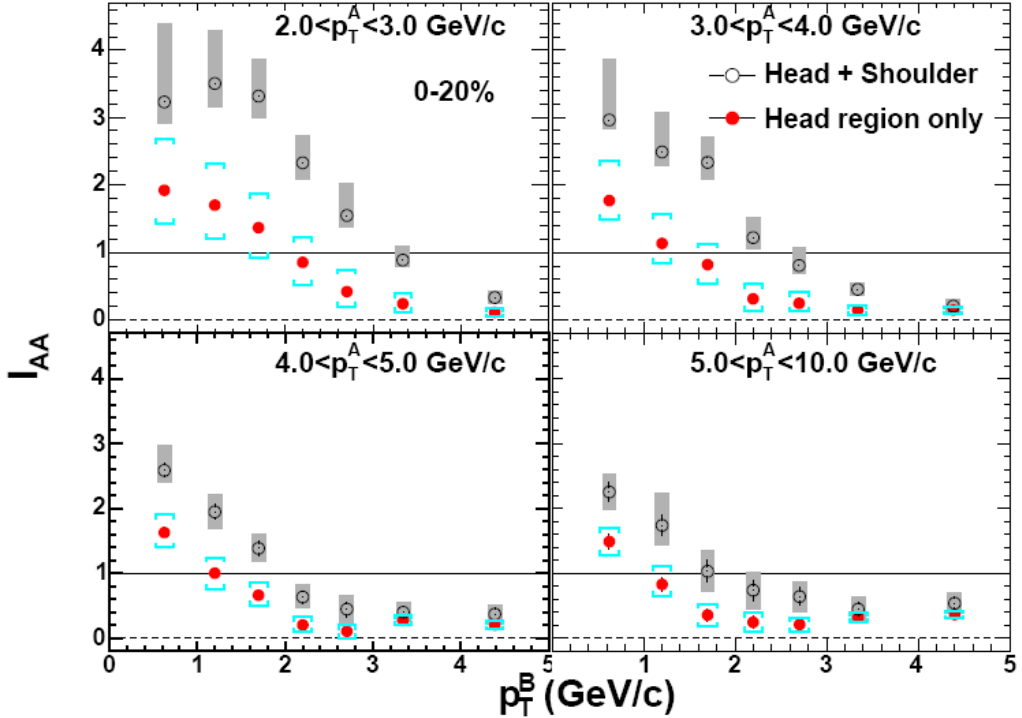


Figure 1.16:  $I_{AA}$  as a function of  $p_{T,a}$  for various selections of  $p_{T,t}$  for the head region ( $|\Delta\phi - \pi| < \pi/6$ ) and the head + shoulder regions ( $-\Delta\phi - \pi < \pi/2$ ) [50].

centered around  $\pi \pm 1.1$  radians which displays the opposite properties. One can compare both of these regions to data from  $p + p$  collisions by defining the quantity  $I_{AA}$ , which is the ratio of the per-trigger yield in  $A + A$  to  $p + p$ . Figure 1.16 shows  $I_{AA}$  for the head region and the head + shoulder region [50]. In the absence of any medium response one would expect the  $I_{AA}$  for the two regions to be the same if parton energy loss changes only the magnitude of the punch-through peak but not its shape. In this picture the medium response appears as an excess of the  $I_{AA}$  of the head + shoulder region over the head alone below about 2-3 GeV depending on the  $p_{T,t}$  selection.

There is a wealth of other interesting data on the shoulder feature including its dependence on orientation with respect to the reaction plane and evidence of its conical nature from three particle correlations. For the present purposes it will suffice to simply have a rough idea of the  $p_T$  range over which the medium response is apparent.

Another interesting feature of two-particle correlations in heavy-ion collisions appears when correlations in pseudo-rapidity dependence are studied.

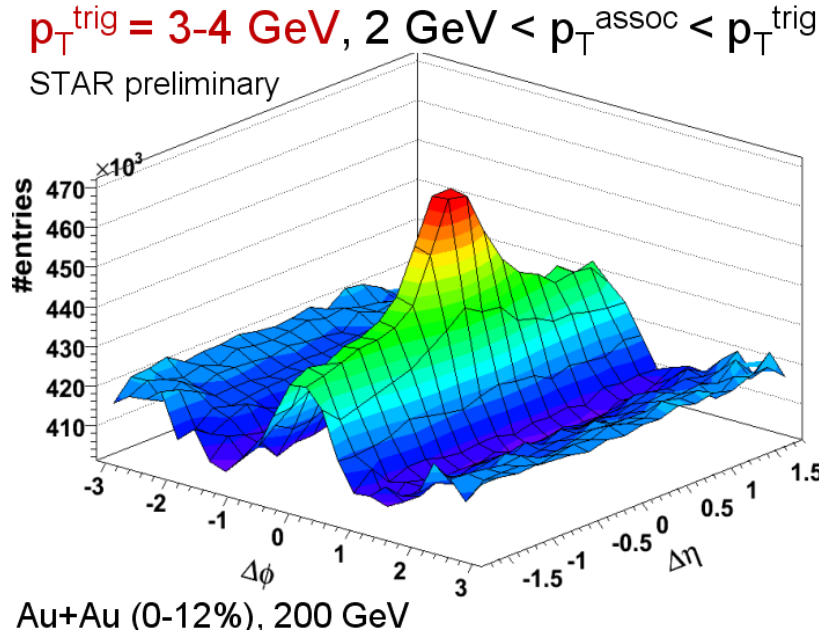


Figure 1.17: Yield of hadron-hadron pairs as a function of both  $\Delta\phi$  and  $\Delta\eta$  in  $\sqrt{s_{NN}} = 200$  GeV Au + Au collisions. [55]

Figure 1.17 shows the per-trigger yield vs. both  $\Delta\phi$  and  $\Delta\eta$  [55]. Beyond the near-side peak a clear long range correlation extending out to the full range of 1.5 units covered by this measurement.

Both the cone and the ridge seem to be aspects of the medium's response to a hard parton and are likely connected. If the theoretical framework of jet energy loss is presently reaching maturity then the correct description of energy redistribution or medium response is only in its infancy or perhaps has not yet been conceived. There are a number of theories on the market to explain both the cone [56], [57] and ridge [58], [59], of which I have only referenced a small sample.

## 1.5 Direct Photons

Now that we have reviewed the landscape of two-particle correlations in nuclear collisions we turn to the other ingredient of the  $\gamma - h$  measurement, the direct photon.

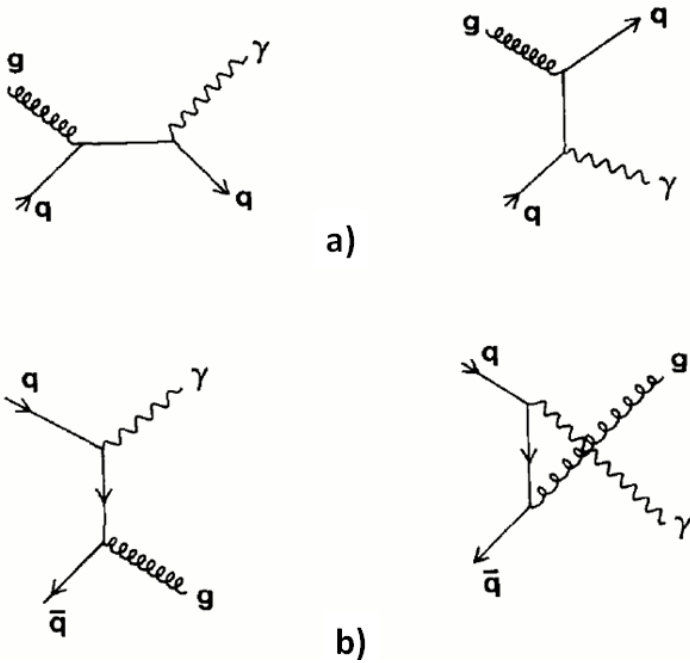


Figure 1.18: Feynman diagrams representing LO direct photon production: a) quark-gluon Compton scattering b) quark annihilation. Figures adapted from [60]

### 1.5.1 Direct Photons at Leading Order

To leading order direct photons have two very important properties that make them a valuable tool in both particle physics and heavy-ion physics.

- There are relatively few leading order (LO) diagrams which contribute to direct photon production
- The photon-quark coupling is point-like and therefore not complicated by long-range QCD behavior (jet fragmentation) in the final state in distinction to hadronic observables

Figure 1.18 shows the two main types of diagrams which contribute to direct photon production. Diagrams a) represent quark-gluon Compton scattering while b) represent the quark-antiquark annihilation process. In  $p + p$  collisions the Compton-type process dominates the cross section by roughly an order of magnitude over annihilation as a result of the scarcity of antiquarks. Due to the presence of the gluon in the initial state, this process is sensitive to the gluon distribution function, a point to which we will return below.

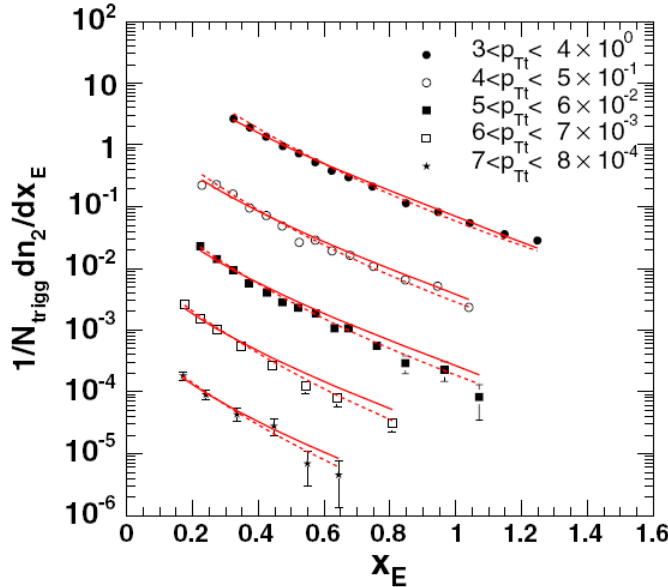


Figure 1.19:  $x_E$  distributions from  $\pi^0$ -h correlations for several ranges of  $p_{T,t}$ , compared to calculations using quark (solid) and gluon (dashed) fragmentation functions as parameterized by the LEP data [61].

## 1.6 Correlations Using Direct Photons

The point-like nature of the photon coupling turns out to be an extremely useful property of the  $\gamma + jet$  channel if one wants to measure the fragmentation function, or effective modifications to the fragmentation function in nuclear collisions, as we shall discuss shortly. It was originally believed that the fragmentation function could be measured using back-to-back correlations by a simple rescaling of the conditional yields *i.e.*, the distribution of  $z_a (\equiv p_{T,a}/p_{T,jet})$  was well approximated by the distribution of  $\langle z_{\text{trigger}} \rangle^{-1} p_{T,a}/p_{T,t}$  [62]. The underlying assumption is that the selection of the trigger particle is the only criterion that determines the energy of the away-side jet, so long as  $p_{T,t} > p_{T,a}$ . Unfortunately, as a result of the jet's steeply falling cross section the sample of jets selected also depends strongly on  $p_{T,a}$ . This is clearly demonstrated in figure 1.19 which compares  $x_E$  ( $\equiv p_{T,a}/p_{T,t} \cos \Delta\phi$ )<sup>3</sup> distributions for  $\pi^0$  triggers to estimates using quark and gluon fragmentation based on parameterizations of the LEP data [61]. Despite the fact that the two fragmentation functions were taken to be quite dissimilar,  $D_g \propto e^{-11z}$  and  $D_q \propto e^{-8z}$ , they only result in a slight difference in the  $x_E$  distributions.

---

<sup>3</sup>We postpone a discussion of jet fragmentation variables until section 6.4. Note that  $x_E$  is essentially the same as  $z_T (\equiv p_{T,a}/p_{T,t})$  which is often used instead.

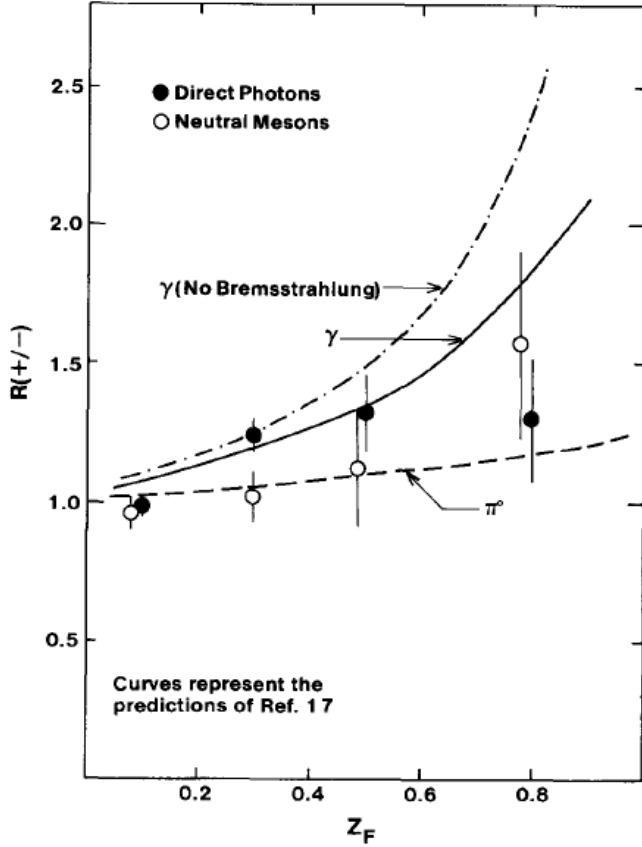


Figure 1.20: Ratio of positively to negatively charged hadrons on the away-side of a direct photon as a function of  $z_F (= x_E)$  [60].

For  $\gamma - h$  correlations, on the other hand, the conditional yield should be much more closely related to the fragmentation function. In the leading order picture, the direct photon exactly balances the away-side jet and therefore, the measureable quantity,  $p_{T,a}/p_{T,t}$ , is nothing but the fragmentation variable  $p_{T,a}/p_{T,jet}$ . This explains why  $\gamma - h$  correlations are a powerful measurement. They provide a source of recoil partons of fixed momentum. Their conditional yields in p + p collisions only probe the jet fragmentation. By contrast, hadron correlations are controlled by the jet cross section which also depend on the PDF's and the parton scattering cross sections.

The dominance of the Compton process means that  $\gamma$ -triggered jets are likely to be quark jets. In nuclear collisions this fact may be exploited to measure the difference between quark and gluon energy loss as by comparing them to  $\pi^0$  triggered jets which are more likely to be initiated by a gluon.

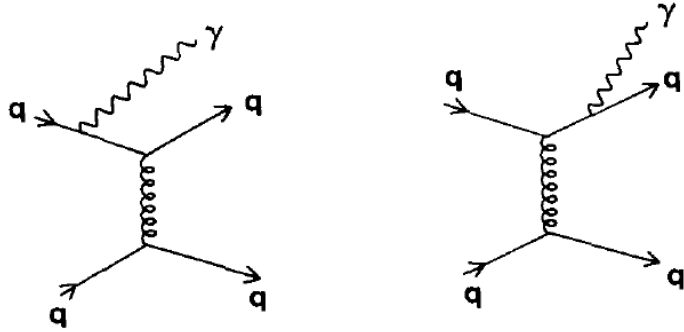


Figure 1.21: Examples of Feynman diagrams for photon bremsstrahlung processes at NLO. Figures adapted from [60].

Unlike identified baryon and meson spectra which will here be shown to have only a very tenuous connection to the parton flavor, the correspondence of  $\gamma$ -triggered jets to their up quark progenitors may be readily verified. Since there are two valence up quarks in a proton, each of charge  $2/3$ , compared to only 1 valence down quark of charge  $1/3$ , than the recoil jet will be initiated by an up quark a factor of  $2 \left(\frac{2/3}{1/3}\right)^2 = 8$  times more often than a down quark. As a result, one expects to see more positively charged hadrons on the away-side than negative. Figure 1.20 shows the ratio of positively to negatively charged hadrons associated with a direct photon from the R110 experiment at the ISR [60]. There is a substantial excess of positive charge at large  $p_{T,a}/p_{T,t}$  for the direct photon triggers as compared to the  $\pi^0$  triggered sample, although the effect is diluted by the creation of charge pairs in the jet fragmentation process. The data are consistent with theory predictions when NLO effects, which are the topic of the next section, are included.

### 1.6.1 Beyond Leading Order

If the direct photon production was really described solely by leading order pQCD then photon phenomenology would be considerably simpler. There exists an additional class of diagrams, however, which temper the simple interpretation suggested by the LO picture of  $\gamma + jet$ . At NLO, for example, one may add an additional QED vertex to a  $2 \rightarrow 2$  QCD scattering which corresponds to photon radiating from a quark. Feynman diagrams corresponding to such a process are shown in figure 1.21. This introduces an additional scale into the calculation. Below this fragmentation scale photon production is non-perturbative and is absorbed into a parton  $\rightarrow$  photon fragmenta-

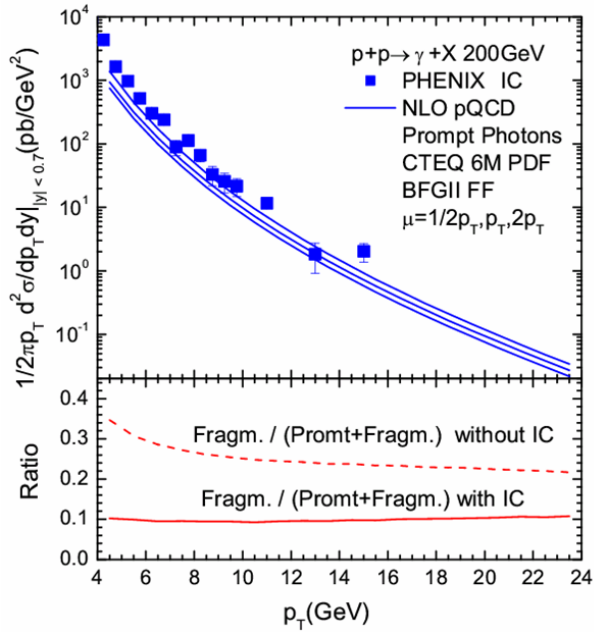


Figure 1.22: Top panel: NLO calculations [66] compared to the PHENIX direct photon photon cross section [67]. Bottom panel: The ratio of fragmentation to total photon with and without an isolation cut.

tion function. Although in principle, at high  $p_T$  or more precisely at high  $z$ , the bremsstrahlung contribution is calculable in perturbation theory, it must be matched to the non-perturbative photon fragmentation function which is poorly constrained by data [63, 64]. Surprisingly, these diagrams effectively contribute to the same order as the LO processes due to the  $\mathcal{O}(\alpha/\alpha_s)$  behavior of the fragmentation function [65].

Experimentally, the bremsstrahlung component can be suppressed using an isolation cut, in which any photon with hadronic activity nearby is vetoed. Such cuts have been successfully applied to theoretical calculations as well and the resulting cross section calculations agree fairly well with the experimental data. Figure 1.22 shows an NLO calculations of the prompt photon cross section compared to the PHENIX data. The bottom panel shows the ratio of next to leading order calculations with and without an isolation cut. Without an isolation cut fragmentation photon are on the order of 30% of the total photon sample. With an isolation cut they are reduced to a 10% contribution. While isolation cuts have long been used successfully in elementary particle collisions, we note that their application in heavy-ion collisions would be non-trivial and has never been demonstrated.

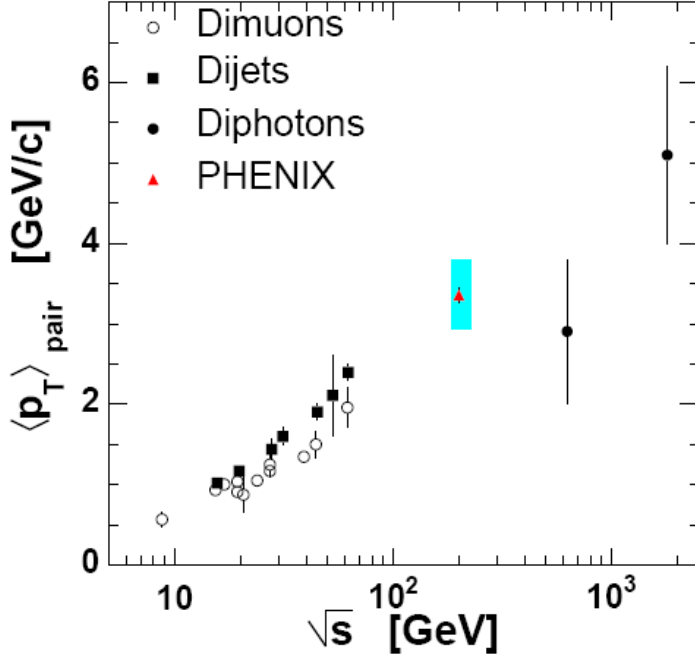


Figure 1.23:  $p_{T,pair}$  as function of  $\sqrt{s}$  from various two particle measurements from [61] and references therein.

## 1.7 Initial State Radiation and the $k_T$ Effect

As it turns out photon fragmentation at NLO is not the only subtlety involved in direct photon phenomenology. In order to understand the somewhat controversial topic of the  $k_T$  effect, some historical context is useful. At one time direct photon data was considered to be the most promising avenue to constrain the gluon distribution function due to the dominance of the Compton scattering process. By the mid 90's the full NLO calculations had been performed and new, precise direct photon data at higher values of  $x$  were becoming available from the Tevatron experiments. Around the same time a number articles appeared questioning the consistency amongst the various photon measurements and the completeness of the theoretical description. Although at the time it appeared that data from the two Tevatron experiments were not mutually compatible, the crux of the argument revolved primarily around (and still does revolve around) a data set from the E706 fixed target experiment. This discrepancy, it turns out, is thought to arise not from NLO effects but rather from higher order, and even non-perturbative, processes associated with an observation known as the  $k_T$  effect [68].

In LO pQCD a pair of hard-scattered partons emerges exactly back-to-

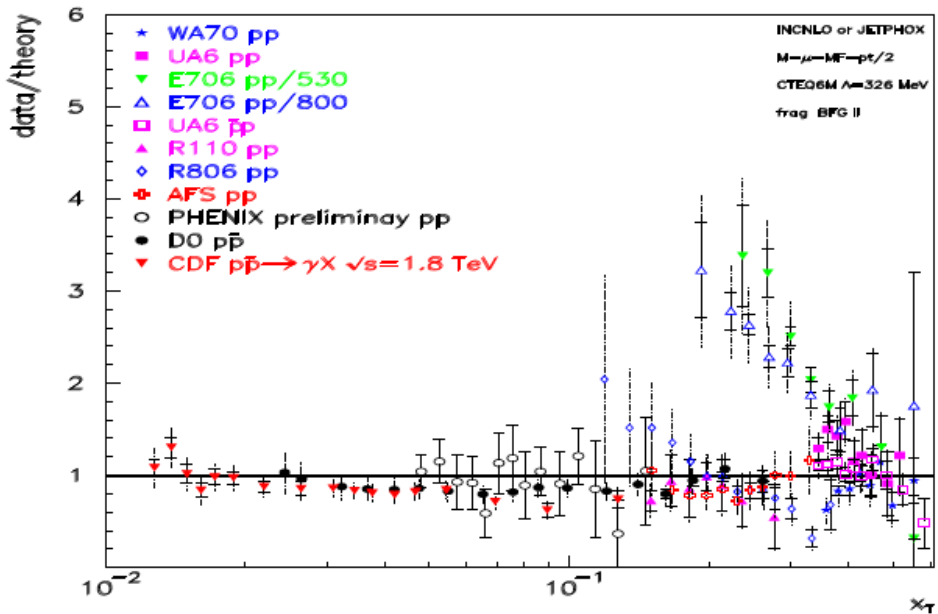


Figure 1.24: Compilation of direct photon data compared to NLO calculations from [69], [70].

back. Due to the finite size of the proton however, the colliding partons each have a small transverse momentum on the order of 300 MeV due to the uncertainty principle. At NLO, an additional momentum kick may be incurred by the emission of a single parton in the initial state. The component of the kick transverse to the outgoing parton pair causes them to be acoplanar while the longitudinal component gives them a momentum imbalance. This results in a flattening of the direct photon  $p_T$  spectrum particularly for  $p_T \approx k_T$ . Numerous measurements, compiled in figure 1.23, have been made of the net  $p_T$  of outgoing parton pair ( $p_T^{pair} = \sqrt{2}k_T$ ) from Drell-Yan, di-jet and di-photon events [61]. The data are consistent with a  $k_T$  which is independent of the observable and rises roughly as  $\log \sqrt{s}$  attaining values far in excess of the  $k_T \approx 1$  GeV which can be attributed to NLO pQCD at the Tevatron energies.

Apanasevich *et al.* showed that by adding an *ad hoc* phenomenological momentum smearing to the theory they were able to fit the world data with such "  $k_T$ -enhanced" NLO calculations quite well [71]. This was taken as evidence that the theory was incomplete. Aurenche *et al.* however, argued (see figure 1.24) that all data except the E706 results could be described at NLO without any additional  $k_T$  smearing by fine-tuning the gluon distribution function [69], [70]. Given this controversy, and the model dependence inherent to

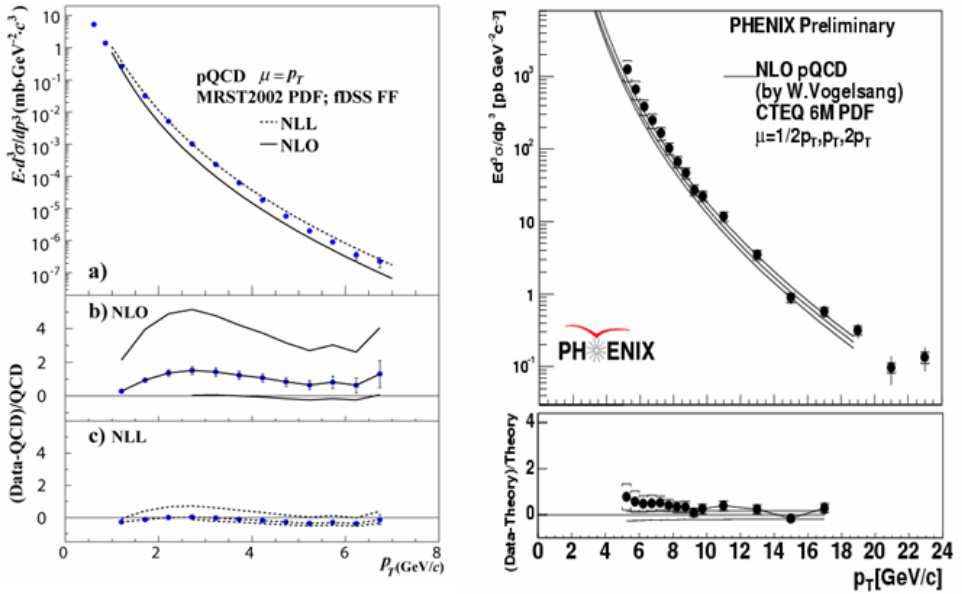


Figure 1.25: PHENIX  $\pi^0$  cross section at 62.4 GeV and direct photon cross section at 200 GeV [75] compared to NLO calculations [76].

the  $k_T$  smearing approach, the CTEQ collaboration discontinued the use of direct photon data in their global fits and this exclusion has since become standard [72].

The mechanism that gives rise to the anomalously large  $k_T$  is generally believed to arise from soft gluon emission from the initial state partons and its recoil effects. The calculation of such effects requires a procedure requires a *resummation* in which effects from all fixed orders are taken into account. In [73] it was shown that these calculations can, in principle, significantly improve agreement between data and theory at fixed target energies. Recent result at from the D0 collaboration show that there are still discrepancies between the direct photon cross section and NLO calculations at collider energies [74]. It is not clear, at present, whether these issues can be resolved by the introduction of resummation techniques.

It is important to address what, if any, concerns this raises for correlations studies at RHIC energies. Figure 1.25 the PHENIX direct photon cross section at 200 GeV. The data are consistent with the NLO calculation but the scale uncertainties in the theory are considerable. For comparison, the 62.4 GeV  $\pi^0$  cross section is also shown. In that case the NLO calculation was even more uncertain. A resummed calculation, however, was able to dramatically reduce the uncertainties. This example serves to illustrate that the effects

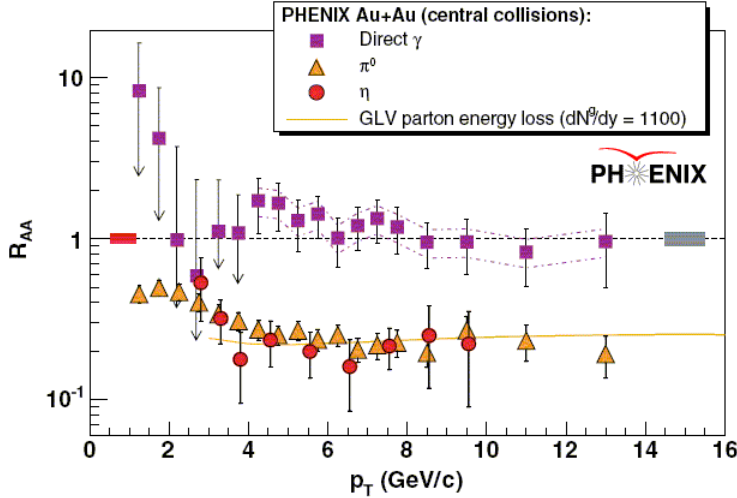


Figure 1.26: Nuclear modification factor for photons as well as  $\pi^0$ 's and  $\eta$ 's as a function of  $p_T$  for central Au + Au collisions [77].

which lead to an anomalously large  $k_T$ , which are precisely those quantified in the resummation calculation, can have substantial consequences. As we will discuss momentarily, photons will be used to constrain the momentum of the recoil parton. Their momentum balance is, however, spoiled to some extent by the  $k_T$  effect. In this regard, it will be useful to directly measure the magnitude of the  $k_T$  effect from data, and determine its effect on the observed  $p_{T,a}/p_{T,t}$  distributions.

## 1.8 Direct Photons in Nuclear Collisions

Photons are useful in nuclear collisions because of their comparatively small cross section for interaction with both hadronic and partonic matter. In the leading order picture one expects photons to display no high  $p_T$  suppression at all and, until quite recently, PHENIX data indicated that this was the indeed the case, as shown in figure 1.26. Since no isolation criterion is applied to this data one might expect that the bremsstrahlung component of the photon sample would exhibit the same suppression as observed in hadronic spectra. Newer preliminary data shown in figure 1.27 do indeed show that  $R_{AA} < 1$  although the effect is only significant in the highest  $p_T$  data point. Also shown is a theoretical prediction including energy loss, as calculated in the BDMPS framework <sup>4</sup> [78]. The theory reproduces the qualitative features

---

<sup>4</sup>Initial state effects from shadowing and isospin are also included

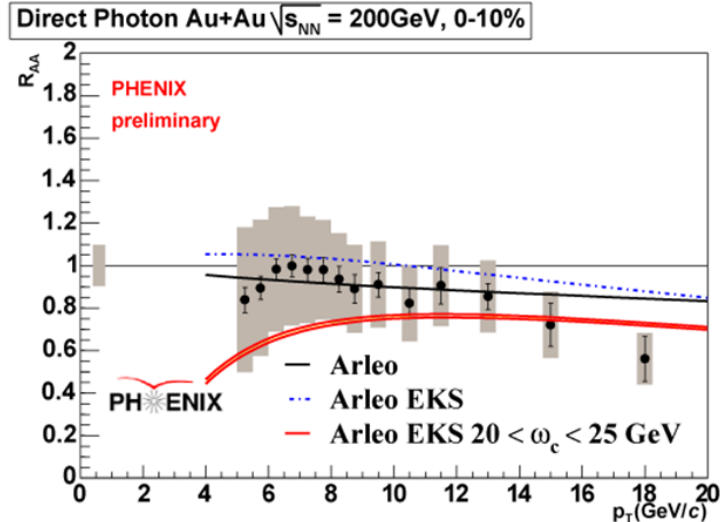


Figure 1.27: Preliminary results for the nuclear modification factor for photons as function of  $p_T$  for central Au + Au collisions compared to a theoretical prediction using the BDMPS model of energy loss [78]. The parameter  $\omega_c$  is related to  $\hat{q}$ . [79]

of the data but describes the shape only marginally well. Even disregarding the uncertainties in the energy loss calculations this is not surprising as it is speculated there may be novel sources of photons in nuclear collisions not considered in this particular model.

Figure 1.28 shows a prediction for the direct photon  $p_T$  spectrum in Au + Au collisions. The jet-plasma contribution represents the following two novel sources of photon production which are thought to be induced by the presence of a QGP.

- Induced Bremsstrahlung - Photons radiated by partons as they are attenuated by the medium [80].
- Jet Conversion - Photons generated by  $2 \rightarrow 2$  processes in which a hard parton rescatters off a medium parton, e.g. a hard quark and medium gluon Compton scattering to produce a photon [81], [82].

The medium induced sources are estimated to be roughly equal in magnitude to the direct component at 5 GeV and become less significant with increasing  $p_T$  representing about a third of the total cross section by 15 GeV [83]. Signatures of these sources include an enhancement in  $R_{AA}$  and a negative  $v_2$  (elliptic flow which is oriented out-of-plane with respect to the reaction plane). Neither of these signatures have yet been observed with any certainty.

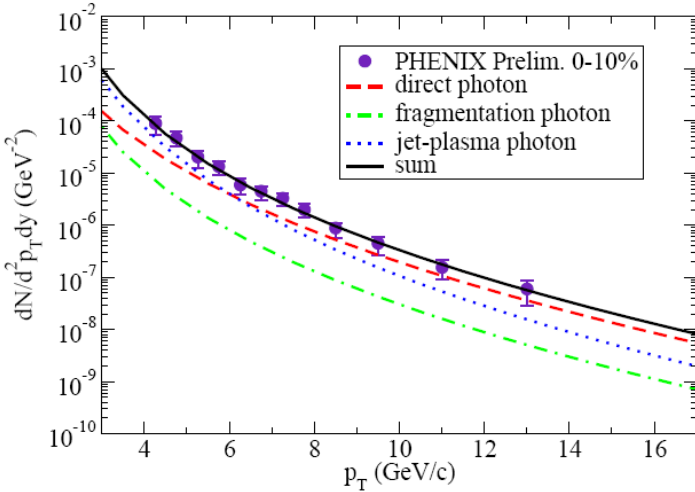


Figure 1.28: Calculation of the direct photon cross section in central Au + Au events broken down into its constituents. [83]

## 1.9 $\gamma + jet$ : The Golden Channel

$\gamma + jet$  is often referred to as the “golden channel” for jet tomography studies<sup>5</sup>. In contrast to single or di-hadron measurements where the initial parton energy is not known, jets recoiling from direct photon exactly balance the photon’s momentum, modulo beyond-leading-order effects such as bremsstrahlung and initial state radiation ( $k_T$ ). This allows for the determination of the initial parton momentum without full jet reconstruction, which is difficult in the high multiplicity environment of heavy-ion collisions. Moreover, hadronic observables are strongly biased towards surface production, whereas photons sample the entire collision and should therefore favor the core of the overlap zone where the nucleon density is greatest.

As discussed in section 1.3.2, it is difficult to disentangle the properties of the dense medium from the nuclear geometry and space-time evolution of the system, in part, due to the surface bias in hadron triggered measurements. The situation is further complicated by the lack of a definitive model of the energy loss itself. For example, in some models partons have a finite probability to emerge from the center of the collision zone without interacting at all while in others unsuppressed jet production is exclusively surface production. Due to its penetrating nature, photon-hadron correlations have greater sensitivity to the path-length dependence as will be discussed below.

The use of the  $\gamma + jet$  channel as a tomographic tools was first advocated

---

<sup>5</sup>The history of the field warns us to beware of such bold proclamations

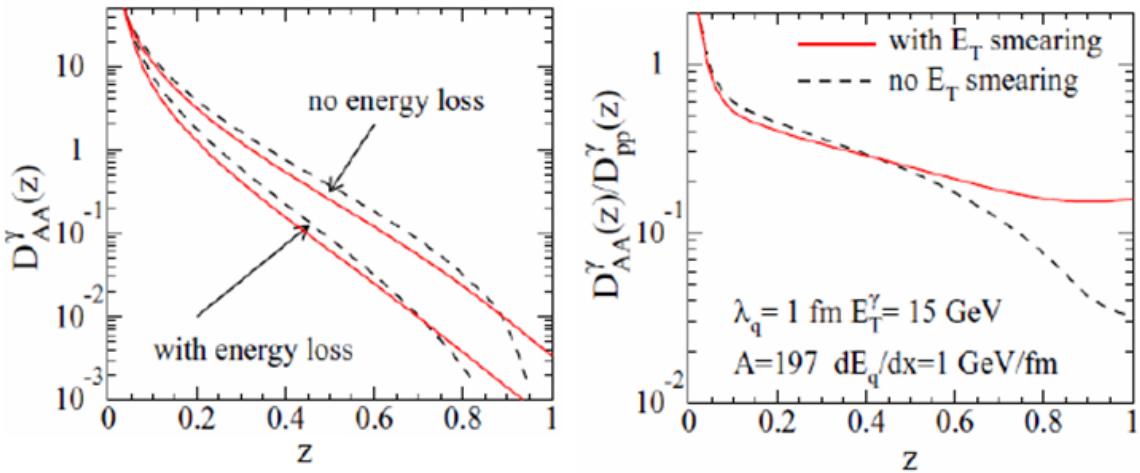


Figure 1.29: Left: Modified fragmentation function for  $\gamma - h$  correlations with and without energy loss and also with and without the  $k_T$  ( $E_T$ ) effect. Right: - The ratio of the modified fragmentation function to the vacuum one ( $I_{AA}$ ) in the presence of energy loss with and without  $k_T$  [84, 85].

by Xin-Nian Wang and collaborators in a pair of seminal articles on the subject about 10 years ago [84, 85]. They define an effective medium modified fragmentation function which simply the observed distribution of  $p_T^h/p_T^\gamma$  (labeled  $z$  in the figure). The results, shown in figure 1.29, demonstrate the sensitivity of the measurement to the energy loss which is implemented in an ad-hoc fashion by assuming a loss 1 GeV/fm. Also noteworthy, the modified fragmentation function is also sensitive to the inclusion of the  $k_T$  effect (they use the notation  $E_T$ ). In the ratio of Au + Au to p + p associated yields ( $\equiv I_{AA}$ ) they show that this sensitivity cancels in the ratio at low  $p_T^h/p_T^\gamma$  but is pronounced at higher values.

The benefit of  $\gamma - h$  correlations over single hadron spectra was studied by Renk in [86]. He created a toy model where he inserted various energy loss profiles, let the system evolve hydrodynamically and then studied the sensitivity of  $R_{AA}$  and the  $\gamma - h$  per-trigger yield ( $p_T^\gamma = 15$  GeV) to the model input [86]. Figure 1.30 shows his prediction for  $R_{AA}$  (left) and a quantity proportional to  $I_{AA}$  of  $\gamma - h$  pairs for the different energy loss profiles. For  $R_{AA}$  nearly all of the models follow the  $\pi^0 R_{AA}$  data fairly closely. The  $\gamma - h$  predictions, on the other hand, appear to be quite well separated, particularly at small  $p_{T,a}$  where they differ by about a factor of 3. This study indicates that most informative measurements are those at low  $z$ , provided that the medium response, which is not considered in this model, does not dominate the signal.

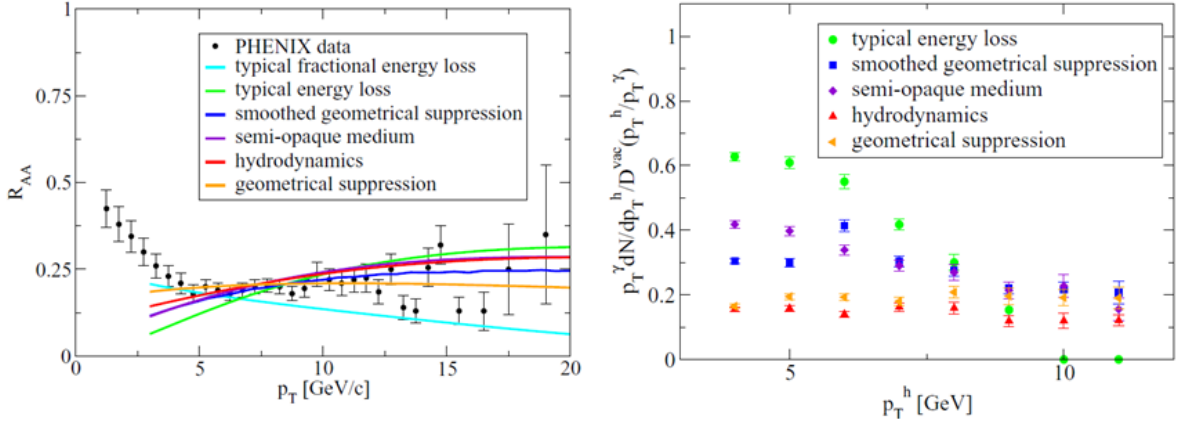


Figure 1.30: Left - Comparison of a toy model which compares various energy loss profiles to the  $\pi^0 R_{AA}$ . Right - The  $p_T^\gamma dN/dp_T^h$  normalized to the vacuum fragmentation expectation for  $\gamma - h$  correlations for the different energy loss profiles. [86]

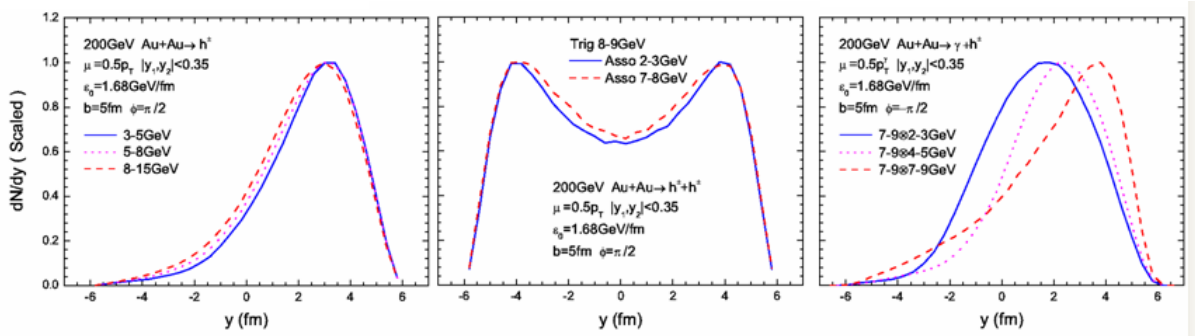


Figure 1.31: Calculation of scattering centers for several observables in the ZOWW model. From left to right: Single particles, di-hadrons and direct photon-hadron pairs. [66, 87].

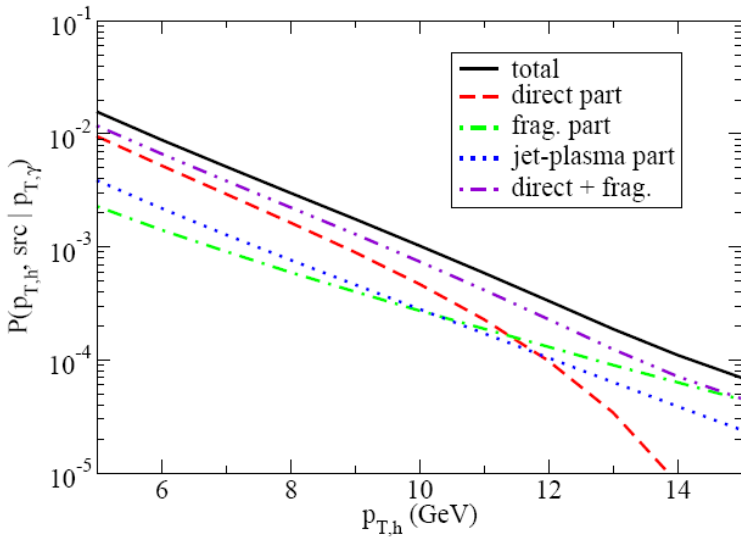


Figure 1.32: Prediction for yield associated with 15 GeV direct photons as a function of  $p_{T,a}$  in central Au + Au collisions using the AMY formalism [83].

Recently, updated predictions of energy loss using the modified fragmentation function approach were made available [66, 87]. They calculate the distribution of scattering centers sampled by several observables as shown figure 1.31. In this model, both the measurement of both single hadrons and hadron pairs are biased to the surface of the collision zone. Moreover, this conclusion is independent of  $p_T$  selection. For direct photon correlations the measurement is similarly biased when the hadron and photon are chosen to have the same momentum. As the momentum of hadron decreases, however, one samples progressively deeper into the medium. The authors conclude the photon triggered correlations are hence, more sensitive than other observables.

Calculations of energy loss using photon tagged jets are also available using the BDMPS [78] and AMY [83] formalisms in addition to the hydrodynamic evolution. The latter group were also able to include medium induced photon production in their predictions. Figure 1.32 shows their prediction for the total direct photon per-trigger yield and each of its components. At low  $p_{T,a}$  prompt (Compton and annihilation) production dominates, however their results indicate that as  $p_{T,a}$  approaches  $p_{T,t}$  medium induced production may be studied directly.

We point out that one piece of information that is currently lacking from the theoretical literature on  $\gamma - h$  correlations are accompanying predictions for  $\pi^0-h$  correlations using exactly the same energy loss framework, hydro evolution, etc. Since direct photons are a high purity quark jet tag and  $\pi^0$ 's

may recoil against either quark or gluon jets, the comparison of these two observables is sensitive to the color factor of parton energy loss in a much less model dependent way than identified hadron spectra <sup>6</sup>.

This concludes the overview of motivation and theoretical status of  $\gamma - h$  correlations. With these in mind, we outline the goals of the present study.

## 1.10 Statement of Purpose

The motivation of  $\gamma - h$  correlation is to perform tomographic studies of the Quark-Gluon Plasma by measuring the path-length dependence of parton energy loss. As this is one of the foremost goals of the RHIC II program during the next decade, the reader should not presume that the definitive measurement is performed in this study. However, the first measurements of such correlations in Au + Au collisions have been performed, and a number of issues may be addressed, as follows.

- We will develop a methodology to perform  $\gamma$ +jet studies using two particle correlations and investigate.
- By comparing direct photon correlations in Au + Au and p + p collisions, we will investigate whether high  $p_T$  associated hadron production is suppressed, and, if so, compare the level of suppression to single and di-hadron measurements.
- We will compare the nuclear modifications factor to theoretical predictions of parton energy loss.

Agreement between QCD and baseline measurements in elementary collisions is a pre-requisite for the successful modeling of parton energy loss. Using the available RHIC data from p + p collisions, precision studies of two-particle correlations may be performed. In doing so, we investigate the following:

- We will attempt to improve the methodology of  $\gamma - h$  correlations, beyond what was developed for Au + Au collisions, by partial event-by-event identification of direct photon-hadron pairs, taking advantage of the relatively clean environment of p + p collisions.
- The extent to which next to leading order effects, specifically photons from jet fragmentation, play a role will be investigated by comparing direct photon correlations with and without an isolation cut.

---

<sup>6</sup>Since writing the author has learned that such a study using the ZOWW model will be published shortly.

- Measurements of the  $k_T$  effect in the  $\gamma+\text{jet}$  channel will be performed and their consequences for two-particle correlations measurements will be investigated.
- The capacity of direct photon and  $\pi^0$  triggered correlations to tag parton flavor will be investigated and the application of such studies to the measurement of the gluon fragmentation function and the flavor dependence of parton energy loss will be explored.

# Chapter 2

## Experimental Apparatus

### 2.1 Overview

#### 2.1.1 RHIC



Figure 2.1: Aerial view of the RHIC complex.

The Relativistic Heavy-Ion Collider (RHIC) complex, shown in aerial view in figure 2.1 is located at Brookhaven National Laboratory in Upton, New

York. RHIC is a dedicated heavy-ion and proton-proton collider with a maximum  $\sqrt{s_{NN}}$  of 200 GeV in nuclear collisions and 500 GeV in proton collisions. The capabilities of the machine are remarkably flexible. It is capable of colliding a range of species which will soon include ions as heavy as uranium. RHIC is also able to collide polarized protons allowing the spin structure of the nucleon to be probed. Future prospects include low energy operation to search for the QCD critical point.

The RHIC rings is made two counter-circulating beam line with 2.4 mile circumference. There are six interaction sites around the beam. Two small experiments, PHOBOS and BRAHMS have recently finished data taking. Currently, two large detectors are in operation, namely STAR and PHENIX.

### 2.1.2 PHENIX

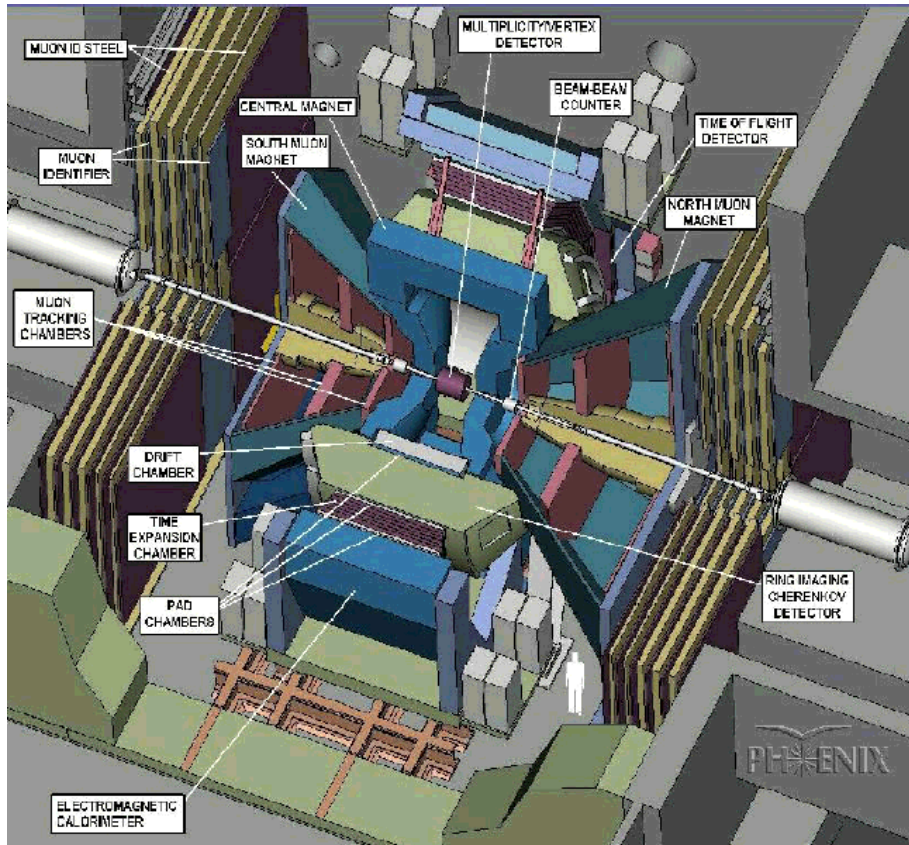


Figure 2.2: Overhead view of the PHENIX detector.

PHENIX (Pioneering High Energy Nuclear Interaction eXperiment) is op-

timized to study rare processes via measurements of leptonic (electron and muon) and photonic channels. In contrast to more hermetic detectors such as STAR, PHENIX has partial angular coverage but provides excellent resolution and momentum reach for a wide variety of observables. Figure 2.2 shows and overhead view of the PHENIX detector. The two central spectrometer arms surround a central magnet which provides an axial magnetic field parallel to the beam axis.

Figure 2.3 shows a side-view of the PHENIX central arms. The various detector sub-systems enable charged particle tracking, particle identification and electro-magnetic calorimetry. Particles pass through the magnetic field before entering the drift chambers (DC). Before reaching the electromagnetic calorimeters (PbSc and PbGl) they traverse additional tracking chambers (PC1, PC2, PC3) and various specialized particle identification detectors (TOF, Aerogel, RICH, TEC). The opposing arms each subtend an azimuthal angle of  $\pi/2$  with pseudo-rapidity of 0.7 units providing reasonable (but not optimal) acceptance for studies of back-to-back particle production from jets. The functionalities of the various detectors used in the present analysis are discussed in this chapter. Muon detection is achieved by the forward spectrometer arms which will not be discussed. The global detectors at forward rapidity, the topic of the next section, are used for event triggering and timing synchronization as well as to measure event characteristics such as the primary vertex, centrality and reaction plane.

## 2.2 Global Detectors

### 2.2.1 Beam-Beam Counters

The Beam-Beam Counters (BBC) [88], shown in figure 2.4, are arrays of photo-multiplier tubes attached to quartz Cherenkov radiators. These 3 cm long Quartz crystals have a threshold of  $\beta = 0.7$ . The BBC's are situated around the beam pipe at  $\pm 144$  cm from the center of the interaction region covering  $3 < \eta < 4$  over the full azimuth. This forward rapidity coverage permits detection of charged particles from nearly all collisions while minimizing correlations with the central arm detectors.

The most important feature of the BBC detectors are their excellent timing resolution. The intrinsic resolution of a single element is  $\sim 40$  ps. The difference in the time from the two BBC's is used to determine the collision vertex to accuracy of order 1 cm for central Au + Au multiplicities. The signal from the BBC is rapidly digitized and forms the basis of the Local Level 1 trigger which rejects collisions occurring outside the center of the interaction

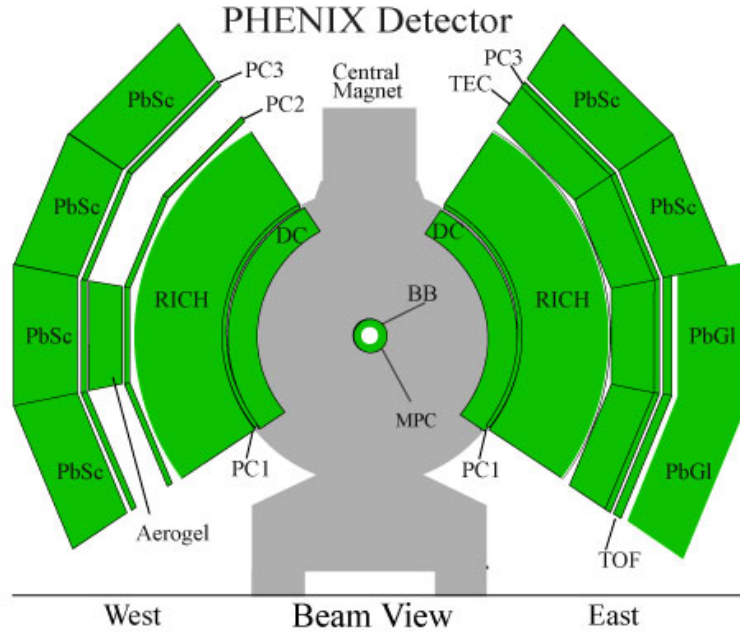


Figure 2.3: The PHENIX central arm configuration during Run 6.

region ( $> 30$  cm). The BBC's record the start time of the collision,  $T_0$ , to a resolution of about 20 ps in Au + Au events which is used with information from the TOF detectors to identify hadrons.



Figure 2.4: The Beam-Beam Counters. Left: A single element consisting of a PMT and a quartz radiator. Middle: One of the two assembled BBC detector arrays. Right: BBC array cabled and installed around the beam pipe on the face of the central magnet.

## 2.2.2 Zero Degree Calorimeters

The Zero Degree Calorimeters (ZDC) [88], shown in figure 2.5 are hadronic calorimeters located 18 m from the interaction point very close to the beam axis ( $\eta \sim 6$ ). They are positioned behind the dipole bending magnets such that charged particles are deflected out of their paths by the magnetic field. They are designed to catch spectator neutron fragments whose trajectory lie at small angle with respect to the beam axis, typically only a few mrad. The detectors are made of tungsten plates sandwiched with optical fibers which are read out by PMT's. The large radiation length of  $50X_0$  ensures that hadronic showers are well-contained. The ZDC has an energy resolution of about 25 % for single neutrons.

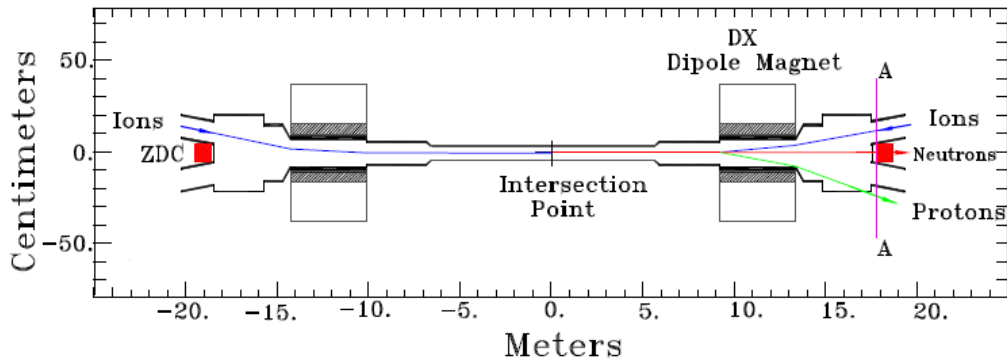


Figure 2.5: Diagram of the beam line near the interaction region showing the position of the ZDC detectors and the dipole magnets

## 2.3 Centrality Determination

In the Run 4 data the measured response in the ZDC and BBC detectors were used to define the collision centrality. The determination of centrality is of particularly importance in heavy-ion collisions since it is used to estimate the mean impact parameter of a given set of collisions, and by extension, quantities such as number of participant and collisions. This is done using the Glauber model and the Woods-Saxon parametrization of the nuclear density profile [23]. Figure 2.6 demonstrates how the centrality is determined from the response of these two detectors. The correlation between the energy deposited in the ZDC's and the total charge measured in the BBC's is plotted. Based on this distribution the collisions are sub-divided into centrality classes indicated by the colored bands. The ZDC shows maximal sensitivity in peripheral collisions the signal from charged particles that reach the BBC is small. By mid-peripheral centralities the ZDC response becomes anti-correlated to that of the BBC as spectator neutrons are increasingly less likely. The coincidence of the BBC and ZDC are used to define the minimum bias trigger condition. Using HIJING simulations that  $92 \pm 2\%$  of the total inelastic cross section is measured in Au + Au collisions.

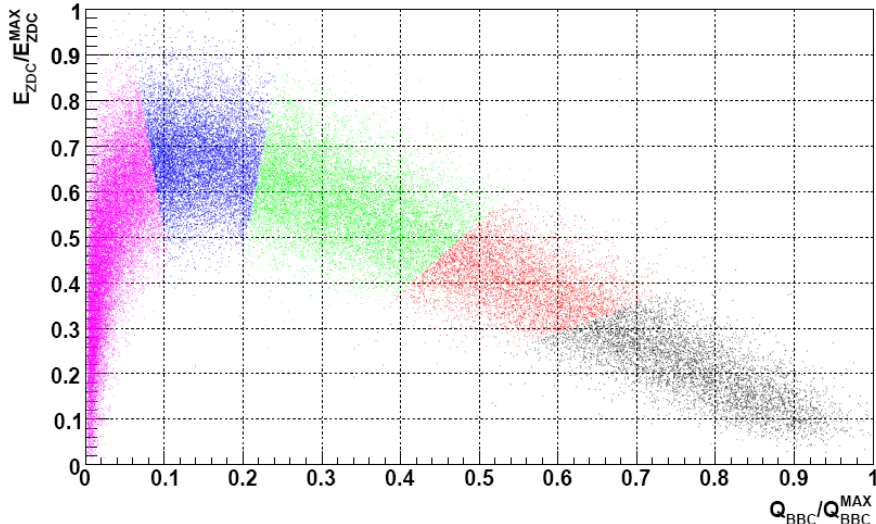


Figure 2.6: Centrality determination from the normalized ZDC energy deposition and BBC charge sum. Color indicates the centrality selection (black: 0-10%, red: 10-20%, green: 20-40%, blue: 40-60%, magenta: 60-92%.

## 2.4 Central Tracking

### 2.4.1 Drift Chambers

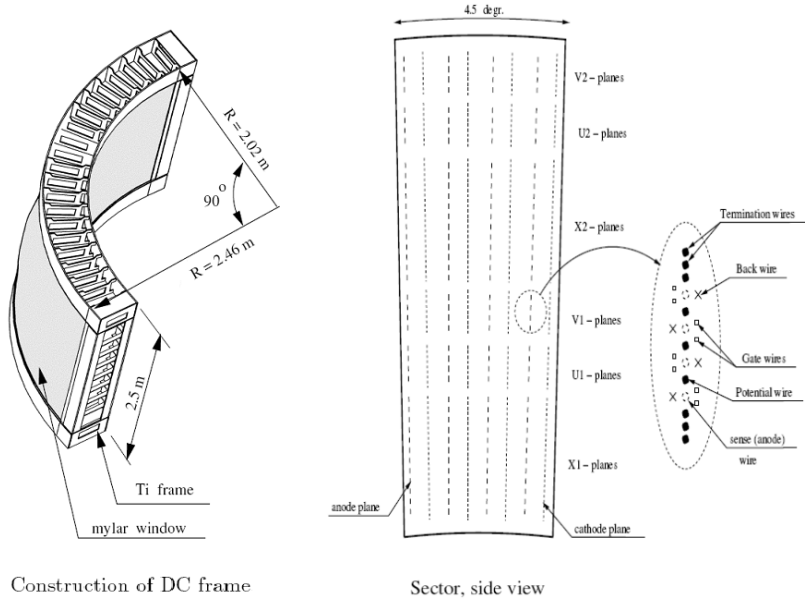


Figure 2.7: The Drift Chamber. Left: View of the drift chamber frame and its dimensions. Right: A side-view of the one sector of the drift chamber showing the wire layout with an inset showing one group of wires.

The workhorse of the central tracking system is the PHENIX Drift Chamber System [89] shown in figure 2.7. The chambers are cylindrical titanium frames with mylar windows on the front and rear surfaces which lie at radial distance of 2 and 2.46 meters from the beam axis, respectively. They are filled with a gas mixture composed of 50% argon, 50% ethane. A total of 6500 anode wires are stretched across the chamber to collect electrons ionized from the gas by charged particles. The distance of a track from an anode wire is calculated from the drift time of the electrons. Each of the wires is segmented by a piece of non-conductive kapton in the center of the detector and defining the two "sides" of each chamber each of which is read out separately. A side is composed of twenty sectors or "keystones" one of which is diagrammed in figure 2.7. Two layers of anode wires (X1 and X2) lie in the direction of the beam axis. Stereo wires (U and V) are placed at an angle of 6° with respect to the X wires such that they start in one sector and end in the neighboring one. The inset shows an individual cell which contains four anode wires and

a number of other wires of various functionalities. The potential wires hold voltage to create an electric field which terminates at the cathode. The field is controlled by gate wires which define the boundaries between neighboring anode wires. A set of back wires are held at a small potential to shield the anodes from one side such that each wire anode wire is only sensitive to tracks from one direction.

The drift chamber is optimized to measure the  $p_T$  of charged tracks in a high multiplicity environment. The single tracks resolution achieved is about  $165 \mu\text{m}$  in the  $r\phi$  plane with a track finding efficiency of better than 99%. Determination of the momentum vector, however, requires more information on the longitudinal direction of track (along the beam axis) than can be achieved from U and V stereo wires alone. This supplementary information is obtained from the pad chambers.

#### 2.4.2 Pad Chambers

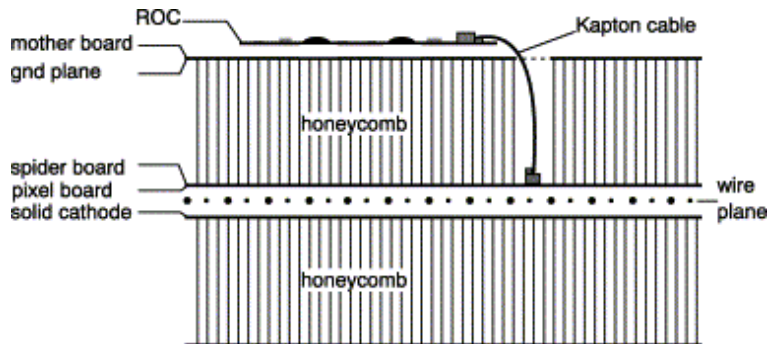


Figure 2.8: A diagram of one of the Pad Chambers (PC1)

The pad chambers (PC) [89] are multi-wire proportional chambers in which a single plane of anode wires is bounded by two cathode planes. One of the cathode planes are divided into pixels for two dimensional readout with 4320 channels per chamber. The pad chambers are over 99% efficient and have a position resolution of 1.7 mm. The PC1 is mounted directly behind the drift chamber and together with the primary vertex from the BBC, they determine the momentum of tracks with resolution  $\delta p/p \simeq 0.7\% \oplus 1.0\% p$  (GeV) where the first term is due to multiple scattering before the drift chamber and the second is the intrinsic angular resolution [24]. Shown in cross section in figure 2.8, the PC1 lacks a frame due to space restrictions, and is instead self-supported by the addition of rigid honeycomb sandwich structures. The other two pad chambers are placed behind the RICH and in front of the electromagnetic

calorimeter, respectively. Hits from these pad chambers are often required to reject accidental associations with secondary tracks produced from decay and conversions.

## 2.5 Electromagnetic Calorimeters

The electromagnetic calorimeters (EMC) [90] are primarily responsible for measuring the energy and position of photons and electrons. There are two sets of detector technologies employed, lead scintillator sampling calorimeters (PbSc) and lead glass cherenkov calorimeters (PbGl), which have very different characteristics providing a valuable cross-check on photon measurements. The calorimeter is composed of eight sectors of which two are PbGl.

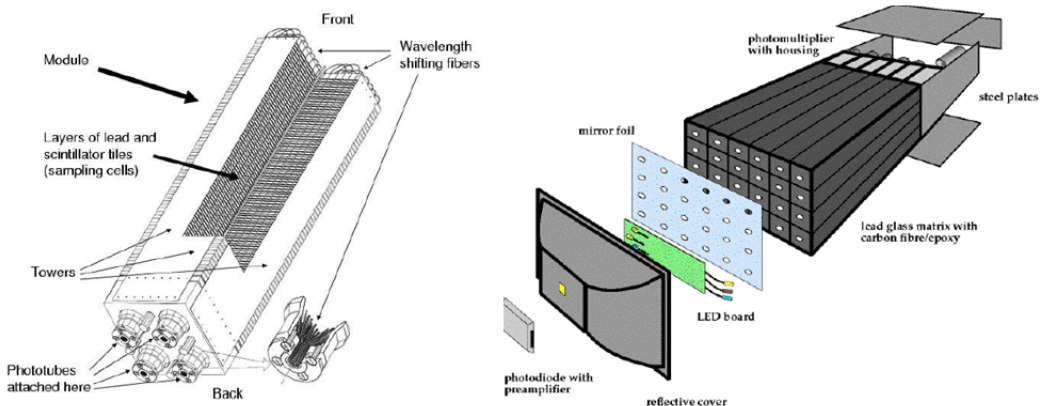


Figure 2.9: Diagrams of the electromagnetic calorimeters. Left: A module of PbSc towers. Right: A supermodule of PbGl towers.

The 15552 PbSc towers are made of alternating layers of Pb absorber and scintillating plastic with a total radiation length of  $18X_0$ . Light is read out of the towers via wavelength shifting fibers into phototubes. A module which consists of four towers is shown in figure 2.9 (left). The PgGl calorimeter previously served as part of the WA98 detector at the SPS. The two PbGl sectors have a total of 9216 towers. Groups of 24 towers, called supermodules, are bonded together as shown 2.9 (right). In contrast to the PbSc, the PbGl is a homogenous calorimeter, i.e., the energy absorption and signal generation take place in a single material. The addition of Pb-oxide to glass increases its index of refraction ( $n=1.648$ ) enhancing the Cherenkov radiation. Each tower has a radiation length  $14.4X_0$  and a Molière radius of 3.68 cm. The

resolution of the PbGl and PbSc detectors as measured in the test beam data are  $\delta E/E = 5.9\%/\sqrt{E} \oplus 0.8\%$  and  $\delta E/E = 8.1\%/\sqrt{E} \oplus 2.1\%$ , respectively.

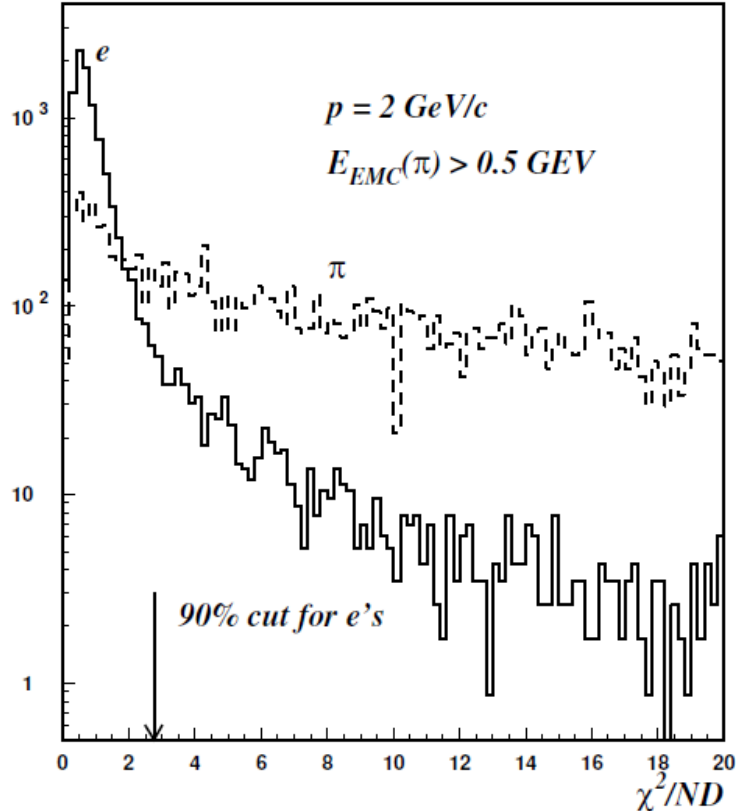


Figure 2.10: The  $\chi^2$  per degree of freedom distribution for electrons and pions in the PbSc detector.

Electromagnetic showers are distinguished from hadronic ones via a statistical analysis of their shower profile. For the PbSc an analytical parametrization of the shower shape fluctuations including energy sharing was developed [91]. Deviation from the expected shower shape is quantified as  $\chi^2 = \sum_i \frac{(E_i^{pred} - E_i^{meas})^2}{\sigma^2}$  where  $E_i^{meas}$  and  $E_i^{pred}$  are the measured and predicted energies of the  $i$ th tower contributing to the photon cluster. Figure 2.10 shows the  $\chi^2$  for electrons and pions. The arrow indicates the value of  $\chi^2$  corresponding to 90% electron efficiency. A similar shower shape cut is applied to clusters in the PbGl. Hadron rejection in both detectors may be enhanced through the use of a veto cut using information from the central tracking detectors, as discussed in section 3.2.4, or by using the time-of-flight information from the calorimeter. The latter methodology is largely redundant given the  $\chi^2$  and veto

cuts used in the present analysis and is therefore not employed. The timing information is, however, used for a different purpose, to identify hadrons.

Above 500 MeV the PbSc has a nearly constant time resolution of  $\sim 120$ ps for electrons and  $\sim 270$  ps for protons as shown in figure 2.11. As discussed in the next chapter the timing information can be used to identify pions and protons below 1.5 and 2.0 GeV, respectively. The PbGl cannot be used to identify hadrons as they typically shower closer to the back end of the calorimeter than electromagnetic particles such that their signal arrives at the electronics first despite their longer flight time. Higher resolution time-of-flight information is available from the limited acceptance TOF detector described in the next section.

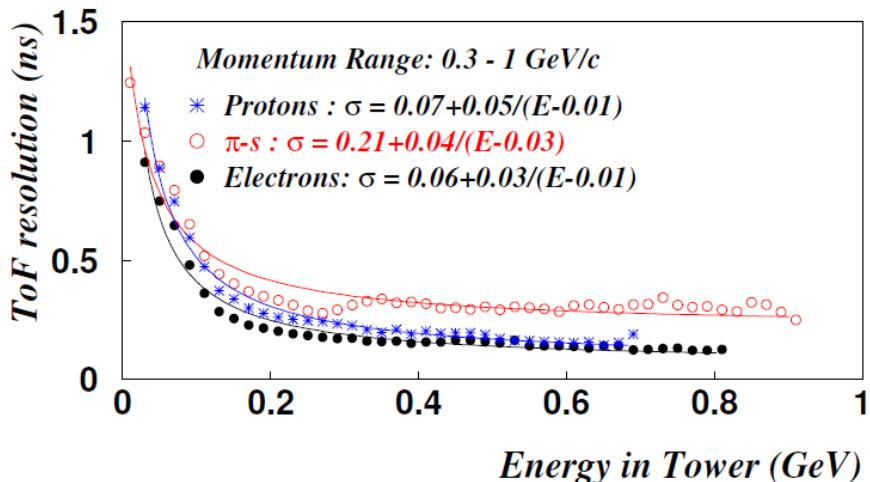


Figure 2.11: Timing resolution of the PbSc for electrons, charged pions and protons from beam test studies.

The EMC front-end electronics are fast enough to provide triggering capability. The EMCal-RICH Triggers (ERT) are used to quickly discriminate events likely to contain high  $p_T$  photons or electrons based on energy deposition in the EMC. The name ERT is something of a misnomer as information from the RICH detector, which is described in the next section, is only used for electron triggering. The basic unit of triggering, known as a tile, is composed of four towers. Each tile is served by an ASIC (Application-Specific Integrated Circuit) chip which calculates the analog sum of their signals, a useful approach since photon showers typically spread over more than one tower. Individual hot or dead towers can be masked out. Each ASIC receives the signal from the neighboring chip and overlapping 4x4 groups of towers are used as triggers. Each trigger is defined by a different threshold: 2.1, 2.8 and

1.4 GeV for the so-called 4x4a, 4x4b and 4x4c triggers, respectively. In the p + p data considered in this study, data satisfying any of the three triggers are used. Only minimum bias data is used for the Au + Au results.

## 2.6 Particle Identification Detectors

### 2.6.1 Ring Imaging Cherenkov Counters

The Ring Imaging Cherenkov Detectors (RICH) [92] diagrammed in figure 2.12 are located radially between the drift chamber and the calorimeter. The detector is designed to identify electrons by identifying their Cherenkov rings. The detector volume is filled with  $CO_2$  which has a Cherenkov threshold of 18 MeV for electrons and produces an average of 12 photons for a  $\beta \approx 1$  particle over a path-length of 1.2 m. The diameter of the produced ring is about 11.8 cm. The detector is fitted with mirrors which focus the photons towards PMTs before the signal is sent to the front end electronics. At high  $p_T$ , electrons from both the primary vertex and from secondary sources, such as photon conversions, contaminate the sample of hadron track candidates. Pions have a much higher Cherenkov threshold of 4.65 GeV so the RICH is used in this study to remove these electrons from the hadron sample below the pion threshold.

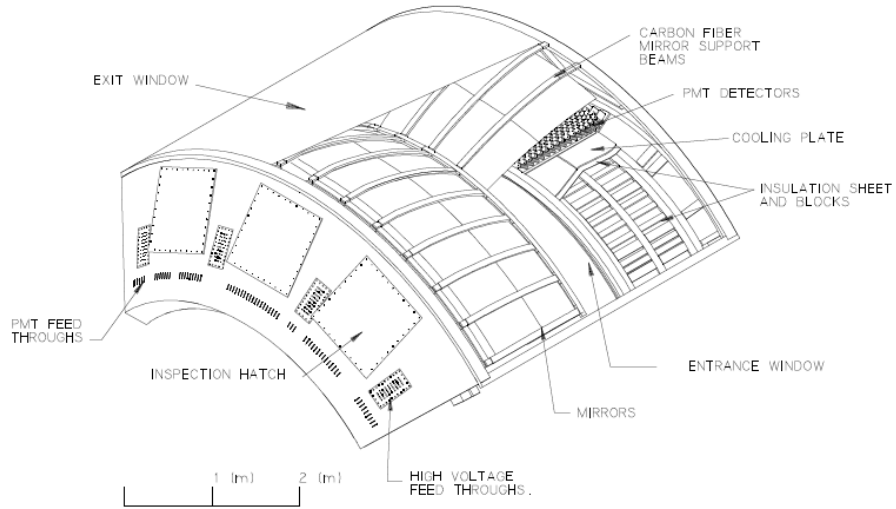


Figure 2.12: Cut-away drawing of the RICH Detector.

## 2.6.2 Time of Flight Detector

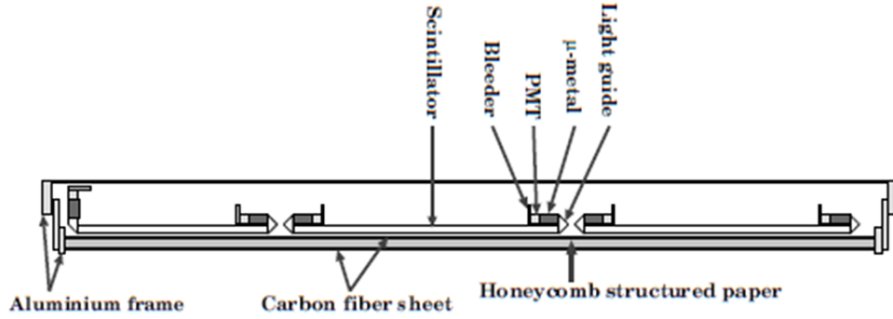


Figure 2.13: A section of slats in the TOF Detector.

The high resolution Time of Flight (TOF) [92] detector is located in front of the PbGl sectors of the EMC at a distance of 5.1 m from the collision vertex. It has a limited acceptance, covering only  $30^\circ$  in azimuth. The TOF is made up of 960 slats of plastic scintillator. The slats are mounted on a honeycomb paper structure supported by a carbon fiber sheet as depicted in figure 2.13. Each slat has two PMT's. The time difference between the PMT's is used to locate the hit along the length of the slat.

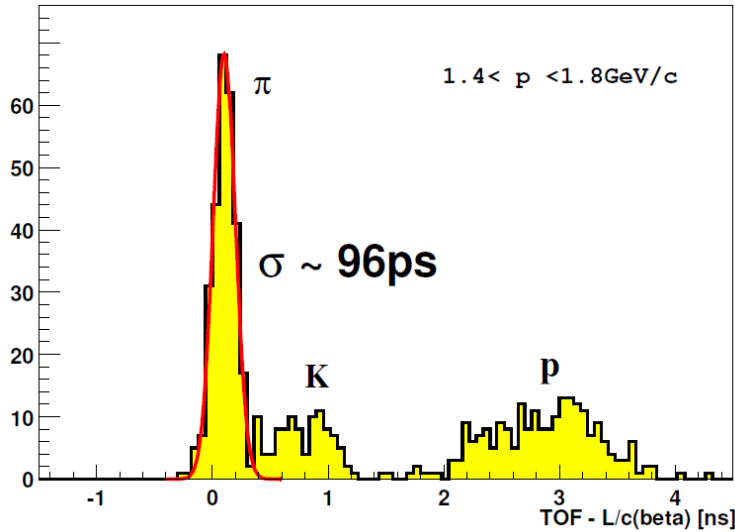


Figure 2.14: Flight time resolution for hadrons in the TOF Detector.

Particle identification is performed by associating reconstructed tracks from the tracking system with hits from the TOF. The flight time of the particle is

Run	Year	Species	$\sqrt{s}$ [GeV]	$\int L dt$	Nevt (samp.)
Run 1	2000	Au+Au	130	$1 \mu b^{-1}$	10 M
Run 2	2001/02	Au+Au	200	$24 \mu b^{-1}$	170 M
		Au+Au	19		<1 M
		p+p	200	$0.15 pb^{-1}$	3.7 B
Run 3	2002/03	d+Au	200	$2.74 nb^{-1}$	5.5 B
		p+p	200	$0.35 pb^{-1}$	6.6 B
Run 4	2003/04	Au+Au	200	$241 \mu b^{-1}$	1.5 B
		Au+Au	62.4	$9 \mu b^{-1}$	58 M
Run 5	2005	Cu+Cu	200	$3 nb^{-1}$	8.6 B
		Cu+Cu	62.4	$0.19 nb^{-1}$	0.4 B
		Cu+Cu	22.4	$2.7 \mu b^{-1}$	9 M
		p+p	200	$3.8 pb^{-1}$	85 B
Run 6	2006	p+p	200	$10.7 pb^{-1}$	230 B
		p+p	62.4	$0.1 pb^{-1}$	28 B
Run 7	2007	Au+Au	200	$813 \mu b^{-1}$	5.1 B
Run 8	2008	d+Au	200	$80 nb^{-1}$	160 B
		p+p	200	$5.2 pb^{-1}$	115 B
		Au+Au	9		< 1M

Table 2.1: Summary of the PHENIX recorded data sets

calculated using the start time (T0) as calculated by the BBC and the arrival time measured by the TOF. The resolution, shown in figure 2.14, is calculated as the difference between the flight time measured in the TOF and an estimate of the expected time based on the flight-path of the particle as determined from the tracking. A fit to the pion peak gives an estimate of 96 ns for the TOF resolution. A more detailed discussion of particle identification of the TOF and its resolution is found in section 3.2.4

## 2.7 Summary of PHENIX Data Set

Data from eight running periods have so far been written to tape. Table 2.1 summarizes the luminosity and number of events recorded for each of the running periods. The present analysis used the Runs 4, 5 and 6 p + p and Au + Au data sets.

# Chapter 3

## Data Analysis

### 3.1 Direct Photons and $R_\gamma$

#### 3.1.1 Photon Sources

The definition of 'direct' photons is not always consistent throughout the literature. Here, we define direct to denote any photon not produced from the decay of a hadronic bound state. The inclusive photon sample is then the sum of two components:

$$N_{inclusive} = N_{decay} + N_{direct} \quad (3.1)$$

Direct, defined as such, includes photon production from bremsstrahlung which is present at NLO, for example, by addition of a hard photon radiation to either of the outgoing partons in the LO parton scattering diagrams. In principle, photons from medium-induced sources are also included. The two most significant sources of decay photons are the two photon channel decays of the  $\pi^0$  and  $\eta$  meson. As the lightest hadron bound state the branching ratio of this decay from the  $\pi^0$  is  $\approx 99.98\%$ . The  $\eta$  meson di-photon branching ratio is about 39% while alternate channels feed down to the  $\pi^0$ . PHENIX measurements exist for the cross sections of  $\pi^0$  and  $\eta$  mesons in both p + p and Au + Au collisions, as well as in  $d + Au$  and  $Cu + Cu$ . The measured ratio of the  $\eta$  to  $\pi^0$  cross section ( $R_{\eta/\pi^0}$ ) is nearly constant at high  $p_T$  with a value of between 0.4-0.5 above 2 GeV in both data sets [77] consistent with the world average. Interestingly, in Au + Au  $R_{\eta/\pi^0}$  does not deviate from its value in elementary particle collisions despite the factor of 5 suppression suffered by the individual spectra. PHENIX has also published data on next largest photon contributer, the  $\omega$  meson, in p + p collisions and preliminary Au + Au data exists as well. In this study as in [67] the fraction of the total photon

contribution of the  $\eta$  and  $\omega$  are taken to be 19% and 5%, respectively. These three sources account for around 99% of the total decay photon cross section and all remaining decay sources are neglected in this study. Due to the partial cancelation of systematic uncertainties it is useful to tabulate the quantity  $R_\gamma$ , where  $R_\gamma \equiv N_{\text{inclusive}}/N_{\text{decay}}$ .

### 3.1.2 $R_\gamma$

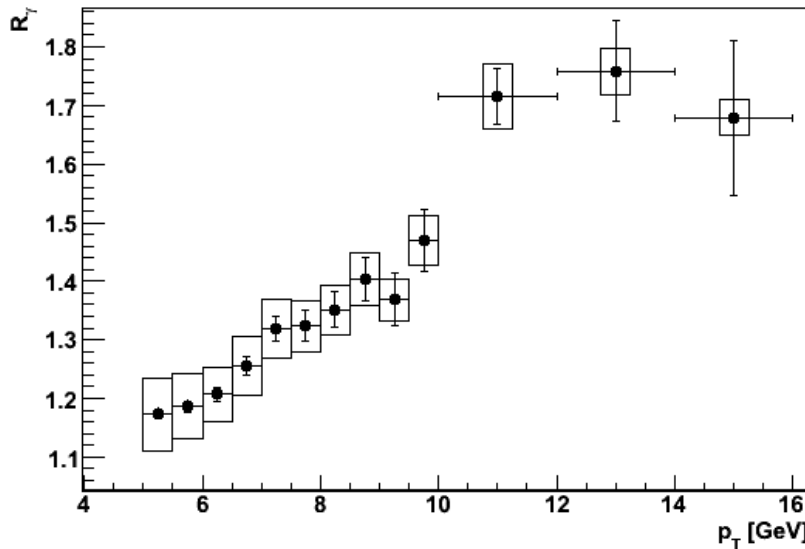


Figure 3.1:  $p + p R_\gamma$  values determined from the Run 5 data. Merged clusters are excluded.

The values of  $R_\gamma$  in Au + Au and  $p + p$  collisions are determined externally to the present analysis from the Run 4 and Run 5 data, respectively and are shown in figures 3.1 and 3.2. The appropriate value of  $R_\gamma$  to use in the subtraction of the measured per-trigger yields is slightly different than the natural value given by these fully corrected data. There are two effects that, although fairly small, are addressed. Firstly, above 10 GeV a fraction of  $\pi^0$  decay photons fail the shower shape cut due to cluster merging. The merging effect is addressed in simulations which are discussed in section 4.7<sup>1</sup>. Secondly, the results presented in this study are not corrected for the resolution of the trigger particle. Since the decay photon spectrum is slightly steeper than that

<sup>1</sup>Merging corrections are only required in Au + Au  $R_\gamma$ , the  $p + p R_\gamma$  values were provided with merged clusters already excluded

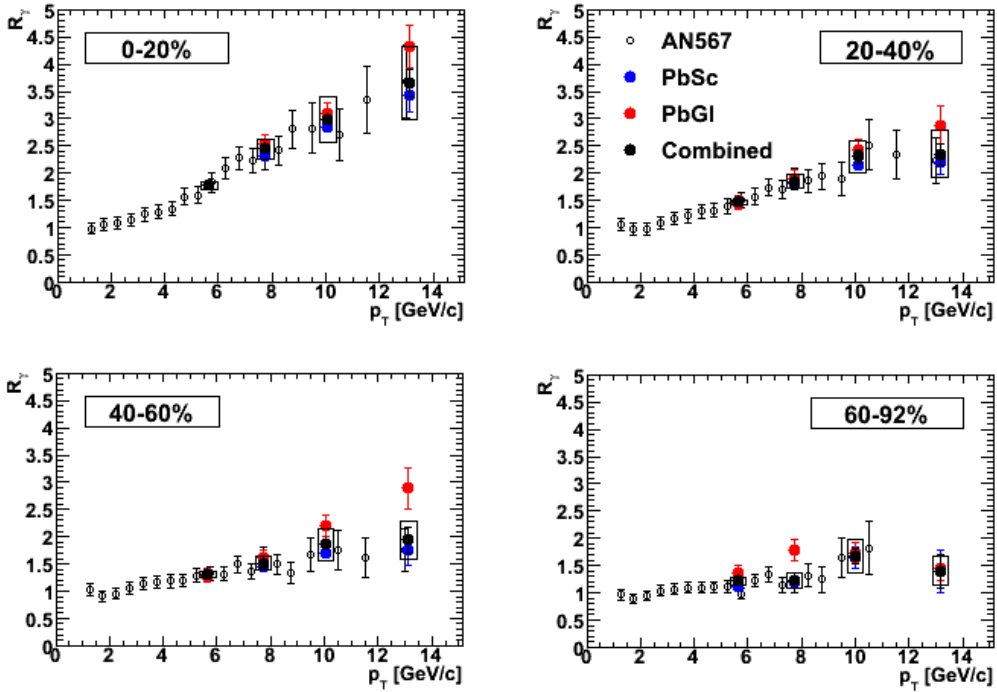


Figure 3.2: Au + Au  $R_\gamma$  values determined from the Run 4 data. Red and blue points show the PbSc and PbGl results while the black points show the combined result. Open points are a previous analysis.

$p_T$ [GeV]	0-20%	20-40%	40-60%	p + p
5-7	1.5	1.0	0.8	0.6
7-9	1.8	1.3	1.0	0.8
9-12	2.2	1.6	1.4	1.0
12-15	2.2	1.8	1.6	1.2

Table 3.1: Resolution Corrections to  $R_\gamma$  (as a percentage of  $R_\gamma$ )

of direct photons the resolution smearing effect them slightly differently. This has a negligible effect on the associated yields since they change fairly slowly with  $p_T$ , however, the apparent value of  $R_\gamma$  can be as much as  $\sim 2\%$  smaller than the natural value in central Au + Au. The effect is evaluated by a simple Monte Carlo calculation which applies a Gaussian smearing to the decay and direct photon spectra and calculates the effective change to  $R_\gamma$ . The correction (actually an un-correction) values are listed in table 3.1.

## 3.2 Particle Identification

### 3.2.1 Photon Identification

Clusters in the EMC are identified as photons according to the following criteria:

- shower shape cut:  $\chi^2 < 3$
- track-based charged hadron veto
- hot and dead tower exclusion
- fiducial cut:  $|z_{EMC}| < 155$  cm
- two tower cut around the edge of each sector

The fiducial and sector edge cuts exclude photons for which some of the energy was lost and to bring the acceptance of single photons closer to that of  $\pi^0$ 's, as will be discussed in the next section.

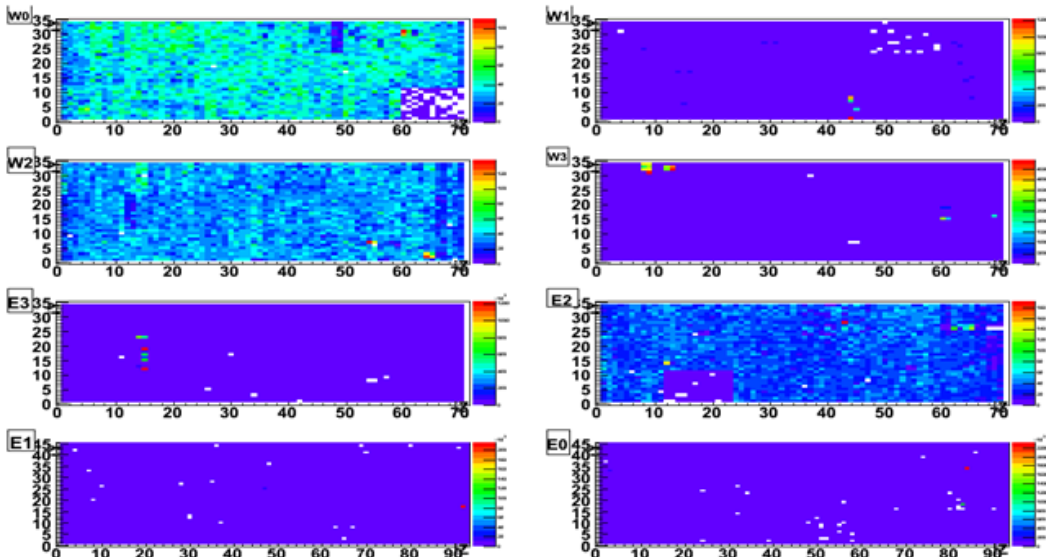


Figure 3.3: Central tower distributions for photons of  $p_T > 5$  GeV for each sector in the EMC as a function of the z and y index of each tower from the Run 6 ERT triggered data set before hot tower exclusion.

Hot towers report a signal in the absence of real energy deposition. Their removal from the data is particularly essential for the statistical subtraction

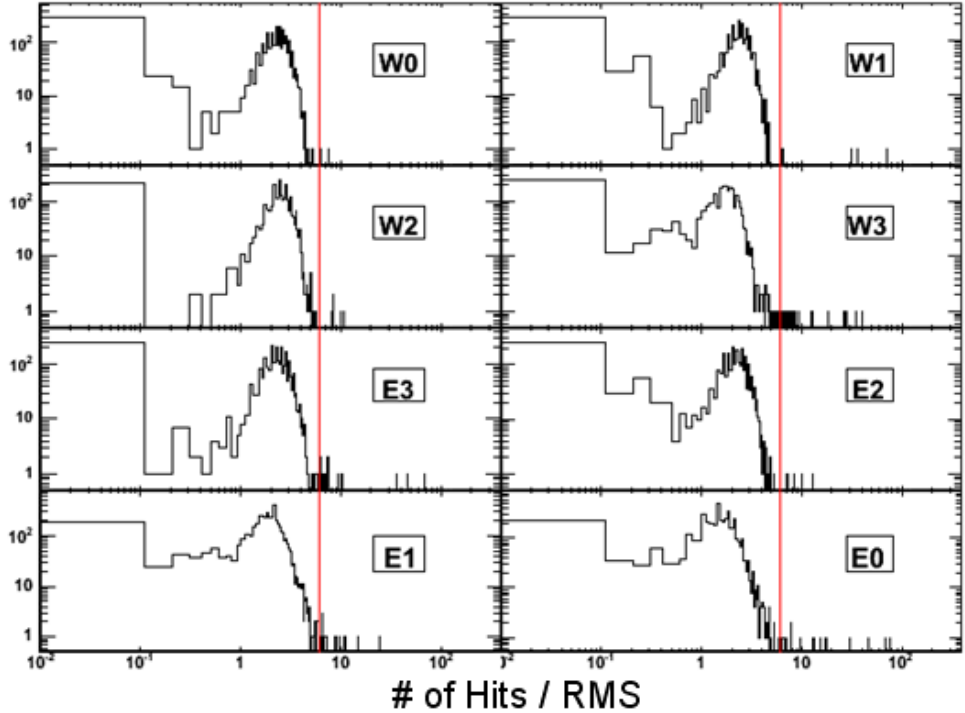


Figure 3.4: The distribution of hit frequencies (log-log scale) normalized by the sector RMS of central towers for photons of  $p_T > 5$  GeV for each sector in the EMC from the Run 6 ERT triggered data set before hot tower exclusion.

method since they contaminate the inclusive photon sample at a much higher level than the decay sample, the difference being due to the invariant mass cuts used in decay photon identification. For the Run 4 and 5 data hot towers were obtained from other photon analyses. For the Run 6 data, on the other hand, the hot tower list was determined as part of this analysis as that data set was relatively new at the time of this work.

The central tower of each cluster was used to determine whether a tower is unusually active. Figure 3.3 shows the central tower distributions for high  $p_T$  photons ( $> 5$  GeV) from the Run 6 data before hot tower exclusion. Hot towers are clearly visible in all sectors with the possible exception of W0. Figure 3.4 shows the distribution of towers divided by the RMS hit frequency for each sector. Towers for which the hit frequency is greater than 6 times the RMS are removed from the analysis. Figure 3.5, the hit map after hot tower removal, shows a much more uniform hit distribution. The dark blue boxes correspond to areas in which the triggered was masked off.

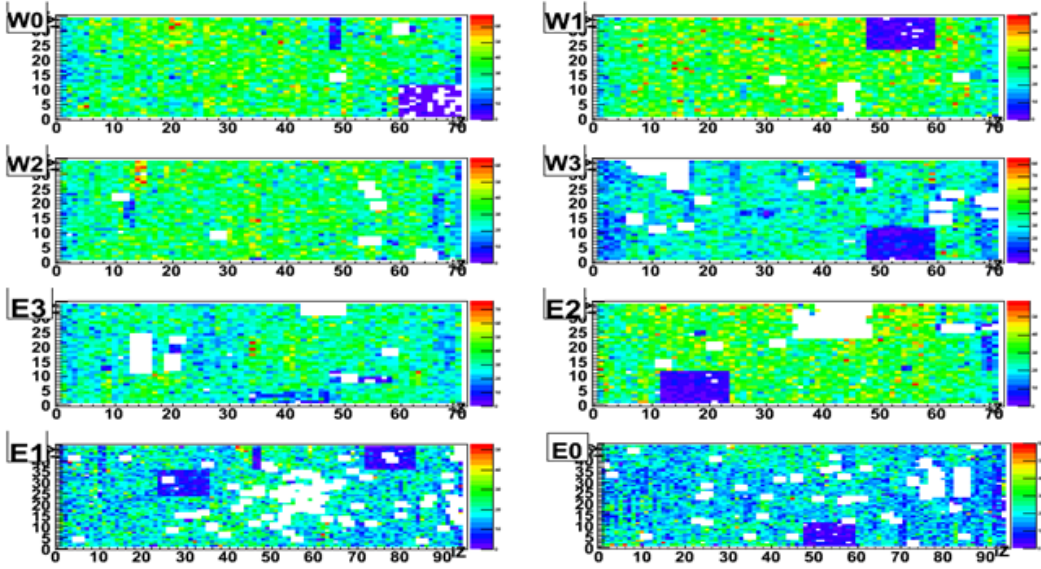


Figure 3.5: Central tower distributions for photons of  $p_T > 5$  GeV for each sector in the EMC as a function of the  $z$  and  $y$  index of each tower from the Run 6 ERT triggered data set after hot tower exclusion.

Although the hot tower maps for Runs 4 and 5 were largely completed by the time this study began the same hit distributions were created for those runs. In addition to finding a small number of additional hot towers in both data sets, a small number of runs were found to have anomalous hit distributions in the Run 4 data. These runs, an example of which is shown in figure 3.6 appear to have a much larger number of clusters in one of the PbGl sectors suggesting that the gain was not set properly.

Although the shower shape cut removes much of the hadronic contamination, a non-negligible contribution from hadronic showers remains. In most analyses these clusters are excluded by matching them to hits in the PC3. Only the distance to the closest PC3 hit is stored rather than the PC3 hit information itself. This means that such an approach not feasible in mixed events (discussed in section 3.3). An alternative approach using track information from the drift chamber was employed. In order to asses the reliability of this method of charge rejection, the contamination was first isolated by selecting tracks for which there is no close PC3 hit. Figure shows the  $\Delta\phi$  distribution for cluster-track pairs for which each track's nearest PC3 hit is beyond  $> 20$  cm in  $z$  and  $> 0.04$  radians in  $\phi$ . The peaks correspond to pairs in which the cluster and track arise from the same charged hadron. As they emerge from the magnetic field positively and negatively charged tracks are

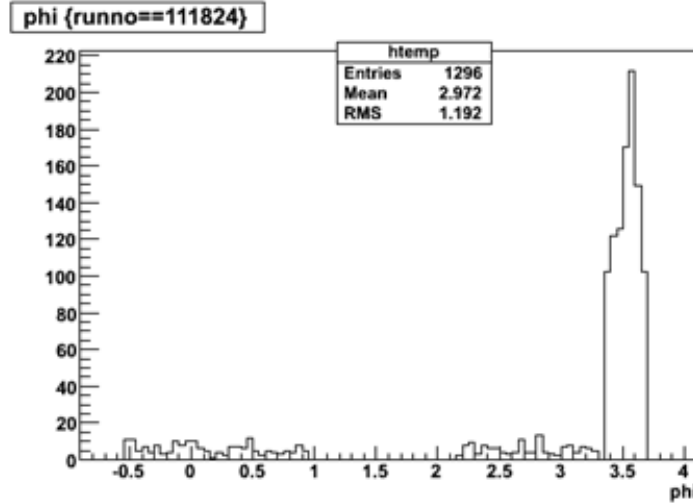


Figure 3.6:  $\phi$  distribution of clusters from run 111824 from the Run 4 Au + Au data set.

bent in opposite directions giving rise to a double peak structure.

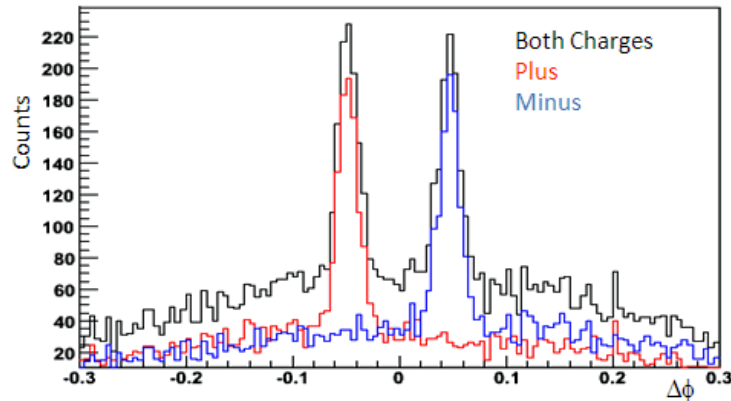


Figure 3.7:  $\Delta\phi$  distribution of cluster-track pairs for tracks with no near PC3 hit. Positively and negatively charged track are shown separately.

Veto candidates are selected from drift chamber tracks by requiring only that a hit is found in a X1, X2 and UV wire (quality > 7). No information from the pad chambers is required in order to minimize the effect of dead areas and inefficiencies. The distance to the nearest track is shown in figure 3.8 for photons of energy > 5 GeV in both p + p (right) and minimum bias Au + Au

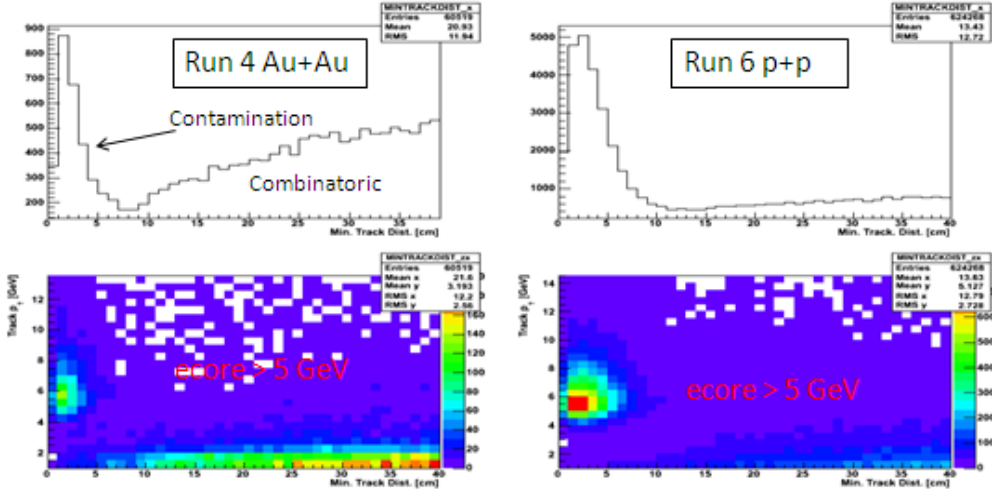


Figure 3.8: Distance between high energy ( $> 5 \text{ GeV}$ ) clusters and the nearest charged track for Au + Au (left) and p + p (right). The bottom set of plots also shows the distribution as a function of the track  $p_T$ .

data left. In the Au + Au data an  $< 8 \text{ cm}$  cut appears to remove nearly all of the hadron contamination while removing very few real photon clusters. In the p + p data the contamination shows a slightly broader peak which can be attributed to the poorer resolution of the event vertex in the z-direction. In that case an elliptical cut was implemented with principal axes of 12 cm in the longitudinal direction (z) and 8 cm in the transverse direction ( $\phi$ ).

### 3.2.2 $\pi^0$ and $\eta$ Identification

$\pi^0$  and  $\eta$  mesons are reconstructed by evaluating the invariant mass of photon pairs

$$m_{\gamma\gamma} = 2E_1E_2 \cos(1 - \Psi) \quad (3.2)$$

where  $\Psi$  is their opening angle. In order to suppress combinatorial pairs only photons above 1 GeV are considered. The charge veto and shower shape cuts are applied only to the leading photon as applying those cuts to the sub-leading photon does little to improve the purity. As will become clear it is important to use a set of cuts for which the inclusive photon and  $\pi^0$  sample have roughly the same acceptance. Therefore the leading photon is required to pass the same fiducial cut ( $|z_{EMC}| < 155 \text{ cm}$ ) as is applied to the inclusive photon sample. The sub-leading photon, on the other hand, may be obtained from towers out to the two tower edge cut ( $|z_{EMC}| < 165 \text{ cm}$ ).

Both the  $\pi^0$  and  $\eta$  peaks are visible in figure 3.9 which shows the invariant mass distribution from p + p collisions. Red lines indicate the  $\pi^0$  and  $\eta$  selection cuts which are  $120 < m_{\gamma\gamma} < 160$  MeV for the  $\pi^0$  and  $530 < m_{\gamma\gamma} < 580$  MeV for the  $\eta$ . The signal-to-background in the  $\pi^0$  mass window is large enough that no attempt is made to subtract the background. The effect of combinatorial matches is discussed in section 4.3.  $\eta$  reconstruction, on the other hand, has a purity of 60 – 70% depending on the  $p_T$  selection in p + p collisions. The contribution of false matches to the per-trigger yield is subtracted using a sideband analysis which discussed in section 3.4.6.

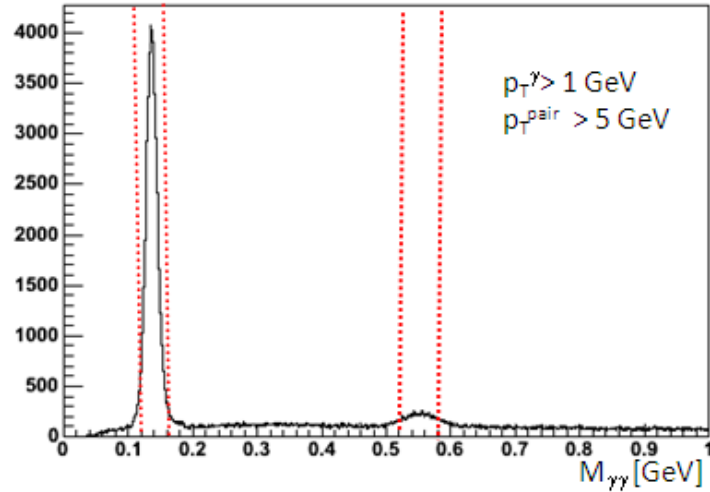


Figure 3.9: Invariant mass distribution of photon pairs with  $p_T^\gamma > 1$  GeV and  $p_T^{pair} > 5$  GeV from p + p collisions.

### 3.2.3 Charged Hadron Identification

Drift chamber tracks are identified as charged hadrons according to the following criteria:

- Quality Selection
- PC3 and EMC matching
- RICH ring veto

The selection of tracks with a quality of 63 requires that there are hits in an X1, X2 and UV wire as well as a hit in the PC1. Quality 31 tracks are also used where the UV and PC1 hits are not required to be unique. Background from

off-vertex tracks from decays, conversion and albedo are reduced by requiring a match at the  $3\sigma$  level to the PC3 and the EMC. Electrons are rejected by vetoing tracks with a ring in the RICH detector ( $N_0 \leq 0$ ).

### 3.2.4 Proton and Pion Identification

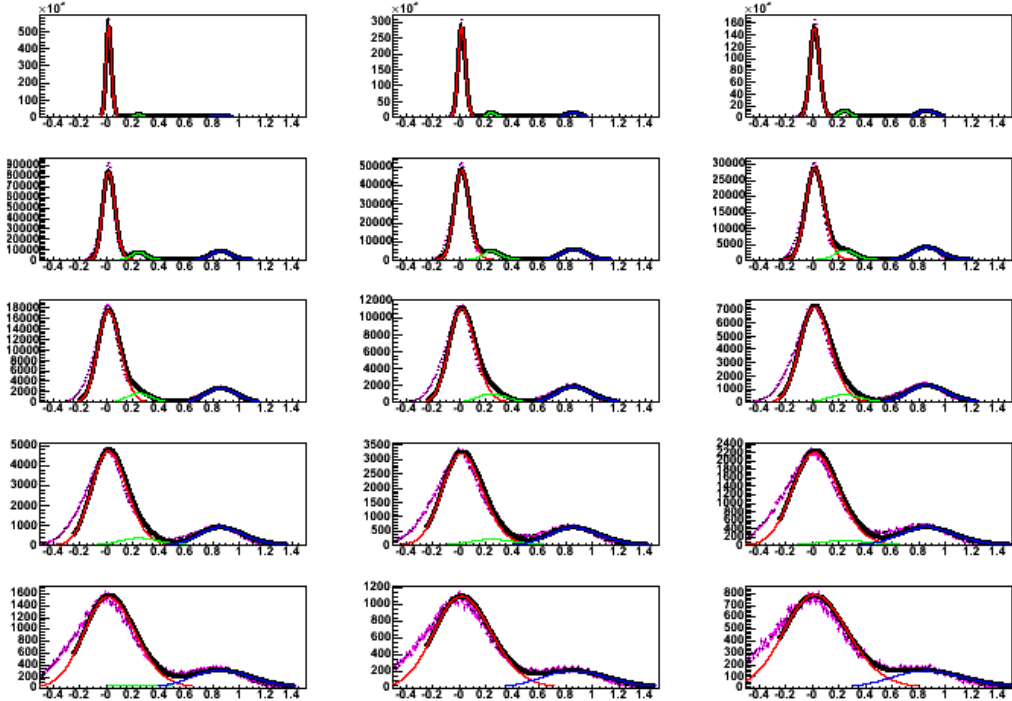


Figure 3.10:  $m^2$  distributions from the EMC in 100 MeV  $p_T$  bins starting at  $500 < p_T < 600$  MeV (upper left) and ending with  $1.4 < p_T < 1.5$  GeV (lower right). The red, green and blue lines show the identified pion, kaon and proton peaks, respectively.

Protons and pions are identified using the EMC and TOF detectors. At low momentum the timing resolution of these detectors is such that the pion, kaon and proton signals are all well separated from one another. As the momentum increases the peaks in the  $m^2$  distribution begin to overlap as shown in figures 3.10 and 3.11. Eventually Gaussian fits are not able to resolve the peaks without additional constraints. The dependence of the widths on momentum is, however, known to obey the following equation to good approximation [93].

$$\sigma_{m^2}^2 = \frac{\sigma_\alpha^2}{K_1^2}(4m^4 p^2) + \frac{\sigma_{ms}^2}{K_1^2} \left[ 4m^4 \left( 1 + \frac{m^2}{p^2} \right) \right] + \frac{\sigma_{TOF}^2 c^2}{L^2} [4p^2(m^2 + p^2)] \quad (3.3)$$

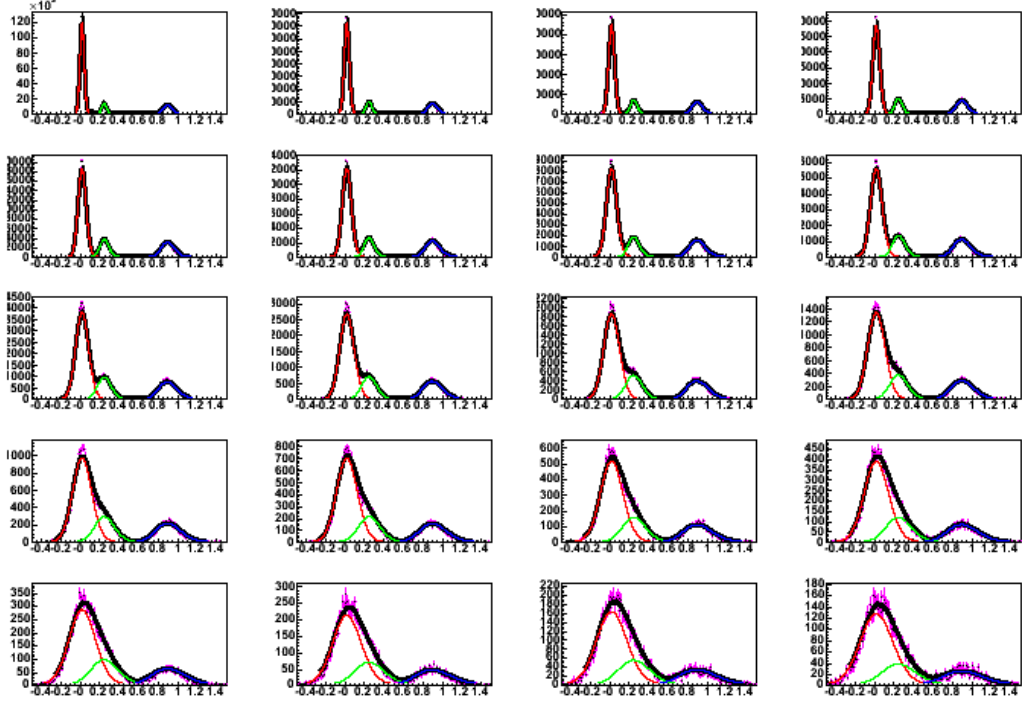


Figure 3.11:  $m^2$  distributions from the TOF in 100 MeV  $p_T$  bins starting at  $1 < p_T < 1.1$  GeV (upper left) and ending with  $2.4 < p_T < 2.5$  GeV (lower right). The red, green and blue lines show the identified pion, kaon and proton peaks, respectively.

where  $p$  is momentum and  $m$  is particle mass.  $\sigma_\alpha$  corresponds to the inherent angular resolution,  $\sigma_{ms}$  accounts for multiple scattering and  $\sigma_{TOF}$  is the overall detector resolution.  $K_1$  is the field integral value. In the lowest  $p_T$  bin, where the peaks are well separated, the mass $^2$  distributions are fit using this equation treating  $\frac{\sigma_\alpha^2}{K_1^2}$ ,  $\frac{\sigma_{ms}^2}{K_1^2}$  and  $\frac{\sigma_{TOF}^2 c^2}{L^2}$  as free parameters. These parameters are then held fixed in the higher  $p_T$  bins allowing only the amplitude of the Gaussians to float. The three Gaussian fit is shown in black while the individual  $\pi$ ,  $k$  and  $p$  components are shown in red, green and blue, respectively. A  $2\sigma$   $m^2$  window is used to set the identification range of protons and pions for  $p_T$  bins in which all three peaks are well separated. After that point the window is set by the  $2\sigma$  limit of the contaminating peak. Using this method pions are

identified in the EMC to out  $p_T = 1.5$  GeV after which the kaon peak is no longer discernable. Protons are still identifiable out to 2 GeV as the largest contamination comes from the pion peak. Using the TOF all three peaks can be separated out to 2.5 GeV.

### 3.3 Two Particle Correlations

In this study we concern ourselves primarily not with the production rate of photons (and  $\pi^0$ 's and  $\eta$ 's) themselves, but rather with that of the *partner* particles associated with these *trigger* particles. Therefore, instead of quoting the yield of pairs (often denoted simply by  $N$ ) it is useful to divide by the number of triggers leaving the associated yields, also referred to as the conditional or per-trigger yield:

$$Y \equiv \frac{N^{pair}}{n^{triggers}} \quad (3.4)$$

This quantity is typically plotted as function of the azimuthal angle between the trigger and partner particle,  $\Delta\phi$ , as the jet structure is particularly evident. In order to isolate correlations due to jets one must remove other sources of correlation whether they arise from physical mechanisms, such as collective flow (see section 3.3.4), or are artifacts of the detector geometry. The latter case is particularly important for PHENIX given its two arm configuration.

#### 3.3.1 Background Normalization

Correlations amongst high  $p_T$  particles in elementary particle collisions are widely accepted to be a manifestation of jet production. In a central heavy-ion collision the correlation signal from jets is embedded in a background of copious particle production, since the number of participating nucleons is of order 100. Since hard collisions are rare, this combinatorial background can be estimated by event mixing of the triggered sample with a set of similar events in which no trigger is required. Stated differently, one estimates the mean rate of uncorrelated production by measuring the mean rate of particles that satisfy the trigger and partner conditions, independently. Hence this procedure, which has been successfully employed in previous PHENIX results [94,50,95], is often referred to as the *Mean Seeds / Mean Partners* (MSMP) method.

The background we wish to subtract is not purely combinatorial, however. In heavy-ion collisions there is an additional source of azimuthal correlations, namely the elliptic flow described in section 1.3.1. Immense insight has been

gained via measurements of the elliptic flow as evidenced, for example, by the number of recent PHENIX publications on the subject [21, 96, 97]. In the present study, however, we are interested in the correlation signal from jets. We proceed by applying a two source model, *i.e.*, that particle pairs can be decomposed into a jet signal and a background. For a perfect detector, it follows that the pair rate as a function of their azimuthal opening angle, sometimes referred to as the Jet Function,  $J(\Delta\phi)$ , can be represented by:

$$\frac{dN_{total}}{d\Delta\phi} = \frac{dN_{jet}}{d\Delta\phi} + \frac{dN_{bknd}}{d\Delta\phi} \quad (3.5)$$

The background contribution may be expressed as the product of the mixed event pair rate modulated by the collective flow which can be represented as a Fourier expansion. Only the second harmonic term, corresponding to elliptic flow, is considered since the contribution from other harmonics are known to be small [98], [99]:

$$\frac{dN_{bknd}}{d\Delta\phi} = \frac{dN_{mix}}{d\Delta\phi} (1 + 2v_2^{trigger} v_2^{partner} \cos(2\Delta\phi)) \quad (3.6)$$

Although this expression seems intuitively reasonable, in practice, there is a rather subtle correction that must be considered. In order to accurately represent the combinatorial pairs, the mixed event sample must have exactly the same *global* characteristics as the triggered set. The most important example of such a characteristic is collision centrality. Since the pair rate is a strong function of centrality, mixing triggers from central events with partners from peripheral events, as an extreme example, would vastly underestimate the level of combinatorial background. The centrality determination, discussed in section 2.3, is limited in its resolution by the finite multiplicity observed in the BBC and ZDC detectors. By mixing in progressively finer bins, it was determined that mixing with centrality bins smaller than 5% approaches the limit of the precision that can be achieved by event mixing alone [100].

The effect of the finite centrality binning is estimated by the following procedure. For each  $p_T$  selection, the number of triggers and partners as a function of centrality is determined from a sample of minimum bias collisions. These distributions (figure 3.12) are plotted as a function of both  $N_{part}$  and  $N_{coll}$  (based on Glauber calculations performed in [101]). The dependence on both these quantities is then parameterized using two different functional forms, the “arctangent”:  $\alpha \arctan | - \beta | x^\kappa$  and the “saturated exponential”:  $\alpha(1 - \exp(-|\beta| \kappa^C))$ .  $\alpha, \beta$  and  $\kappa$  are free parameters and  $x$  is taken to be  $N_{part}$  and  $N_{coll}$ , in turn.

For each of the 5% centrality bins one can then calculate the expected

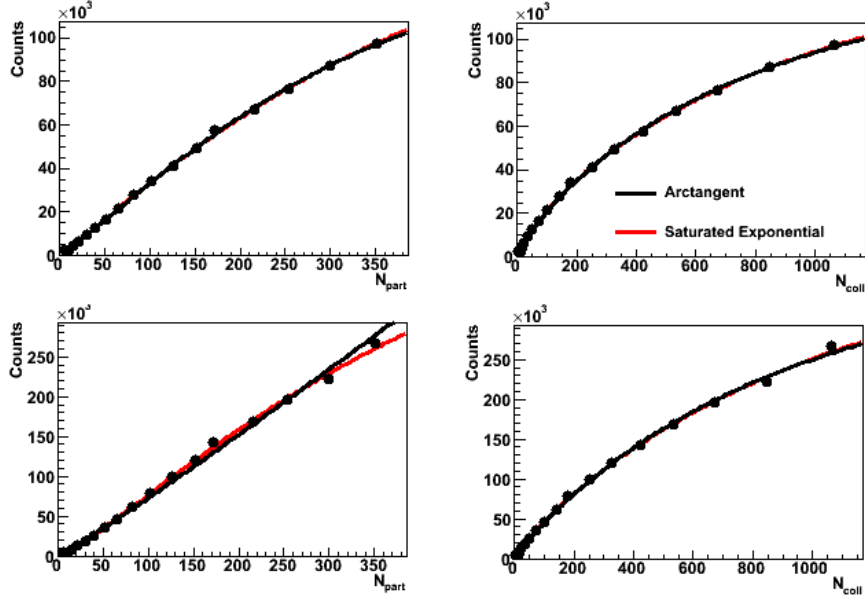


Figure 3.12: Number of inclusive photon triggers (top row) and charged hadron partners (bottom row) as a function of  $N_{part}$  (left) and  $N_{coll}$  (right) for the  $p_T$  combination  $5 < p_{T,t} < 7$  and  $1 < p_{T,a} < 2$  GeV. The distributions are each fit with two functional forms.

number of pairs in real events,  $\langle n^{trigger} n^{partner} \rangle$ , and in independent (mixed) events,  $\langle n^{trigger} \rangle \langle n^{partner} \rangle$ , as follows. At each value of  $N_{part}$  ( $N_{coll}$ ) the corresponding number of triggers and partners is evaluated from the two functional forms that were fit to the data. The probability  $\phi$  for that value of  $N_{part}$  ( $N_{coll}$ ) to contribute to the centrality selection in question is taken from the Glauber calculations. The ratio of the joint probability to the independent probabilities,  $\xi$ , is then given by

$$\xi \equiv \frac{\langle n^{triggers} n^{partners} \rangle}{\langle n^{triggers} \rangle \langle n^{partners} \rangle} = \frac{\sum_i \phi_i n^{triggers} n^{partners}}{\sum_i \phi_i n^{triggers} \sum_i \phi_i n^{partners}} \quad (3.7)$$

where  $i$  runs over all values of  $N_{part}$  or  $N_{coll}$ . The average of the four  $\xi$  values obtained using  $N_{part}$  and  $N_{coll}$  with each of the two fit functions is used as the final correction value. The maximum spread of the values was used to assign a systematic error on the procedure.  $\xi$  values were obtained for each trigger and associated  $p_T$  selection, although, no significant  $p_T$  dependence was observed. A typical example of a  $\xi$  correction function is shown in 3.13.

Accounting for the multiplicity resolution correction equation 3.6 becomes

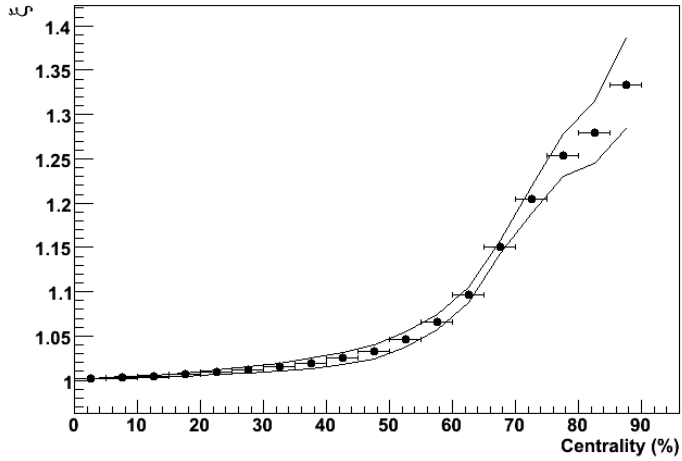


Figure 3.13: An example of the multiplicity resolution correction as a function of centrality for inclusive photons of  $5 < p_T < 7$  and charged hadrons of  $1 < p_{T,a} < 2$  GeV. The error band indicates the systematic uncertainty described in the text.

$$\frac{dN_{bknd}}{d\Delta\phi} = \xi \frac{dN_{mix}}{d\Delta\phi} (1 + 2v_2^{trigger} v_2^{partner} \cos(2\Delta\phi)) \quad (3.8)$$

Although this expression is valid for a perfect detector, effects arising from finite acceptance, efficiency and resolution must be considered. The fully corrected per-trigger yield is evaluated according to

$$Y \equiv \frac{1}{n^{triggers}} \frac{dN_{jet}}{d\Delta\phi} = \frac{\epsilon^{partner}}{n^{triggers}} \left[ \frac{1}{A(\Delta\phi)} \frac{dN_{total}}{d\Delta\phi} - \frac{\xi}{A(\Delta\phi)} \frac{dN_{mix}}{d\Delta\phi} (1 + 2v_2^{trigger} v_2^{partner} \cos(2\Delta\phi)) \right] \quad (3.9)$$

$A(\Delta\phi)$  and  $\epsilon^{partner}$  are the acceptance and charged hadron efficiency corrections and their application will be explained in the following two sections. Before addressing them some final remarks concerning the MSMP method are in order. Event mixing is also performed in 5% bins in  $z$  coordinate of the collision vertex. Any  $\xi$ -type correction from the  $z$ -vertex binning was found to be negligible [102]. An alternate normalization of the jet functions, the *Zero Yield at Maximum* (ZYAM) procedure is more frequently used in the literature

(see for example [53]). This method determines the background by a fit and is thus sensitive to statistical fluctuations, especially at high  $p_T$ , where PHENIX does not sample the region around  $\pi/2$  very well. In the current analysis, we will be subtracting per-trigger yields, namely the inclusive and decay correlations, whose combinatorial background should be approximately the same. Using the ZYAM method, one would introduce an extra source of uncertainty by determining the background by using a separate fit for the inclusive and decay associated yields.

### 3.3.2 Acceptance Corrections

In the absence of any acceptance correction procedure even isotropic particle production will exhibit a two peak structure in  $\Delta\phi$  in the PHENIX aperture. The acceptance of the detector is determined by the mixed event distribution. It is normalized such that the average correction value is unity.

$$A(\Delta\phi) = \frac{1}{C} \frac{dN_{mix}}{d\Delta\phi}, \quad \text{where} \quad C = 2\pi \int_0^{2\pi} \frac{dN_{mix}}{d\Delta\phi} d\Delta\phi \quad (3.10)$$

This corrects the yield in the two arm acceptance to the yield over the full azimuth with the same average efficiency.

Figure 3.14 shows examples of real and mixed event  $\Delta\phi$  distributions and the resulting correlation function found by taking their ratio. The normalization of the mixed event distribution is chosen such that the average value of the correction is unity. The acceptance corrected yield is then equivalent to that of a detector with full azimuthal coverage with the same average efficiency for charged hadron detection. The jagged features in the raw distribution are due to non-uniformities in the acceptance and are removed in the correlation function. It is important to note that we do not correct for the pair acceptance as a function of the longitudinal opening angle ( $\Delta\eta$ ) and instead simply quote per-trigger yields in the PHENIX aperture. This has the effect that some fraction of the near-side pairs are missed. This fraction becomes smaller at large  $p_T$  as the jet becomes narrower. On the away-side the jet is often missed entirely because the two jets may have different rapidities when the colliding partons take different values of Bjorken  $x$ . The finite  $\Delta\eta$  acceptance will be shown to have consequences with regard to the direct photon correlation subtraction method discussed in 3.4.

### 3.3.3 Charged Hadron Efficiency Corrections

In order to determine the charged hadron efficiency for Run 2, detailed GEANT studies were performed. Rather than repeat the simulations for each run there-

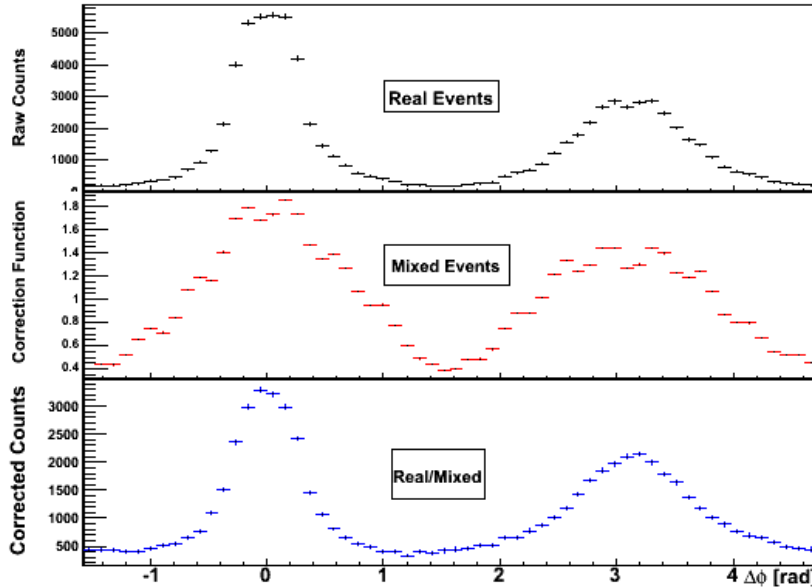


Figure 3.14: Demonstrating the acceptance correction procedure are the uncorrected  $\Delta\phi$  distribution from real events (top), the (normalized) mixed event distribution (middle), and the acceptance corrected distribution obtained by taking the ratio of the real and mixed event distributions.

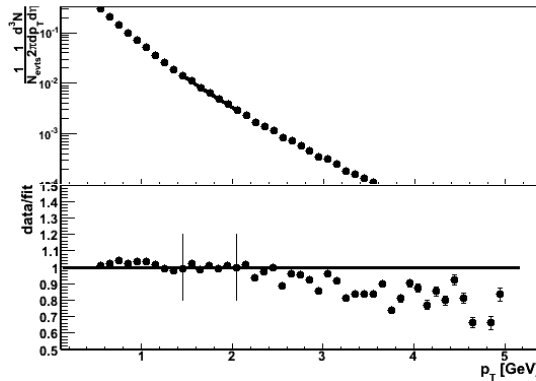


Figure 3.15: An example of a fit to the fully corrected non-identified charged hadron yield from Run 2  $p + p$  collisions.

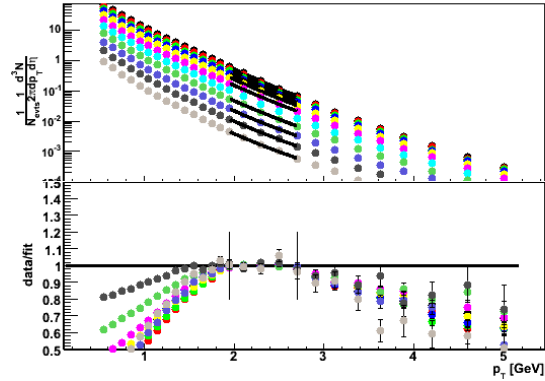


Figure 3.16: Example of fits to the fully corrected non-identified charged hadron yield for 5% centrality bins from Run 2 Au + Au collisions.

after the efficiency corrections are determined by boot-strapping to these published results. Specifically, the correction factors are determined by taking the ratio of PHENIX published, fully corrected charge hadron yields in [24]

and [103] to the raw charged hadron yields in the current analyses. The published data are converted from cross-sections to per-event yields and fit in small  $p_T$  ranges as shown in figures 3.15 and 3.16.

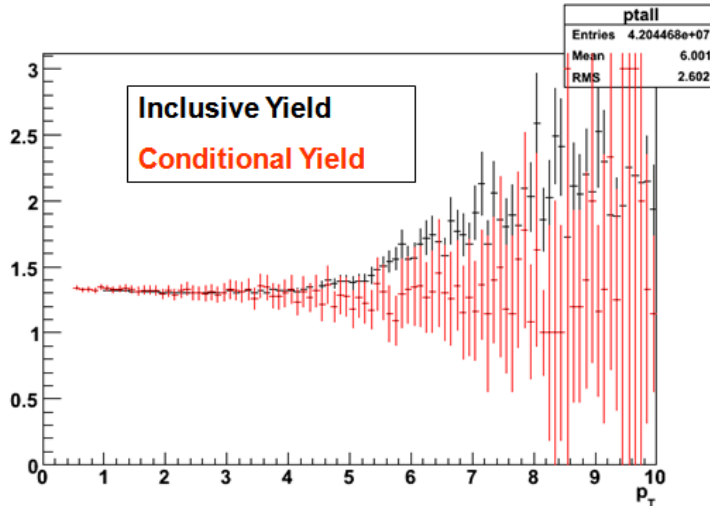


Figure 3.17: The ratio of the raw  $p_T$  spectra of non-identified charged hadrons with 3 sigma and 2 sigma matching cuts for inclusive (black) and conditional (red) yields in  $p + p$  collisions.

The efficiency must be determined from the raw yield in minimum bias data since the presence of a high  $p_T$  particle enhances the overall yield. At high  $p_T$  however, the spectral shape in minimum bias events becomes distorted by the presence of background from low  $p_T$  tracks that are mis-reconstructed. Although such tracks are also present in triggered events it will be shown that they comprise a much smaller fraction of the total sample due to the overwhelming jet associated signal. The onset of background contamination can be seen by varying the matching cuts since the mis-reconstructed background will have a wider matching distribution. Figures 3.17 shows the ratio of the raw  $p_T$  distribution for 2 and 3  $\sigma$  matching cuts in  $p + p$  for data with a high  $p_T$  trigger (red points) and for the minimum bias data (black points). The ratio is fairly constant at low  $p_T$  for both data samples with a difference in shape becoming visible around 5 GeV. Figure 3.18 shows the triggered (left) and inclusive (right) distributions from central Run 4 Au + Au collisions. The effect in the minimum bias Au + Au data is of a much larger magnitude and is visible at lower  $p_T$ , 3 GeV. The absence of such an excess of tracks for the looser matching cuts in the triggered sample indicates that these background tracks do not contribute any significant rate to the jet correlations.

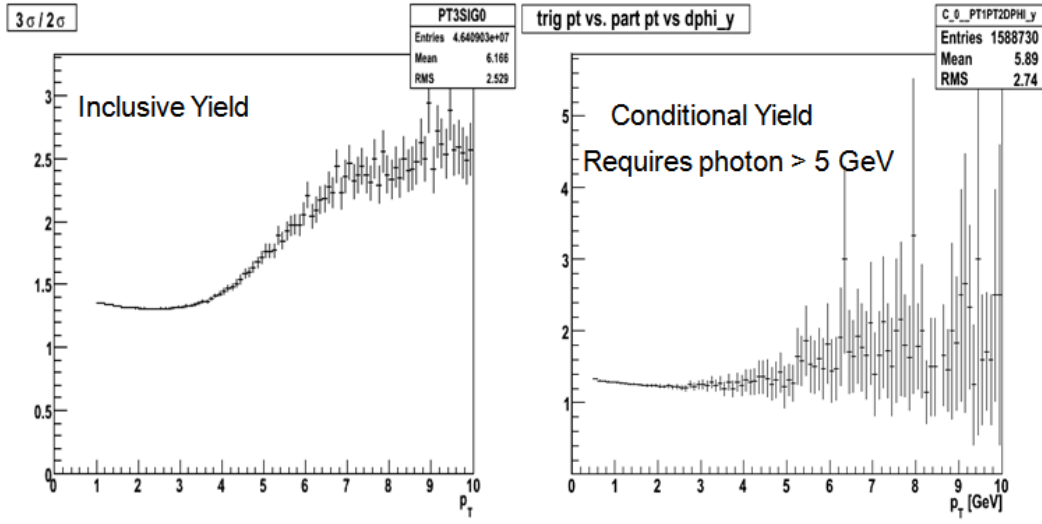


Figure 3.18: The ratio of the raw  $p_T$  spectra of non-identified charged hadrons with 3 sigma and 2 sigma matching cuts for inclusive (left) and conditional (right) yields in Au + Au collisions.

They should therefore be excluded from the calculation of the charged hadron efficiency.

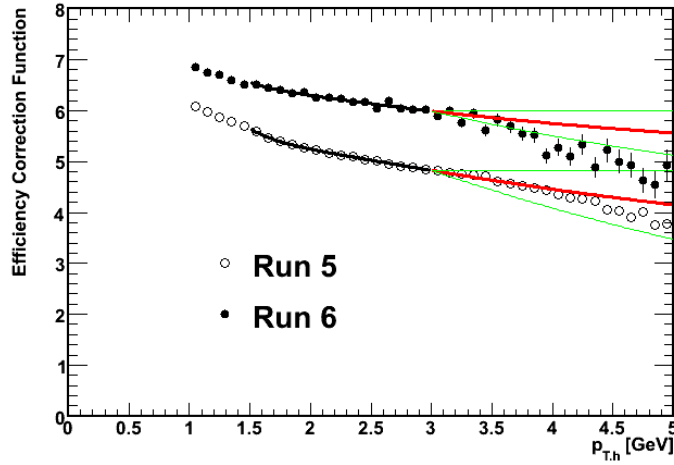


Figure 3.19: Efficiency correction functions for  $p + p$  collisions. The black curve is a fit and the red curve is the extrapolation of the fit to high  $p_T$ . The green lines are used to estimate the uncertainty in the extrapolation.

Figure 3.19 shows the correction function for the  $p + p$  data from Runs 5 and 6. The Run 6 correction is slightly larger due to increased dead area in the drift chamber during that running period. The curves are explained as follows. In the previous simulation studies it was shown that the efficiency correction becomes nearly constant at high  $p_T$  where the bending from the magnetic field and occupancy effects become small [104]. The strategy employed in a recently published article on di-hadron correlations from Run 4 was to assign a constant hadron efficiency above 3 GeV [50]. In the present analysis we adopt a slightly more sophisticated approach by extrapolating the efficiency from its values at low  $p_T$ . The difference between our extrapolated efficiency and value of the efficiency at 3 GeV (above which the efficiency is nearly constant) is treated as an extra source of systematic error in addition to the 9.6%  $\otimes$  4% scale uncertainty which is applied to hadron cross sections.

In order to perform the extrapolation the correction function for each run is fit in the signal dominated region,  $1.5 < p_T < 3.0$  GeV using

$$1/\epsilon(p_T) \propto A/p_T^3 + Bp_T^2 + 4.0165/p_T + 8.55 \quad (3.11)$$

This functional form is very similar to one shown to reasonably describe the Run 2 data [104] but is modified so that it becomes a constant asymptotically at high  $p_T$ . It should be noted however that this form is not motivated by any underlying physics, but rather should be viewed simply as a parametrization of the efficiency correction function in a  $p_T$  range known to be free of background contamination. For the Au + Au data  $A$  and  $B$  are determined in the peripheral data (4.28 and -3.02, respectively) where the contamination rate is low and subsequently held fixed in fits to the other centralities, allowing only the normalization to vary. The efficiency corrections and fits for Run 4 are shown in Figure 3.20. The fit function is taken as the correction in the range 2 to 3 GeV and its extrapolation above 3 GeV. Below 2 GeV the efficiency is known to be centrality dependent due to occupancy effects so the data points are used instead of the fit. The green lines delimit the systematic uncertainty assigned extrapolation. The upper green line is a flat line set to the value of the black fit at 3 GeV. The lower green line is a reflection of the flat line over the red extrapolation line.

### 3.3.4 Elliptic Flow

The correlation signal due to flow is subtracted using measured values of  $v_2$  from external analyses. Figure 3.21 shows the  $v_2$  as a function of  $p_T$  for inclusive photons and for  $\pi^0$ 's as measured in the Run 4 Au + Au collisions <sup>2</sup>.

---

<sup>2</sup>These data have been provided by Chin-Hao Chen [105]

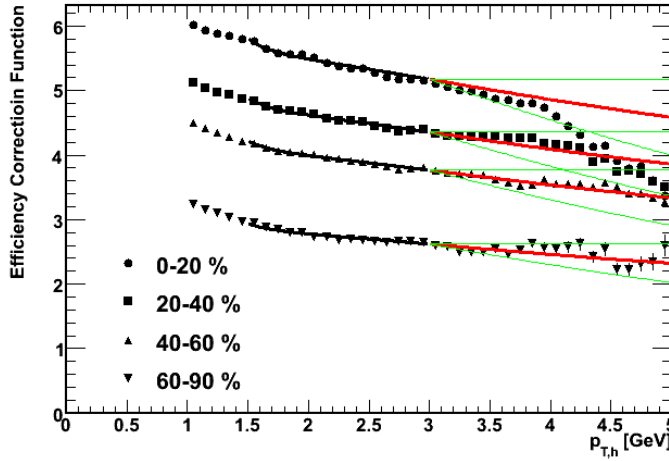


Figure 3.20: Efficiency correction function for Au + Au collisions from Run 4. From top to bottom 0-20, 20-40, 40-60 and 60-92% centrality selections are shown. The black curves are a fit to the points and the red is the extrapolation of those fits to high  $p_T$ . The green lines are used to estimate the systematic error on the extrapolation.

Also shown is a recent  $\pi^0$  measurement from Run 7 Au + Au collisions [106]<sup>3</sup>. Since the Run 7 result has somewhat different  $p_T$  binning we determined the value by a combined fit the Run 4 and 7 data sets. Since the data are well described by a constant at high  $p_T$  we fit the data to a constant to determine the central value. The data were then refit, this time allowing the slope of the fit to vary. The error bands shown in the figure are defined by allowing the constant and linear fits to vary independently within their uncertainties. Although this procedure is slightly convoluted, the uncertainty band obtained is reasonable given the expectation of monotonic behavior for the elliptic flow. The  $v_2$  values for charged hadrons used in this analysis are compared to results from a parallel analysis in figure 3.22.

### 3.4 Statistical Subtraction Method

Event-by-event identification of direct photons is complicated by the presence of the high multiplicity background in Au + Au collisions. A straight-forward alternative is to extract the direct photon per-trigger yield by a completely

---

<sup>3</sup>The Run 4 and Run 7 measurements have been performed by Chin-Hao Chen and Kentaro Miki

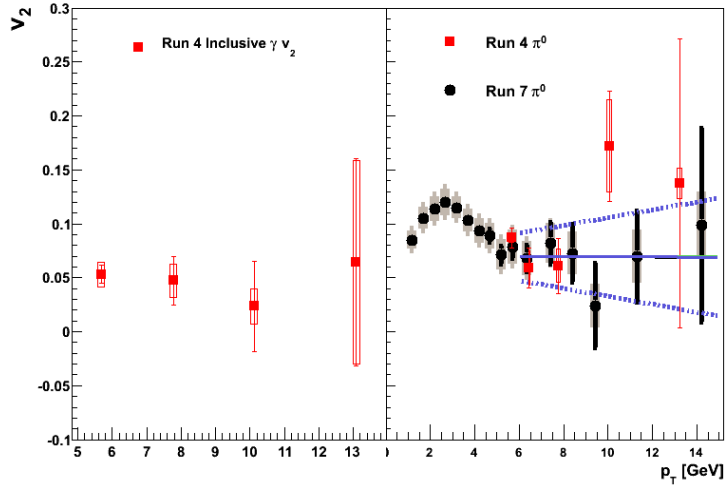


Figure 3.21: The magnitude of the elliptic flow ( $v_2$ ) for inclusive photon (left) from the Run 4 data and for  $\pi^0$ 's (right) from the Run 4 and Run 7 data. The lines on the right panel indicate the value of  $v_2$  and its uncertainty that were used in this analysis.

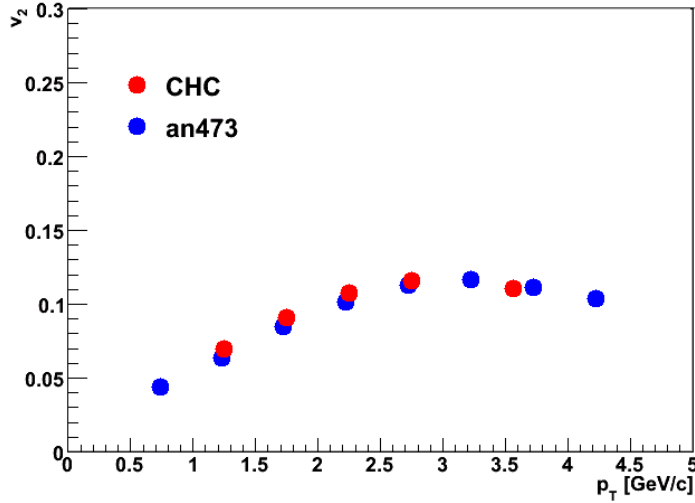


Figure 3.22: The magnitude of the elliptic flow ( $v_2$ ) for non-identified charged hadrons from the Run 4 data. The points labeled 'CHC' were used in this analysis.

statistical subtraction of the decay component from the inclusive photon triggered yield.

The inclusive photon per-trigger yield is expressed in terms of the decay and direct component as

$$Y_{inc} = \frac{N_{decay}}{N_{inclusive}} Y_{decay} + \frac{N_{direct}}{N_{inclusive}} Y_{direct} \quad (3.12)$$

Inserting the definition of  $R_\gamma$  ( $\equiv N_{inc}/N_{dec}$ ) and solving for  $Y_{direct}$  we obtain

$$Y_{direct} = \frac{1}{R_\gamma - 1} (R_\gamma Y_{inclusive} - Y_{decay}) \quad (3.13)$$

The applicability of equation 3.13 to the measured  $Y_{inclusive}$  assumes the photon detection efficiency is the same for direct and decay photons. A correction to this assumption which accounts for cluster merging is discussed in section 4.6.  $Y_{decay}$  is estimated from the measured  $\pi^0$ -h and  $\eta$ -h per-trigger yields. Since decay photons comprise as much as 85% of the inclusive photon sample in the lowest  $p_T$  bin measured in p + p collisions, this is a procedure that must be performed with great care.

### 3.4.1 Parent to Daughter Mapping

In what follows we consider the dominant source of decay photons, the  $2\gamma$  decay of neutral mesons. For definiteness we restrict the discussion to the  $\pi^0$  yields, however all of the same procedures were applied to the  $\eta - h$  measurement with additional considerations relevant to that measurement being discussed in section 3.4.6. The main challenge is that we need to evaluate  $Y_{decay}$  as a function of the decay photon  $p_T$ . Some fraction of the decay photons can be identified event-by-event by reconstructing their invariant mass. On first approximation the per-trigger yield of these tagged photons can be taken to represent that of all decay photons, however the tagging introduces a bias. Symmetric decays are more likely to be reconstructed than are asymmetric ones both due to the smaller opening angle and, more importantly, due to the analysis cuts. This means that the parent  $p_T$ ,  $p_T^\pi$ , for tagged photons will be larger, on average, than the unbiased sample of decay photons which must be subtracted from the inclusive sample.

The solution is to find the decay mapping function  $P(p_T^\pi, p_T^\gamma)$  (sometimes called the two-photon Green's function) which represents the probability of a  $\pi^0$  at some  $p_T^\pi$  to decay into a  $\gamma$  at some  $p_T^\gamma$ . Quite generally one then obtains

$$\frac{dN^\gamma}{dp_T^\gamma} = \int dp_T^\pi P(p_T^\pi, p_T^\gamma) \frac{dN^\pi}{dp_T^\pi} \quad (3.14)$$

where  $N$  is taken to represent either the yield of decay  $\gamma$  or decay  $\gamma - h$  pairs.

As described above, since we measure per-trigger yields we will be interested in the ratio of those two quantities. Since the normalization of the  $P$  cancels in the ratio we will often not bother to normalize its integral to unity as one would a proper probability. Formally, the integral extends over all  $p_T^\pi$  values from  $p_T = 0$  to  $p_T = \infty$ , although for collisions at fixed  $\sqrt{s}$ ,  $\frac{dN^\pi}{dp_T^\pi} \rightarrow 0$  as  $p_T^\pi \rightarrow \sqrt{s}/2$ . In practice photon measurements only extend to much more modest values of  $p_T$ . A truncation procedure is described in section 3.4.5.

Under simple assumptions, an analytic form for  $P$  can be obtained which gives insight into its basic structure, to which more realistic considerations will subsequently be added. Since the probability to yield a photon with energy  $E^\gamma$  from a  $\pi^0$  with momentum  $p^\pi$  is uniform between 0 and  $p^\pi$ , the likelihood of yielding a photon at any particular  $E^\gamma$  decreases as the decay phase space grows, i.e.  $dN^\gamma/dE^\gamma = 2/p^\pi$ , where the factor of 2 reflects the total number of photons in the final state. At the position of the EMC,  $p_T^\gamma \approx E_\gamma$ , and to a good approximation

$$\frac{dN^\gamma}{dp_T^\gamma} = \frac{2}{p_T^\pi}. \quad (3.15)$$

$P$  for a finite sized bin  $a < p_T^\gamma < b$ , which we will refer to as the decay probability function, is then

$$P_{a-b}(p_T^\pi) = \begin{cases} 0 & , p_T^\pi < a \\ \int_a^{p_T^\pi} dp_T^\gamma \frac{2}{p_T^\pi} = 2 \left( 1 - \frac{a}{p_T^\pi} \right) & , a < p_T^\pi < b \\ \int_a^b dp_T^\gamma \frac{2}{p_T^\pi} = 2 \left( \frac{b-a}{p_T^\pi} \right) & , p_T^\pi > b \end{cases} \quad (3.16)$$

This function, shown in figure 3.23 for  $a = 5$  and  $b = 7$  is sometimes referred to colloquially as the shark-fin function.

### 3.4.2 Pair-by-pair weighting

In practice, we would like to evaluate the integral in equation (3.14) for both decay photons and decay photon-hadron pairs by looping over a sample of reconstructed  $\pi^0$ 's. For a perfect detector the number of  $\gamma$ 's or pairs in some bin ( $N_{a-b}^\gamma$ ) would then be determined by performing the summation

$$N_{a-b}^\gamma = \sum_i^{N^\pi} P_{a-b}(p_{T,i}^\pi) \quad (3.17)$$

Note that the shape of the  $\pi^0$  spectrum which was explicit in equation (3.14) is

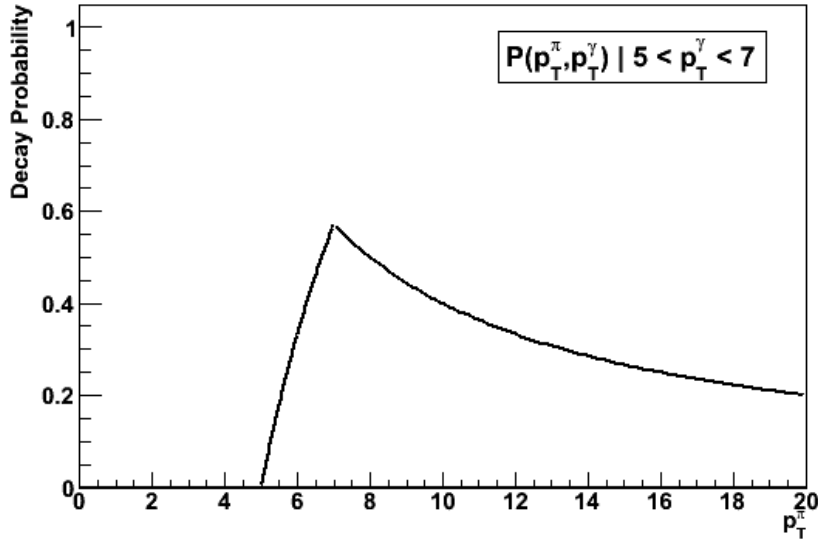


Figure 3.23: Probability for decay into a photon of  $5 < p_T^\gamma < 7$  as a function of  $p_T^\pi$ .

implicit in shape of the distribution of the  $\pi^0$ 's which are being summed over. In a real detector however, the reconstructed sample of  $\pi^0$ 's differs in both momentum and position from the true distribution due to the  $\pi^0$  identification cuts, detector resolution, and acceptance effects including dead areas and variations in efficiency. In this context we will refer to these effects collectively as the  $\pi^0$  reconstruction efficiency which depends rather strongly on momentum, but also on position as discussed below. Moreover, we are not actually interested in estimating the true decay per-trigger yield but instead only the yield we actually measure as part of the inclusive sample. Therefore we need to reproduce as closely as possible the same efficiency (resolution, acceptance, cuts, etc.) that are imposed on the decay photon and decay photon-hadron pairs in their measurement as part of the inclusive photon sample. The schematic shown in figure 3.24 demonstrates the pair-by-pair weighting method for a detector with finite efficiency. One first removes the reconstruction biases from the  $\pi^0$  sample, then decay them and finally simulates the detector response to the decay photons and pairs.

The  $p_T$  dependence of the  $\pi^0$  reconstruction efficiency is fairly easy to understand.  $\pi^0$ 's whose trajectory lies near detector edges are less likely to be reconstructed since one of the daughters often misses the detector. As the momentum of the  $\pi^0$  decreases a progressively larger fraction of the  $\pi^0$ 's are

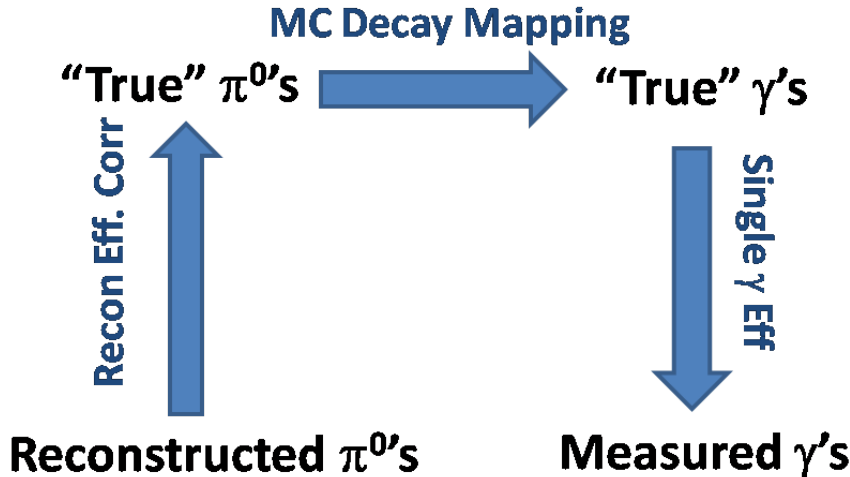


Figure 3.24: Schematic describing the procedure to obtain decay correlations from those of reconstructed parent mesons.

lost due to the edge effect. Large momentum ( $> 12\text{GeV}$ )  $\pi^0$ 's also suffer a loss in efficiency due to primarily to cluster merging as the opening angle becomes very small and the clusters large. The position dependence of the  $\pi^0$  efficiency is a slightly more subtle matter since the true  $\pi^0$  and  $\pi^0 - h$  yields should be very nearly constant over the small rapidity acceptance. Although we correct our per-trigger yields for acceptance effects in the azimuthal direction we do not do so in the longitudinal direction as discussed in section 3.3.2. The yield of pairs in a jet is sharply peaked in  $\Delta\phi$  and  $\Delta\eta$ . If a trigger photon or  $\pi^0$  is near the edge of the detector a large fraction of the associated hadrons on the near-side fall outside the acceptance. Since  $\pi^0$ 's near the edge cannot usually be reconstructed they will lose fewer associated hadrons as compared to the single decay photons signal which we wish to reproduce. This artificial increase in the jet yield will therefore cause an over-subtraction in the determination of the direct photon per-trigger yield. This effect is partially ameliorated by introducing fiducial cuts to match the  $\pi^0$  and single photon acceptances, however such acceptance effects must still be accounted for in the Monte Carlo in order to achieve the desired precision given the small signal-to-background.

To help guide the intuition it's useful to think of the procedure in the continuous limit of equation (3.14) and make the calculation as explicit as possible:

$$N_{a-b}^{\gamma,meas} = \int_0^\infty dp_T^\pi \int_0^b dp_T^\gamma \int dz^\pi \int dz^\gamma \varepsilon_\pi^{-1}(p_T^\pi, z^\pi) \frac{dN^{\pi,meas}}{dp_T^\pi} P(p_T^\pi, p_T^\gamma) \varepsilon_\gamma(p_T^\pi, p_T^\gamma, z^\gamma) \quad (3.18)$$

This equation implicitly assumes that the  $\pi^0$  production is flat in the longitudinal direction which is true to good approximation in the small pseudo-rapidity coverage of PHENIX. Also, collisions have a wide distribution of vertex positions along the beam axis which has been neglected.

In practice it turns out to be simpler to factorize the various effects somewhat differently than shown in equation 3.18. The single photon efficiency as well as the longitudinal dependence of the  $\pi^0$  efficiency are absorbed into the decay probability function ( $P^{MC}$ ) using a Monte Carlo based calculation which is described in the next section.  $P^{MC}$  is calculated as function of position in the coordinate system of the EMC taking into account a realistic distribution of z-vertex positions. Only the most important detector effect, the  $p_T$  dependence of the  $\pi^0$  reconstruction efficiency, is calculated explicitly as described in the section following. The actual procedure to determine the decay photon per-trigger yield is then most properly expressed as

$$\frac{N_{a-b}^{\gamma-h}}{N_{a-b}^\gamma} = \frac{\sum_i^{N^{\pi-h}} \varepsilon_\pi^{-1}(p_T^\pi) P_{a-b}^{MC}(p_T^\pi, z_{EMC_i})}{\sum_i^{N^\pi} \varepsilon_\pi^{-1}(p_T^\pi) P_{a-b}^{MC}(p_T^\pi, z_{EMC_i}^\pi)} \quad (3.19)$$

### 3.4.3 Decay Photon Estimate from Monte Carlo

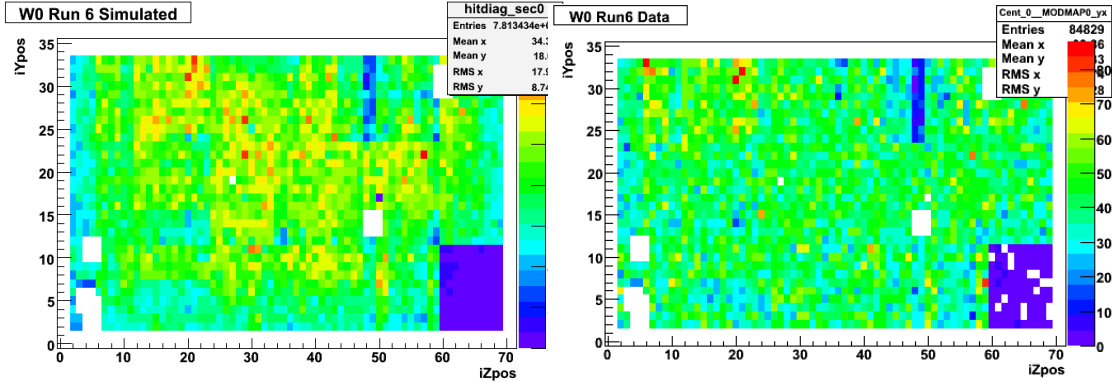


Figure 3.25: Cluster distribution in sector W0 from Run 6 simulation.

Figure 3.26: Cluster distribution in sector W0 from Run 6 data.

The Monte Carlo calculation is performed by decaying single  $\pi^0$ 's using a generator called EXODUS which handles the kinematics. Around 1 billion

$\pi^0$ 's are decayed according to flat distribution in both  $p_T$  and  $\eta$ . A realistic parametrization of the geometrical acceptance of the PHENIX EMC including the location of each tower is implemented. The simulation is run separately for each run with the appropriate hot tower map applied. In order to simulate the ERT trigger efficiency for the p+p runs the photons are weighted by the hit distributions from data. Fig 3.25 shows the hit distribution for one sector in data while 3.26 shows the same distribution in the simulation.

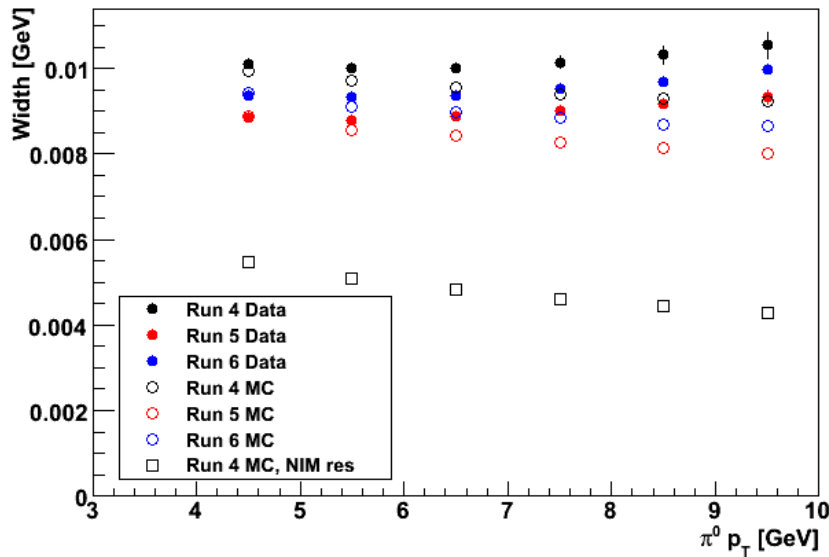


Figure 3.27:  $\pi^0$  peak widths for Run 4 data w/ exodus simulation comparison.

The Monte Carlo uses a gaussian smearing function based on the parametrization of the PbSc and PbGl detector resolution and a gaussian distribution of z-vertex positions whose width is determined by fitting the data. The detector resolutions measured from the test beam data (see section 2.5) are considerably better than in actual running conditions. In order to account for this the energy independent term of the resolution was tuned to roughly match the data for each data set. Figure 3.27 compares the  $\pi^0$  peak width as function of  $p_T$  in data and Monte Carlo. Also shown are the widths in Monte Carlo using the test beam (NIM) resolution values with the Run 4 configuration. The Run 4,5 and 6 Monte Carlo results use an 4, 3 and 2% smearing, respectively. The Monte Carlo reproduces the data fairly well although  $p_T$  dependence is different. Since the variation of the resolution from the NIM value to the larger value led to only a small shift in the final results no further tuning of the

Monte Carlo was pursued <sup>4</sup>.

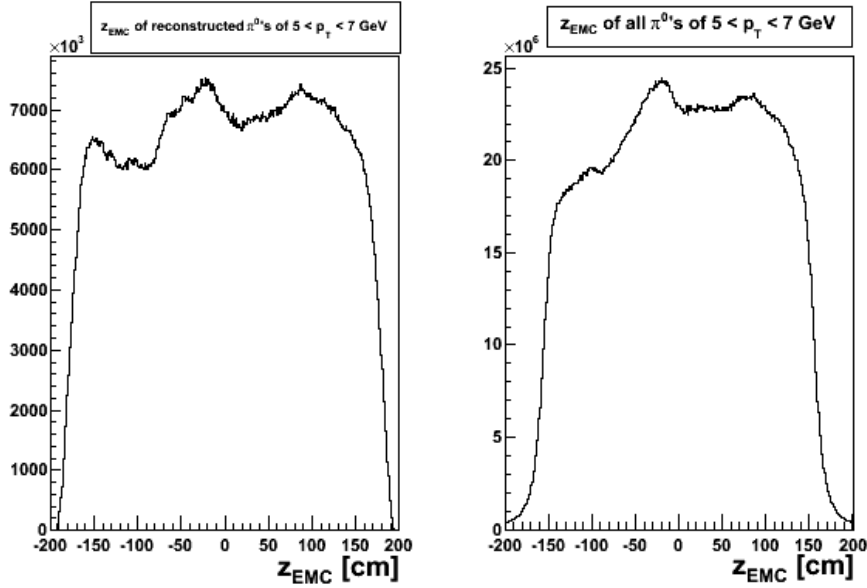


Figure 3.28:  $z_{EMC}$  distributions for reconstructed  $\pi^0$ 's with  $5 < p_T^{\pi^0} < 7$  GeV (left) and  $\pi^0$ 's with  $5 < p_T^{\pi^0} < 7$  GeV with one photon passing the analysis cuts from the Run 6 EXODUS Monte Carlo simulation.

Figure 3.28 shows the  $z_{EMC}$  dependence for both reconstructed  $\pi^0$ 's (left) and all  $\pi^0$ 's which decay with at least one photon of  $p_T > 1$  GeV which falls into the acceptance (right). Features in the distribution due to dead areas and efficiency variations show up differently in the two cases. Figure 3.29 shows  $P_{5-7}^{MC}$  for several  $z_{EMC}$  bins. In the middle of the detector the  $z_{EMC}$  dependence is relatively small due to the approximate cancelation of the  $z_{EMC}$  dependent efficiency of single photons and reconstructed  $\pi^0$ 's.  $\pi^0$ 's at large  $|z_{EMC}|$ , near the edge of the detector are weighted by relatively small values of  $P$  (only the relative and not the absolute normalization of the curves can change the per-trigger yield). The explanation of this effect is that these  $\pi^0$ 's are close to the edge of the detector and are thus very unlikely to contribute a photon to the 5-7 GeV decay sample that falls within the fiducial cut.

Figure 3.30 compares the decay probability function (integrated over  $z_{EMC}$ ) from the Run 6 Monte Carlo to the analytic result. The smearing of the features is due to the detector resolution. One particularly important consequence

---

<sup>4</sup>Since the time of writing the  $p_T$  dependence of the data was reproduced in Monte Carlo by introducing position resolution smearing. The results were indeed insensitive to this improvement.

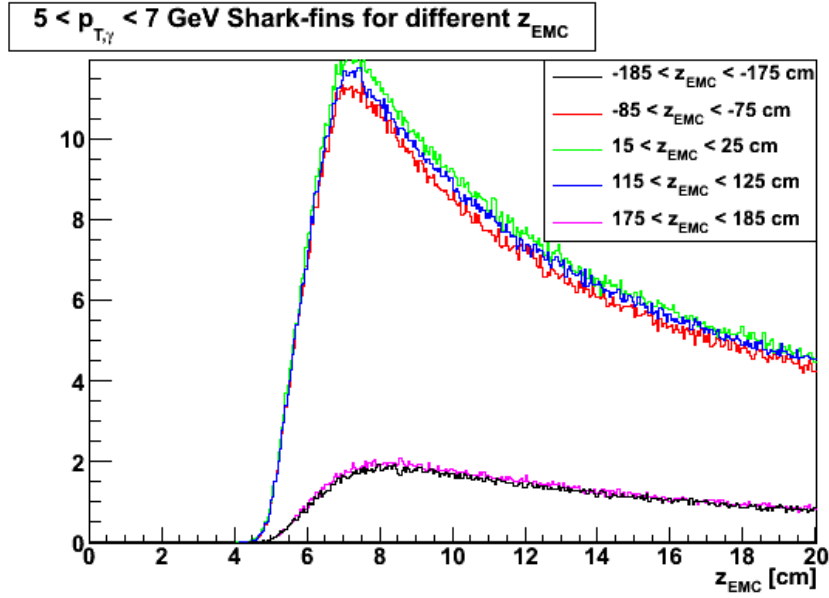


Figure 3.29: Probability for decay into a photon of  $5 < p_T^\gamma < 7$  GeV for several different  $z_{EMC}$  bins from the Run 6 Monte Carlo

of this is that  $\pi^0$ 's of reconstructed  $p_T < 5$  GeV can decay into the photon sample of  $p_T > 5$  GeV. In order to properly account for this we reconstruct  $\pi^0$ 's down to 4 GeV. The difference between the analytic and Monte Carlo  $P$  seems fairly small but it is important to recall that this function is weighted by the  $p_T$  spectrum of  $\pi^0$ 's such that small changes in the features at low  $p_T$  can be significant.

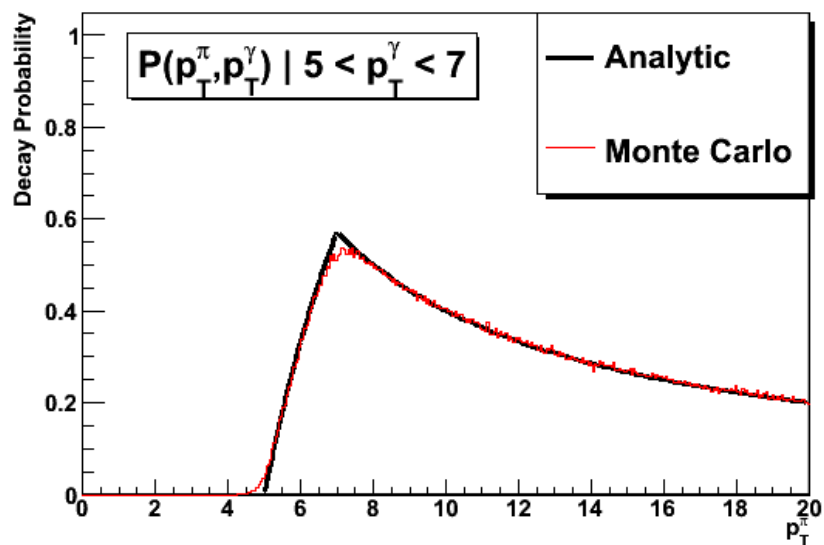


Figure 3.30: Probability for decay into a photon of  $5 < p_T^\gamma < 7$  GeV as a function of  $p_T^\pi$ .

### 3.4.4 $\pi^0$ Reconstruction Efficiency

The  $p_T$  dependence of the  $\pi^0$  reconstruction efficiency is determined in much the same manner as for the charged hadrons. The published PHENIX  $\pi^0$  spectra from Au + Au [42] and p + p [107] collisions are fit with a power-law function which describes the data very well in the  $p_T$  range of interest. The raw and corrected spectra for Run 6 are shown in figure 3.31 along with the correction function which is the ratio of the corrected to the raw distributions.

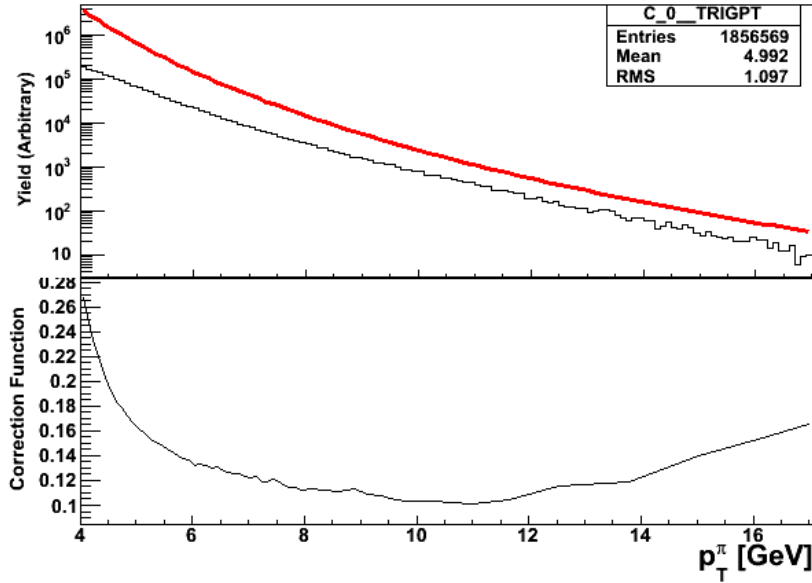


Figure 3.31: Raw  $\pi^0$   $p_T$  distribution from Run 6 p + p data (top), a power-law fit to the (corrected) Run 3  $\pi^0$   $p_T$  spectrum (red) and the  $\pi^0$  efficiency correction function formed by taking the ratio of two.

### 3.4.5 Cutoff Correction for Decay Yields

Note the high  $p_T$  behavior of the efficiency correction in figure 3.31. The rise at high  $p_T$  is due to the known merging loss of  $\pi^0$ 's. The input  $\pi^0$  spectrum is more uncertain where this correction is the largest, so it is good to avoid using the  $\pi^0$  spectrum above a point where this correction becomes too large. Also, the weighting procedure does not give the correct statistical uncertainties when the  $\pi^0$   $p_T$  distribution is not sufficiently well-sampled. In addition, formally the integral in equation 3.14 extends to infinite  $p_T^\pi$  (actually it's bounded by  $\sqrt{s_{NN}}$ ), but the statistical reach of the data is much more limited. This results in an underestimate in the calculated decay photon yields.

For both of these reasons, we applied a cutoff in the maximum  $\pi^0$   $p_T$  used in the decay weighting procedures of  $p_T^\pi = 17$  GeV/c, same for all trigger  $p_T$  bins. This value avoids the higher  $p_T^\pi$  regions where both the merging uncertainties are largest and the statistics in the  $\pi^0$  and  $\pi^0$ -h pairs start to dissipate too much, which would make estimating the decay calculation's deficiency difficult. The cutoff deficiency  $D_{cutoff}$  (the inverse of which will be applied as a correction) can then be written:

$$D_{cutoff} = 1/C_{cutoff} = \frac{\int_{<17} dp_T^{\pi-h} P(p_T^{\pi-h}) \frac{dN^{\pi-h}}{dp_T^{\pi-h}} / \int_{<\infty} dp_T^{\pi-h} P(p_T^{\pi-h}) \frac{dN^{\pi-h}}{dp_T^{\pi-h}}}{\int_{<17} dp_T^\pi P(p_T^\pi) \frac{dN^\pi}{dp_T^\pi} / \int_{<\infty} dp_T^\pi P(p_T^\pi) \frac{dN^\pi}{dp_T^\pi}} \quad (3.20)$$

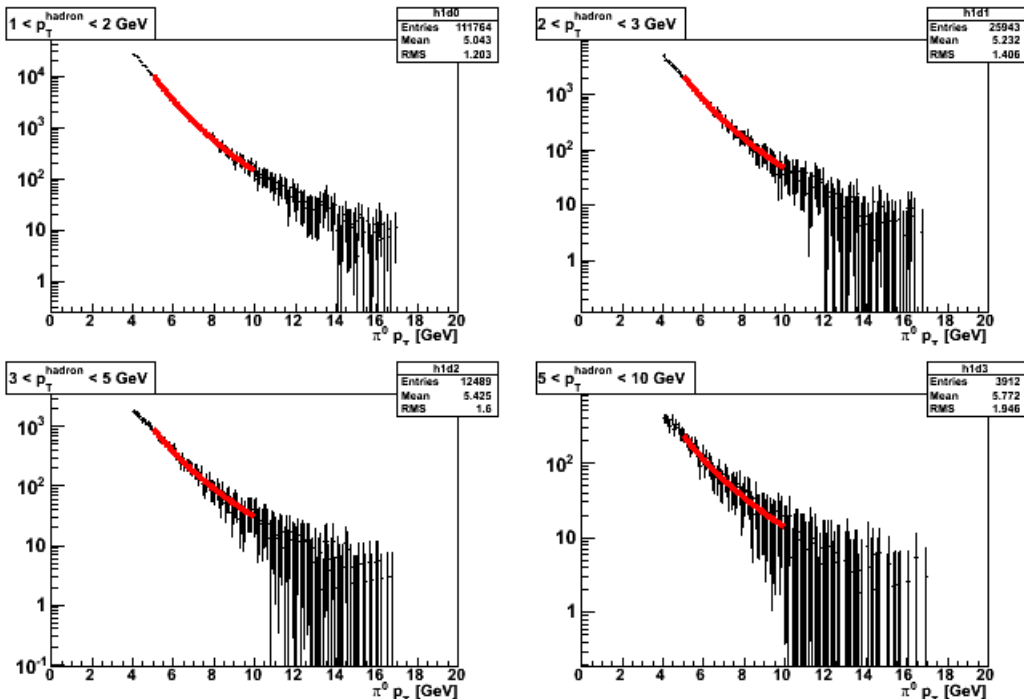


Figure 3.32: Power law fits to associated yields as a function of  $p_T^\pi$  in different ranges of  $p_T^{hadron}$  for the cutoff corrections.

The lower bound of the integral is the low end of the trigger  $p_T$  bin we are calculating the correction for ( $P$  is 0 below that anyway), and the yields (spectra) of  $\pi^0$  and  $\pi^0$ -h pairs, are determined from data, correcting the measured raw yields of both with the same  $\pi^0$  efficiency correction from the last section. These yields are fit with a pure power law functional form, and these

$p_T^\gamma$ [GeV]	$p_T^{\text{hadron}}$ [GeV]	Correction
5-7	1-2	0.999884
	2-3	0.99964
	3-5	0.999204
	5-10	0.997009
7-9	1-2	0.99929
	2-3	0.997983
	3-5	0.995967
	5-10	0.987933
9-12	1-2	0.99658
	2-3	0.99095
	3-5	0.98327
	5-10	0.95814
12-15	1-2	0.984445
	2-3	0.961687
	3-5	0.934492
	5-10	0.862696

Table 3.2: Cutoff corrections for  $\pi^0$  and reconstruction

functional forms are used to calculate  $C_{\text{cutoff}}$  from the above equation. Only  $p + p$  yields are used in the fits for simplicity, since the spectral shapes in Au+Au, even for jet yields, have been measured to be the similar for both single  $\pi^0$ 's [42] and hadron-hadron pairs at high  $p_T$  [50]. Examples of the fits are shown in figures 3.32. The cutoff calculations are tabulated in table 3.2. A 50% error relative to the size of the correction is assumed on these corrections.

### 3.4.6 $\eta$ -hadron Correlations

As the second largest contribution to the decay photon yield the measurement of  $\eta - h$  correlations is an important part of the  $\gamma - h$  analysis. *A priori* it would seem unlikely that  $\eta$  correlated production would be significantly different from that of the  $\pi^0$  since effects the mass of the  $\pi^0$  and the  $\eta$ , 135 and 548 MeV, respectively, are small compared to the momenta considered in this study ( $> 5$  GeV). However, scarce information is available on  $\eta - h$  correlations in the literature. Without a proper measurement the direct photon correlations measured by the subtraction method would then have to be viewed with some scepticism since the jet fragmentation process is not well enough understood to definitively rule out the possibility of a substantially different  $\eta$  associated yield.

Due to the much larger combinatorial background for  $\eta$  reconstruction

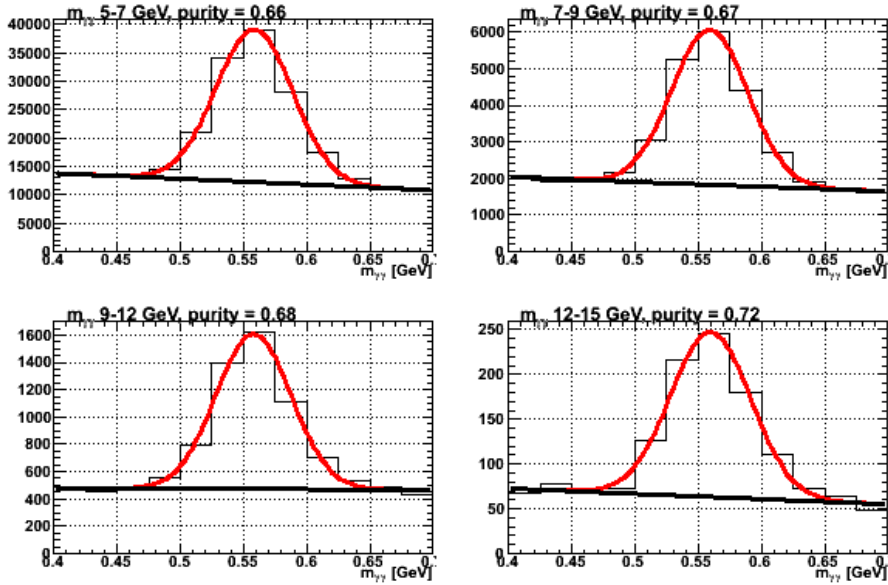


Figure 3.33: Fits to the two photon invariant mass distributions for various  $p_{T,\eta}$  selections.

compared to  $\pi^0$  it is necessary to subtract false matches from the  $\eta - h$  yields. A method of doing so has been developed for the p + p data. In the Au + Au data the signal-to-background for  $\eta$  reconstruction is so poor that no such subtraction can be applied. Nevertheless, the  $\eta$  contribution in Au + Au is estimated based on the p + p results measurements and is discussed in section 5.

$\eta$  mesons are tagged by their invariant mass in the window  $0.53 < m_{\gamma\gamma} < 0.58$  GeV. Figure 3.33 shows fits to the invariant mass distributions for two photon pairs for the  $p_{T,\eta}$  bins used in this analysis. The purity values indicated on the plots are the signal/(signal+background) evaluated from the fits. In contrast to the  $\pi^0$  the rate of false tagging due to the combinatorial background is not negligible for  $\eta$ 's. In order to get a handle on the contribution from this background we measure the per-trigger yields in the sideband region defined as  $0.4 < m_{\gamma\gamma} < 0.46 \&& 0.64 < m_{\gamma\gamma} < 0.7$  GeV where the fits indicate that false  $\eta$  tagging is dominant. The flatness of the combinatorial background suggests that the sidebands adequately approximate the falsely tagged contribution in  $\eta$  peak region. The per-trigger yield from the sideband region is then subtracted from that of the peak region using the purities derived from the fits to the invariant mass distributions according to:

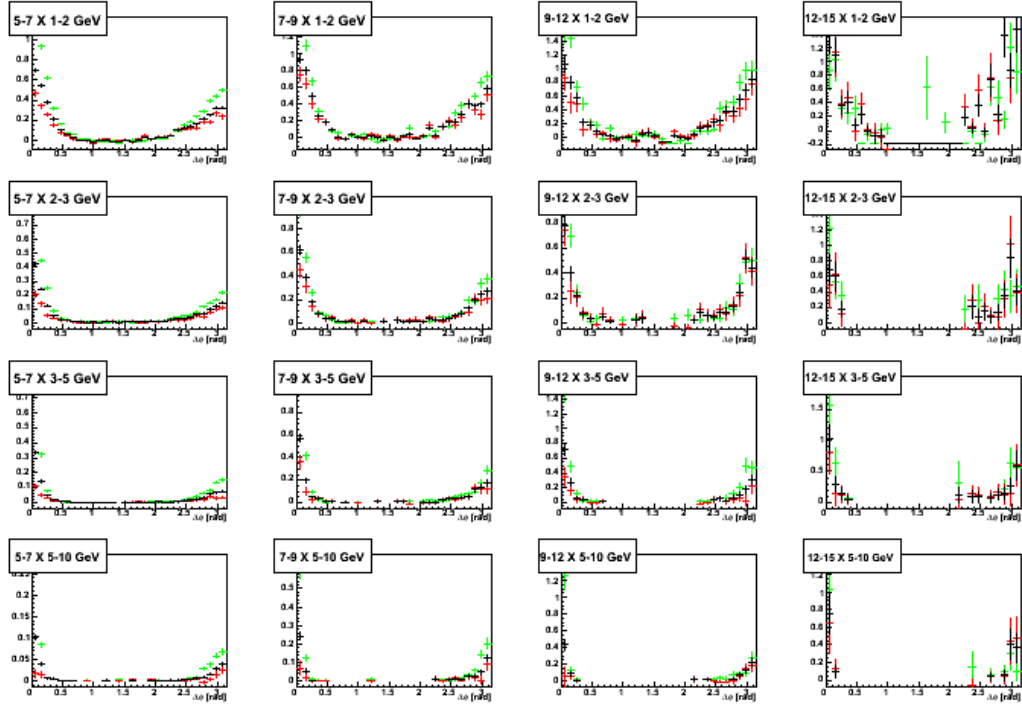


Figure 3.34:  $\Delta\phi$  distributions for the peak region (black), sideband region (green), and the subtracted  $\eta$ -h yields (red).

$$Y_\eta = 1/P Y_{peak} - (1 - 1/P)Y_{sideband} \quad (3.21)$$

where  $P$  is defined as Signal/(Signal+Background).

Figure 3.34 shows per-trigger yields of the peak and sideband regions along with the subtracted  $\eta$  per-trigger yields as a function of  $\Delta\phi$ . Note that the sideband per-trigger yields (mostly due to the  $\pi^0$ ) tend to be larger than that of the  $\eta$ . To estimate the  $\eta$  contribution to the decay  $\gamma$  per-trigger yields we perform the same fill-time weighting procedure that is used to determine the  $\gamma(\pi^0)$ -h yields. In order to estimate the  $\eta$  efficiency we find the  $p_T$  spectrum of  $\eta$ 's by subtracting the sideband yields in small  $p_T$  bins. Figure 3.35 shows the raw  $p_T$  spectra for the peak and sideband regions (top panel) and the subtracted distribution (bottom panel). Figure 3.36 shows the same subtracted  $p_T$  distribution and a power-law with  $n = 7$  (top panel). The power-law function divided by the data gives the efficiency correction function (bottom panel). The  $\eta$  decay probability functions were run through the Monte Carlo program. No significant difference between the results for  $\eta$  and  $\pi^0$  was observed. To evaluate the purity as a function of the  $\eta$  daughter photon  $p_T$  we applied

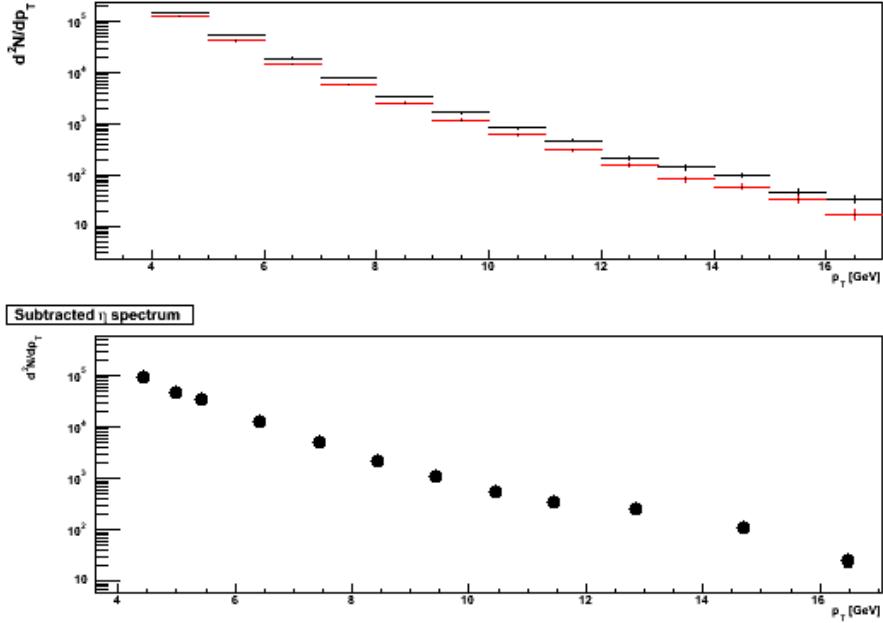


Figure 3.35: The raw  $p_T$  spectra for the peak (black points, top panel) and sideband regions (red points, top panels) and the subtracted distribution (bottom panel)

the fill-time decay weighting to the invariant mass distributions. Figure 3.37 shows the invariant mass distributions binned by daughter  $p_T$ . Finally, figure 3.38 shows the peak, sideband, and subtracted  $\gamma(\eta)$ -h per-trigger yields as a function of  $\Delta\phi$ .

### 3.5 Isolation Cut Method

The statistical subtraction method will be shown to be a very reliable technique to extract direct photon correlations. However, statistical and systematic uncertainties may be minimized by partial event-by-event identification. The direct photon signal is enhanced by applying an isolation criterion which requires that the sum of the momentum of charged tracks and energy of clusters in a cone of 0.5 radians be < 10% of the photon energy. This cut is fairly standard throughout the literature and can be applied in pQCD calculations [108].<sup>5</sup> It is important to note that, in addition to decay photons, the isolation cut removes some fraction of the direct photon sample, presumably the photon fragmentation component. Therefore, the difference between statistical and

---

<sup>5</sup>For some subtleties regarding the application of isolation cuts see [109].

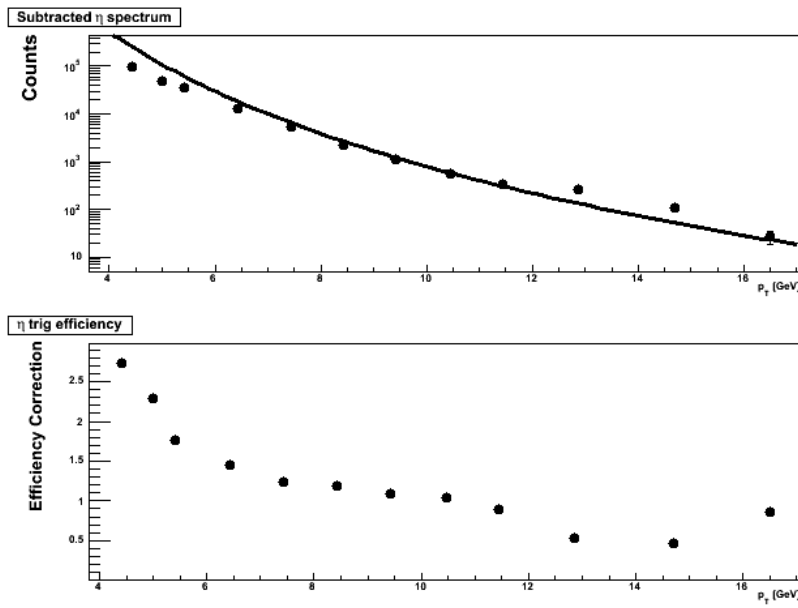


Figure 3.36: Subtracted, uncorrected  $\eta$   $p_T$  and a power law function with  $n=7$  (top panel). Efficiency correction function for  $\eta$ 's (bottom panel)

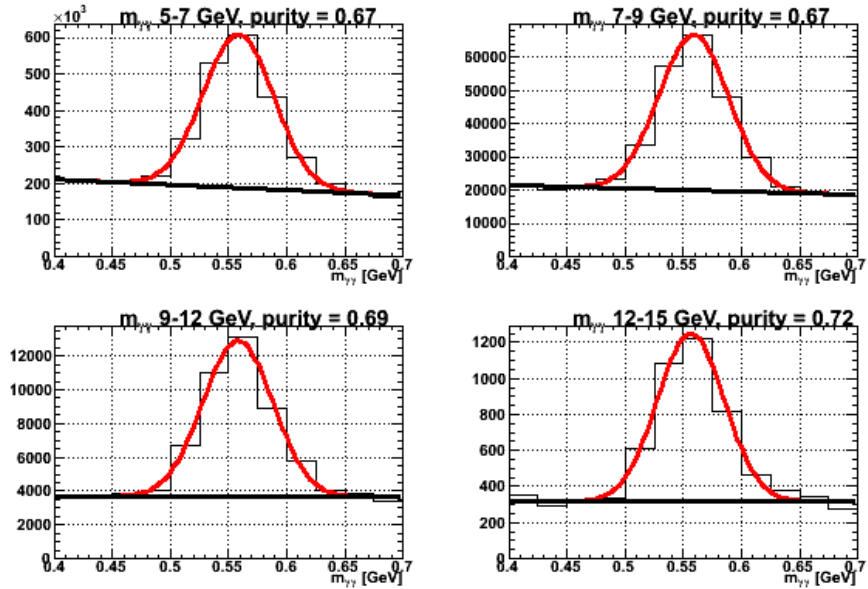


Figure 3.37: Fits to the two photon invariant mass distributions for various  $p_{T,\gamma(\eta)}$  selections.

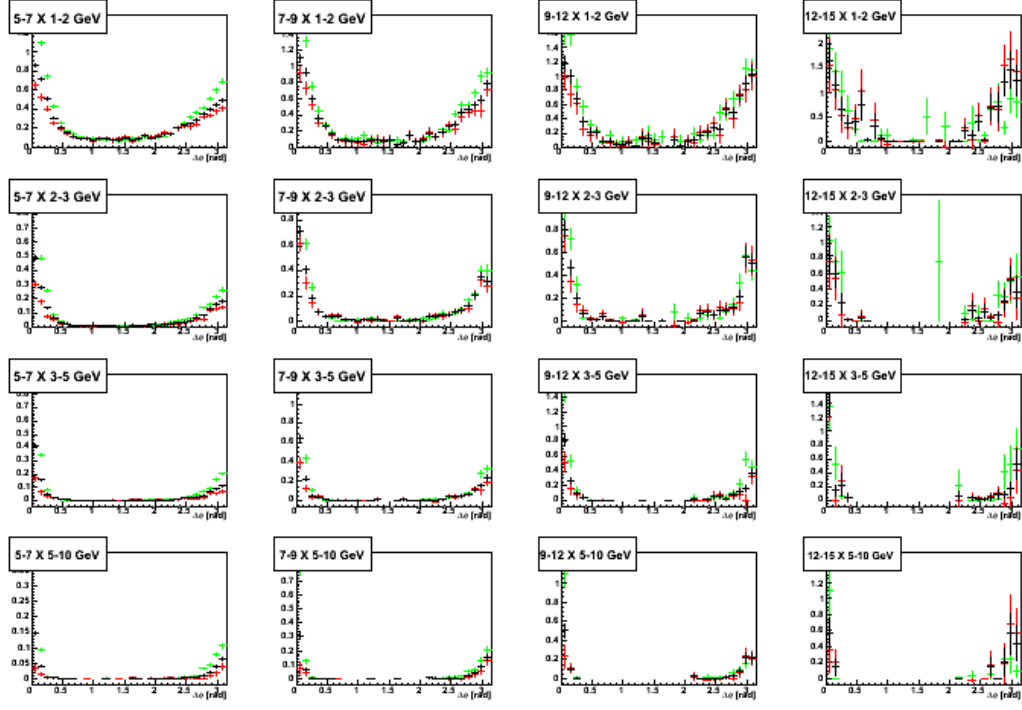


Figure 3.38:  $\Delta\phi$  distributions for the peak region (black), sideband region (green), and the subtracted  $\gamma(\eta)$ -h yields (red).

isolation methods is not solely one of methodology, they are actually measurements of different quantities.

In addition to the isolation cut the decay photon background is reduced by 'tagging' or reconstruction of  $\pi^0$  and  $\eta$ . The 'tagging' cuts used to remove decay photons from the inclusive sample are somewhat more aggressive than those used estimate the decay photon per-trigger yields:

- photon energy  $> 500\text{MeV}$
- $\pi^0$  mass window:  $120 < m < 160 \text{ MeV}$
- $\eta$  mass window:  $500 < m < 600 \text{ MeV}$

As a reminder, in the purely statistical method the direct photon per-trigger yield is obtained according to:

$$Y_{direct} = \frac{1}{R_\gamma - 1} \cdot (R_\gamma Y_{inclusive} - Y_{decay}) \quad (3.22)$$

One may write down a similar expression to describe the statistical subtraction of the remaining decay contribution after the isolation and tagging cuts have been applied.

$$Y_{direct} = \frac{1}{R_\gamma' - 1} \cdot (R_\gamma' Y_{inclusive} - Y^{miss,iso}) \quad (3.23)$$

$R_\gamma'$  is now the effective  $R_\gamma$  after removing photons that were not isolated or were tagged as a  $\pi^0$  or  $\eta$ . There is still, however, a residual background from decay photons which were not reconstructed and happen to be isolated. In order to visualize the the various quantities consult the Venn diagram shown in 3.39. Two cuts, the isolation and tagging cuts are made on the inclusive sample. The union of the those two cuts we define as the inclusive' sample for the subtraction of the residual decay component after the event-by-event cuts. For the moment we assume that all photons that have been tagged are really decay photons. The decay photons which are not tagged are denoted by *miss*. *iso* denotes photons that are isolated and *niso* will denote the opposite. In the right diagram we reconstruct  $\pi^0$ 's ( $\eta$ 's) and apply the isolation cut to them as well. In analogy with the statistical method, we do so to estimate the residual decay background  $Y^{miss,iso}$ .

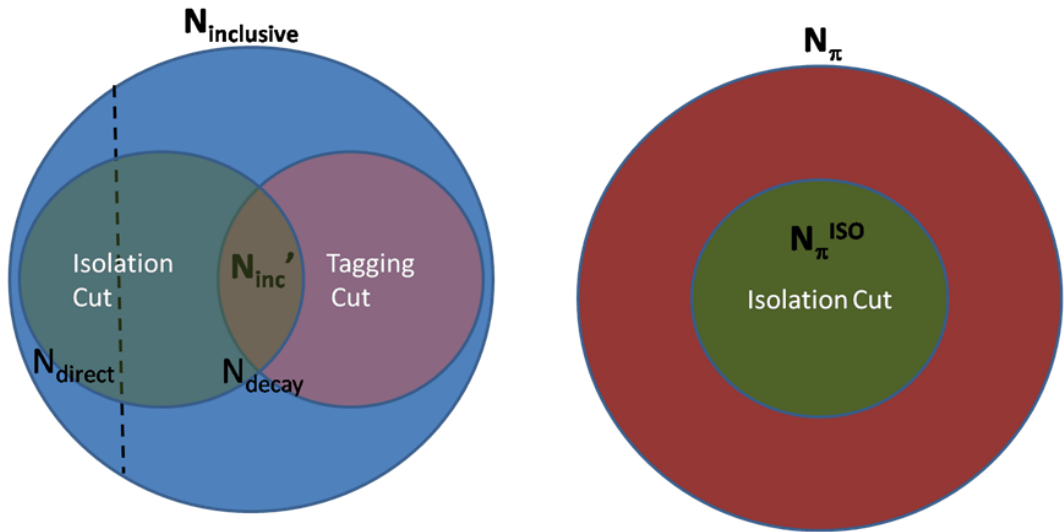


Figure 3.39: Venn diagram illustrating the various quantities in the isolation method

Since we were not able to tell missed, isolated decay photons apart from direct photons in the first place we will have to estimate them by an indirect route. The way we proceed is by identifying isolated  $\pi^0$ 's (and  $\eta$ 's, although

we drop them from the discussion for simplicity) and decaying them using the now familiar Monte Carlo mapping procedure. Hence we can evaluate the efficiency of the isolation cut efficiency for  $\pi^0$ 's, where we can easily obtain a both an isolated and non-isolated sample, and map that efficiency into the daughter  $p_T$ . We will, however, have to modify the Monte Carlo so that it also removes tagged photons from the sample. In this way we can obtain the decay probability function for 'missed' photons.

Figure 3.40 shows the distribution  $\pi^0$  which contribute to the 5-7 GeV decay photon bin with tagging (red) and without tagging black. The effect of the tagging is most pronounced in this lowest decay photon  $p_T$  bin because the opening angle is largest. Photons which pass the tagging cut are, on average, closer to the parent  $\pi^0$   $p_T$  than without tagging. This is because we preferentially miss asymmetric pairs, due to the fact that they have larger opening angles and that we only reconstruct  $\pi^0$  and  $\eta$  using photons of  $p_T > 1$  GeV.

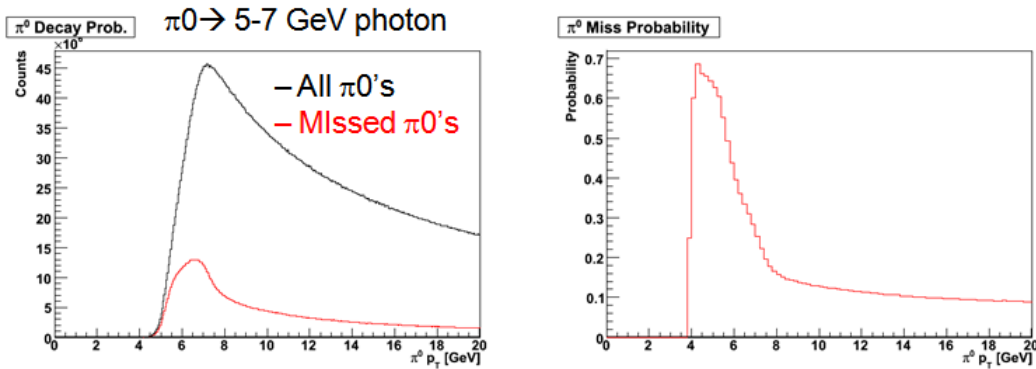


Figure 3.40: Left panel - the probability function (arbitrarily normalized) for a  $\pi^0$  to decay into a photon with  $5 < p_T < 7$  as a function of  $p_T^{\pi^0}$  with tagging (red) and without tagging black. Right panel - The probability that a  $\pi^0$  that decays into a 5-7 GeV photon, which goes into the acceptance, is not reconstructed.

Now that we have determined the per-trigger yield for missed, isolated decay photons ( $Y_{miss}^{iso}$ ), all that remains is to determine the value of  $R_\gamma'$ . We subtract the number of photons we tagged and that were not isolated to obtain:

$$R_\gamma' = \frac{N_{inclusive} - N_{tag} - N^{iso}}{N_{miss}^{iso}} \equiv \frac{N'_{inclusive}}{N_{miss}^{iso}} \quad (3.24)$$

$N_{inclusive}$  is *total* number of photons which survive the tagging and isolation cuts. Note that this is not the same quantity as  $N_{miss}^{iso}$ . 'miss' is used to imply

that they were really decay photons and we missed them. We showed above that we can evaluate the per-trigger yield of missed, isolated decay photons, but we still do not know what fraction of the remaining sample they comprise. In order to evaluate  $N_{miss}^{iso}$  we decompose the total decay yield into components:

$$N_{decay} = N_{tag} + N_{miss}^{iso} + N_{miss}^{niso} \quad (3.25)$$

Here we have assumed that all photons that are tagged come from decay. Falsely tagged direct photons are discussed in the systematics section 4.8. We then utilize the fact that the fraction of  $\pi^0$ 's which are isolated depends only on the  $\pi^0$  momentum and is independent of the  $\pi^0$  decay kinematics (and therefore whether I was able to tag it or not). Hence, we can measure the the fraction of  $\pi^0$ 's which are isolated and use the  $\pi^0$  decay probability function to make the transformation from  $\pi^0 p_T$  to  $\gamma p_T$ .

$$N_{miss}(p_T^\gamma) = P^{miss}(N_{\pi^0}(p_T^{\pi^0})) \quad (3.26)$$

Since we can identify  $\pi^0$ 's that are both isolated and non-isolated we can go one step further and map the isolation fraction to  $p_T^\gamma$ .

$$\frac{N_{miss}^{iso}}{N_{miss}^{niso}} = P^{miss} \left( \frac{N_{\pi^0}^{iso}}{N_{\pi^0}^{niso}} \right) \quad (3.27)$$

Solving 3.25 and 3.27 for  $N_{miss}^{iso}$  I obtain:

$$N_{miss}^{iso} = \frac{N_{decay} - N_{tag}}{1 + P^{miss} \left( \frac{N_{\pi^0}^{niso}}{N_{\pi^0}^{iso}} \right)} \quad (3.28)$$

The expression for  $R_\gamma'$  then becomes:

$$R_\gamma' = \frac{\frac{N'_{inclusive}}{N_{inclusive}}}{1/R_\gamma - \varepsilon_{tag}} \left( 1 + P^{miss} \left( \frac{N_{\pi^0}^{niso}}{N_{\pi^0}^{iso}} \right) \right) \quad (3.29)$$

where I've inserted  $R_\gamma \equiv N_{inclusive}/N_{decay}$  and  $\varepsilon_{tag} \equiv N_{tag}/N_{inclusive}$ . Now we have an expression in terms of quantities we can evaluate. The numerator is determined simply by the number of photons surviving the cuts. The denominator is composed of three terms:  $R_\gamma$  the tagging efficiency and the isolated decay photon fraction.  $R_\gamma$  is evaluated from the published spectra while the latter two quantities are determined from the raw data (with some help from Monte Carlo).

Figure 3.41 demonstrates the effects of the cuts in stages. The black curve

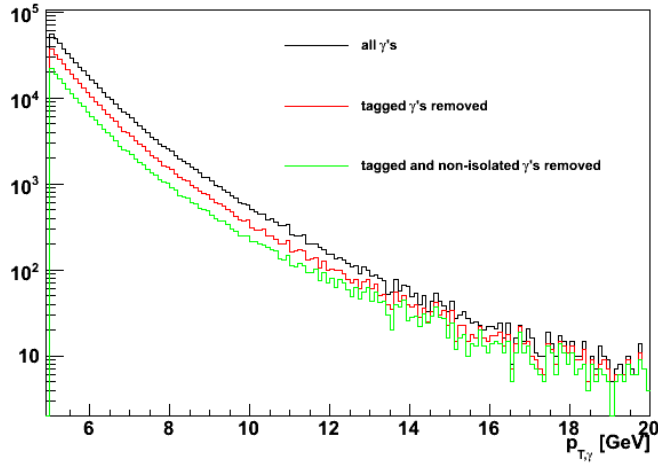


Figure 3.41: Inclusive (black), tagged (red), and non-isolated (green) photon  $p_T$  distributions. Tagged photons have already been removed from the non-isolated sample.

$p_{T,t}$ [GeV]	$R_\gamma$	$R_\gamma'$	$\varepsilon_{tag}$	$P_{miss} \left( \frac{N^{niso}}{N^0} \right)$	$\frac{N_{inclusive}}{N_{inclusive}}$
5-7	1.183	1.380	0.355	0.571	0.383
7-9	1.326	1.988	0.382	0.519	0.384
9-12	1.532	3.075	0.363	0.480	0.428
12-15	1.787	4.513	0.296	0.457	0.545

Table 3.3: Effective  $R_\gamma$  for isolation method and the quantities used to calculate it

is the inclusive photon  $p_T$  distribution (before any cuts). The red curve is to the number of photons left after decay tagging. The green curve is after the isolation cut. Note that tagged photons have already been removed from non-isolated distribution.

$R_\gamma'$  and the quantities which were used to obtain it are shown in table 3.3. Comparing the  $R_\gamma'$  to the natural value we find that the event-by-event cuts increase the signal-to-background by a factor of 2-5.

# Chapter 4

## Cross Checks and Systematic Errors

Revisiting the  $\gamma - h$  subtraction equation,

$$Y_{direct} = \frac{1}{R_\gamma - 1} \cdot (R_\gamma Y_{inclusive} - Y_{decay}) \quad (4.1)$$

it is evident that there are at least three categories of systematic uncertainty:  $Y_{inclusive}$ ,  $Y_{decay}$  and  $R_\gamma$ . There is also an uncertainty on the normalization of each of the yields of associated hadrons due to the ZYAM/pedestal subtraction procedure. In the Au + Au data the uncertainty in the magnitude of the elliptic flow is considered as yet another source of uncertainty on the per-trigger yields, independently of the ZYAM error. Finally there is an overall scale uncertainty on the hadron cross-section for each running period from the measurement of the BBC cross-section. These uncertainties are each considered in turn.

### 4.1 $R_\gamma$

The uncertainties in  $R_\gamma$  have been evaluated in the course of the Run 4 Au + Au and Run 5 p + p direct photon cross section analyses. The largest uncertainties in those analyses are attributed to the following effects.

- Non-linearity of the energy scale
- $\pi^0$  signal extraction
- Decay contribution from sources other than  $\pi^0$ .
- Cluster merging ( $> 10$  GeV only)

## 4.2 Inclusive Photons

The uncertainty on the inclusive photon efficiency was evaluated to be 1% in [67] (neglecting the scale uncertainty the cross section does not contribute to the per-trigger yield). Since other uncertainties dominate we assign the same uncertainty to the associated yields, which is a conservative estimate.

## 4.3 $\pi^0$ Combinatorics

The  $\pi^0$  combinatoric background is a significant source of uncertainty in the Au + Au  $\pi^0$  h and decay  $\gamma$ -h per-trigger yields. Figure 4.1 shows fits to the two photon invariant mass distribution and signal-to-background resulting from those fits. The situation is somewhat ameliorated by the decay photon mapping which is shown in figure 4.2 which compares the signal-to-background (S/B) for  $\pi^0$  (black) and  $\gamma(\pi^0)$ 's (red).

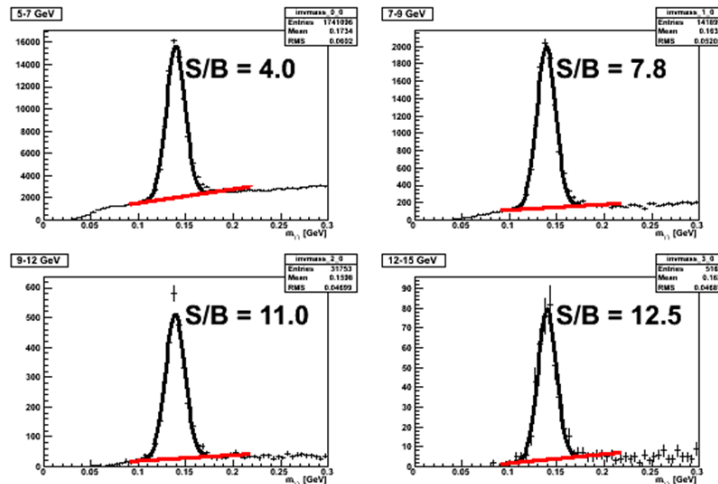


Figure 4.1: Fits to the  $\pi^0$  invariant mass distributions and signal-to-background in 0-20% central Au + Au.

In the instances where the S/B is lowest a sideband analysis is done to constrain the contribution from false  $\pi^0$  tagging. Figure 4.3 shows the ratio of the  $\pi^0$  per-trigger yields from the peak vs. the sideband region for the invariant mass range 0.165 – 0.200 GeV. Figure 4.4 shows the ratio of the  $\pi^0$  per-trigger yields from the peak vs. the sideband region for the invariant mass range 0.065 – 0.115 GeV. In the 5-7 X 1-2 GeV  $p_T$  bin the sideband per-trigger yields are within 10% of the peak per-trigger yields and for 5-7 X 2-3 GeV they are within 20%. We then evaluate the systematic error as

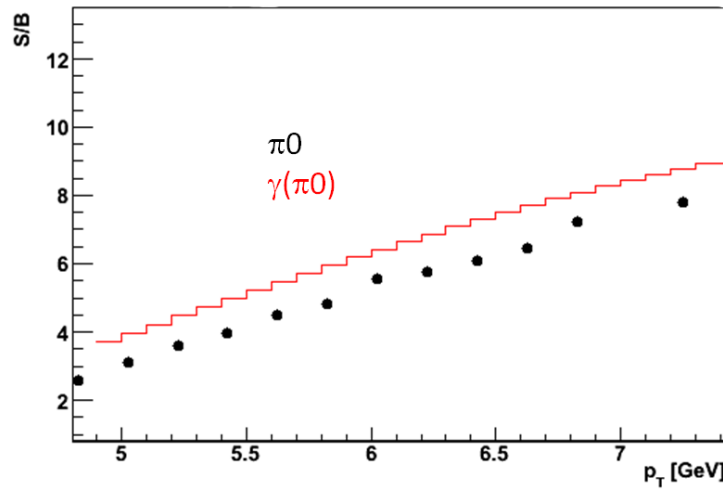


Figure 4.2: Signal-to-background for  $\pi^0$  and  $\gamma(\pi^0)$  in 0-20% central Au + Au.

$1/(S/B + 1/(Y_{peak}/Y_{sideband} - 1))$ . Outside of these two bins the systematic uncertainty due to  $\pi^0$  combinatorics is small due to the large S/B. In this instance we apply this formula using a conservative bound of 2 for the ratio of the peak to sideband per-trigger yields which does not enhance the overall systematic error appreciably.

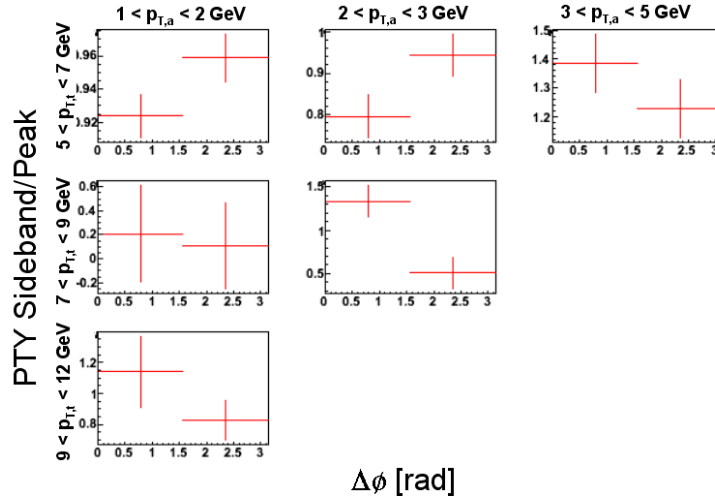


Figure 4.3: Peak divided by high-end sideband per-trigger yields for different  $p_T$  combinations.

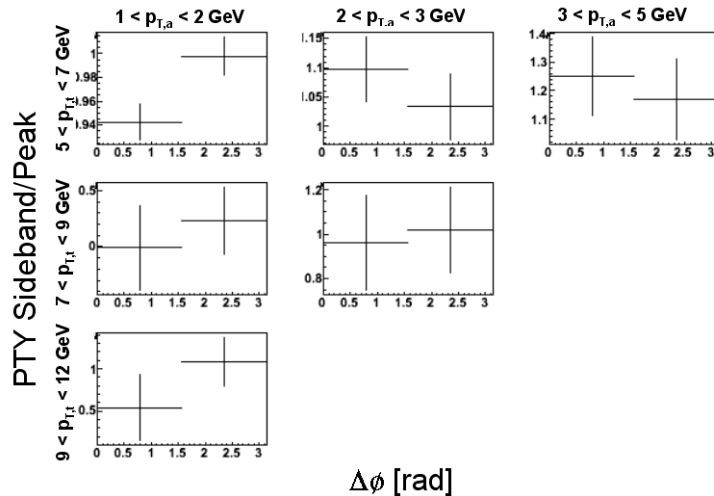


Figure 4.4: Peak divided by low-end sideband per-trigger yields for different  $p_T$  combinations.

#### 4.4 Two-Body Decay Kinematics and the Opening Angle Effect

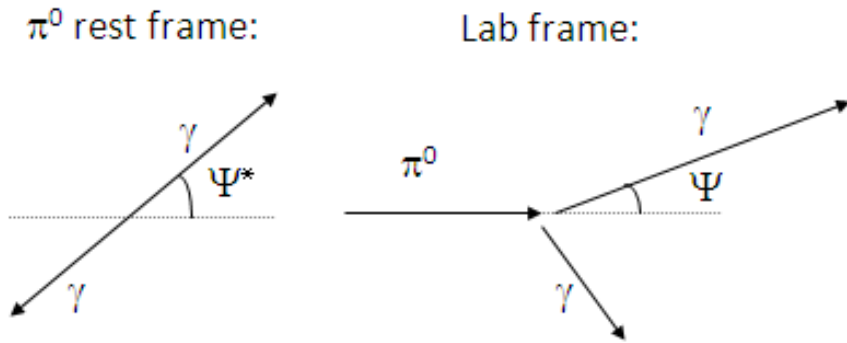


Figure 4.5:  $\pi^0 \rightarrow 2\gamma$  decay in the parent rest frame and the lab frame.

One would expect that the decay photon associated yield would have a broader angular distribution than for the parent meson since the decay photon is not collinear with the parent. In order to estimate the size of the effect the angle between the parent and daughter ( $\Psi$ ) was calculated for the  $p_T$  range of interest. Figure 4.5 shows the  $\pi^0 \rightarrow 2\gamma$  decay in  $\pi^0$  rest frame and the lab frame. In the parent rest frame the two decay photons have equal in opposite

momenta. The Lorentz transformation for photon energy and opening angle are

$$\tan \Psi = \frac{\sin \Psi^*}{\gamma(\beta + \cos \Psi^*)} \quad (4.2)$$

$$E = \gamma E^* + \gamma \beta p_{||}^* = \gamma \frac{m}{2} + \gamma \beta \frac{m}{2} \cos \Psi^* \quad (4.3)$$

where  $\beta$ ,  $\gamma$  and  $m$  are the velocity, Lorentz factor and mass of the parent, respectively. Combining the two equations one may eliminate  $\Psi^*$  obtaining

$$\tan \Psi = \frac{\sqrt{1 - (\frac{1}{\beta} - \frac{2p}{\beta \gamma m})^2}}{\gamma(\beta - \frac{1}{\beta} + \frac{2p}{\beta \gamma m})} \quad (4.4)$$

The left panel of figure 4.6 shows the opening angle as a function of the daughter momentum for the  $\eta \rightarrow 2\gamma$  decay as evaluated by this equation. Several selections of parent momentum are shown. The accompanying points are a Monte Carlo calculation which agrees with the analytic result modulo finite bin size effects. The right panel shows the distribution of the azimuthal projection of the opening angle from the Monte Carlo calculation for each of the three parent momentum selections. The azimuthal angle between the parent and daughter is of the order of several hundredths of a radian and hence may be safely neglected.

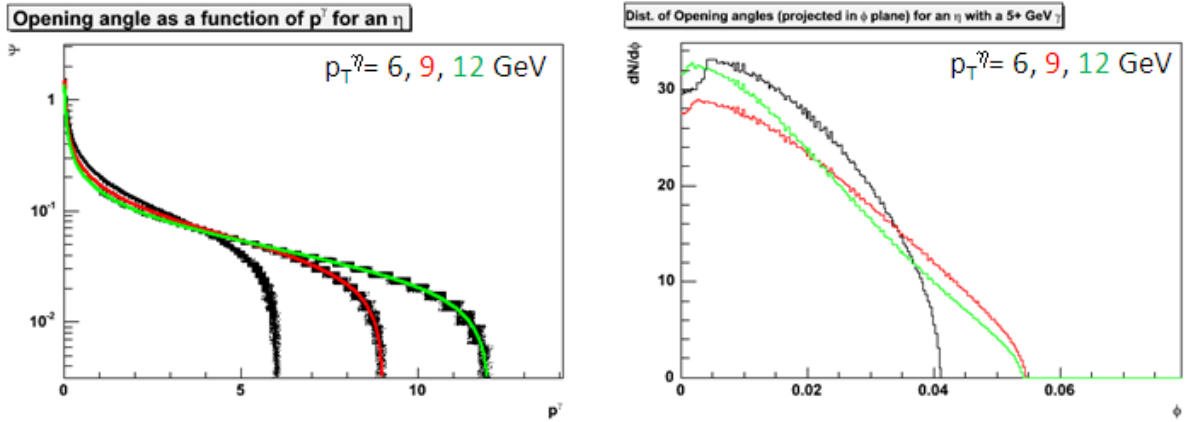


Figure 4.6: Left: The opening angle as a function of decay photon momentum for several values of parent  $\eta$  momentum calculated analytically (lines) and by Monte Carlo (points). Right: The distribution of the azimuthal projection of the opening angle for several values of parent  $\eta$  momentum.

## 4.5 PYTHIA studies

In order to test the veracity of the  $\gamma - h$  subtraction technique the method was applied to PYTHIA events. More specifically the simulations address the following effects and to assign a systematic uncertainty where appropriate:

- Decay photon mapping procedure
- $\eta - h$  sideband subtraction method
- Decay contribution from sources other than  $\pi^0$  and  $\eta$
- The opening angle effect

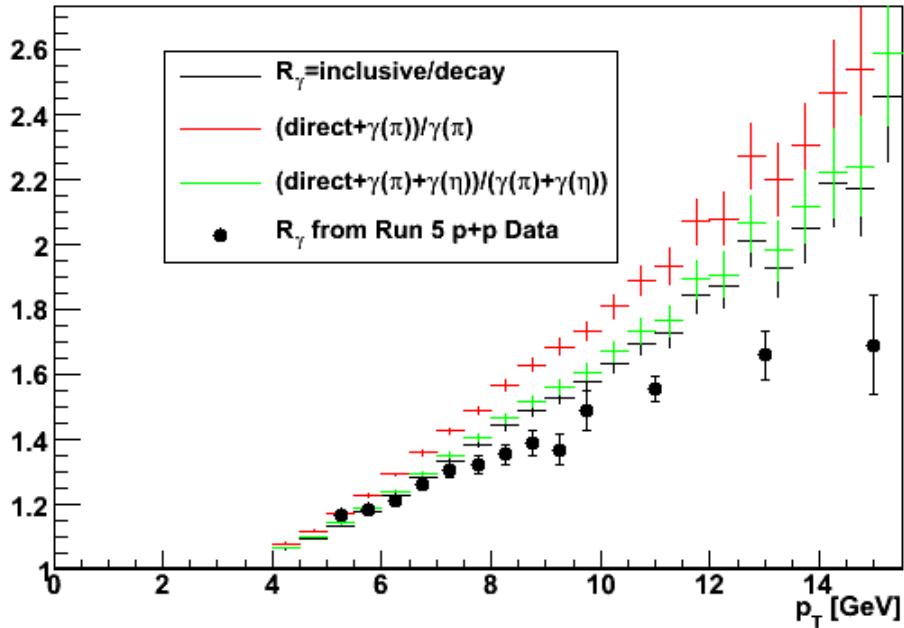


Figure 4.7:  $R_\gamma$  and similar quantities in PYTHIA

Around 20 million events were generated with both default QCD and direct photon scattering processes activated. These events were selected to contain a photon,  $\pi^0$ , or  $\eta$  of  $p_T > 4$  GeV. Non-default parameters were used in only a few cases. The cutoff for  $2 \rightarrow 2$  processes that diverge as  $p_T \rightarrow 0$  (CKIN(3),CKIN(5),CKIN(6)) were set to 4 GeV, below the threshold of direct photons considered in this study. The values of  $\sqrt{k_T^2}$  and  $\sqrt{j_T^2}$  (PARP(91)

and PARJ(21)) were chose to 2.5 GeV and 585 Mev, respectively, roughly consistent with PHENIX measurements from [61]. Figure 4.7 shows the value of  $R_\gamma$  for the PYTHIA sample as well as variants of this quantity in which only certain components of the decay photon signal are considered. Also shown are the p + p data described in section 3.1.2. Although it is interesting that PYTHIA overestimates the direct photon contribution, agreement in this regard was not essential for the current study and was not further investigated.

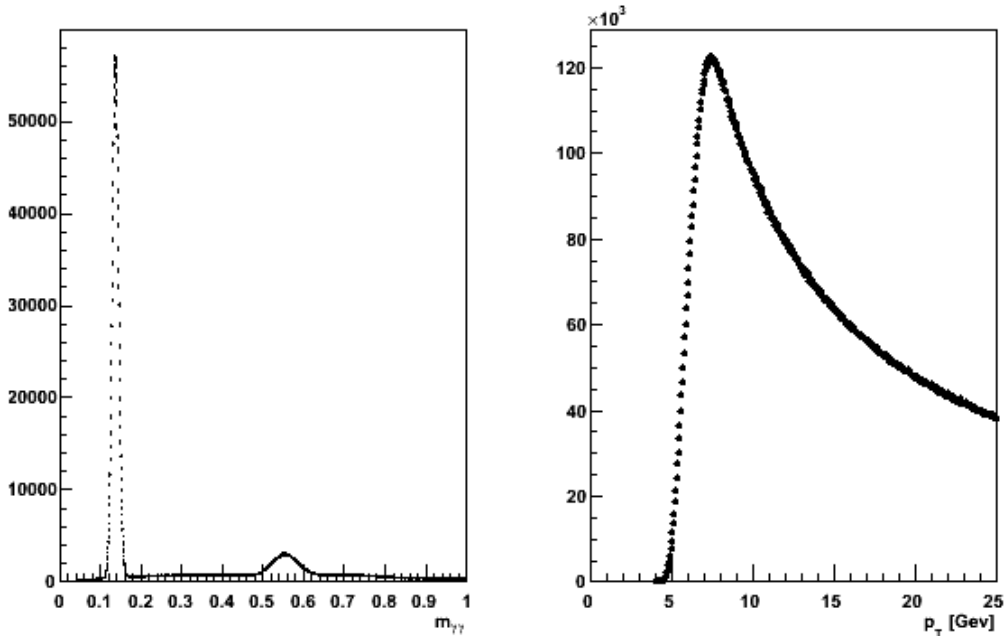


Figure 4.8: Examples of the two photon invariant mass distribution ( $5 < p_T^\gamma < 7$  GeV) and decay photon probability function ( $5 < p_T^\pi < 7$  GeV) from PYTHIA with resolution smearing.

The decay weighting procedure scheme was tested in two stages. First  $\gamma(\pi^0)$  correlations were obtained by applying the analytic form of the decay weighting function to all the  $\pi^0$ 's in the sample. Subsequently,  $\pi^0$  reconstruction and its associated efficiency corrections were implemented as well. To simulate detector response an energy resolution smearing of width  $\sigma(E)/E = 6\% \oplus 8\%/\sqrt{E(\text{GeV})}$  was used. Figure 4.8 shows the two-photon invariant mass for 5-7 GeV  $\pi^0$ 's and decay photons, respectively, from the resolution smeared PYTHIA events. Figure 4.9 shows the ratio of the decay photon per-trigger yields estimated by the decay photon weighting procedure with and without

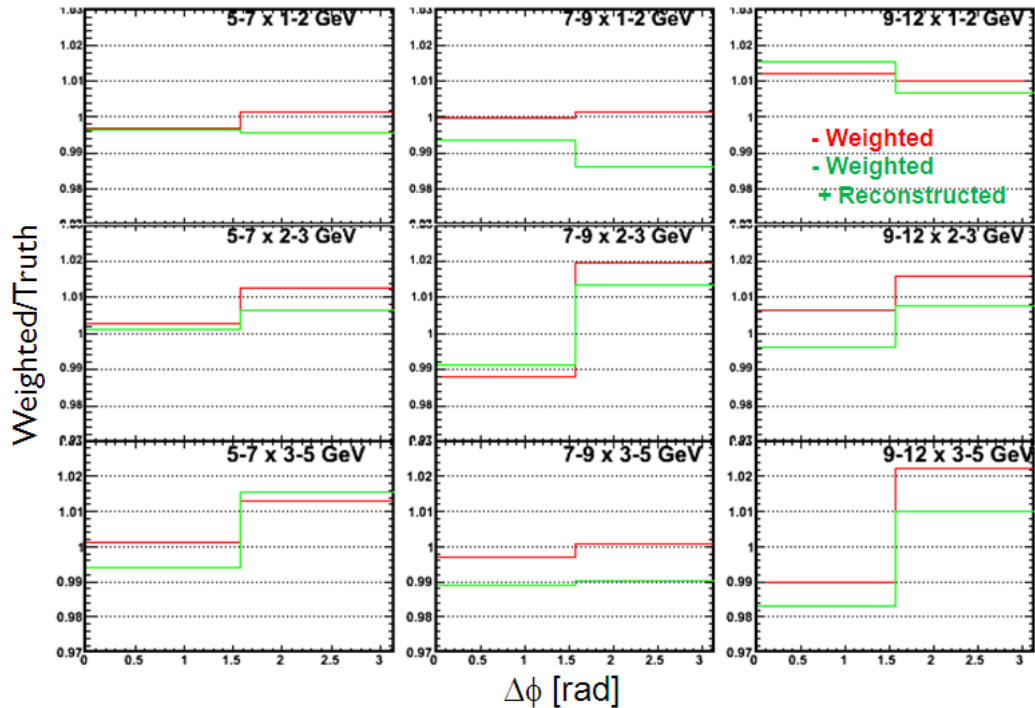


Figure 4.9: The ratio of the weighted to true  $\gamma(\pi^0) - h$  yields from PYTHIA. The red lines include the decay weighting only while the green lines include  $\pi^0$  reconstruction and resolution smearing.

$\pi^0$  reconstruction and resolution smearing to the truth (input) values. The deviation from the decay weighting procedure take a maximum value of about 2%. The effect shows no obvious  $p_T$  dependence.

Around 5% of decay photons come from channels other than  $\pi^0$  and  $\eta$ . Figure 4.10 shows the decay per-trigger yields with and without the contribution from these decay sources. The difference between the yields is no more than 1.5% on the near-side and 1% on the away-side.

## 4.6 Cluster Merging

At high  $p_T$  ( $\approx 10$  GeV in the PbSc and  $\approx 15$  GeV in the PbGl) pairs of photons from  $\pi^0$  decay begin to be reconstructed as single clusters. The vast majority of these merged clusters,  $> 99\%$  for  $p_T < 15$  GeV, are rejected from the inclusive photon sample by the  $\chi^2$  cut [110]. Nevertheless, cluster merging affects the  $\gamma - h$  subtraction method in two ways. Firstly, the removal of photon pairs preferentially from the decay sample as compared to the direct

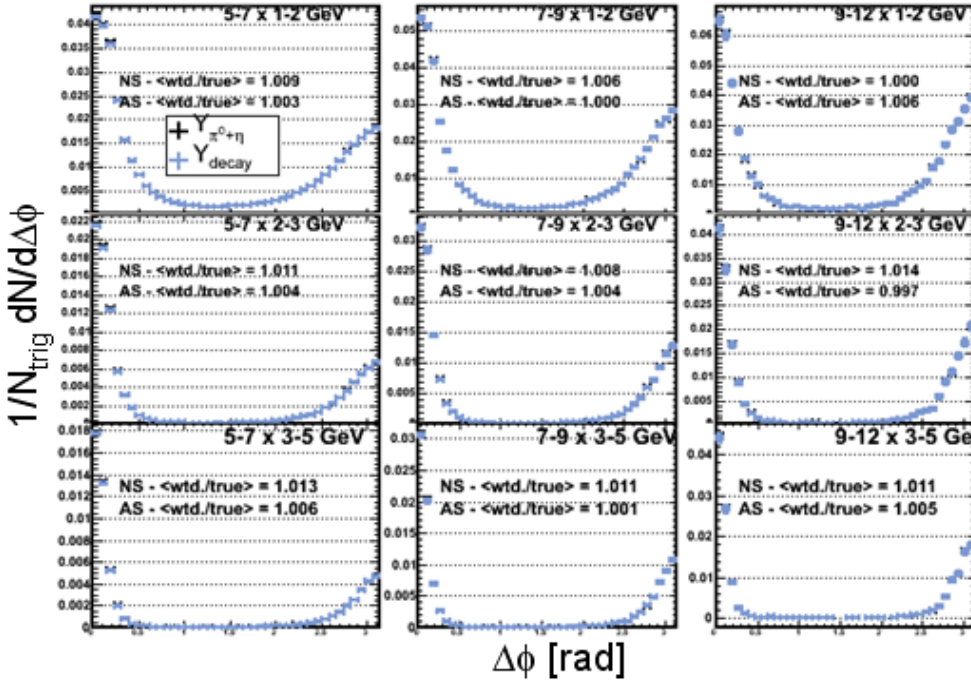


Figure 4.10: Comparison of total decay photon hadron yield to the yield from  $\pi^0$  and  $\eta$  only in PYTHIA

effectively changes  $R_\gamma$  for reconstructed photon clusters from its natural value. Secondly, the single photon efficiency used in the determination of the decay photon associated yields will be altered such that the contribution of high  $p_T$   $\pi^0$ 's will be deemphasized.

Cluster merging in the EMC was previously studied using shower profiles from the test-beam data [90]. It is instructive to estimate the effect of cluster merging on the decay photon yield using this information<sup>1</sup>. In what follows the separation efficiency is defined as the probability to resolve photon pairs which hit the calorimeter. Figure 4.11 shows the separation efficiency as a function of  $\pi^0 p_T$  for photon pairs in the PbSc (red) and PbGl (blue). An 80% asymmetry cut has been applied to this data. The dependence of the efficiency on daughter photon  $p_T$  is determined using the  $\pi^0$  decay probabilities and  $\pi^0 p_T$  spectrum according to:

---

<sup>1</sup>Prior to the simulation studies described in section 4.7 these estimates were used as correction factors to the data.

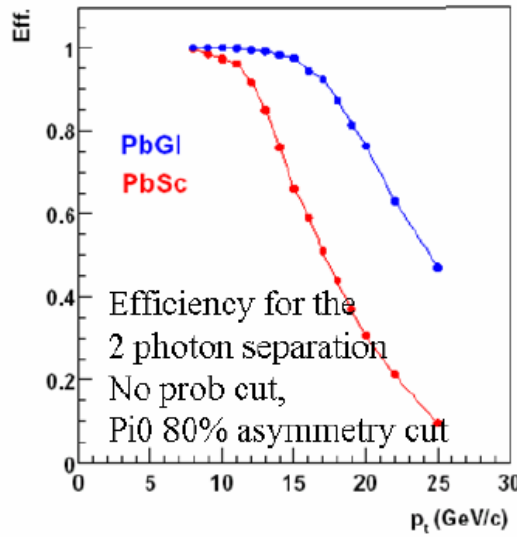


Figure 4.11: Separation efficiency from a GEANT simulation using input from the test beam data for PbSc (red) and PbGl (blue) [90]

$$\epsilon(p_T^\gamma) = \frac{\int \epsilon(p_T^\pi, p_T^\gamma) P(p_T^\pi, p_T^\gamma) dN^\pi / dp_T}{\int P(p_T^\pi, p_T^\gamma) dN^\pi / dp_T} \quad (4.5)$$

The efficiency,  $\epsilon$ , is a function of both  $p_T^\pi$  and  $p_T^\gamma$  since it depends primarily on the opening angle which is a function of both of these quantities. We evaluated the dependence on  $p_T^\gamma$  according to the following two extremal assumptions since the exact dependence on opening angle was not readily available.

- Assumption #1: Only the most symmetric decays, corresponding to decays with the smallest opening angle, are merged.
- Assumption #2:  $\epsilon$  depends only on  $p_T^\pi$ ; photons at all asymmetries are equally likely to be merged

Figure 4.12 shows the  $p_T^\pi$  vs.  $p_T^\gamma$  for all  $\gamma$ 's in the acceptance in the Monte Carlo (left) and for only the  $\gamma$ 's which are separated according to assumption #1 (right). The efficiency values evaluated by the two assumptions are shown in the right panel. Figure 4.13 shows the efficiency vs.  $p_T(\gamma)$  for the two assumptions. A more accurate estimate of the merging effect was obtained by through the simulation described in the next section.

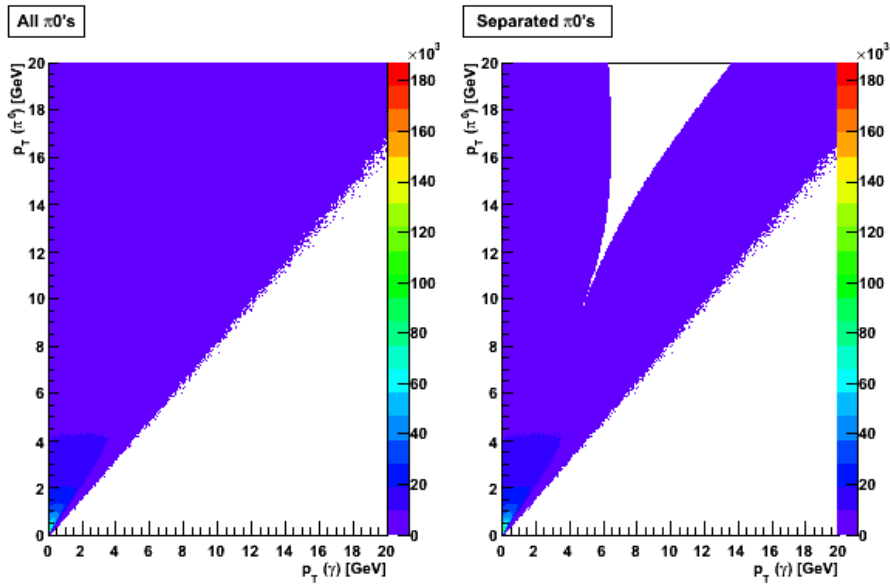


Figure 4.12: Parent vs. daughter  $p_T$  for photons from  $\pi^0$  decay in the EXODUS simulation with no merging included (left) and with merging parameterized according to assumption #1 (right).

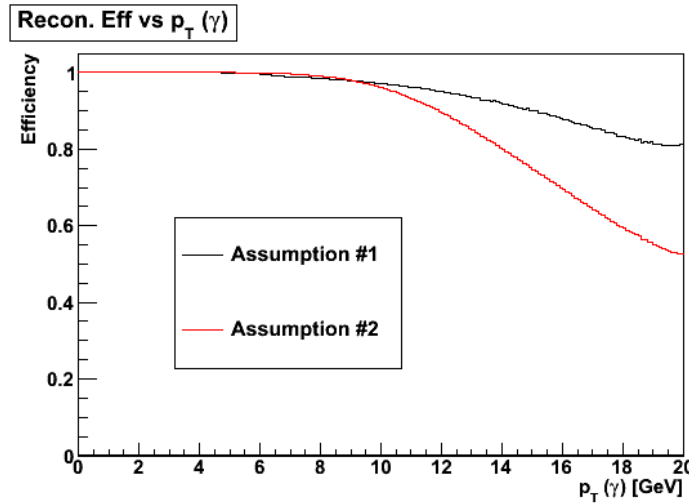


Figure 4.13: Separation efficiency as a function of photon  $p_T$ .

## 4.7 PISA Studies

The Monte Carlo simulations described in 3.4.3 provide a fairly accurate implementation of the EMC acceptance and a semi-realistic description of detector

resolution, however; there are a number of detector effects that are not accounted for in such a simple approach. In particular it was determined that the following effects might warrant investigation:

- Conversions
- Merging
- Hadron contamination
- More realistic detector resolution/calibration effects

In order to estimate the magnitude of such effects on the correlation results GEANT simulations were performed. The GEANT implementation of the PHENIX detector setup is part of simulation package called PISA (PHENIX Integrated Simulation Package) which is described in [111].

Initially, the PISA was run on entire PYTHIA events to simulate p + p collisions as realistically as possible. The PYTHIA sample was filtered for events containing at least one high  $p_T$  (+4 GeV) final state particle. The rate of contamination to the photon sample by charged hadrons was found to be very small ( $\sim 1\%$ ) providing a cross-check on the charged veto cut described in 3.2.1. Unfortunately, reconstructing entire PYTHIA events in PISA turned out to be rather computing-intensive. Since the other detector effects of concern were thought to be dominant at high  $p_T$  and relatively insensitive to multiplicity effects it was reasoned that they would be more thoroughly addressed by single particle simulations.

Samples of a few million single photons,  $\pi^0$ 's and  $\eta$ 's were generated in EXODUS. Flat  $p_T$  distributions ( $3 < p_T < 20$  GeV) were used. Figure 4.14 shows the decay probability function from single  $\pi^0$ 's in PISA compared to the analytic and fast Monte Carlo results. The difference between the PISA result and the other two results arises from the single photon efficiency term  $\varepsilon_\gamma(p_T^\pi, p_T^\gamma, z^\gamma)$  in equation 3.18 which not taken into account in the latter two approaches. The bottom panel of the same figure shows the ratio of the PISA decay probability function to the fast Monte Carlo result. The ratio was fit to a straight line. For values of  $p_T$  above the point at which the fit intersects unity the fit value was used as a correction factor to the fast Monte Carlo probability function. The fit values of each of the  $p_T$  bins are given in table 4.1.

As discussed above, cluster merging affects not only the decay probability function but  $R_\gamma$  as well. The separation efficiency can be estimated as the product of the correction functions in table 4.1 and the decay photon  $p_T$  spectrum which is well approximated by a power law of  $dN/dp_T \sim p_T^{-7}$ .

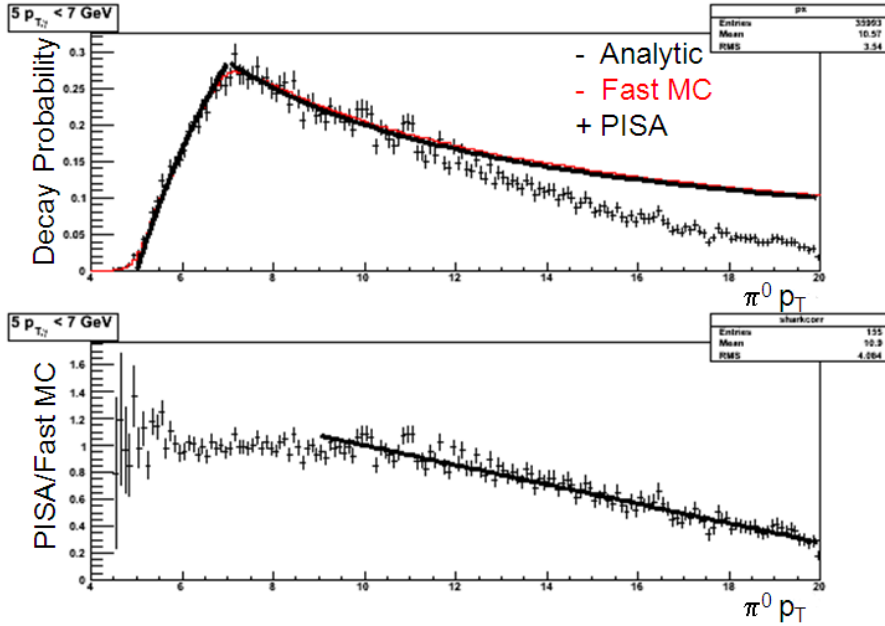


Figure 4.14:  $\pi^0 \rightarrow 2\gamma$  probability function for  $5 < p_T^\gamma < 7$  GeV estimated analytically (black line), by fast Monte Carlo (red line) and by PISA (black points)

$p_T$ [GeV]	slope( $\times 10^{-2}$ )	y-intercept
5-7	-7.85	1.85
7-9	-8.7	2.0
9-12	-9.65	2.2
12-15	-12.5	2.8

Table 4.1: Values of fit parameters for single photon efficiency correction function evaluated in PISA

The separation efficiencies calculated as such are compared to those obtained by both assumptions discussed in the previous section in table 4.2. The agreement between the two approaches is only approximate, but is sufficient given the other statistical and systematic uncertainties at high  $p_T$ . The effective change to  $R_\gamma$  is determined from the PISA obtained efficiencies by

$$\Delta R_\gamma = (R_\gamma + 1) \left( \frac{\epsilon - 1}{\epsilon} \right) \quad (4.6)$$

$\eta$  mesons were also decayed in PISA. The decay function for  $\eta$ 's is shown in 4.15. Due to the larger opening angle for the  $\eta$  decay there is no additional

$p_T$ range (GeV)	$\epsilon$ (Assumption #1)	$\epsilon$ (Assumption #2)	PISA
5-7	0.999	0.998	0.998
7-9	0.989	0.984	0.989
9-12	0.977	0.968	0.954
12-15	0.948	0.880	0.868

Table 4.2: Separation Efficiency for photon pairs from  $\pi^0$  decay estimated according to the two assumptions discussed in section 4.6 and from PISA

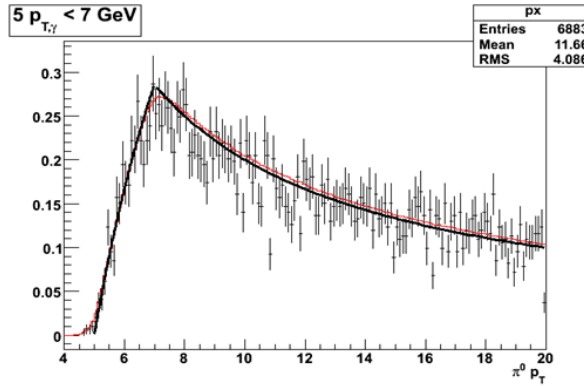


Figure 4.15:  $\eta \rightarrow 2\gamma$  probability function for  $5 < p_T^\gamma < 7$  GeV estimated analytically (black line), by fast Monte Carlo (red line) and by PISA (black points)

effect beyond what is accounted for in the fast Monte Carlo.

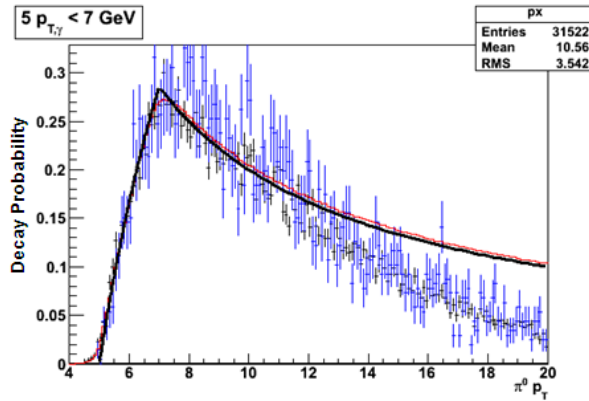


Figure 4.16:  $\pi^0 \rightarrow 2\gamma$  probability function for  $5 < p_T^\gamma < 7$  GeV for electrons from photon conversion that pass the photon ID cuts and for true photon cluster. Lines are as in previous figures.

With regard to photon conversions, the simulations indicate that a surprisingly large fraction ( $\sim 14\%$ ) of clusters which pass the photon cuts are actually initiated by electrons (or positrons). Most of these electrons come from conversions close to the EMC such that they are not reconstructed (and thus vetoed) as charged tracks. The decay probability function is shown for photon and electron showers in figure 4.16. Within the statics of the study no difference is observed between the two types of clusters.

## 4.8 Isolation Method: $R_\gamma'$

The uncertainty in  $R_\gamma$  propagates to  $R_\gamma'$  as

$$\sigma R_\gamma' = \sigma R_\gamma \left[ \frac{\frac{N'_{inclusive}}{N_{inclusive}}}{1 + P_{miss} \left( \frac{\pi^0}{N^{niso}} \right)} \right] (1 - R_\gamma \varepsilon_{tag})^2 \quad (4.7)$$

An additional uncertainty is introduced by the decay photon tagging.  $R_\gamma'$  is over-estimated when direct photons are falsely tagged as decay photons. This effect should be small since direct photons are rarely associated with particle production on the near-side. Nevertheless, the systematic effects are evaluated under the most conservative assumptions since a large bremsstrahlung component could, in principle, lead to a over-estimation of the tagging efficiency.

Falsely tagged photons change not only the tagging efficiency but also decay photon isolated fraction. Falsely tagged direct photons lead to an over-estimation of  $R_\gamma'$  both in the case when they are isolated and non-isolated. However, if the direct photons are isolated the change to the tagging efficiency and isolation fraction are partially compensating. Also, the combinatorial background for photon pairs is larger when the pairs are not isolated so I evaluate the uncertainty assuming that all falsely tagged photons are non-isolated. The total number of falsely tagged, non-isolated direct photons is estimated from the combinatorial background level for photon tagging of non-isolated photon pairs taking the direct photon contribution to be the same as in the absence of photon tagging (i.e., given by  $R_\gamma$ ):

$$N_{false}^{dir} = \frac{N_{direct}}{N_{inclusive}} N_{bknd}^{niso} = \left( 1 - \frac{1}{R_\gamma} \right) \left( 1 - \frac{S}{T} \right) N_{tag}^{niso} \quad (4.8)$$

where  $S/T$  is the purity (signal/total) of the tagged sample as measured from the invariant mass distributions. Figure 4.17 shows the invariant mass distributions for non-isolated photons and the resulting tagging purity for the wide set of cuts.

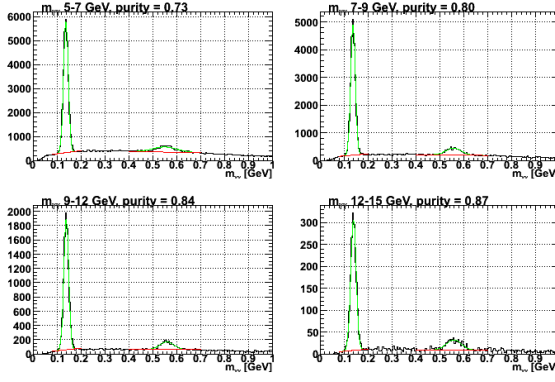


Figure 4.17: Invariant mass distributions for several ranges of tagged photon  $p_T$  for non-isolated photons. Also shown are the fits determining the total (green) and background (red) contributions.

The isolation fraction is evaluated using the narrow set of tagging cuts and only the  $\pi^0$  mass window. The purity of this sample, shown in figure, is evaluated by applying the decay photon probability function to the invariant mass distributions.

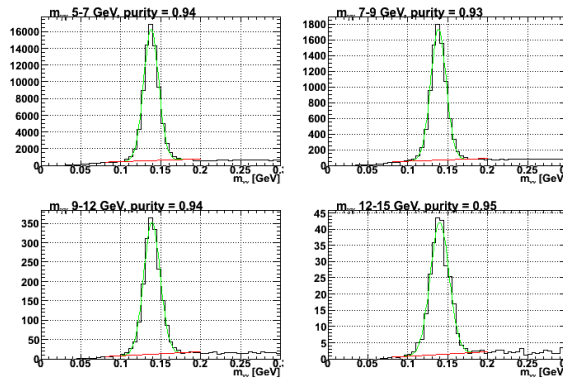


Figure 4.19: Invariant mass distributions for several ranges of decay photon  $p_T$  for non-isolated pairs. Also shown are the fits determining the total (green) and background (red) contributions.

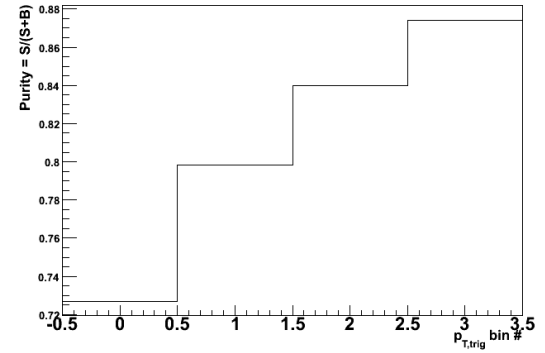


Figure 4.18: The purity of photon pairs as determined by the fits shown in figure 4.17.

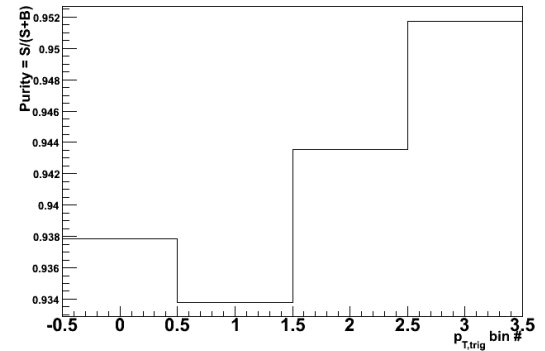


Figure 4.20: The purity of photon pairs as determined by the fits shown in 4.19.

$p_{T,t}[\text{GeV}]$	$R_\gamma$	$R_\gamma'$	$\Delta R_\gamma'(R_\gamma)$	$\Delta R_\gamma'(tag)$
5-7	1.18	1.39	0.16	0.04
7-9	1.33	1.99	0.26	0.09
9-12	1.48	2.85	0.50	0.16
12-15	1.65	3.82	1.17	0.21

Table 4.3:  $R_\gamma$  and  $R_\gamma'$  values and uncertainties on  $R_\gamma'$

Since the systematic uncertainty due to tagging is likely a very conservative estimate I do not move the central value of the per-trigger yield but rather apply the tagging systematic as a one directional systematic uncertainty in the direction of increasing  $R_\gamma$ . Table 4.3 shows the  $R_\gamma$ ,  $R_\gamma'$  and its systematic uncertainties. The uncertainty due to  $R_\gamma$  is the dominant systematic uncertainty.

The uncertainties on the decay per-trigger yields are taken to be the same as in the standard statistical subtraction analysis. Any additional contribution due to the tagging can be neglected compared to the already substantial uncertainties in the decay photon mapping.

## 4.9 Summary of Systematic Uncertainties

### 4.9.1 p + p

Figure 4.21 shows a breakdown of the systematic uncertainties in the p + p measurement as a relative error on the subtracted direct photon yields. The dominant uncertainty is the estimate of the decay associated yields. Although the uncertainties on the decay yield itself are typically small, they propagate to a larger error on the direct photon yields, due to the smallness of the signal. The decay uncertainty is can be sub-divided into several components: the weighting procedure (2%), decay from heavy hadrons (1.5%),  $\eta$  sideband subtraction (2.6%) and the cutoff correction (varies, see 3.4.5).

### 4.9.2 Au + Au

The relevant systematic uncertainties can be separated into four sources: The direct photon excess ( $R_\gamma$ ), decay photon correlations,  $v_2$  subtraction, and combinatorial background normalization.  $R_\gamma$  and its uncertainties were determined in an independent analysis. In p + p collisions the estimate of the decay photon contribution is limited by the Monte Carlo mapping and  $\eta$  sideband subtraction procedures. In Au + Au, on the other hand, the dominant

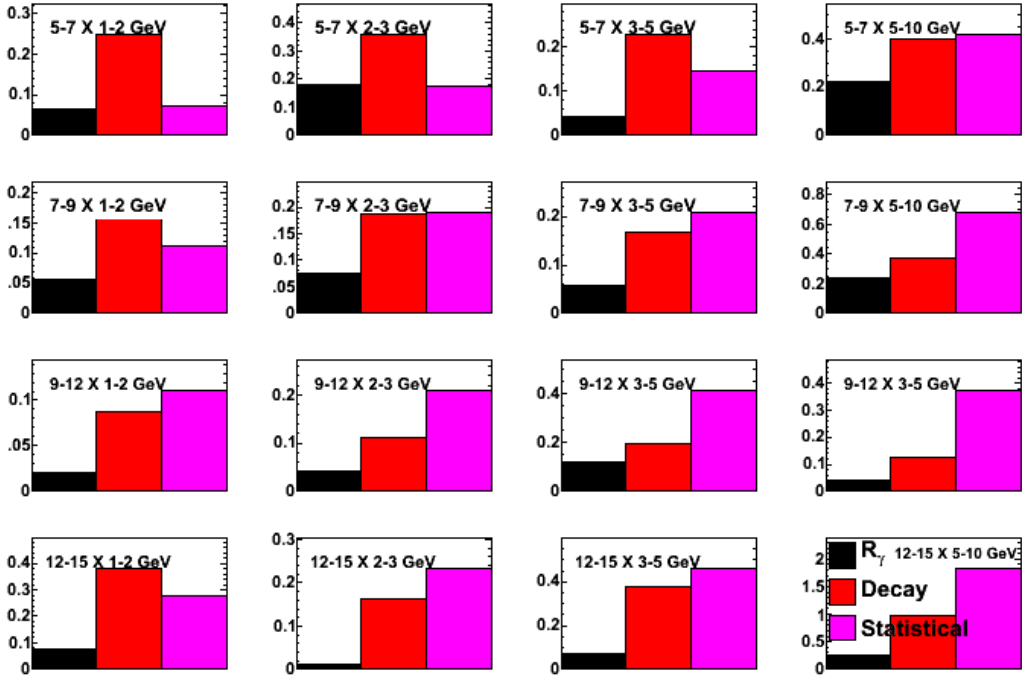


Figure 4.21: Breakdown of relative statistical and systematic uncertainties (%) for the away-side direct photon associated yields in central  $p + p$  collisions

uncertainty, by far, is false  $\pi^0$  reconstruction due to combinatorial photon pairs as discussed in section 4.3. The uncertainty due to the  $v_2$  subtraction is determined by varying the magnitude of the elliptic flow within its uncertainties as determined in independent analyses. The uncertainty in the combinatorial background is determined by varying the assumptions in the estimate of residual multiplicity correlations as discussed in section 3.3.1. Finally, there is additional source from the determination of the charged hadron efficiency corrections. A 10% and 12% scale uncertainty is applied independently to both the  $p + p$  and Au + Au data. There is also a  $p_T$  dependent component to the uncertainty in the efficiency corrections arising from mis-reconstructed secondary tracks, as discussed in section 3.3.3. This effect only contributes a significantly to the overall scale uncertainty above 5 GeV.

Figure 4.22 shows the relative uncertainties on the away-side direct photon associated yields for each  $p_T$  combination. The dominant source of systematic uncertainty is non-uniform over the measured range of  $p_{T,t}$  and  $p_{T,a}$ . There are several reasons for this:

- The direct photon signal-to-background increases with  $p_{T,t}$ .

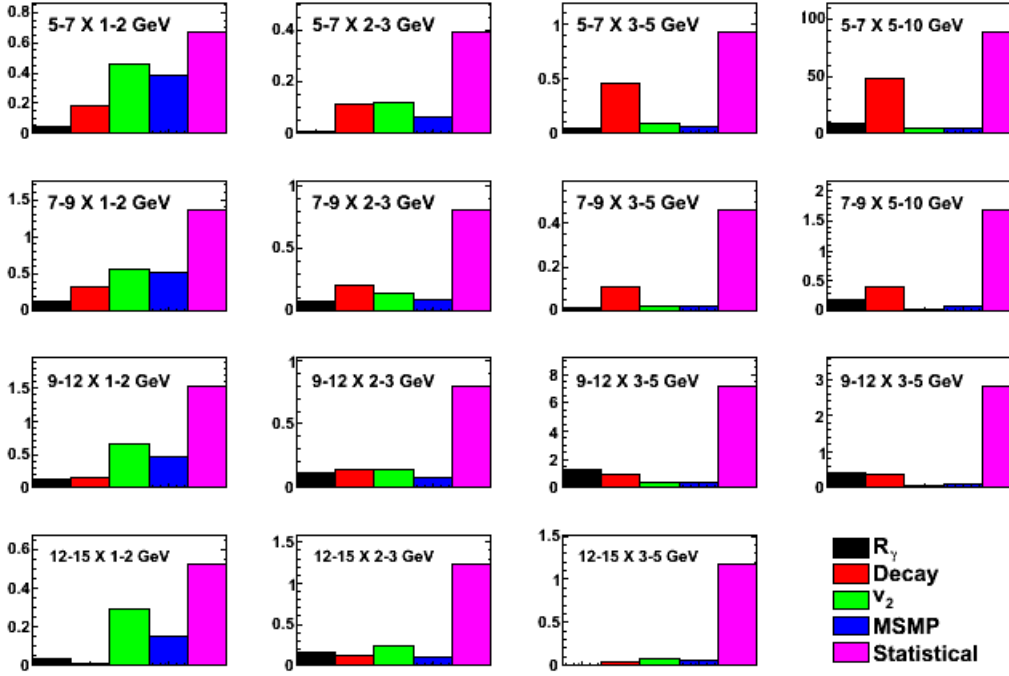


Figure 4.22: Breakdown of relative statistical and systematic uncertainties (%) for the away-side direct photon associated yields in central (0-20%) Au + Au collisions

- The combinatorial background decrease with  $p_{T,a}$ .
- The  $\pi^0$  reconstruction purity increases with  $p_{T,t}$ .

The net effect is that at low values of  $p_{T,a}$ , the  $v_2$  and MSMP errors dominate. At large  $p_{T,a}$ , but small  $p_{T,t}$ , the decay uncertainty is largest. At large  $p_{T,t}$  and large  $p_{T,a}$  the uncertainty in  $R_\gamma$  takes over. Across all bins, however, the statistical uncertainties are larger than the systematic ones. Although many of the systematic uncertainty estimates in the present work are rather conservative, it is clear that more precise estimates provide diminishing returns for the Run 4 data set. Measurements of the larger Run 7 data set are already in progress and efforts are underway to reduce the systematic errors.

### 4.9.3 A Note on Correlated Errors

Each of the four sources of error described above is at least partially correlated across  $p_T$  ranges sampled. In many instances, however, these correlations are negligible. To provide an example, a fit to the conditional yield as a function of

$p_{T,a}$  would more accurately treat the errors as uncorrelated since the dominant source of uncertainty at small  $p_{T,a}$  is different (and independent) from the one at large  $p_{T,a}$ . Generally, however, we will represent the systematic uncertainties as error bands rather than combining them with the statistical error, since there are instances in which these correlations are important. In what follows, the reader should assume that uncertainties in the Au + Au data have been treated as uncorrelated unless otherwise stated.

# Chapter 5

## Measurements of Nuclear Effects via Direct Photon Correlations

### 5.1 Direct Photon Correlations in p+p

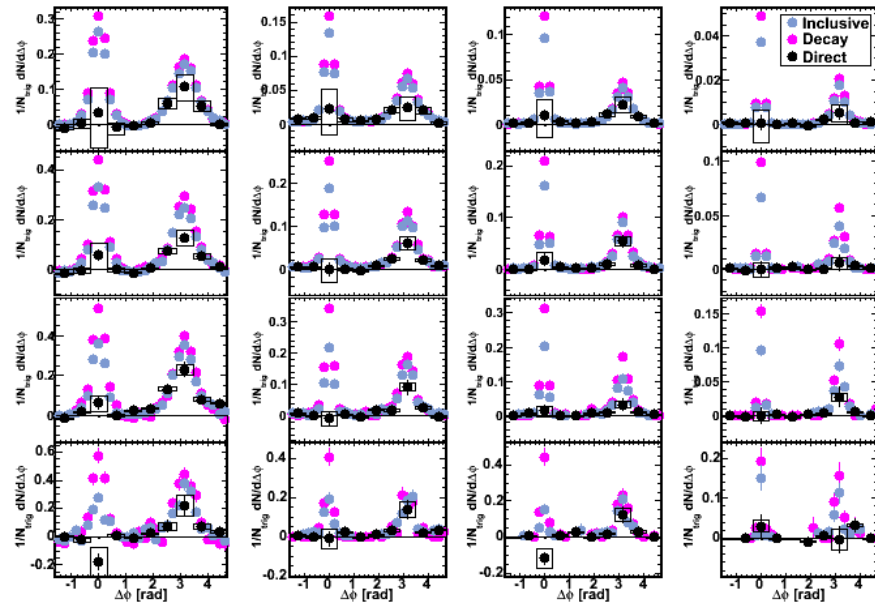


Figure 5.1: Per-trigger yields of charged hadrons with inclusive, decay and direct photon triggers using the statistical subtraction method.

The direct photon associated yields in p + p collisions are shown figure in 5.1.

Also shown are the ingredients in the subtraction, the inclusive photon and decay photon associated yields. The decay photon per-trigger yields are estimated from the measured  $\pi^0$  and  $\eta$  correlations via the Monte Carlo mapping procedure discussed in section 3.4.

To first approximation, one expects to observe the behavior predicted at leading order, *i.e.*, that direct photons should be accompanied by no near-side particle production and should have an opposite-side correlation qualitatively similar to di-jet events. The absence of a near-side correlation therefore serves as a useful benchmark for the statistical subtraction method. The systematic uncertainties become large when the decay associated background is large and the direct photon signal is small. Hence, the uncertainties are largest at low  $p_{T,t}$  and near  $\Delta\phi = 0$ .

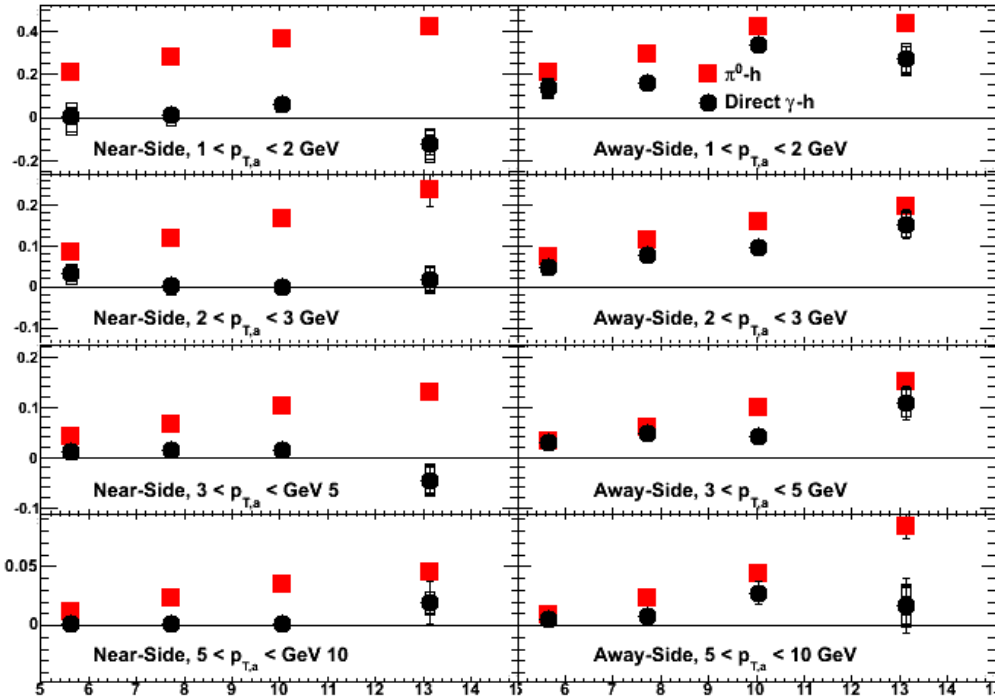


Figure 5.2: Comparison of direct photon and  $\pi^0$  associated yields as a function of  $p_{T,t}$  on the near ( $-\pi < \Delta\phi < \pi$  radians) and away-sides ( $\pi < \Delta\phi < 3\pi/2$  radians)

A more direct comparison between  $\gamma+\text{jet}$  and di-jet events is achieved by comparing the direct photon to  $\pi^0$  associated yields. Figure 5.2 shows the yields integrated over the near and away-sides. The absence of near-side yield for direct photon triggers as compared to  $\pi^0$ 's is rather striking. This indicates that the fraction of photons at moderate values of  $z$  is fairly small. We will

return to this point in section 6.2. For the present purposes will we interpret the lack of near-side yield to demonstrate that a fairly pure sample of prompt photons has been obtained.

On the away-side, a significant correlation signal is measured in nearly every bin. The yields are generally smaller than those of the  $\pi^0$ . This is due to the higher jet momentum for decay photon triggered jets for fixed  $p_{T,t}$ . As a rule of thumb, The  $\langle z \rangle$  of  $\pi^0$  triggers of  $4 < p_T < 5$  GeV was estimated to vary from about 0.5-0.7 depending on  $p_{T,a}$  [61]. Since the direct photons are expected to come values of  $z$  closer to unity, the smaller away-side yield can also be taken as evidence for successful direct photon identification.

## 5.2 $\eta$ Correlations

$\eta$  mesons are the second largest contributor to the decay photon background.  $\eta$  correlations have been measured in p + p collisions. Due to the overwhelming size of the combinatorial background in central Au + Au collisions, however, it was not possible to make the same measurement in that collisions system. Instead the contribution of  $\eta$  correlations in Au + Au was estimated from the p + p data, employing a scaling argument as follows. The spectra of  $\eta$  mesons in Au + Au were shown to exhibit the the same level of suppression at high  $p_T$  as is observed for  $\pi^0$ 's [112]. In fact,  $\eta/\pi^0$  has been measured in p+p, d+Au and Au+Au [77]. Above 2 GeV, all are consistent with a constant value of  $0.45 \pm 0.05$ , compatible with expectations from PYTHIA and  $m_T$  scaling. Since, jet fragmentation is thought to occur outside the medium, it is reasonable to assume that the difference between  $\eta$  and  $\pi^0$  associated hadron production in Au + Au can be attributed to the same (vacuum) jet fragmentation effects that are measured in p + p collisions.

In order to correct for the effect of  $\eta$ , we measure the ratio of the  $\gamma(\eta)$  to  $\gamma(\pi^0)$  per-trigger yields in p + p collisions, shown in figure 5.3. There is a ten percent uncertainty (not shown) assigned to the ratio, from the  $\eta$  sideband subtraction method (section 3.4.6). Predictions from PYTHIA are also shown in the figure. Where statistics are high, the ratio in data is slightly higher than the PYTHIA on the near-side and slightly lower on the away-side, however given the quoted systematic uncertainty, this difference is not very significant. These ratios ( $R_\eta$ ) are applied as a correction factor to the Au + Au  $\gamma(\pi^0)$  associated yields according to

$$Y_{decay} = \left( \frac{1}{A} + R_\eta \left( 1 - \frac{1}{A} \right) \right) Y_{\gamma(\pi^0)} \quad (5.1)$$

where A (= 1.24) is ratio of total decay photons to photons from  $\pi^0$  decay, as

discussed in section 3.1.1.

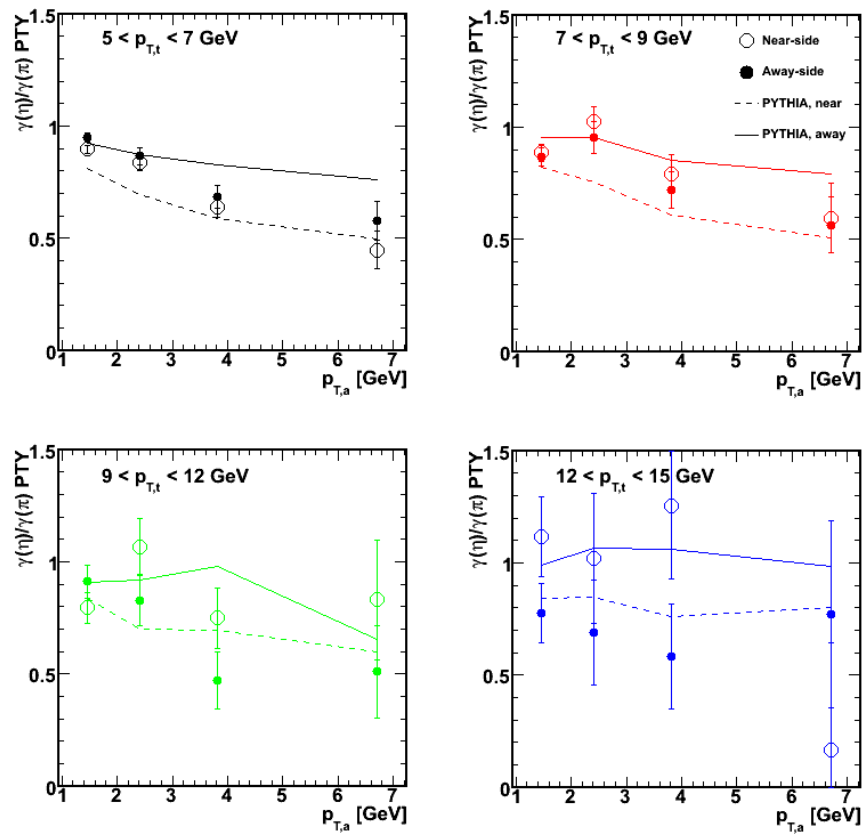


Figure 5.3: The ratio of  $\gamma(\eta)$  to  $\gamma(\pi^0)$  per-trigger yields as a function of  $p_{T,a}$  for several selections of  $p_{T,t}$  for the near-side and away-side. The lines correspond to PYTHIA (version 6.1) calculations.

### 5.3 Comparison to Au + Au Collisions

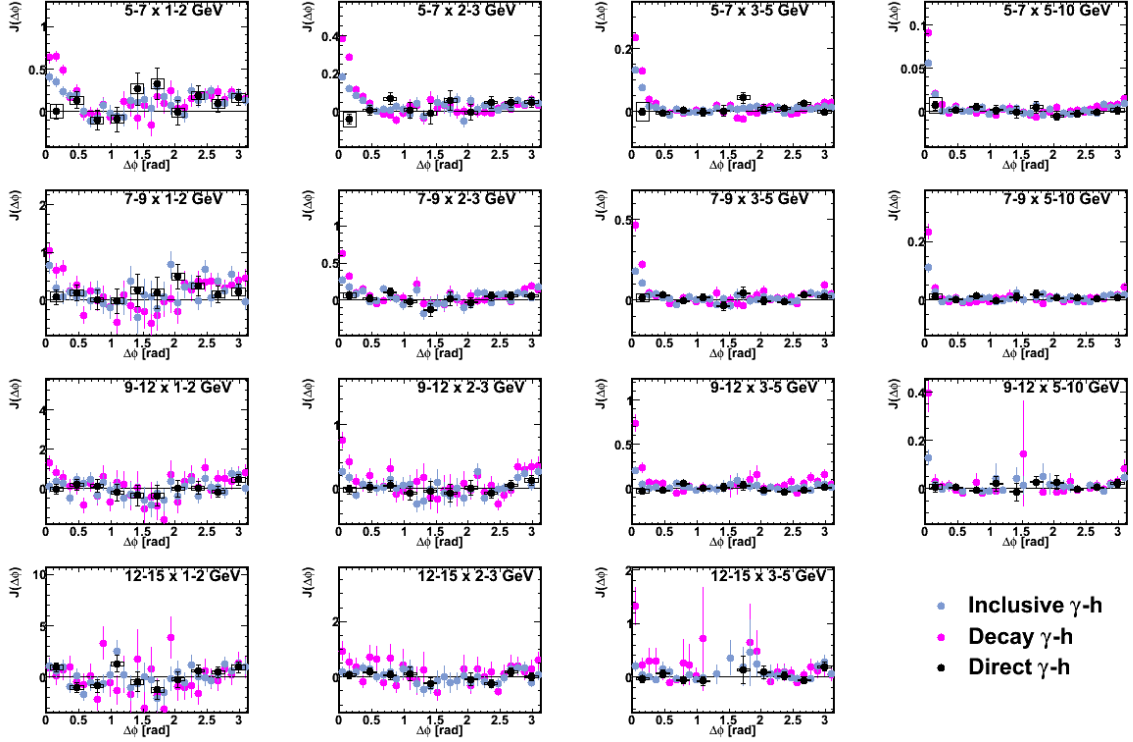


Figure 5.4: Inclusive, decay and direct photon associated yields in 0-20% Au + Au collisions.

Figures 5.4 shows the direct photon associated yields in central (0-20%) Au + Au collisions. The ingredients in the subtraction method: the inclusive and decay correlations, are also shown. The relative sizes of the yields demonstrate the signal-to-background of the decay photon statistical subtraction.

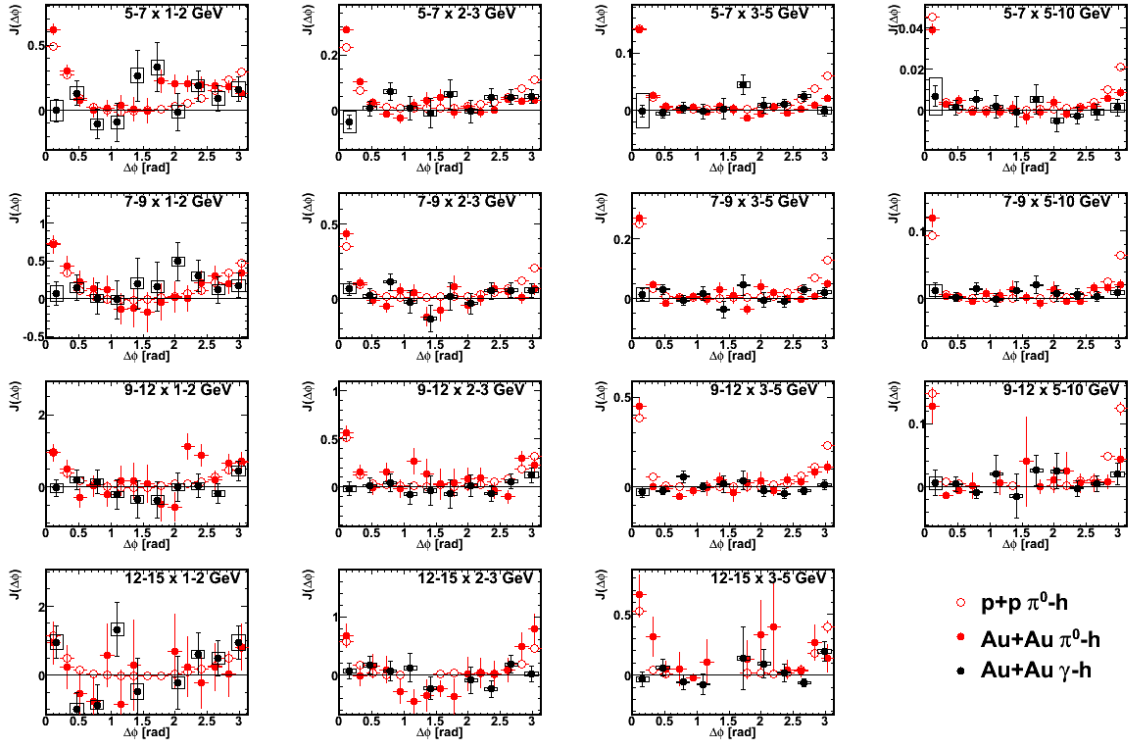


Figure 5.5: Direct photon and  $\pi^0$  associated yields in central (0-20%) Au + Au collisions. Also shown are the  $\pi^0$  associated yields from p + p collisions.

Figure 5.5 compares the Au + Au direct photon correlations to  $\pi^0$  triggered correlations in Au + Au and p + p. Again, the absence of a near-side correlation is observed, where precision allows. On the away-side back-to-back correlations are largely absent above  $p_{T,a} = 2$  GeV, for both  $\pi^0$  and direct photon triggers. This is the first observation of the, now familiar, phenomenon of jet suppression in the  $\gamma + jet$  channel.

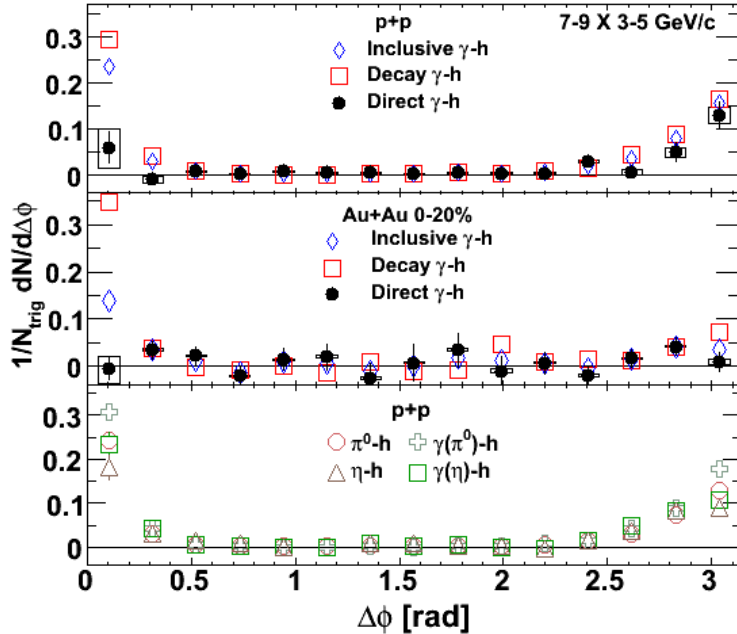


Figure 5.6: Jet functions for all of the ingredients in the direct photon subtraction method for one bin of  $p_{T,t}$  and  $p_{T,a}$  for  $p + p$  and central  $\text{Au} + \text{Au}$  (0-20%). Top: Inclusive, decay and direct jet function in  $p + p$  collisions. Middle: Inclusive, decay and direct jet functions in central  $\text{Au} + \text{Au}$  collisions. Bottom:  $\pi^0$ ,  $\eta$ ,  $\gamma(\pi^0)$  and  $\gamma(\eta)$  associated yields in  $p + p$ .

Figure 5.6 collects all of the jet functions (flow and combinatorial background subtracted per-trigger yields) used in both the  $p + p$  and central  $\text{Au} + \text{Au}$  analyses for one selection of  $p_{T,t}$  and  $p_{T,a}$ . This particular bin is representative, in that the features apparent in this bin are shown throughout much of the data, albeit with reduced precision. Comparing the inclusive and decay photon near-side correlations for  $p + p$  (top) and  $\text{Au} + \text{Au}$  (middle) the larger direct photon signal-to-background in  $\text{Au} + \text{Au}$  is evident. Again, the absence of a near-side correlation is apparent in the  $\text{Au} + \text{Au}$  data, as well as in  $p + p$ . The disappearance of the away-side correlation in  $\text{Au} + \text{Au}$  can be seen by comparing to the  $p + p$  correlations. The components of the decay photon measurement are shown in the lower panel. The decay photon associated yields for both  $\pi^0$  and  $\eta$  are larger than the parent meson as estimated by the Monte Carlo mapping procedure. The  $\eta$  associated yields are slightly smaller than those of  $\pi^0$ , reducing the total estimated decay contribution by about 5%.

## 5.4 Near-Side Correlations: Implications for Induced Radiation and the Ridge

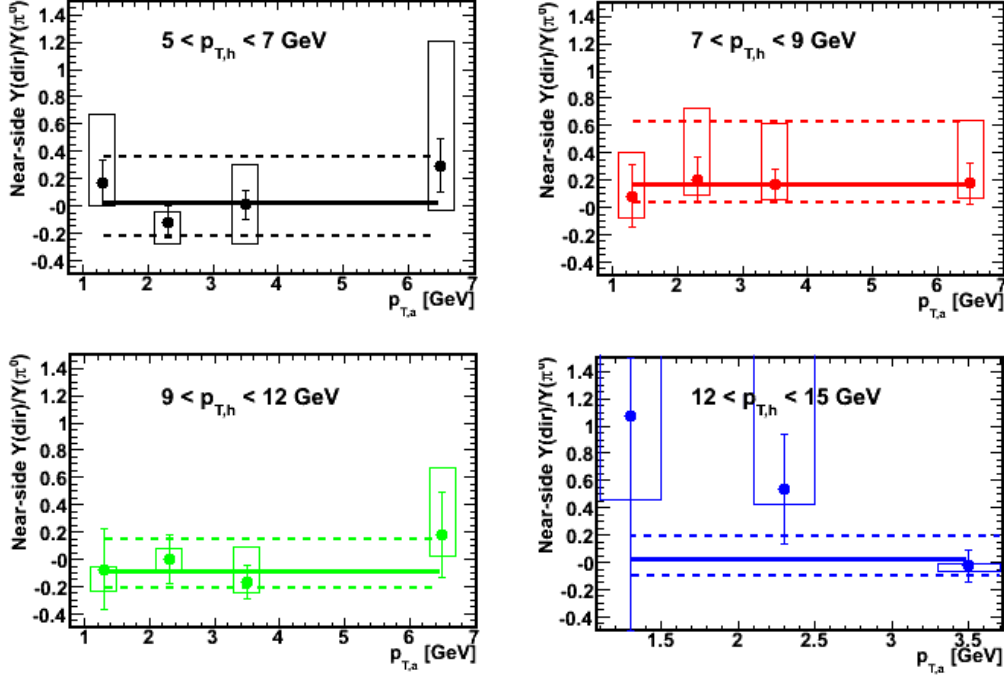


Figure 5.7: The ratio of the near-side ( $|\Delta\phi| < 0.5$  radians) direct photon associated yield to that of  $\pi^0$  in central (0-20%) Au+Au collisions.

Although  $\gamma$ +jet tomography relies on opposite-side correlations, near-side correlations have important implications as well. Sources of medium-induced radiation, namely additional bremsstrahlung [80] and jet-photon conversion [81], would be expected to result in near-side correlations. Moreover, a recent calculation claims that the sum of these induced sources is equal to the size of the prompt signal itself at 6 GeV, and is of order 50% of the prompt signal at 10 GeV [83].

$\gamma$ +jet studies may also help to elucidate the character of the “ridge” phenomenon observed as a low  $p_T$  enhancement of near-side correlations in hadron-hadron correlations (see section 1.4.2). If the ridge is indeed a manifestation of the medium response to the passage of the hard parton, than it should be absent for photon triggers, as expounded upon in [113].

The ratio of the direct photon to  $\pi^0$  associated yields in central Au + Au collisions are shown as a function of  $p_{T,a}$  in figure 5.7, for the range  $|\Delta\phi| <$

0.5 radians. The data are well described by fits to a constant for each  $p_{T,t}$  bin, the results of which are shown in table 5.1. Below 9 GeV these fits indicate that a near-side yield as large as 50% cannot be excluded. At high  $p_T$  however, the data favors a near-side correlation of < 20% of the  $\pi^0$  signal. This statement is particularly convincing in the  $9 < p_{T,t} < 12$  GeV range, where all the data points have relatively good precision. Assuming the per-trigger yield of induced sources is the same as for  $\pi^0$ , we would exclude a medium induced rate on the order to 50% of the  $\pi^0$  signal as indicated in [83].

$p_{T,t}$ [GeV]	$\langle Y_{dir}/Y_\pi \rangle$	$\sigma_{\text{STAT}}$	$\sigma_{\text{SYS}}(\text{low/high})$
5-7	0.024	0.067	0.231/0.329
7-9	0.168	0.007	0.116/0.45
9-12	-0.084	0.091	0.094/0.209
12-15	0.025	0.11	0.046/0.118

Table 5.1: The ratio of the direct photon to  $\pi^0$  associated yields on the near-side for several  $p_{T,t}$  selections averaged over  $p_{T,a}$ .

## 5.5 Energy Loss via $\gamma + \text{Jets}$

Turning now to the primary objective of direct photon correlations, we consider the away-side yields. The direct photon and  $\pi^0$  conditional yields are shown in 5.8 as function of  $p_{T,a}$  for both p + p and Au + Au collisions. The yields are integrated over a fairly narrow range of  $4/5\pi < \Delta\phi < 6/5\pi$  radians. The reasons for choosing a such a narrow window of integration are twofold. Firstly, the influence of statistical fluctuations are reduced by choosing to restrict the integration range to an interval where the jet signal is relatively large. Secondly, the interval corresponds to the so-called "head" region where one observes a jet-like correlation of reduced amplitude in hadron-hadron correlations as opposed to the "shoulder" region where one observes a modified structure presumed to be the medium response [53, 114, 50]. The statistical and systematic uncertainties depend on a variety of factors ( $R_\gamma$ , jet combinatorial background, etc.) and vary from bin to bin. The highest precision data are at intermediate  $p_{T,t}$  and  $p_{T,a}$ , so the interpretation of the data will be steered by the data in this range. It is tempting to try and compare the slopes of the p + p and Au + Au yields however the uncertainties are still too large to constrain the slope of the Au + Au data.

In order to place the current results in the context of previous observations we compare the direct photon  $I_{AA}$  to the  $\pi^0$   $I_{AA}$  and  $R_{AA}$ . To understand

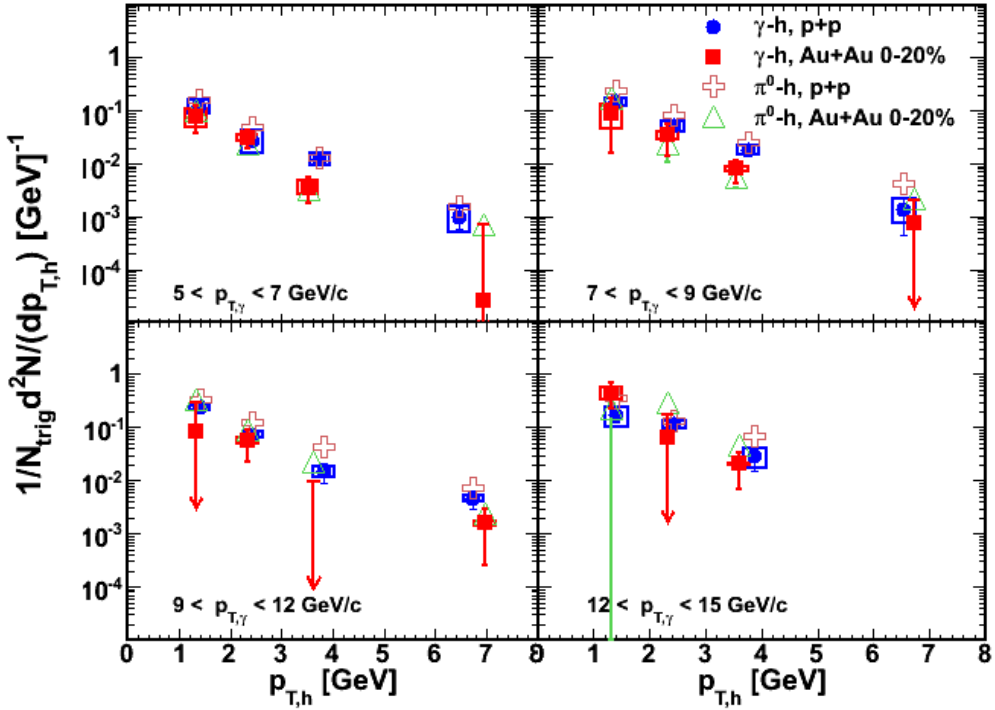


Figure 5.8: Away-side ( $4/5\pi < \Delta\phi < 6/5\pi$  radians) direct photon and  $\pi^0$  associated yields as a function of  $p_{T,a}$  in  $p + p$  and central (0-20%)  $Au + Au$  collisions.

how these individual measurements may differ, consider the different hard-scattering configurations illustrated in figure 5.9. Two different profiles of an absorbing medium are shown, an infinitely black core surrounded by a corona and a diffuse medium. We can consider them to be static for simplicity. In the black core limit all hadrons must come from the surface, whereas in the diffuse limit they have a finite probability to reach the surface. Hadron pairs may similarly be totally or partially biased towards tangential emission in the two cases, respectively. As pointed out in [66], photons probe deeper into the medium, on average, because of their small interaction cross section. In the black core limit, however, their back-to-back correlations will be destroyed by the medium. In a more diffuse model hadrons may emerge from anywhere in the medium, but with reduced probability depending on the path length.

The energy loss profile depends not only on the details of geometry but also on the energy loss calculation employed. In the BDMPS limit of continuous energy loss, a black core geometry will appear completely opaque. In a GLV-type model, however, a parton has some probability to pass through the entire length of medium without any interaction at all. Since the geometry and

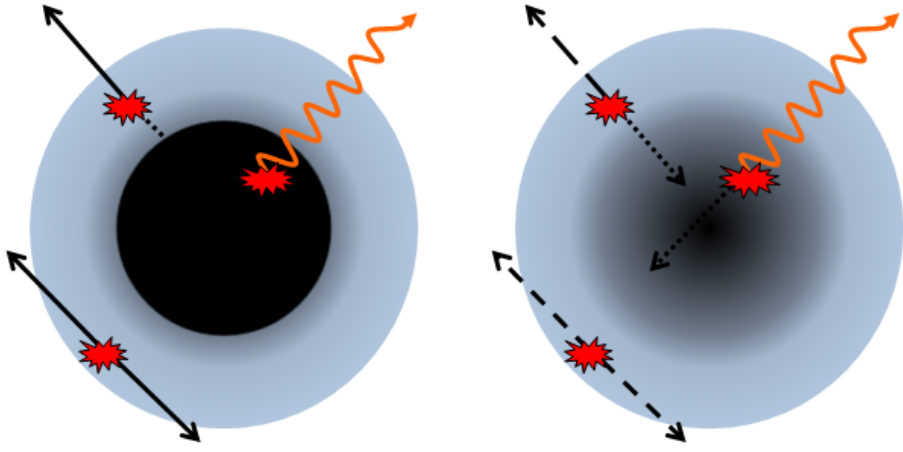


Figure 5.9: Cartoon depicting several different types of two-particle observables in the presence of a black core medium (left) and diffuse medium (right). Shown are di-hadrons from surface emissions, di-hadrons from tangential emission, and photon-hadron emission from the center of the medium.

the energy loss model are coupled, not to mention the space-time dependence we have neglected, it will be essential to simultaneously constrain our models using as many observables as possible.

Figure 5.10 shows the  $I_{AA}$  for direct photons compared to  $I_{AA}$  and  $R_{AA}$  for  $\pi^0$ . Generally, we observe that all three models give a similar suppression. To that extent, the current measurement adds to the body of knowledge that demonstrates that the medium is opaque, and hence requires high precision, differential probes to elucidate its properties. The statistical and systematic uncertainties are highly non-uniform. This is due to the fact that different background sources dominate in different kinematic ranges. This indicates that a targeted approach towards interpreting the data is in order.

Figure 5.11 compares the data for 7-9 GeV photon triggers to recent predictions from [66]. The authors use NLO pQCD with an effective model of energy loss which resembles the GLV-type approach. The parameter  $\epsilon^0$  has units of GeV/fm and is proportional to the initial gluon density. The data are consistent with all the curves, but the models nearly span the uncertainty in the best data point. We may conclude that the energy loss per unit fermi is compatible with the range of  $\epsilon^0$  considered by the authors. It is clear that higher statistics would help, but the constraints are all coming from one data point.

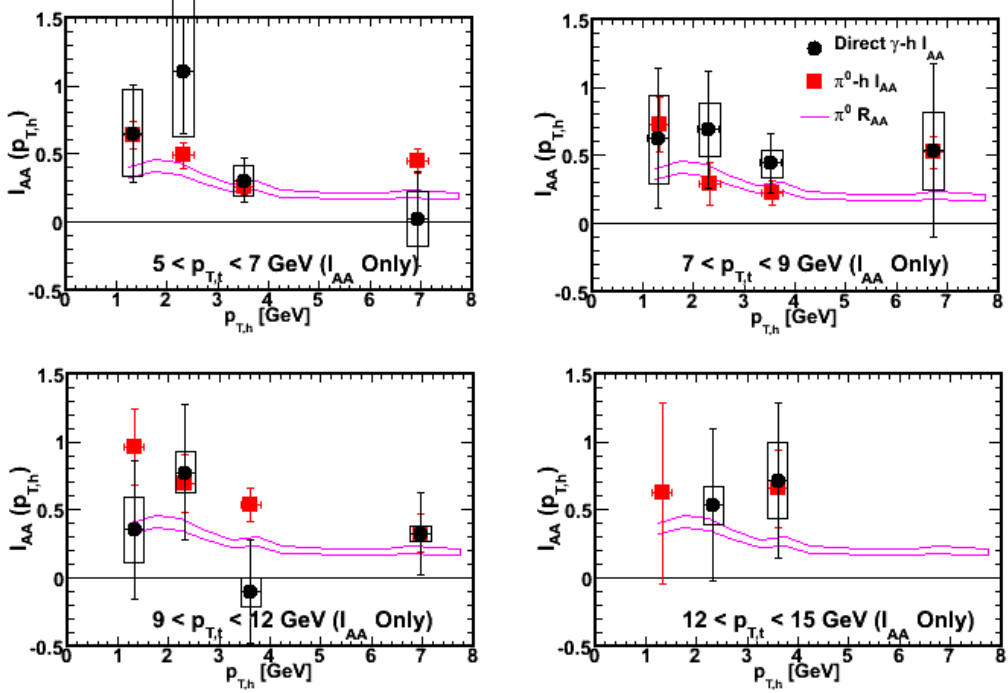


Figure 5.10: Direct photon  $I_{AA}$ ,  $\pi^0 I_{AA}$  and  $\pi^0 R_{AA}$  [42] as a function of  $p_{T,a}$  in central (0-20%) Au + Au collisions.

Moreover although the authors argue that the greatest sensitivity is obtained at low  $z_T$ , they have not consider the medium response, which is a background in terms of this measurement.

In order to avoid low  $p_{T,a}$  where uncertainties are large and a medium response may be present, we can used a fixed range of  $p_{T,a}$  and vary  $p_{T,t}$ . Figure 5.12 shows the yields and  $I_{AA}$  for the  $3 < p_{T,a} < 5$  GeV bins plotted as a function of  $z_T$ . Since a set of predictions for this bin were not obtained, we plot the predictions for the  $7 < p_{T,t} < 9$  GeV, as a demonstration. This may not be unreasonable as one naively expects such a modified fragmentation function approach to approximately scale with  $p_{T,t}$ , a least over the limited range of  $p_{T,t}$  measured. The benefit is clear. More of the data points have sensitivity to the model.

The current measurements indicate that we are not far from being able to make quantitative constraints on the energy loss using direct photon correlations. As a point of reference, a combined fit to the single and di-hadron data constrained  $\epsilon_0$  to be in the range 1.6-2.1. [87]. Since the Run 7 results currently being analyzed are a four-fold increase in statistics, and improvements in the measurement itself are anticipated, direct photon correlations may surpass the

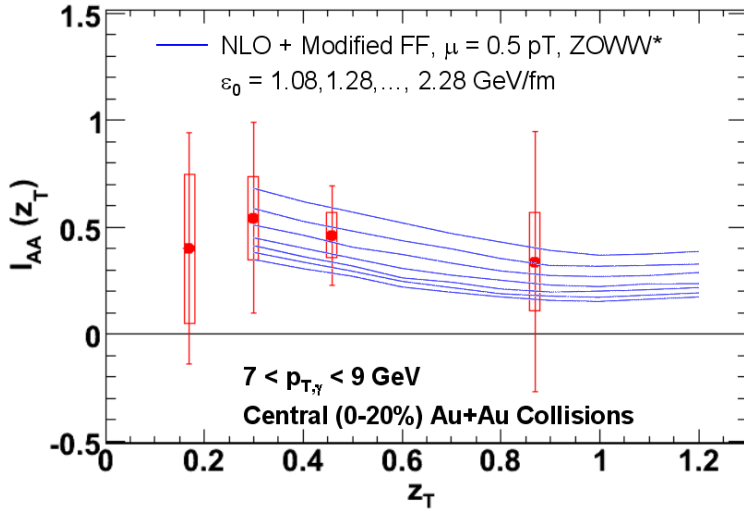


Figure 5.11:  $I_{AA}$  as a function of  $z_T$  for 7-9 GeV direct photons compared to a model of energy loss calculated to next to leading order accuracy. Predictions are from Zhang, Owens, Wang and Wang. [66].

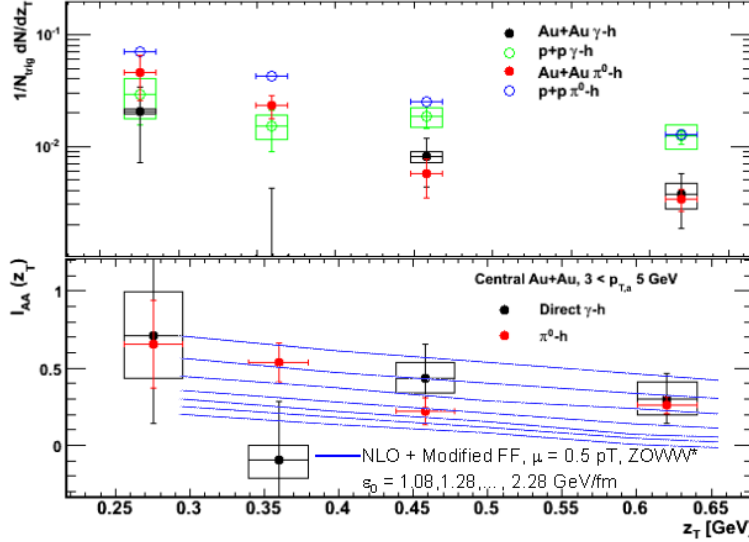


Figure 5.12:  $I_{AA}$  as a function of  $p_{T,t}$  for  $3 < p_{T,a} < 5$  GeV with predictions for 7 – 9 GeV direct photons from ZOWW as a demonstration.

hadron triggered observables as the best constraint on partonic energy loss in the near future.

## Chapter 6

# Insights into Vacuum QCD Processes Using Isolated Direct Photon and $\pi^0$ Correlations

The results presented in the previous chapter remove the decay associated yield by a purely statistical subtraction. A method of partial event-by-event identification of the direct photon signal using isolation cuts and decay photon tagging, as discussed in section 3.5, greatly improves the direct photon signal-to-background reducing the statistical and systematic uncertainties. This chapter presents results from p+p collisions using the isolation method.

## 6.1 Correlation Functions

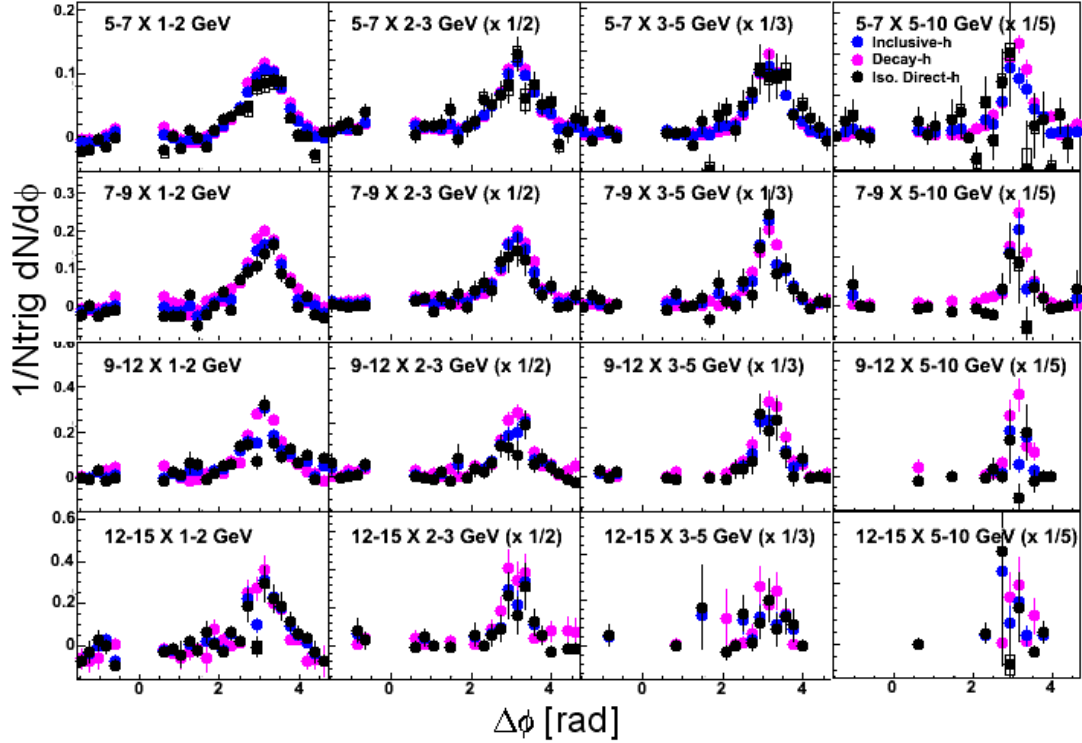


Figure 6.1: Per-trigger yields of charged hadrons with inclusive, decay and direct photon triggers using the isolation method.

Figure 6.1 shows the isolated inclusive, decay and direct photon per-trigger yields. No data is shown for  $|\Delta\phi| < 0.5$  radians where the isolation criterion removes most of the acceptance. The uncertainties are visibly improved with respect to the fully statistical method.

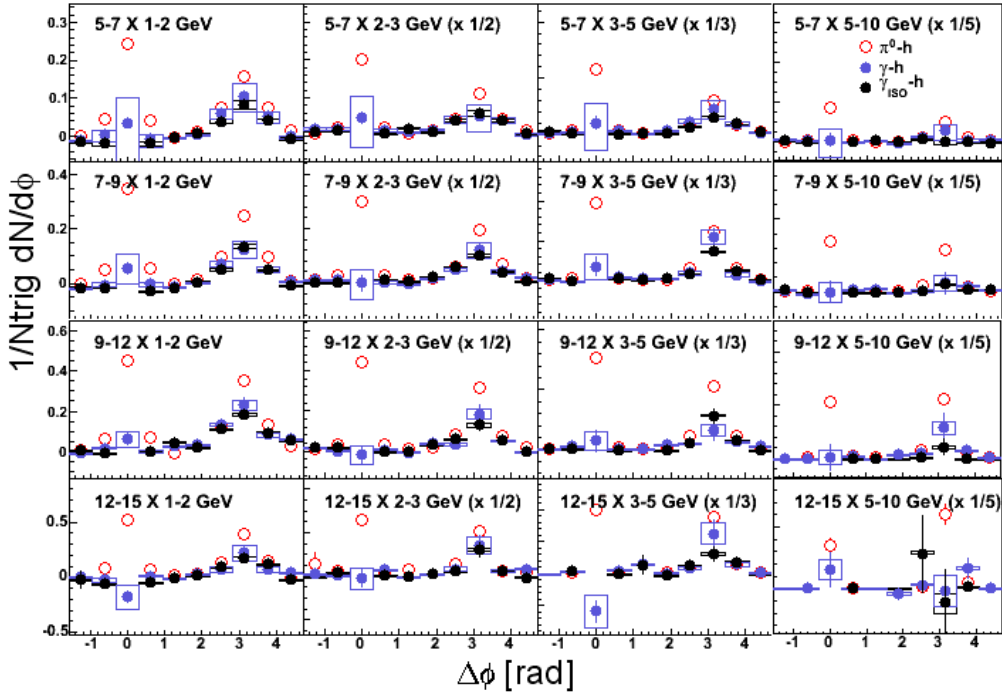


Figure 6.2: Per-trigger yields of charged hadrons for isolated direct photon, direct photon and  $\pi^0$  triggers.

The isolated direct photon per-trigger yields are compared to the direct photon per-trigger yields obtained by the purely statistical subtraction (referred to henceforth as 'inclusive') in figure 6.2. The  $\pi^0 - h$  per-trigger yields are also shown to illustrate the size of a typical near-side jet correlation peak. Although the isolated and inclusive direct photon associated yields are fairly similar, the isolated sample has slightly lower yield, on average, which will be quantified below. Since fragmentation photons are not suppressed in the inclusive photon sample, a difference between the inclusive and isolated direct photons per-trigger yields provides an indirect measurement of fragmentation photon correlations.

## 6.2 Isolating the Effects of Photon Fragmentation

Photons from jet fragmentation are a background for  $\gamma$ +jet tomography studies and may also be an interesting energy loss observable themselves [115]. For fixed  $p_{T,t}$  one would expect a larger yield associated with triggers from

jet fragmentation due to the larger  $\langle Q^2 \rangle$  of the hard scattering. This effect is responsible for the larger yield associated with  $\pi^0$  triggers, as compared to direct, although, as will be discussed in section 6.8, a different flavor composition for  $\pi^0$  triggered jets could similarly result in a difference in the jet multiplicity.

The obvious signature of fragmentation photons would be a near-side correlation for direct photon triggers. As was demonstrated in figure 5.2, the near-side (inclusive) direct photon associated yields, are fairly small compared to that of  $\pi^0$ . The ratio of the yields is shown in figure 6.3. The data show no obvious  $p_T$  dependence. Since the uncertainties are fairly constant as a function of  $p_{T,a}$ , each value of  $p_{T,t}$  was fit to a constant, tabulated in 6.1. The near-side yield for direct photons is sensitive not only to the fraction of photons from fragmentation, but also to their fragmentation function, which is poorly constrained (see, for example, [64]). If one assumes that the photon fragmentation function is the same as that of the  $\pi^0$ , then the ratio of the near-side conditional yields should be approximately equal to the fraction of non-isolated photons which is predicted to be  $10 \pm 5\%$  above 7 GeV [67]. This argument is compatible with the data which favor a ratio of  $< 20\%$  above 7 GeV.

$p_{T,t}$ [GeV]	$\langle Y_{dir}/Y_\pi \rangle$	$\sigma_{STAT}$	$\sigma_{SYS}(\text{low/high})$
5-7	0.167	0.037	0.409/0.287
7-9	0.063	0.046	0.018/0.158
9-12	0.112	0.048	0.100/0.092
12-15	-0.133	0.075	0.199/0.188

Table 6.1: The ratio of the inclusive direct photon to  $\pi^0$  associated yields on the near-side for several  $p_{T,t}$  selections averaged over  $p_{T,a}$ .

On the away-side, we can attempt to extract the fragmentation photon correlations by comparing the inclusive and isolated direct associated yields. Using the NLO predictions for the fragmentation/total ( $f_{inc}^{frag}$ ) and isolated fragmentation/total ( $f_{iso}^{frag}$ ) shown in figure 1.22 [116], we can express the conditional yields as follows:

$$Y_{inc} = f_{inc}^{frag} Y_{frag} + (1 - f_{inc}^{frac}) Y_{prompt} \quad (6.1)$$

$$Y_{iso} = f_{iso}^{frag} Y_{frag} + (1 - f_{iso}^{frac}) Y_{prompt} \quad (6.2)$$

Solving these two equations simultaneously one obtains:

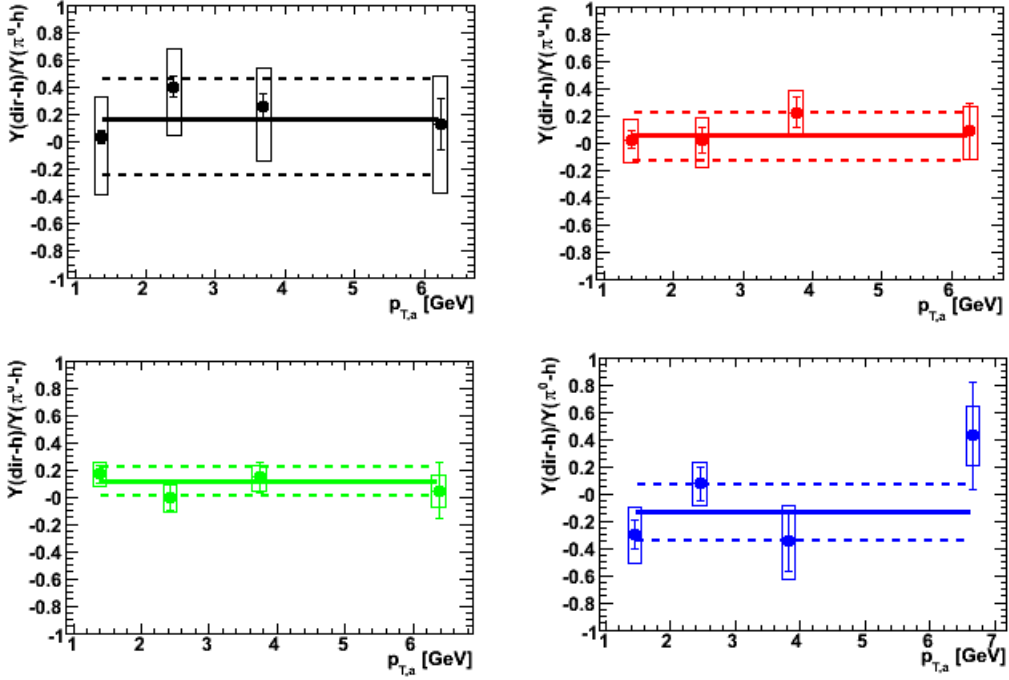


Figure 6.3: The ratio of inclusive direct photon to  $\pi^0$  associated yields on the near-side for several  $p_{T,t}$  selections as a function of  $p_{T,a}$ . The solid lines are fits to a constant value with dashed lines indicating the total error.

$$Y_{frag} = \frac{1}{1 - \frac{f_{frag}^{inc}}{1 - f_{frag}^{iso}}} Y_{inc} - \frac{1}{\frac{1 - f_{frag}^{iso}}{1 - f_{frag}^{inc}} - 1} Y_{iso} \quad (6.3)$$

Since the isolated direct photons are a subset of the inclusive sample, the statistical uncertainty of the isolated associated yields are correlated to the inclusive data and hence, are added in quadrature to the systematic errors (which are also correlated). The statistical error of the inclusive yield is separated into correlated and uncorrelated pieces as  $\sigma_{corr} = \sigma_{iso}$  and  $\sigma_{uncorr}^2 = \sigma_{inc}^2 - \sigma_{corr}^2$ , respectively.

Figure 6.4 shows the fragmentation photon associated yield, estimated by equation 6.3. Also shown are the  $\pi^0$  associated yields. Generally, the fragmentation associated yields agree well with those of  $\pi^0$ , indicating that the fragmentation process is not radically different. Conversely, one may take this to be evidence that the NLO calculations successfully describe  $\gamma + \text{jet}$  production. It should be emphasized that this measurement should not be taken too literally, since the uncertainties in the NLO calculation have not been quanti-

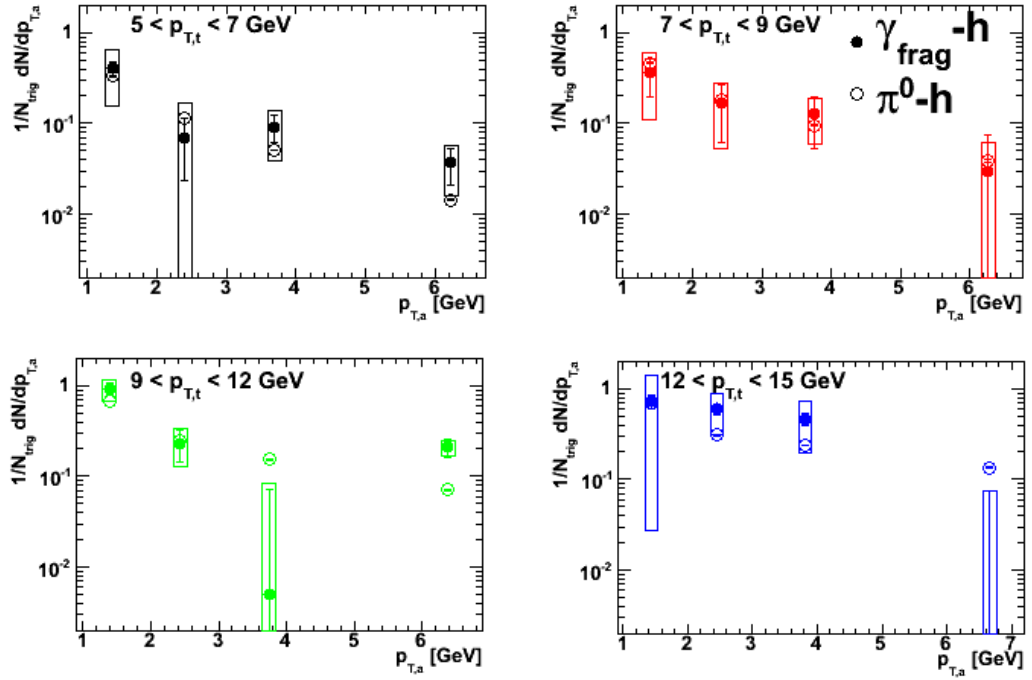


Figure 6.4: The away-side fragmentation photon associated yields obtained with the use of NLO calculations from Owens *et. al.* [116]

fied. The consistency between data and calculation is, however, encouraging. For a less model dependent approach to fragmentation photon correlations, the reader is referred to [115].

To the extent that these estimates may be accepted, photon fragmentation comprises a non-negligible background for tomographic studies. Although naively, one expects photon fragmentation to be suppressed in the same manner as for hadrons, it can be induced by the medium, as well [80]. So far, no evidence of induced radiation has been observed as an excess in direct photon [117]  $R_{AA}$  or as a near-side correlations in this analysis, although systematic uncertainties are still large, particularly in the present study. On the other hand, the expected suppression of fragmentation photons has not been conclusively observed either<sup>1</sup>.

Ultimately, the tool of choice to avoid the issue of fragmentation photons altogether, is to obtain a sample of isolated direct photons. Figure 6.5 compares

<sup>1</sup>Recent PHENIX preliminary Au + Au do hint at suppression at very high  $p_T(> 15\text{GeV})$ . The Cu+Cu data do not, however, support that trend. For details, see [79] and references, therein.

the isolated per-trigger yields to NLO predictions from [116]<sup>2</sup>. The agreement is excellent. One should note that much of the large scale uncertainties typical of NLO calculations can cancel at the level of per-trigger yields.

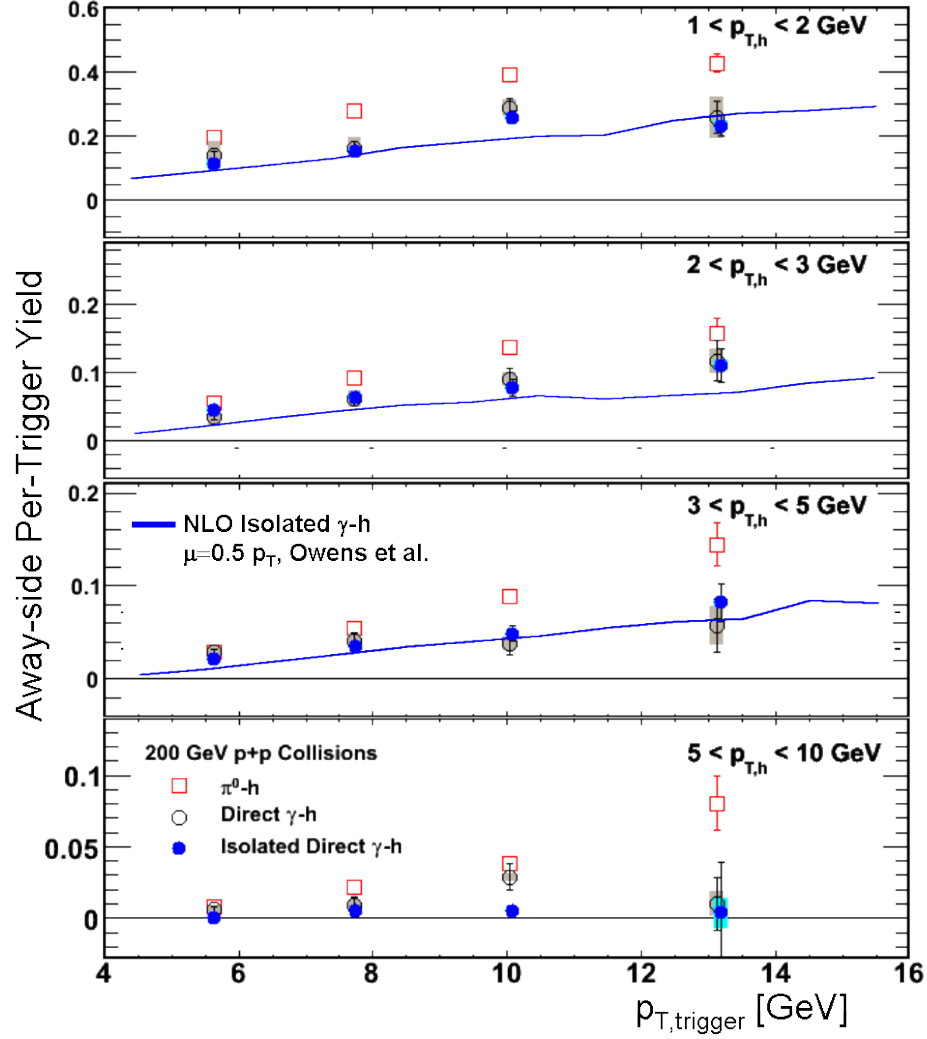


Figure 6.5: Comparison of away-side isolated direct photon associated yields to an NLO calculation [116].

---

<sup>2</sup>Note that these predictions use the KKP set of fragmentation functions, to be discussed below.

## 6.3 Leading Order Monte Carlo Event Generator

The interpretation of the two particle correlations in Au + Au relies on thorough understanding of baseline effects. Although the agreement with NLO calculations is encouraging, there are several issues we wish to further address. In order to do so, a Monte Carlo generator was composed which calculates back-to-back correlations using the Born level pQCD cross sections and with a Gaussian  $k_T$  smearing. There were several reasons to choose this approach. Firstly, there are instances in which NLO calculations are thought to be insufficient, as evidenced by their exclusion from global fit analyses (see 1.7). Following the approach of [71], we can tune the Monte Carlo calculations to match the data and contribute a new piece of evidence, one way or the other, to the debate surrounding this issue.

The second reason for choosing such an approach was a matter of practicality. We would like to compare our results against predictions using several different fragmentation functions without the relatively complex machinery of NLO calculations.

The starting point of the Monte Carlo is the general expression for the two particle cross section from a  $2 \rightarrow 2$  scattering process ( $1+2 \rightarrow 3+4$ ) assuming independent fragmentation:

$$\frac{d^5\sigma}{dx_1 dx_2 d\cos\theta^* dz_3 dz_4} = \sum_{a,b,c,d} F_a(x_1) F_b(x_2) G(\vec{k}_T) \frac{\pi\alpha^2(Q^2)}{\hat{s}} \hat{\Sigma}_{a,b}(\cos\theta^*) D_c(z_3) D_d(z_4) \quad (6.4)$$

The leading order partonic cross sections for hadron and photon production processes can be found in [118] and [119], respectively. The sum is performed over all flavor permutations, neglecting charm and other heavy quarks.

The PDFs used in this study are the CTEQ6 set [120] which was obtained from the Durham HEP database [121]. The parton distributions are taken as fixed since they are better constrained than the fragmentation functions ( $D(z)$ ) in the kinematic range of interest. Examples of the  $x$  dependence of the PDF's at a fixed value of  $Q^2 = 49\text{GeV}^2$ , determined by the interpolation, are shown in figure 6.6. The  $Q^2$  evolution of the PDF's was evaluated at NLO and is interpolated by sampling in 1 GeV intervals of  $Q$  from 1 – 50. Charm and heavier quarks are neglected.

Several sets of fragmentation functions are tested with the Monte Carlo calculation. Here I briefly describe the most salient differences between the parameterizations. The oldest of the sets considered, KKP [122], was shown

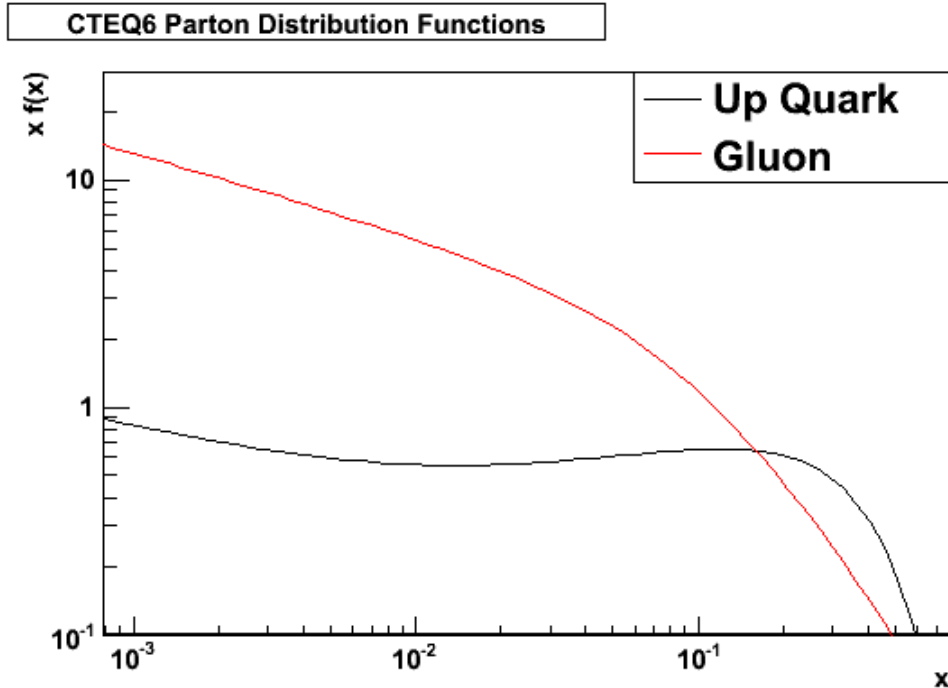


Figure 6.6: Up and Gluon CTEQ6 PDFs evaluated at  $Q^2 = 49 \text{ GeV}^2$

to describe the PHENIX  $\pi^0$  cross section reasonably well [107]. The first set by the AKK group (here denoted AKK05) [123] represents the first attempt to distinguish the contributions of the light quarks (unresolved in KKP) by using a set of data from the OPAL collaboration in which they use the valance quark composition of identified hadrons to tag the quark flavor of the jet [124]. The AKK set was shown to describe the STAR proton spectra from p+p collisions better than KKP [125]. Both of these sets are obtained exclusively by fits to  $e^+e^-$  data. The tightest constraints on the gluon fragmentation functions from these data are from 3-jet events and from scaling violations; however, the fits may be varied by a factor of 5 or more while still maintaining reasonable  $\chi^2$  values [126].

Recently, two newer sets of fragmentation functions, by the DSS [127, 128] and AKK [129] groups, have emerged which include data from DIS experiments and from RHIC to further constrain, in particular, the gluon fragmentation functions. The difference between the two sets are numerous, but perhaps most noteworthy, is that the new AKK set places more emphasis on OPAL flavor tagged data which is viewed with some skepticism by the DSS group. As an example the gluon to proton fragmentation function from each of the analyses is shown in figure 6.7. Even with the inclusion of the RHIC data a

### Gluon $\rightarrow$ Proton Fragmentation Functions

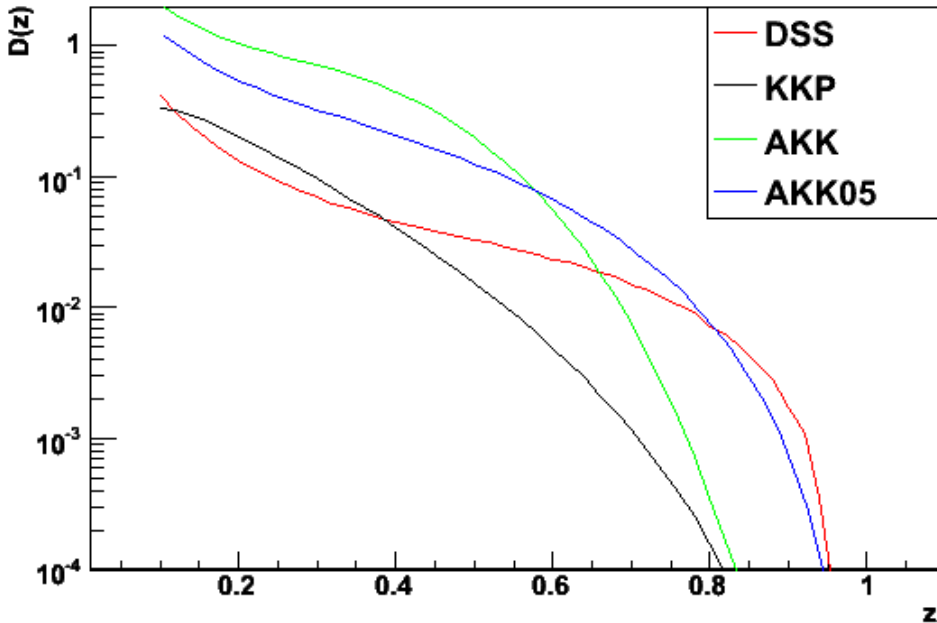


Figure 6.7: Examples of several parameterizations of gluon to proton fragmentation function evaluated at  $Q^2 = 49$  GeV $^2$ .

large uncertainty in this fragmentation function is evidenced by the spread in these results.

$G(k_T)$  is a smearing function which introduces a momentum kick in the direction transverse to the initial parton pair whose magnitude is sampled according to a Gaussian distribution. Some subtleties which arise in the Gaussian description, necessitating a cutoff procedure, are discussed in section 6.6. Although not shown in equation 6.4 there is an additional momentum broadening due to the hadronization process. To account for this,  $\vec{j}_{T,t}$  and  $\vec{j}_{T,a}$ , as shown in figure 6.8, are also smeared, with a width of  $\sigma = 585$  MeV, in accordance with previous PHENIX results [61]. The rest of the quantities in figure 6.8 are discussed below.

## 6.4 Hard Scattering Kinematics: $x_E$ and $p_{OUT}$

Due to hadronization we cannot measure the parton kinematics directly<sup>3</sup>. As a result, we can measure neither the fragmentation function nor the magnitude

---

<sup>3</sup>Although, one may argue that the photon effectively plays the role of a parton.

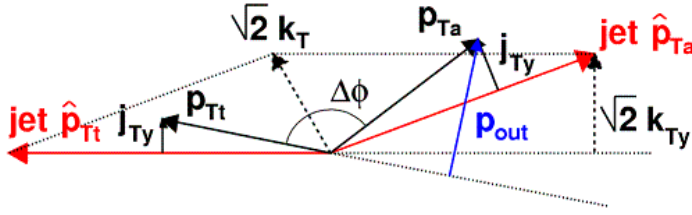


Figure 6.8: A diagram showing the kinematics underlying the measurement of jet correlations between back-to-back particles [61].

of  $k_T$  directly. In a sense, these two are orthogonal quantities, one being a measurement of the dynamics longitudinal to the parton pair and the other transverse<sup>4</sup>. Hence, it is important to choose a set of hadronic observables that maximizes sensitivity.

Figure 6.8 diagrams the kinematics underlying the correlation of back-to-back particles hadronizing from a di-jet. The transverse momentum of the parton pair is related to  $\vec{k}_T$  by  $\vec{p}_{T,pair} = \sqrt{2}\vec{k}_T$ . The vector  $\vec{p}_{OUT}$  measures the same out-of-plane momentum, but uses the axis of the trigger particle, instead of the parton, as a reference. The fragmentation variable  $z$  is also approximated by substituting the parton axis with that of the leading hadron.

The quantity  $x_E$ ,

$$x_E = -\frac{\vec{p}_{T,t} \cdot \vec{p}_{T,a}}{|\vec{p}_{T,t}|^2} \quad (6.5)$$

is obtained by taking the projection of the associated particle onto the trigger axis in the azimuthal plane. It measures the  $p_T$  balance between the pair.

$\vec{p}_{OUT}$  has its origin in the parton pair imbalance, which is described by the  $k_T$  effect, as well as the finite transverse jet widths which arise in the course of the non-perturbative parton hadronization process. The latter effect is typically of smaller magnitude, i.e., ( $\langle |k_T| \rangle > \langle |j_T| \rangle$ ).

It is important to note, however, that the using hadronic observables introduces a mixing between longitudinal and transverse effects. This is clearly evident in the relation between  $p_{OUT}$  and  $k_T$  as given in [61] (equation 6.6). Here,  $x_E$  appears as a scale factor from the partonic observable,  $k_T$  to the hadronic observable,  $p_{OUT}$ .

---

<sup>4</sup>Actually, in the rest frame of the final state parton pair, the  $k_T$  effect has both a transverse and a longitudinal component. Since it is solely responsible for the transverse momentum of the parton pair it can be measured more easily in the transverse direction.

$$\langle |p_{OUT}| \rangle^2 = x_E^2 [2\langle |k_{Ty}| \rangle^2 + \langle |j_{Ty}| \rangle^2] + \langle |j_{Ty}| \rangle^2 \quad (6.6)$$

Similarly, the true fragmentation variable  $z$  does not depend

Before discussing the distributions of these quantities in data, a comment about notation is in order. Often, instead of  $x_E$ , the quantity  $z_T (\equiv p_{T,a}/p_{T,t})$  is tabulated, as in the previous chapter. At some point this quantity was actually defined to be equivalent to  $x_E$ , but, somewhere along the line, it came to change meanings (for an example of the old usage, see: [119]). This quantity has the advantage that one doesn't need to know the azimuthal angle between the particles, but at the same token, one would expect reduced sensitivity to the fragmentation function. It turns out not to make much of a difference, however, for our purposes. Figure 6.9 compares the  $x_E$  and  $z_T$  distributions for one  $\pi^0 - h$  bin.

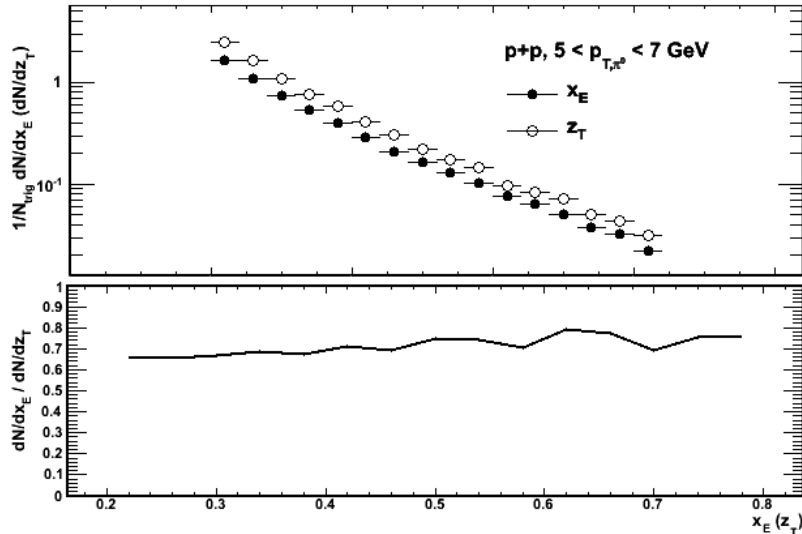


Figure 6.9: Comparison of  $\pi^0$   $x_E$  and  $z_T$  distributions (top) and their ratio (bottom) for  $5 < p_{T,t} < 7$  GeV.

Figure 6.10 shows the  $x_E$  distributions for fixed ranges of  $p_{T,t}$  for  $\pi^0$  and isolated direct photon triggers. The  $p_{T,a}$  range covered is 1-5 GeV. The data have been fit with the exponential function  $dN/dx_E \propto \exp(-bx_E)$  where  $b$  will be referred to as the negative slope parameter. Exponentials describe fragmentation functions well at least over a limited range. At large  $z$ , exponential fits

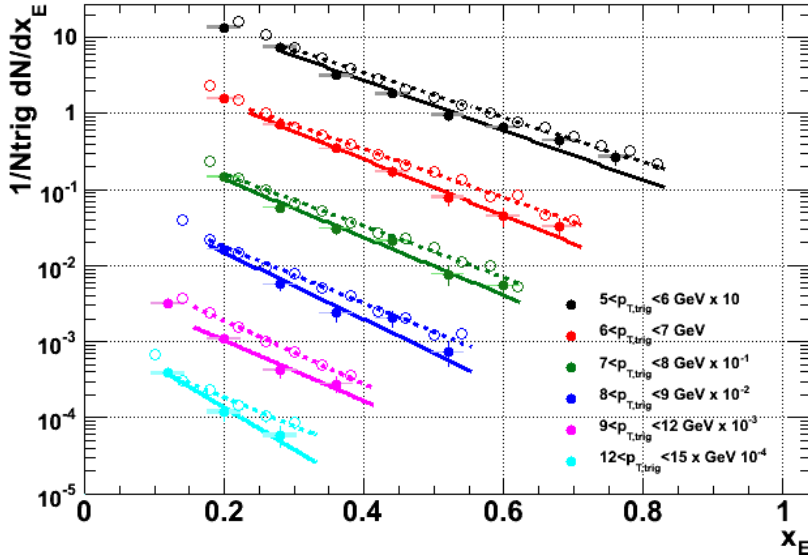


Figure 6.10:  $x_E$  distributions for  $\pi^0$  triggers (open) and isolated direct photon triggers (solid) with exponential fits.

naturally break down because of the kinematic limit <sup>5</sup>. This is a moot point, however, since we do not directly measure fragmentation functions. Figure 6.11 shows  $x_E$  distributions for  $\pi^0$  triggers using the KKP fragmentation functions. Evidently, the exponential fits describe the Monte Carlo calculation reasonably well.

The E706 experiment has demonstrated that  $\pi^0\pi^0$ ,  $\pi^0\gamma$  and  $\gamma\gamma$  pairs have  $p_{OUT}$  distributions which are well described by a Gaussian fit [131, 132]. They are able to reproduce the shapes of the distributions using LO order calculations with a Gaussian  $k_T$  smearing or, in the latter case, using a fully resummed calculation. The  $p_{OUT}$  distributions for  $\pi^0$  and isolated direct photons are shown in figure 6.12. Gaussian fits are also shown and are listed in tables 6.2 and 6.3. The  $\pi^0$  triggered data are well described by a Gaussian shape at small  $p_{OUT}$  but deviate from that form at large  $p_{OUT}$ . This effect was observed in previous PHENIX preliminary  $\pi^0 - h$  results [133] and is thought to correspond to the emission of a single hard gluon. It's interesting to ask whether there is a similar effect in the isolated photon triggers, but it's difficult to tell on the log scale. Figure 6.13 shows a comparison of the data to the fit for the two lowest  $p_{T,t}$  bins, where the tail is visible for the  $\pi^0$  triggers. The photon triggers exhibit a rise, although not very significant, followed by dip.

---

<sup>5</sup>see Michael Tannenbaum's discussion of this in [130]

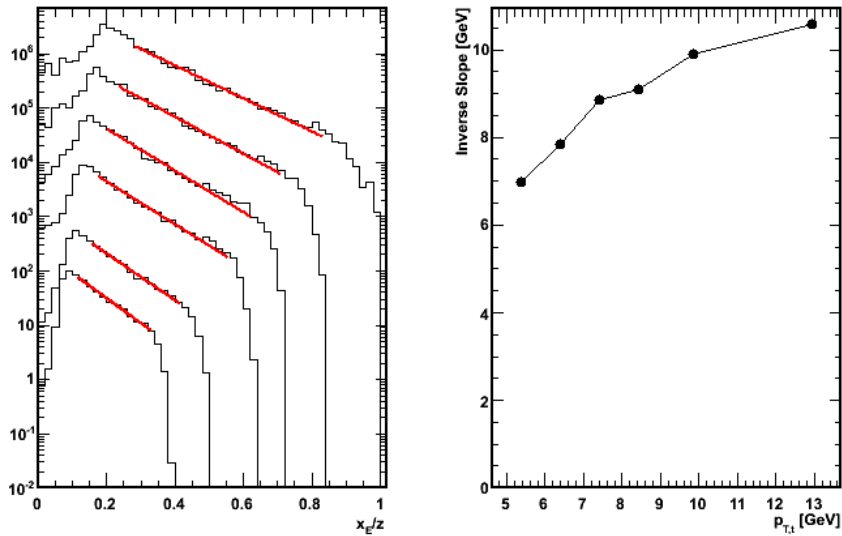


Figure 6.11: Example of isolated direct photon  $x_E$  distributions from Monte Carlo using the KKP fragmentation functions (left) and the slope parameter of exponential fits (right). They date are reasonably well-described by exponential fits.

$p_{T,t}$ [GeV]	Width	Error	$\chi^2/DOF$
5-6	0.900	0.004	18.5
6-7	0.862	0.006	5.7
7-8	0.842	0.010	3.4
8-9	0.804	0.012	4.2
9-12	0.781	0.013	3.5
12-15	0.712	0.027	1.0

Table 6.2: Widths ( $\sigma$ ) of Gaussian fits to  $p_{OUT}$  distributions for  $\pi^0$  triggers.

This is presumably the kinematic limit. If these are prompt photons, then momentum conservation would not allow out-of-plane momenta comparable to  $p_{T,t}$ .

## 6.5 Cross Checks on the Monte Carlo

As the Monte Carlo is tuned to the conditional yields, a useful cross check on the  $k_T$  smearing procedure, and on the Monte Carlo calculations in general, is

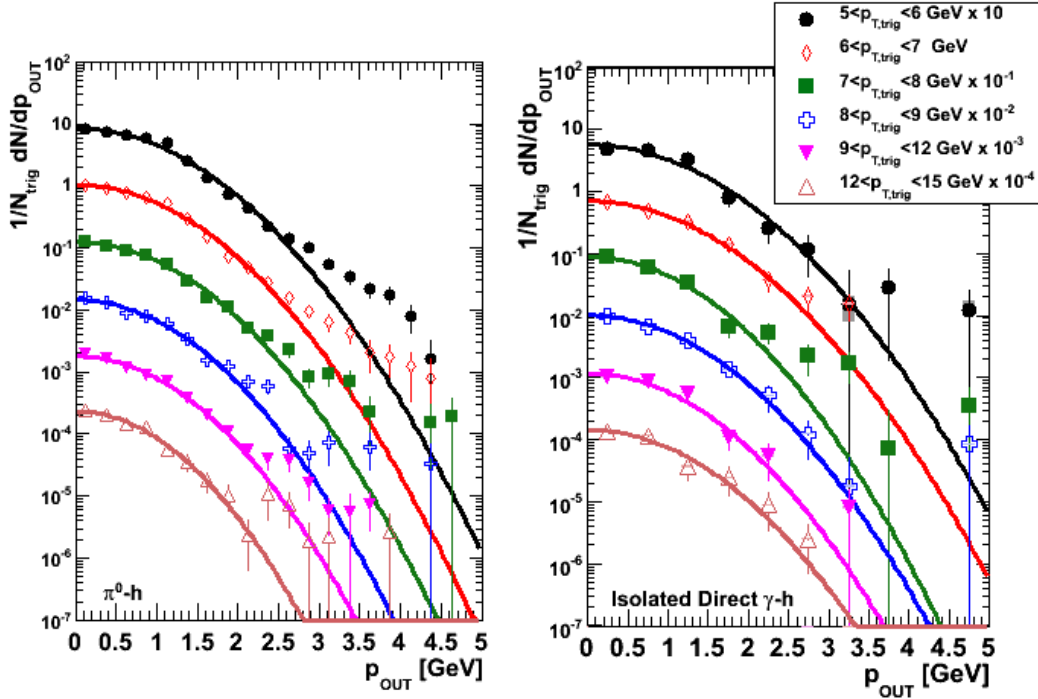


Figure 6.12:  $p_{OUT}$  distributions for  $\pi^0$  triggers (left) and isolated direct photon triggers (right) for  $1 < p_{T,a} < 5$  GeV.

$p_{T,t}$ [GeV]	Width	Error	$\chi^2/DOF$
5-6	0.953	0.095	1.6
6-7	0.941	0.030	3.0
7-8	0.839	0.038	1.9
8-9	0.886	0.034	1.0
9-12	0.851	0.035	1.9
12-15	0.872	0.062	1.0

Table 6.3: Widths ( $\sigma$ ) of Gaussian fits to  $p_{OUT}$  distributions for isolated direct triggers.

to compare the inclusive (unconditional) spectra. The  $\pi^0$  and isolated direct photon spectra are shown in figure 6.14 with and without  $k_T$  smearing (the former using the AKK fragmentation functions). Without  $k_T$  smearing the spectra are slightly harder than the data which are well described by a power law ( $dN/dp_T \sim p_T^{-n}$ ) with  $n \sim 5.5$  for direct photons and  $n \sim 7.1$  for  $\pi^0$ 's [67, 107]. The power of fits is indicated in the legend. With the addition of  $k_T$  smearing the calculations become steeper, but overshoot the data by a

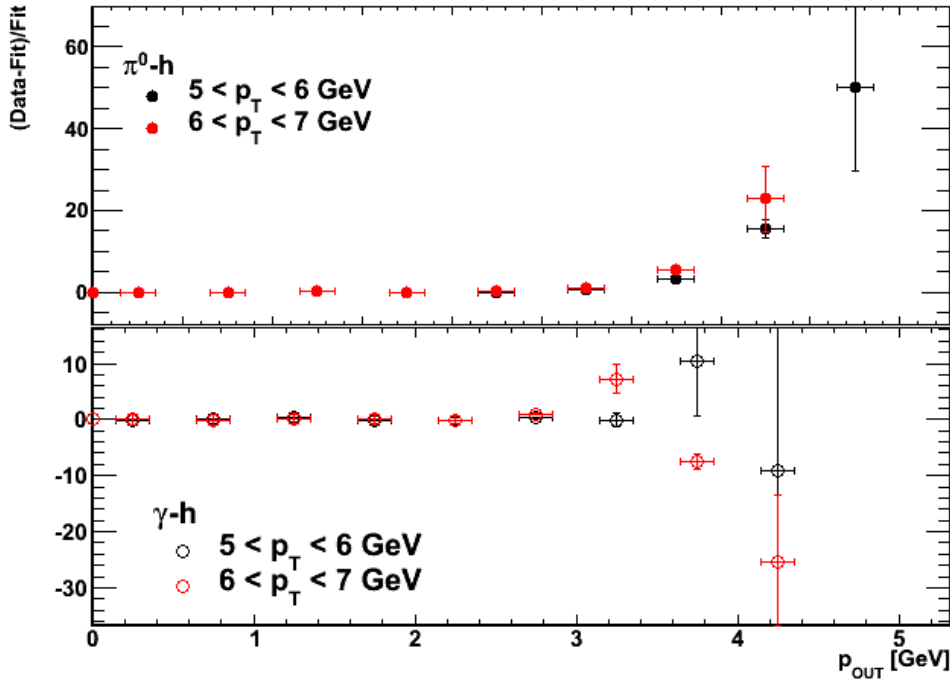


Figure 6.13: Comparison of the Gaussian fits to  $p_{OUT}$  to the data for the  $5 < p_{T,t} < 6$  and  $6 < p_{T,t} < 7$  GeV bins for  $\pi^0$  (top) and isolated direct photons (bottom).

little bit. In general, however, the shapes of the spectra in Monte Carlo are very close to the measured ones.

Another useful exercise is to compare the distribution of processes which are triggered on for a given  $\pi^0 p_T$ <sup>6</sup>. Figure 6.15 shows the process breakdown for the AKK set of fragmentation functions. One finds that gluon scattering dominates at low  $p_T$  whereas quark scattering dominates at high  $p_T$ . The relative contributions are similar to those observed by an older set of fragmentation functions from Kretzer [134].

The number of processes contributing to direct photon production at LO is substantially fewer than for  $\pi^0$  production. The Compton process ( $q+g \rightarrow q+\gamma$ ), for which there is an  $s$  and a  $u$  channel contribution (the latter giving rise to the signature backward peak), is found to dominate at the level of 85-90% of the total cross section in the  $p_T$  range considered (5-20 GeV). The remainder of the cross section is composed of photons produced in the

---

<sup>6</sup>This is fairly trivial for the direct photons since there are only two processes to keep track of.

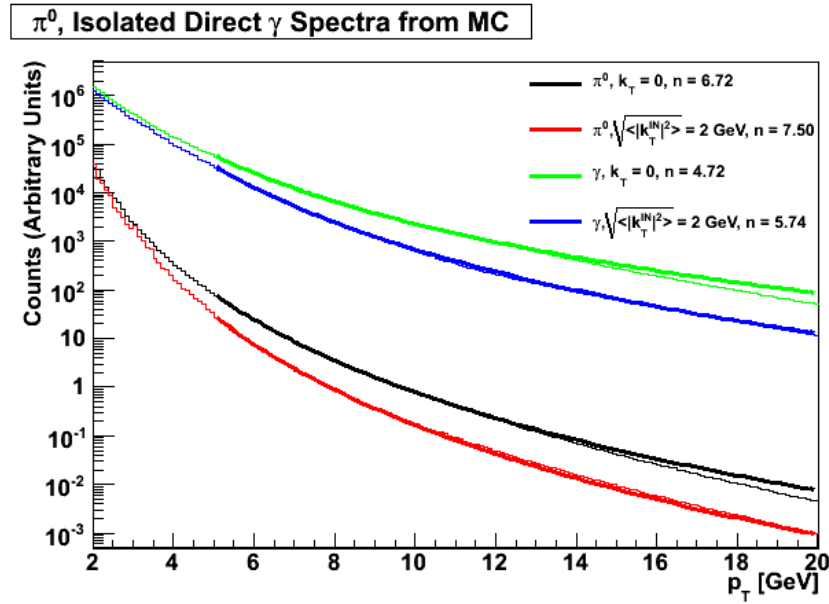


Figure 6.14: Inclusive  $\pi^0$  and isolated direct photon spectra from Monte Carlo with and without  $k_T$  smearing including power law fits.

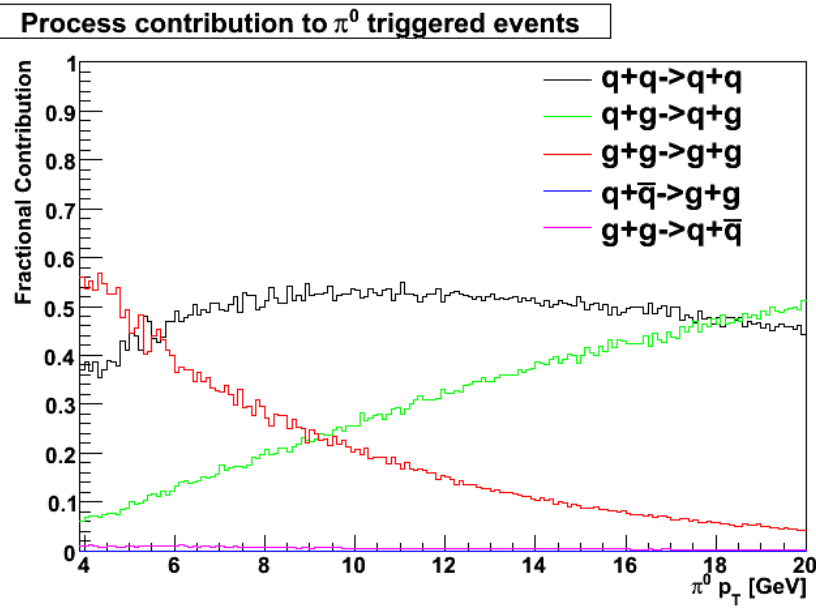


Figure 6.15: The fractional contribution of the different  $2 \rightarrow 2$  processes to the  $\pi^0$  cross-section as determined by Monte Carlo calculation using the AKK fragmentation functions

annihilation process ( $q + \bar{q} \rightarrow g + \gamma$ ). Since the opposing parton for Compton scattered photons is a quark, direct photons should act as a fairly high purity quark tag in  $p + p$  collisions. As was shown in figure 6.15, the converse is true for  $\pi^0$ 's; they act as gluon jet tags for intermediate values of  $p_T$ .

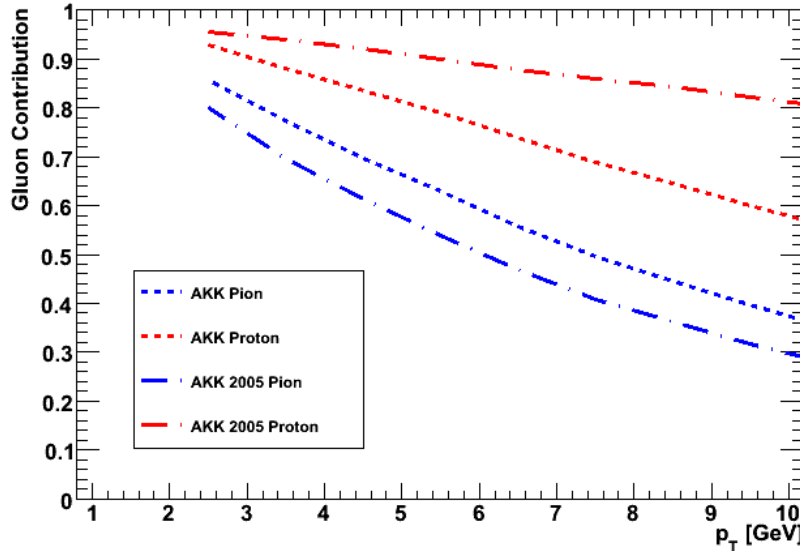


Figure 6.16: The gluon contribution to protons and pions for the AKK05 and AKK08 fragmentation functions as calculated in this Monte Carlo.

A comparison to figure 1.9, which plots the gluon fraction for the AKK(05) set, is interesting for two reasons. Firstly, it allows to test the this leading order Monte Carlo against a next to leading order calculation. Secondly, it allows to check whether the somewhat surprising result from that AKK05 that shows that nearly all protons are from gluon jets can be checked. The LO and NLO calculations agree extremely well suggesting that the particle ratios are not too sensitive to NLO effects. The new set of AKK fragmentations functions indicate a much smaller favoring of the gluon to proton fragmentation function than previously observed. This supports the observations that this fragmentation function is poorly constrained and shows that single proton and pion spectra are not as reliable of a flavor tagging device as previously suggested.

It is evident from this discussion that additional providing additional observables to the global fit analyses could help to better constrain the fragmentation functions. We take this opportunity to point out the fact that two particle correlations probe a region of  $z$  not accessible with single particle ob-

servables in  $p + p$  collisions. We will return to this subject below. First, we discuss the tuning of the Monte Carlo to match the out-of-plane momentum.

## 6.6 Measuring the $k_T$ Effect

The implementation of  $k_T$  smearing into the Monte Carlo calculation is not without subtleties. The LO cross sections are divergent in the forward and/or backward directions and the gluon distribution function becomes very large at low  $x$ . In the absence of  $k_T$  smearing these effects are irrelevant for production at mid-rapidity. However, for a Gaussian distributed  $k_T$  of fixed width one finds that there is a finite probability for a parton to be scattered at large angle, solely by virtue of receiving a large momentum kick from sampling the tail of the  $k_T$  distribution. Due to the largeness of the low  $x$  gluon distribution and the cross sections at small angle these soft partons dominate the cross section. This is clearly an unphysical consequence of the  $k_T$  smearing procedure. The  $k_T$  kick is intended to simulate gluon emission which should clearly be bounded by the momentum of the parton from which it radiates. In order to enforce this requirement we simply truncate the  $k_T$  distribution at the momentum of the parton. This has the consequence that  $k_T$  distribution sampled is not actually a Gaussian. The calculated  $p_{OUT}$  distributions, however, turn out not to be very sensitive to this cutoff.

Another subtlety that then must be considered is that, with a finite cutoff, the input  $k_T$  distribution, is not exactly Gaussian. In practice, this is true, however, even without a cutoff since the requirement of a high  $p_T$  trigger particle preferentially selects  $k_T$  vectors of the same orientation. This implies that  $\sqrt{k_T^2}$  is not necessarily a constant, although it was observed to be constant for  $\pi^0$  triggers in [61]. In order to discriminate between the input and observed values we denote the input value by  $k_T^{IN}$ .

The  $\langle |p_{OUT}|^2 \rangle$  for  $\pi^0$  and isolated direct photon triggers is shown in figures 6.18 and 6.17. The data are compared to Monte Carlo calculations using several values  $\sqrt{\langle |k_T^{IN}|^2 \rangle}$ . The dependence of  $\langle |p_{OUT}|^2 \rangle$  on  $p_{T,t}$  is well described by the Monte Carlo. The value of  $\langle |p_{OUT}|^2 \rangle$  depends somewhat on the choice of fragmentation function as shown by the difference between the AKK and DSS sets. We proceed by finding the optimal value of  $\sqrt{\langle |k_T^{IN}|^2 \rangle}$  for each choice of fragmentation function and using the spread in the calculations as a measure of the systematic uncertainty.

Figure 6.19 shows the  $\chi^2$  per degree of freedom between the data and model calculations of  $\langle |p_{OUT}|^2 \rangle$  as function of  $\sqrt{\langle |k_T^{IN}|^2 \rangle}$  for  $\pi^0$  triggers. The best value of  $\langle |p_{OUT}|^2 \rangle$  varies depending on the choice of fragmentation function within a range of  $2.2 < \sqrt{\langle |k_T^{IN}|^2 \rangle} < 2.6$  GeV. The  $\chi^2$  per degree of freedom

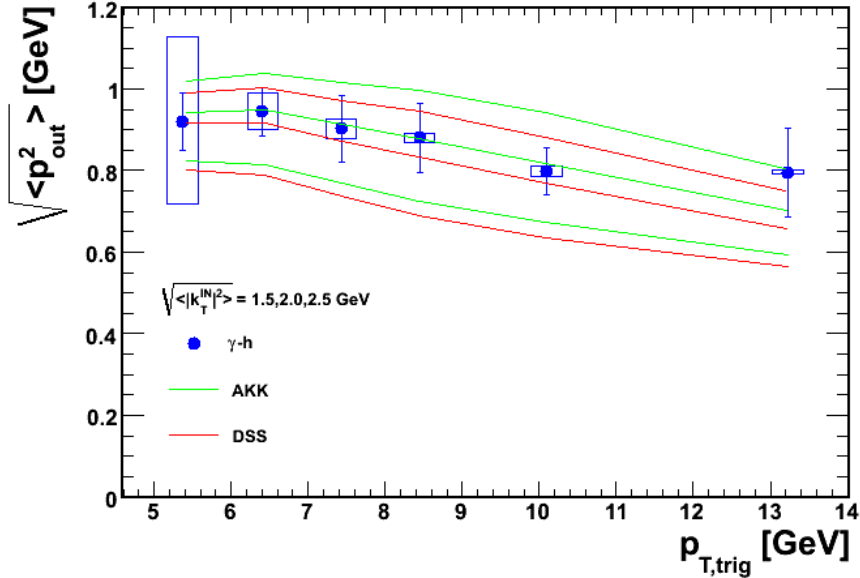


Figure 6.17:  $\langle|p_{\text{out}}|^2\rangle$  as a function of  $p_{T,t}$  for isolated direct photon triggers compared to calculations using the DSS (red) and AKK (green) sets of fragmentation functions. The curves correspond to  $\sqrt{\langle|k_T^{IN}|^2\rangle} = 1.5, 2.0, 2.5 \text{ GeV}$  from bottom to top.

curves for direct photon triggers are shown in 6.20. Value in the range of  $2.0 < \sqrt{\langle|k_T^{IN}|^2\rangle} < 2.2$  fit the direct photon data best. The closer agreement amongst the predictions for direct photons reflects our better knowledge of the quark fragmentation functions as compared to those of the gluon.

Once the best value of  $\sqrt{\langle|k_T^{IN}|^2\rangle}$  has been determined for each set of fragmentation functions the corresponding values of  $\sqrt{\langle|k_T|^2\rangle}$  can then be obtained from the Monte Carlo calculation. Figure 6.21 shows  $\sqrt{\langle|k_T|^2\rangle}$  as a function of  $p_{T,t}$  averaged over the set of values given by the different fragmentation functions. The systematic error bands are given by the maximal extent of this set. The boundary of the band is set by the AKK and KKP sets. The data are compared to the Run 3 results from [61]. In that analysis the fragmentation functions were taken to have the form  $D(z) \propto e^{-8z}$  and  $D(z) \propto e^{-11.1z}$  for quarks and gluons, respectively. The dominant source of uncertainty was assumed to come from the unknown ratio of quark to gluon jets in the  $\pi^0$  triggered sample. The uncertainty band was determined by evaluating  $\sqrt{k_T^2}$  under the extremal assumptions of all quark fragmentation and all gluon fragmentation. No uncertainty was assigned to the fragmentation functions themselves. The present analysis agrees with Run 3 results within

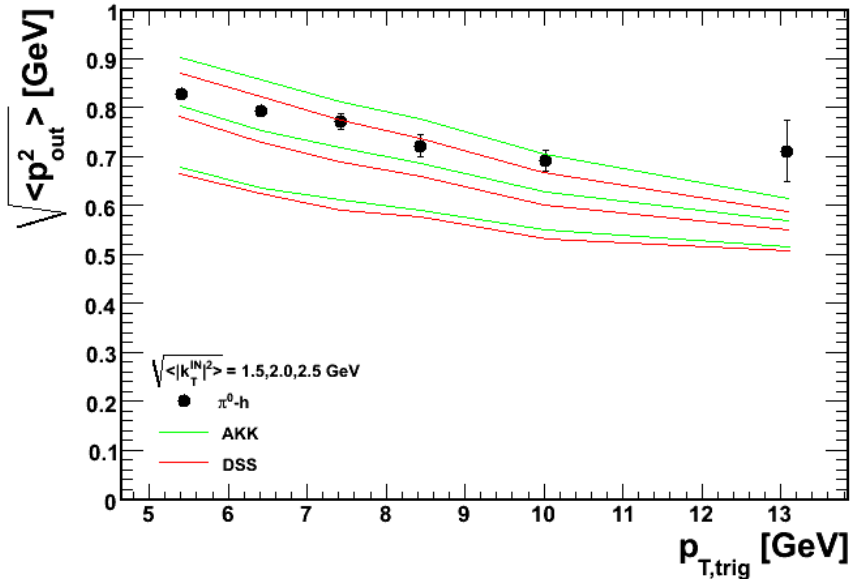


Figure 6.18:  $\langle|p_{out}^2|\rangle$  as a function of  $p_{T,t}$  for  $\pi^0$  triggers compared to calculations using the DSS (red) and AKK (green) sets of fragmentation functions. The curves correspond of  $\sqrt{\langle|k_T^{IN}|^2\rangle} = 1.5, 2.0, 2.5$  GeV from bottom to top.

systematic uncertainties and helps to reduce them. The value of  $\sqrt{\langle|k_T|^2\rangle}$  does not show any dependence on  $p_{T,t}$ .

Figure 6.22 compares  $\sqrt{\langle|k_T|^2\rangle}$  for  $\pi^0$  and isolated direct photon triggers. The systematic uncertainties on the photon triggered sample are smaller due the better agreement of the individual input fragmentation functions. Compared to the  $\pi^0$  sample, the photon triggered data show a significantly smaller value of  $\sqrt{\langle|k_T|^2\rangle}$  at small  $p_{T,t}$ , but then converge to a common value in the highest  $p_{T,t}$  bin. In contrast to the case of  $\pi^0$  triggers, direct photons do show a clear dependence on  $p_{T,t}$ .

## 6.7 Sensitivity of $x_E$ Distributions to the Fragmentation Functions

Now that we found the value of  $\sqrt{\langle|k_T|^2\rangle}$  that best matches the data for each of the sets of fragmentation functions and trigger species, we will use the smearing of that magnitude and compare to other observables. The  $x_E$  distributions for isolated direct photons are shown in figure 6.23. The Monte Carlo is able to

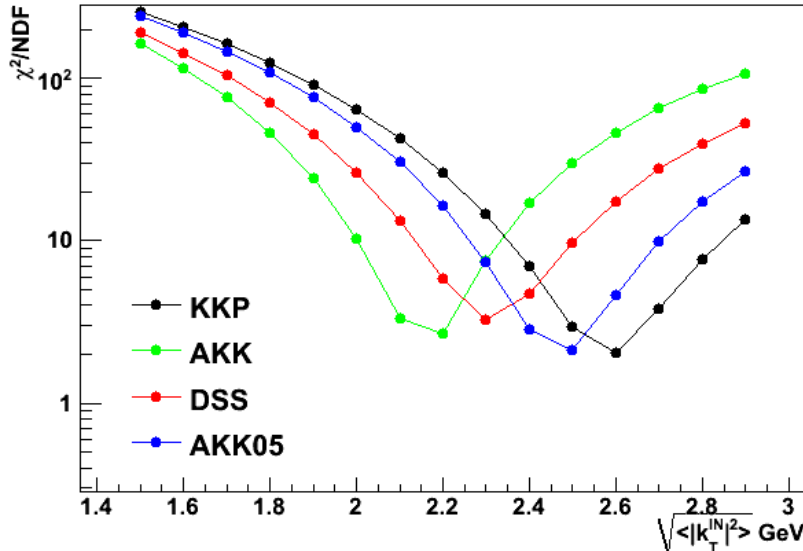


Figure 6.19: The  $\chi^2$  per degree of freedom between  $\langle |p_{\text{OUT}}|^2 \rangle$  as measured in the data and Monte Carlo calculations of the same quantity as function of the input parameter  $\sqrt{\langle |k_T^{\text{IN}}|^2 \rangle}$  for  $\pi^0$  triggers

describe the data well for each of the sets of fragmentation functions. This is perhaps not surprising since photon triggered jets are expected to be quark jets which are well constrained by the LEP data.

In order to test the sensitivity of the data to the choice of fragmentation function, a toy model with a flavor independent exponential fragmentation function was employed. The slope of the exponential was varied to roughly match fits to the LEP data which give a slope of about  $b = 8$  and  $b = 11$  for quark and gluon jets, respectively [61]. The harder slope of  $b = 8$  does indeed match the data well and is within the spread of the different fragmentation function sets. The steeper slope of  $b = 11$  results in correspondingly steeper slopes in the  $x_E$  distributions and is clearly not consistent with the data. This indicates that the  $x_E$  distribution for isolated direct photons is indeed sensitive to the shape of the underlying fragmentation function. The KKP set of fragmentation functions was applied to a set of events which include only the annihilation processes in which the opposing jet is a gluon jet. A steeper slope was again observed, although not quite as steep as the  $b = 11$  ansatz. The KKP functions were also run with  $k_T$  turned off. Poorer agreement with the data was obtained demonstrating the importance of including these effects.

The slopes of the  $\pi^0$   $x_E$  distributions are somewhat more difficult to inter-

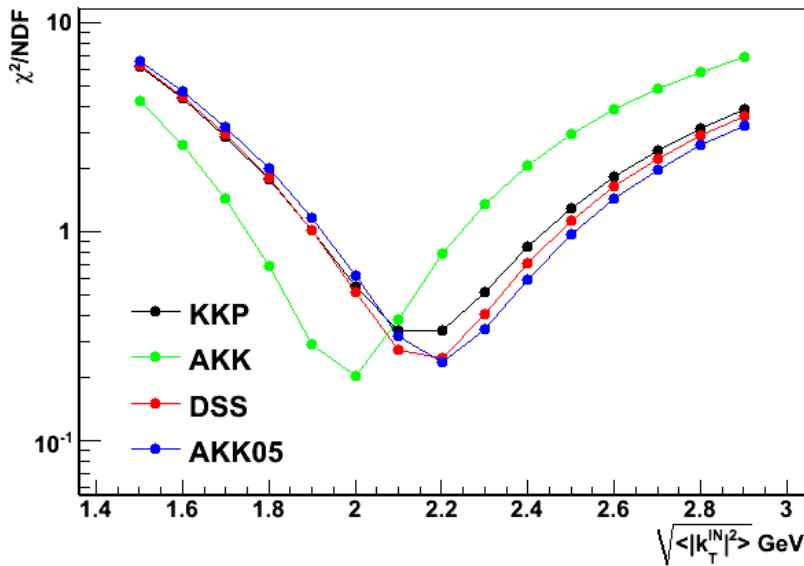


Figure 6.20: The  $\chi^2$  per degree of freedom between  $\langle |p_{\text{OUT}}|^2 \rangle$  as measured in the data and Monte Carlo calculations of the same quantity as function of the input parameter  $\sqrt{\langle |k_T^{\text{IN}}|^2 \rangle}$  for direct photon triggers.

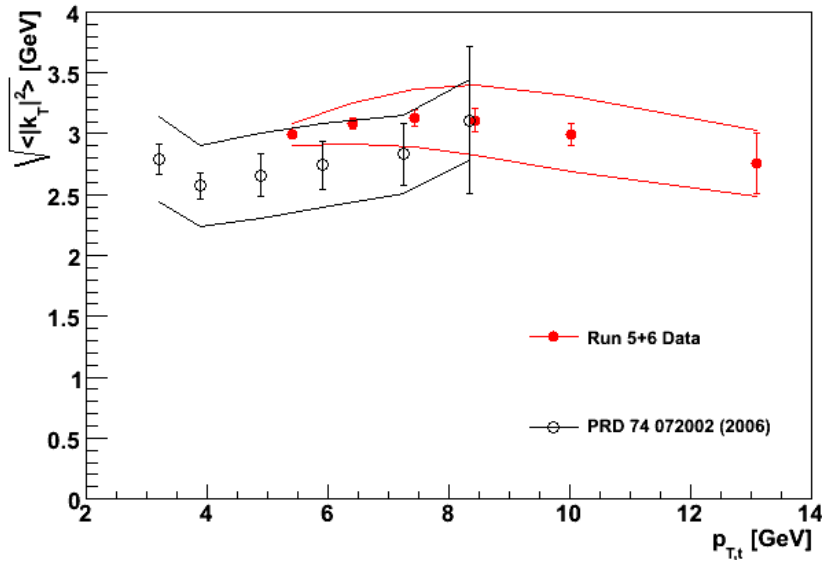


Figure 6.21:  $\sqrt{\langle |k_T|^2 \rangle}$  for  $\pi^0$  triggers from the Run 5+6 data (closed symbols) and from the previous Run 3 results (open symbols) as a function of  $p_{T,t}$ .

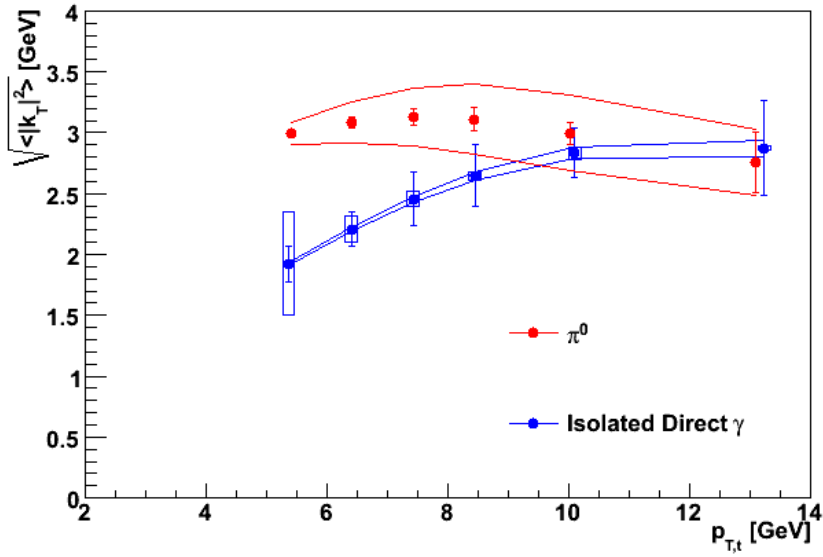


Figure 6.22:  $\sqrt{\langle |k_T|^2 \rangle}$  for isolated direct photon triggers (blue) and  $\pi^0$  triggers (red) as a function of  $p_{T,t}$ .

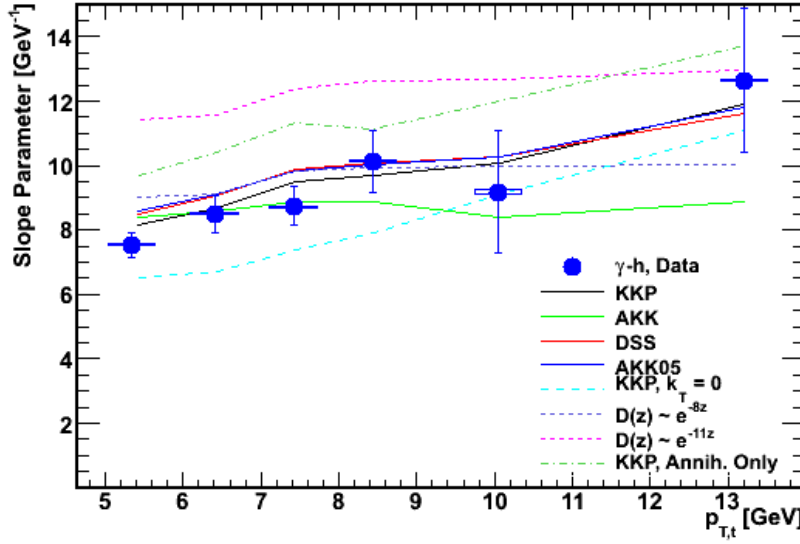


Figure 6.23: Slope parameters for exponential fits to the  $x_E$  distributions for the isolated direct photon triggers shown in figure 6.10. The data are compared to several different model calculations as described in the text.

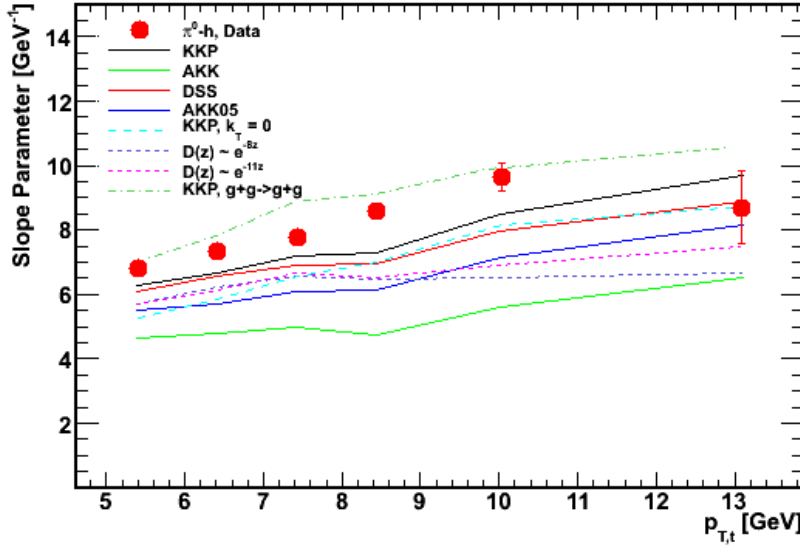


Figure 6.24: Slope parameters for exponential fits to the  $x_E$  distributions for  $\pi^0$  triggers shown in figure 6.10. The data are compared to several different model calculations as described in the text.

prett than the photon triggered results. The Monte Carlo calculation is highly dependent on the choice of fragmentation functions. The KKP and DSS sets come closest to describing the data, but they are not quite steep enough. Admittedly, the uncertainties in the isolated photon data would probably mask such a discrepancy. The difference between the fragmentation functions of slope  $b = 8$  and  $b = 11$  results in little change to the  $x_E$  distribution. As was already pointed out in [61], the shape of the  $x_E$  distribution is controlled, not by the shape of the fragmentation function, but rather by the shape of the parton spectrum. An interesting corollary to this observation though, is that one may change the shape of the  $x_E$  distributions by changing the relative shape of the quark and gluon fragmentation functions. It is shown that by selecting only gluon scattering events one may actually obtain an  $x_E$  distribution that is steeper than the data. This can be understood directly from the expression for the cross section (equation 6.4). The fragmentation functions are linked to the parton distribution functions by the partonic cross section. A change to the relative contribution of quarks to gluons in the fragmentation function changes the mixture of relevant scattering processes. Each of the scattering process has a different spectrum of final-state partons, as determined by shape of the particular parton distribution functions which contribute to that diagram.

While a mis-estimation of the fragmentation functions would indeed affect

the  $x_E$  distribution, other features lacking in this simple description could also be responsible. For example, it seems plausible that by independently changing the level of  $k_T$  smearing from quarks and gluons, which is physically reasonable, one might achieve a similar effect. It turns out however, that a variation of the  $\sqrt{\langle |k_T^{\text{IN}}|^2 \rangle}$  of one flavor while simultaneously decreasing the other by a factor of two did not significantly change the results. Another possibility is that a LO description of  $\pi^0 - h$  correlations is simply not adequate to describe the  $x_E$  distribution. It may well be, for example, that  $2 \rightarrow 3$  scattering plays an important role. In this context this straw man model would be considered a success if it motivates a proper NLO calculation of these two particle correlations which can falsify it.

## 6.8 Jet Multiplicity

To this point we have concerned ourselves mainly with the shape of the conditional yields, but not with their magnitudes. Since quark and gluon jets are known to have different multiplicities, this can also be a useful touchstone [135]. Figure 6.25 shows the ratio of isolated direct photon associated yield to that of the  $\pi^0$ . The largest disparity amongst the models occurs in the lowest  $p_{T,t}$ . It is probably not a coincidence the contribution from gluon jets is expected to be largest there. At intermediate  $p_{T,t}$ , the models all do an excellent job of describing the data. In the largest  $p_{T,t}$  bin, 12-15 GeV, the models agree with each other but overshoot the data. The data vary less across the full  $p_{T,t}$  range than do the model calculations. This may suggest fractional contribution from the different sub-processes is changes more slowly than as calculated.

The fragmentation functions parameterizations do a fairly good job of reproducing the data in the 7-9 and 9-12 GeV bins but less so in the 5-7 and 12-15 GeV bins. Given the large spread amongst the predictions in the 5-7 GeV bin the fact that the data is not well described by any of the calculations is perhaps not surprising. The disagreement between data and calculation in the 12-15 GeV is more striking since the fragmentation function dependence appear to be much smaller. The cause of this effect is not known..

## 6.9 Charge Asymmetry

As discussed in section 1.5.1, dominance of Compton scattering in the direct photon cross section implies that the flavor distribution of valence quarks in the proton should be reflected in the away-side parton. In the limit of  $z \rightarrow 1$  the number of up as compared to down valence quarks combined with their

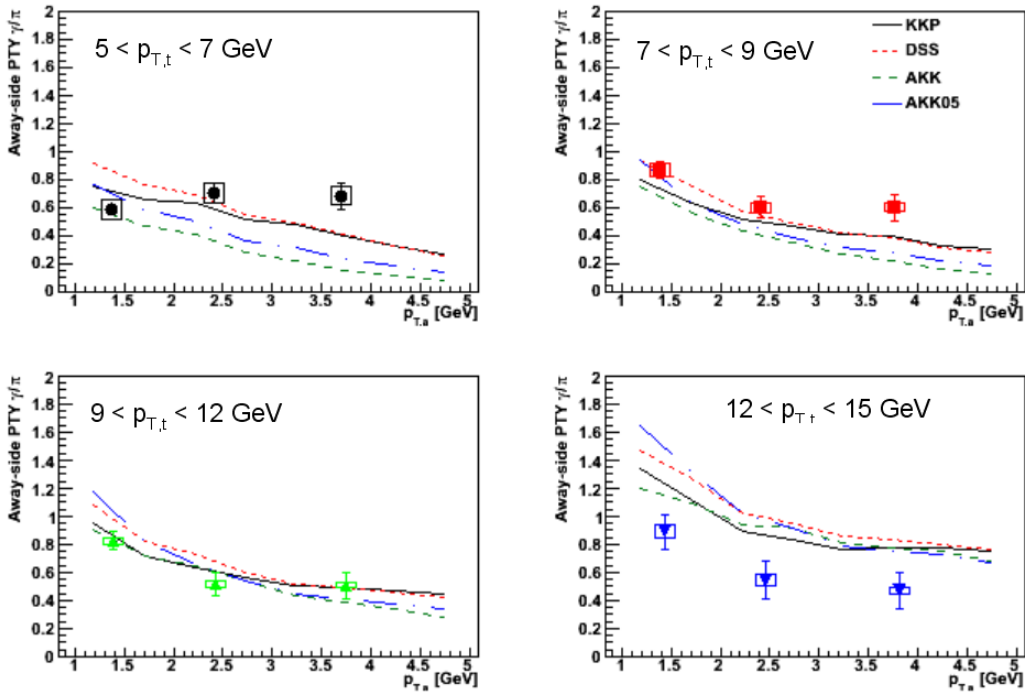


Figure 6.25: as a function of  $p_{T,a}$  for several selections of  $p_{T,t}$  compared to model predictions using several different fragmentation functions.

larger electric charge predicts an asymmetry of 8 : 1 in the number of up as compared to down jets opposite a direct photon at LO. Although one expects a dilution of this factor in the course of the parton shower process, a residual charge asymmetry should be apparent in the final state hadrons. Figure 6.26 shows the ratio of positively to negatively charge hadrons ( $R_{\pm}$ ) on the away-side of both  $\pi^0$ 's and isolated direct photons as a function of  $p_{T,a}$ . Several  $p_{T,t}$  selections are shown along with the corresponding Monte Carlo calculations using the DSS fragmentation functions. For a given  $p_T$  selection the statistics do not permit a strong statement about the charge asymmetry, however, when all the data is considered an excess of positive charge is evident in the direct photon triggered yields. The  $\pi^0$  triggered data, which is dominated by gluon production, shows an  $R_{\pm}$  close to unity for nearly all of the data points. These observations are qualitatively consistent with the ISR data shown in section 1.5.1 and provide further evidence of the efficacy of direct photons as a quark jet tag.

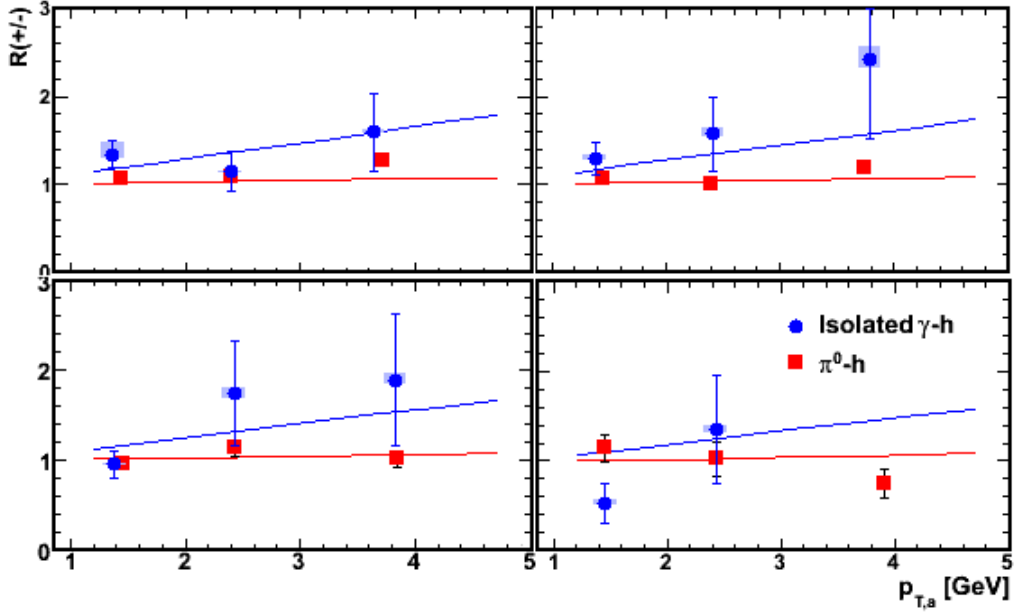


Figure 6.26:  $R(+/-)$  for isolated direct photons (blue) and  $\pi^0$  (red) triggers as a function of  $p_{T,a}$  for several selections of  $p_{T,t}$ . The lines are calculated using the DSS fragmentation functions.

## 6.10 Identified Hadron Partner Results

Having established that isolated direct photon and  $\pi^0$  triggered two-particle correlations are useful tools to study quark and gluon jet fragmentation, respectively, one may then try to determine whether the parton flavor has any effect on the hadrochemistry of produced particles. In particular we wish to determine whether gluon jets are favored in proton production by comparing the proton to pion ratio on the away-side of  $\pi^0$  and direct photon triggers . The  $\pi^0$  and isolated direct photon associated yields of charged pions (left) and protons/anti-protons (right) as a function of  $\Delta\phi$  are shown in figure 6.27.

Figure 6.28 shows the proton to pion ratio ( $R(p/\pi)$ ) on the away-side of 5-7 GeV isolated direct photons as function of  $p_{T,a}$ . These conditional yields have a smaller value of  $R(p/\pi)$  than the inclusive data which, a feature also present in the model calculations (need a plot demonstrating this). The statistical precision of the two-particle correlation data do not distinguish between the model calculations. The different fragmentation functions are very consistent with one another with the exception of the KKP fit which is the oldest of the

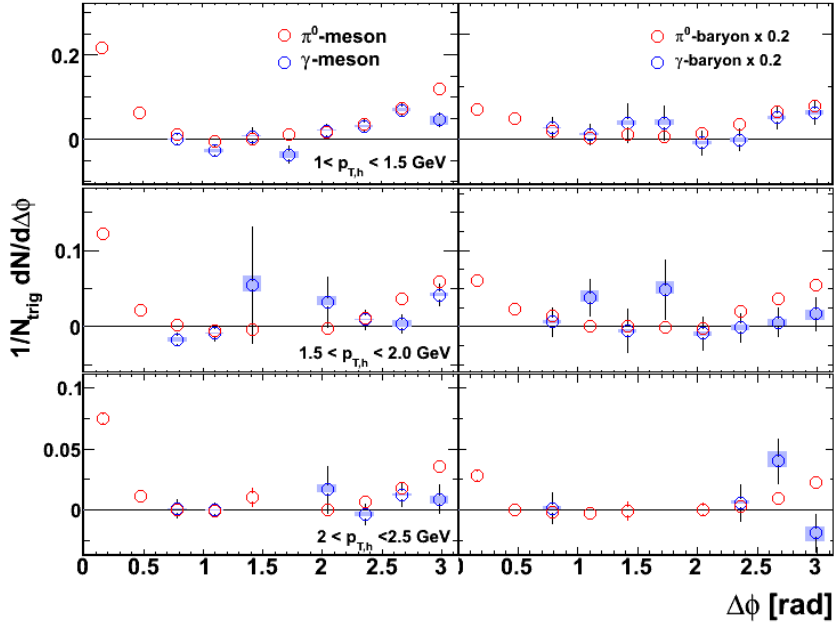


Figure 6.27: Per-trigger yields as a function of  $\Delta\phi$  for isolated direct photon (blue) and  $\pi^0$  triggers (red) with charged pions (left) and protons and anti-protons (right). The level of the pedestal is shown by a dashed line.

four parameterizations.

The  $\pi^0$  triggered data shown in figure 6.29 are, not surprisingly, much more precise than the direct photon data.  $R(p/\pi)$  is consistent with the value observed for direct photon associated data suggesting, perhaps, that the hadro-chemistry of jet fragmentation is not very sensitive to the flavor dependence in this kinematic regime. The model predictions are less uniform, consistent with the notion that the gluon fragmentation function is under-constrained. The data favor the AKK (2005 and 2008) sets over the KKP and DSS sets by about a factor of 2. As a caveat, the current data is limited to rather low  $p_{T,a}$ . Data at higher  $p_T$  would clearly be useful to further constrain the flavor dependence of parton hadronization and to bridge the gap between the momentum fraction sampled by the correlation data and those sampled by the single particle spectra.

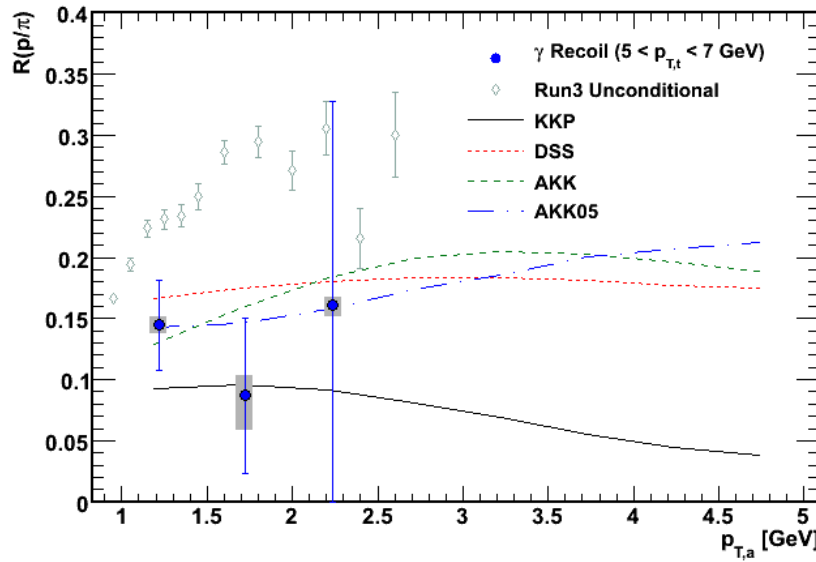


Figure 6.28: Proton to pion ratio on the away-side of isolated direct photons of  $5 < p_{T,t} < 7$  GeV as a function of  $p_{T,a}$  compared to calculations using several different fragmentation functions.

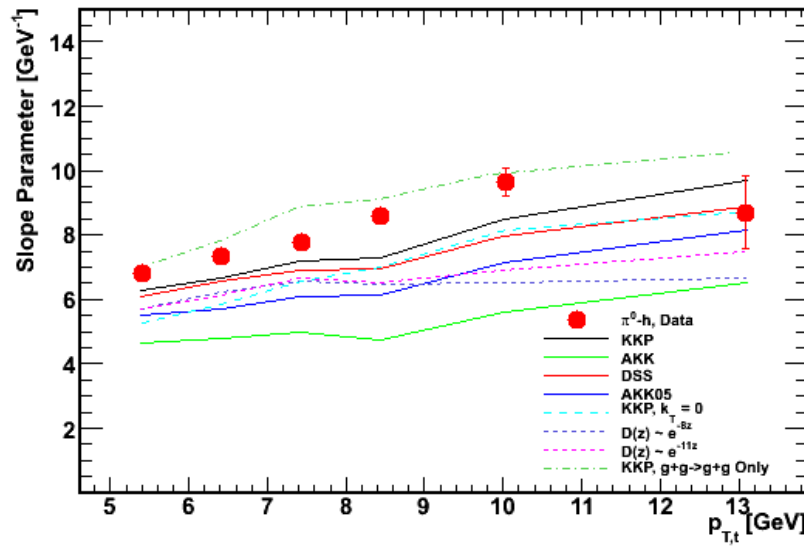


Figure 6.29: Proton to pion ratio on the away-side of  $\pi^0$ 's of  $5 < p_{T,t} < 7$  GeV as a function of  $p_{T,a}$  compared to calculations using several different fragmentation functions.

# Chapter 7

## Conclusions and Outlook

### 7.1 Overview

$\gamma$ +jet studies are widely recognized as important tool to characterize QCD in the high temperature regime. In fact, “ $\gamma$ +jet tomography” figures prominently in the Long Range Plan drafted by the Nuclear Science Advisory Committee (NSAC) which has been charged with prioritizing the objectives of nuclear physics research in the United States [136]. The research presented in this thesis represents significant progress towards achieving one of the primary goals of the RHIC program: to determine the density profile of the Quark-Gluon Plasma created in heavy-ion collisions by measuring its interaction with, and response to, jets.

To this end, a sound methodology has been developed to measure direct photon correlations in the high multiplicity environment. The first measurements of direct photon-hadron correlation in Au + Au collisions have been performed and compared to single and di-hadron data. Precision measurements have been performed in p + p collisions that test our present understanding of vacuum QCD effects, which must be constrained to perform a reliable theoretical modeling of the system. Much remains to be done on both the theoretical and experimental fronts before the full potential of jet tomography is exhausted. A quantitative description of the QGP will require complementary, differential measurements of energy loss effects. The present results suggest promising directions for future experimental efforts and call attention to phenomena for which improved theoretical descriptions are warranted.

## 7.2 Methodology

As described in section 3 a statistical subtraction method has been developed to extract the high  $p_T$  direct photon correlation signal. The background decay photon correlations were estimated by detailed Monte Carlo simulations which take into account decay kinematics and detector effects. With the measurement of  $\eta$ -hadron correlations in p + p collisions, more than 95% of the decay background has been directly measured. Disregarding, for the moment, the physics implications of the measurement, the dearth of near-side yield observed in both p + p and Au + Au collisions attests to the accuracy of the measurements since one expects the photons, at least a large fraction of them, to originate directly from the  $2 \rightarrow 2$  Compton reaction.

Improved precision beyond the purely statistical subtraction can be obtained by event-by-event identification of the direct photon signal as well as event-by-event rejection of the decay photon background. This has been achieved in p + p collisions by decay photon tagging and by applying an isolation criterion. The statistical and systematic uncertainties were shown to be dramatically reduced. In conjunction with the increased luminosity expected to become available over the course of the next decade, the techniques applied here will likely lead to increasingly precise measurements of the path length dependence of parton energy loss.

To provide some historical context, before the WA98 result, published nearly ten years ago, no significant measurement of direct photons in heavy-ion collisions had ever been performed [137]. This was not for lack of effort, as the decade previous produced numerous null results, instead providing only upper limits [138–141]. That we are now able to measure jet correlations using direct photon triggers demonstrates is an indicator of the tremendous progress which has since been made. Much of the credit belongs to the precise PHENIX measurements of the direct photon cross section and corresponding photon excess ( $R_\gamma$ ). We may expect a similar increase in precision of the direct photon correlation studies if projections for luminosity and detector upgrades come to fruition. Hopefully, the analysis techniques developed in this thesis will expedite these future studies.

## 7.3 Interpretation

The foremost paradigm in the study of heavy-ion collisions is the search for signatures which deviate from expectations provided by a control experiment which is absent of nuclear effects. In the present work, measurements of direct photon correlations have been performed in Au + Au collisions where the

signature of parton energy loss may be studied. Comparing to the corresponding measurement in  $p + p$  collisions, we found a similar disappearance of opposite-side jet correlations to that observed in di-jet events [52]. The level of the suppression is comparable to that observed in di-hadron conditional yields and also in the single hadron yields within the level of the current uncertainties.

Since photons are relatively non-interacting we expect the distribution of hard collision vertices to be unbiased by the photon trigger selection. The conditional hadron spectrum should then be suppressed in much the same manner as the inclusive hadron spectrum. This does not mean, however, that the suppression factor should be uniformly identical. The photon trigger fixes the parent parton momentum on the away-side (modulo the  $k_T$  effect), whereas the inclusive hadron spectrum is convoluted with the jet production cross section. For a semi-transparent medium one would expect to observe a  $p_T$  dependence to energy loss effects whose behavior is governed by the exact geometry and space-time evolution of the system (see for example [86]). Only in the limit of a geometry which has an infinitely opaque core with a completely transparent corona would one expect to observe exactly the same level of suppression for all single particle and conditional yields. Hence, the present results support the claim that the medium is indeed rather opaque.

For purposes of jet tomography parton to photon fragmentation is considered a background since it introduces the same geometrical biases present in di-hadron measurements. Although the contribution of fragmentation photons has been calculated to next-to-leading order accuracy their fragmentation function is poorly constrained by data. PHENIX is particularly well suited to address this issue since both inclusive direct and isolated direct photons can be measured out to large  $p_T$ . Inclusive direct photon correlations do not show a significant near-side yield and constrain it to be < 20% of the  $\pi^0$  correlation for the same trigger  $p_T$  selection. Compared to the inclusive direct measurement, the isolated direct photons exhibit a 20% reduction of associated yield on the away-side. The expected difference between these two quantities depends on both the relative contribution of fragmentation photons and the parton to photon fragmentation function. Utilizing the fragmentation to direct ratio calculated in [142] it is shown that a self-consistent description of the data is obtained by assuming that the difference between the inclusive and isolated direct represents the fragmentation photon associated yield and that its correlations are similar to that of the  $\pi^0$ .

Conjectured sources of medium induced photon production would be an interesting probe of energy loss themselves since their production would be path-length dependent, but they would not subsequently thermalize with the

medium and hence, they could be differentiated from the medium response. No significant evidence for induced production is observed in the near-side photon-hadron correlations in central Au + Au collisions. Above 9 GeV, induced production is constrained to be less than 20% of the  $\pi^0$  correlation signal for the same trigger momentum selection.

In addition to providing baseline comparison data for heavy-ion collisions, measurements in p + p collisions address fundamental aspects of QCD that, in some cases, remain poorly constrained. The interpretation of jet correlation measurements in heavy-ion collisions often relies on a robust description of vacuum QCD phenomena for which perturbative calculations are not yet sufficiently accurate or the non-perturbative functions are not sufficiently well-known. In addition to the aforementioned complications arising from the unknown photon fragmentation function, the  $k_T$  effect is another example which is relevant for direct photon correlations. Direct photons are considered an ideal tomographic probe because they determine the initial momentum of the recoil parton uniquely at leading order. However corrections to this approximation,  $k_T$  effects for example, are non-negligible and cannot yet be reliably determined from first principle calculations. However, for several observables these effects have previously been shown to be well described by introducing a Gaussian smearing of the momentum in the direction transverse to the initial parton pair. The magnitude of such effects must be determined in data from baseline collision systems in order for a realistic phenomenological description to be achieved.

In the present study the out-of-plane momentum ( $p_{OUT}$ ) distributions for  $\pi^0$  and isolated direct photon triggers are shown to be Gaussian distributed with similar widths, suggestive of a similar underlying mechanism, despite their somewhat different initial states. Comparing these distribution to a Leading Order calculation including  $k_T$  smearing it is demonstrated that  $k_T$  effects are of comparable size in the  $\gamma$ +jet channel as in the di-jet channel. The  $\sqrt{\langle |k_T|^2 \rangle}$  for isolated photons triggers is shown to depend on  $p_T$  whereas no such dependence is observed for  $\pi^0$  triggers.

The interpretation of correlation measurements similarly necessitates better constraints on the gluon fragmentation function. The  $\pi^0$  and isolated photon data have been compared to leading order calculations using several different parameterizations of the quark and gluon fragmentation functions. Once the  $k_T$  smearing is taken into account the fragmentation functions are able to reproduce the isolated photon longitudinal momentum fraction ( $x_E$ ) distributions. Within the same model the fragmentation function parameterizations differ widely in their predictions. None of the individual predictions is found to give a satisfactory description of the all the data. While the KKP

set best describe the  $\pi^0$   $x_E$  distributions, they give the poorest description of the associated proton to pion ratio.

The model calculations, along with the observed charge asymmetry of the isolated photon conditional yields, indicate that isolated photons are a high purity quark jet tag. Hadron triggered jets, on the other hand, are expected to be dominated by gluon fragmentation in heavy-ion collisions due to the largeness of the nuclear gluon density. This is of particular importance for studies of the flavor dependence of parton energy loss, a fundamental prediction of QCD, which has not yet been observed. Identified particle spectra, in particular those of the proton and pion, are often conjectured to be sensitive to flavor dependent effects. This claim is, however, shown to be model dependent. The comparison of two particle correlations using direct photon and  $\pi^0$  triggers, on the other hand, provides a less ambiguous method of selecting quark and gluon jets, respectively.

## 7.4 Outlook

As we prepare for the unprecedeted energy densities that will become available with the upcoming start of the LHC program, it is clear that  $\gamma$ +jet studies will continue to play a central role in heavy-ion physics. With higher rates will also come new experimental challenges. For example, the fraction of photons from jet fragmentation is expected to be larger [142]. On the other hand,  $Z^0$ +jet correlations will become available, which have the same advantages as  $\gamma$ +jet, but reduced backgrounds, albeit with smaller rates. As at the Tevatron,  $\gamma$ +jet events will play a central role in the calibration of the energy scale for jet studies in hadronic calorimeters [143].

In the upcoming RHIC runs, higher statistics and new methodologies will substantially reduce uncertainties. The potential to measure parton energy loss with  $\gamma$ +jet events has been discussed in this thesis. There are further reaching applications of such studies, however. For example, a planned forward calorimeter upgrade for PHENIX will allow direct photon identification at forward rapidities, probing the saturation regime of the gluon distribution [144]. In p + p collisions,  $\gamma$ +jet with full jet reconstruction will be possible, and is expected to provide the best constraints yet on the gluon spin contribution to the nucleon [145]. In heavy-ion collisions we anticipate that direct photon correlations will become the tool of choice for measuring parton energy loss and a hallmark of the RHIC II program.

# Bibliography

- [1] S. Bethke, Prog. Part. Nucl. Phys. **58**, 351 (2007), hep-ex/0606035.
- [2] A. Bettini, *Introduction to Elementary Particle Physics* (Cambridge University Press, 2008).
- [3] K. G. Wilson, Phys. Rev. **D10**, 2445 (1974).
- [4] unknown, Time Magazine (1957).
- [5] R. Stock, J. Phys. **G30**, S633 (2004), nucl-ex/0405007.
- [6] J. C. Collins and M. J. Perry, Phys. Rev. Lett. **34**, 1353 (1975).
- [7] G. Baym and S. A. Chin, Nucl. Phys. **A262**, 527 (1976).
- [8] M. B. Kislinger and P. D. Morley, Phys. Rev. **D13**, 2765 (1976).
- [9] B. A. Freedman and L. D. McLerran, Phys. Rev. **D16**, 1130 (1977).
- [10] S. V. Edward, Pisma Zh. Eksp. Teor. Fiz. **74**, 408 (1978).
- [11] J. I. Kapusta, Nucl. Phys. **B148**, 461 (1979).
- [12] F. Karsch *Lectures on Quark Matter* Vol. 583 (Springer-Verlag, 2002), .
- [13] P. Arnold and C.-X. Zhai, Phys. Rev. **D50**, 7603 (1994), hep-ph/9408276.
- [14] R. Hagedorn, Nuovo Cim. Suppl. **3**, 147 (1965).
- [15] E. V. Shuryak and I. Zahed, Phys. Rev. **D70**, 054507 (2004), hep-ph/0403127.
- [16] PHENIX, K. Adcox *et al.*, Nucl. Phys. **A757**, 184 (2005), nucl-ex/0410003.
- [17] J. D. Bjorken, Phys. Rev. **D27**, 140 (1983).

- [18] PHENIX, K. Adcox *et al.*, Phys. Rev. **C69**, 024904 (2004), nucl-ex/0307010.
- [19] U. W. Heinz, J. Phys. **G31**, S717 (2005), nucl-th/0412094.
- [20] A. Adil, M. Gyulassy, and T. Hirano, Phys. Rev. **D73**, 074006 (2006), nucl-th/0509064.
- [21] PHENIX, A. Adare *et al.*, Phys. Rev. Lett. **98**, 162301 (2007), nucl-ex/0608033.
- [22] WA98, M. M. Aggarwal *et al.*, Eur. Phys. J. **C18**, 651 (2001), nucl-ex/0008004.
- [23] R. J. Glauber and G. Matthiae, Nucl. Phys. **B21**, 135 (1970).
- [24] PHENIX, S. S. Adler *et al.*, Phys. Rev. **C69**, 034910 (2004), nucl-ex/0308006.
- [25] PHENIX, S. S. Adler *et al.*, Phys. Rev. Lett. **91**, 072303 (2003), nucl-ex/0306021.
- [26] J. D. Bjorken, FERMILAB-PUB-82-059-THY.
- [27] X.-N. Wang and M. Gyulassy, Phys. Rev. Lett. **68**, 1480 (1992).
- [28] M. Gyulassy and X.-n. Wang, Nucl. Phys. **B420**, 583 (1994), nucl-th/9306003.
- [29] R. Baier, Y. L. Dokshitzer, S. Peigne, and D. Schiff, Phys. Lett. **B345**, 277 (1995), hep-ph/9411409.
- [30] R. Baier, D. Schiff, and B. G. Zakharov, Ann. Rev. Nucl. Part. Sci. **50**, 37 (2000), hep-ph/0002198.
- [31] M. Gyulassy, P. Levai, and I. Vitev, Phys. Lett. **B538**, 282 (2002), nucl-th/0112071.
- [32] P. Arnold, G. D. Moore, and L. G. Yaffe, JHEP **11**, 057 (2001), hep-ph/0109064.
- [33] A. Majumder, Phys. Rev. **C75**, 021901 (2007), nucl-th/0608043.
- [34] S. Wicks, W. Horowitz, M. Djordjevic, and M. Gyulassy, Nucl. Phys. **A784**, 426 (2007), nucl-th/0512076.

- [35] PHENIX, A. Adare *et al.*, Phys. Rev. **C77**, 064907 (2008), 0801.1665.
- [36] R. Baier, A. H. Mueller, and D. Schiff, Phys. Lett. **B649**, 147 (2007), nucl-th/0612068.
- [37] R. Baier and D. Schiff, JHEP **09**, 059 (2006), hep-ph/0605183.
- [38] S. A. Bass *et al.*, (2008), 0808.0908.
- [39] A. Majumder, J. Phys. **G34**, S377 (2007), nucl-th/0702066.
- [40] Techqm main page, [https://wiki.bnl.gov/TECHQM/index.php/Main\\_Page](https://wiki.bnl.gov/TECHQM/index.php/Main_Page).
- [41] K. J. Eskola, H. Honkanen, C. A. Salgado, and U. A. Wiedemann, Nucl. Phys. **A747**, 511 (2005), hep-ph/0406319.
- [42] PHENIX, A. Adare *et al.*, Phys. Rev. Lett. **101**, 232301 (2008), 0801.4020.
- [43] S. Albino, B. A. Kniehl, G. Kramer, and C. Sandoval, Phys. Rev. **D75**, 034018 (2007), hep-ph/0611029.
- [44] Z. Xu, (2008), 0806.0200.
- [45] STAR, B. I. Abelev *et al.*, Phys. Rev. Lett. **97**, 152301 (2006), nucl-ex/0606003.
- [46] T. Renk and K. J. Eskola, Phys. Rev. **C76**, 027901 (2007), hep-ph/0702096.
- [47] PHENIX, S. S. Adler *et al.*, Phys. Rev. **C76**, 034904 (2007), nucl-ex/0611007.
- [48] M. J. Tannenbaum, PoS **LHC07**, 004 (2007).
- [49] G. Hanson *et al.*, Phys. Rev. Lett. **35**, 1609 (1975).
- [50] PHENIX, A. Adare *et al.*, Phys. Rev. **C78**, 014901 (2008), 0801.4545.
- [51] CDF, A. A. Affolder *et al.*, Phys. Rev. **D65**, 092002 (2002).
- [52] STAR, C. Adler *et al.*, Phys. Rev. Lett. **90**, 082302 (2003), nucl-ex/0210033.
- [53] PHENIX, S. S. Adler *et al.*, Phys. Rev. Lett. **97**, 052301 (2006), nucl-ex/0507004.

- [54] STAR, J. Adams *et al.*, Phys. Rev. Lett. **97**, 162301 (2006), nucl-ex/0604018.
- [55] J. Putschke, J. Phys. **G34**, S679 (2007), nucl-ex/0701074.
- [56] V. Koch, A. Majumder, and X.-N. Wang, Phys. Rev. Lett. **96**, 172302 (2006), nucl-th/0507063.
- [57] H. Stoecker, Nucl. Phys. **A750**, 121 (2005), nucl-th/0406018.
- [58] C.-Y. Wong, Phys. Rev. **C76**, 054908 (2007), 0707.2385.
- [59] E. V. Shuryak, Phys. Rev. **C76**, 047901 (2007), 0706.3531.
- [60] CMOR, A. L. S. Angelis *et al.*, Nucl. Phys. **B327**, 541 (1989).
- [61] PHENIX, S. S. Adler *et al.*, Phys. Rev. **D74**, 072002 (2006), hep-ex/0605039.
- [62] R. P. Feynman, R. D. Field, and G. C. Fox, Nucl. Phys. **B128**, 1 (1977).
- [63] L. Bourhis, M. Fontannaz, and J. P. Guillet, Eur. Phys. J. **C2**, 529 (1998), hep-ph/9704447.
- [64] ALEPH, D. Buskulic *et al.*, Z. Phys. **C69**, 365 (1996).
- [65] J. F. Owens, Rev. Mod. Phys. **59**, 465 (1987).
- [66] H. Zhang, J. Owens, E. Wang, and X.-N. Wang.
- [67] PHENIX, S. S. Adler *et al.*, Phys. Rev. Lett. **98**, 012002 (2007), hep-ex/0609031.
- [68] J. Huston *et al.*, Phys. Rev. **D51**, 6139 (1995), hep-ph/9501230.
- [69] P. Aurenche *et al.*, Eur. Phys. J. **C9**, 107 (1999), hep-ph/9811382.
- [70] P. Aurenche, M. Fontannaz, J.-P. Guillet, E. Pilon, and M. Werlen, Phys. Rev. **D73**, 094007 (2006), hep-ph/0602133.
- [71] L. Apanasevich *et al.*, Phys. Rev. **D59**, 074007 (1999), hep-ph/9808467.
- [72] CTEQ, H. L. Lai *et al.*, Eur. Phys. J. **C12**, 375 (2000), hep-ph/9903282.
- [73] E. Laenen, G. Sterman, and W. Vogelsang, Phys. Rev. Lett. **84**, 4296 (2000), hep-ph/0002078.

- [74] D0, V. M. Abazov *et al.*, Phys. Lett. **B666**, 435 (2008), 0804.1107.
- [75] PHENIX Preliminary results.
- [76] Private Communication.
- [77] PHENIX, S. S. Adler *et al.*, Phys. Rev. **C75**, 024909 (2007), nucl-ex/0611006.
- [78] F. Arleo, JHEP **09**, 015 (2006), hep-ph/0601075.
- [79] PHENIX, K. Reygers, J. Phys. **G35**, 104045 (2008), 0804.4562.
- [80] B. G. Zakharov, JETP Lett. **80**, 1 (2004), hep-ph/0405101.
- [81] S. Turbide, C. Gale, S. Jeon, and G. D. Moore, Phys. Rev. **C72**, 014906 (2005), hep-ph/0502248.
- [82] R. J. Fries, B. Muller, and D. K. Srivastava, Phys. Rev. **C72**, 041902 (2005), nucl-th/0507018.
- [83] G. Y. Qin, J. Ruppert, C. Gale, S. Jeon, and G. D. Moore, (2008), 0809.2030.
- [84] X.-N. Wang, Z. Huang, and I. Sarcevic, Phys. Rev. Lett. **77**, 231 (1996), hep-ph/9605213.
- [85] X.-N. Wang and Z. Huang, Phys. Rev. **C55**, 3047 (1997), hep-ph/9701227.
- [86] T. Renk, Phys. Rev. **C74**, 034906 (2006), hep-ph/0607166.
- [87] H. Zhang, J. F. Owens, E. Wang, and X.-N. Wang, Phys. Rev. Lett. **98**, 212301 (2007), nucl-th/0701045.
- [88] PHENIX, M. Allen *et al.*, Nucl. Instrum. Meth. **A499**, 549 (2003).
- [89] PHENIX, K. Adcox *et al.*, Nucl. Instrum. Meth. **A499**, 489 (2003).
- [90] PHENIX, L. Aphecetche *et al.*, Nucl. Instrum. Meth. **A499**, 521 (2003).
- [91] G. David *et al.*, IEEE Trans. Nucl. Sci. **45**, 705 (1998).
- [92] PHENIX, M. Aizawa *et al.*, Nucl. Instrum. Meth. **A499**, 508 (2003).
- [93] F. Matathias, *Identified Particle Production in p+p and d+Au Collisions at RHIC Energies*, PhD thesis, Stony Brook University, 2004.

- [94] PHENIX, S. S. Adler *et al.*, Phys. Rev. **C71**, 051902 (2005), nucl-ex/0408007.
- [95] M. McCumber and J. Frantz, Acta Phys. Hung. **A27**, 213 (2006), nucl-ex/0511048.
- [96] PHENIX, S. Afanasiev *et al.*, Phys. Rev. Lett. **99**, 052301 (2007), nucl-ex/0703024.
- [97] PHENIX, A. Adare *et al.*, Phys. Rev. Lett. **98**, 172301 (2007), nucl-ex/0611018.
- [98] STAR, B. I. Abelev *et al.*, Phys. Rev. Lett. **101**, 252301 (2008), 0807.1518.
- [99] the STAR, B. I. Abelev *et al.*, Phys. Rev. **C75**, 054906 (2007), nucl-ex/0701010.
- [100] A. Sickles, PHENIX Analysis Note 261.
- [101] K. Reygers, PHENIX Analysis Note 169.
- [102] M. McCumber, Private Communication.
- [103] PHENIX, S. S. Adler *et al.*, Phys. Rev. **C69**, 034909 (2004), nucl-ex/0307022.
- [104] J. Jia, *High-pT Charged Hadron Suppression in Au-Au Collisions at 200 GeV*, PhD thesis, Stony Brook University, 2003.
- [105] C.H. Chen *et al.* PHENIX Analysis Notes 657 and 625.
- [106] K. Miki *et al.*, PHENIX preliminary results, PHENIX Analysis Notes 684 and 681.
- [107] PHENIX, A. Adare *et al.*, Phys. Rev. **D76**, 051106 (2007), 0704.3599.
- [108] H. Baer, J. Ohnemus, and J. F. Owens, Phys. Rev. **D42**, 61 (1990).
- [109] S. Frixione, Phys. Lett. **B429**, 369 (1998), hep-ph/9801442.
- [110] T. Isobe *et al.*, PHENIX Analysis Note 490.
- [111] C. Maguire *et al.*, Computer Physics Communications **110** (1998).
- [112] PHENIX, S. S. Adler *et al.*, Phys. Rev. Lett. **96**, 202301 (2006), nucl-ex/0601037.

- [113] C.-Y. Wong, (2009), 0901.0726.
- [114] PHENIX, A. Adare *et al.*, Phys. Rev. **C77**, 011901 (2008), 0705.3238.
- [115] PHENIX, A. Hanks, Int. J. Mod. Phys. **E16**, 2182 (2007), 0705.0526.
- [116] H. Zhang, J. Owens, E. Wang and X.N. Wang, Talk given by H. Zhang at ATHIC 2008 conference. Slides: [http://utkhii.px.tsukuba.ac.jp/ATHIC2008/Talk\\_Slides.html](http://utkhii.px.tsukuba.ac.jp/ATHIC2008/Talk_Slides.html).
- [117] PHENIX, S. S. Adler *et al.*, Phys. Rev. Lett. **94**, 232301 (2005), nucl-ex/0503003.
- [118] B. L. Combridge, J. Kripfganz, and J. Ranft, Phys. Lett. **B70**, 234 (1977).
- [119] T. Ferbel and W. R. Molzon, Rev. Mod. Phys. **56**, 181 (1984).
- [120] J. Pumplin *et al.*, JHEP **07**, 012 (2002), hep-ph/0201195.
- [121] <http://durpdg.dur.ac.uk/hepdata/pdf3.html>.
- [122] B. A. Kniehl, G. Kramer, and B. Potter, Nucl. Phys. **B597**, 337 (2001), hep-ph/0011155.
- [123] S. Albino, B. A. Kniehl, and G. Kramer, Nucl. Phys. **B725**, 181 (2005), hep-ph/0502188.
- [124] OPAL, G. Abbiendi *et al.*, Eur. Phys. J. **C16**, 407 (2000), hep-ex/0001054.
- [125] STAR, J. Adams *et al.*, Phys. Lett. **B637**, 161 (2006), nucl-ex/0601033.
- [126] D. de Florian, private communication.
- [127] D. de Florian, R. Sassot, and M. Stratmann, Phys. Rev. **D75**, 114010 (2007), hep-ph/0703242.
- [128] D. de Florian, R. Sassot, and M. Stratmann, Phys. Rev. **D76**, 074033 (2007), 0707.1506.
- [129] S. Albino, B. A. Kniehl, and G. Kramer, Nucl. Phys. **B803**, 42 (2008), 0803.2768.
- [130] M. Tannenbaum, ECT Workshop on Parton Fragmentation: [www.phenix.bnl.gov/phenix/WWW/publish/sapin/conferences/TrentoFragmentation2008/Tannenbaum-Trento2008-post.ppt](http://www.phenix.bnl.gov/phenix/WWW/publish/sapin/conferences/TrentoFragmentation2008/Tannenbaum-Trento2008-post.ppt).

- [131] Fermilab E706, M. Begel, Nucl. Phys. **A783**, 335 (2007).
- [132] L. Apanasevich *et al.*, Phys. Rev. **D59**, 074007 (1999), hep-ph/9808467.
- [133] J. Jia, PHENIX Preliminary Result.
- [134] S. Kretzer, AIP Conf. Proc. **698**, 603 (2004).
- [135] Opal, M. Z. Akrawy *et al.*, Phys. Lett. **B261**, 334 (1991).
- [136] The Frontiers of Nuclear Science: A Long Range Plan  
<http://www.sc.doe.gov/np/nsac/nsac.html>.
- [137] WA98, M. M. Aggarwal *et al.*, Phys. Rev. Lett. **85**, 3595 (2000), nucl-ex/0006008.
- [138] T. Akesson *et al.*, Z. Phys. **C46**, 369 (1990).
- [139] WA80, R. Albrecht *et al.*, Z. Phys. **C51**, 1 (1991).
- [140] CERES, R. Baur *et al.*, Z. Phys. **C71**, 571 (1996).
- [141] WA80, R. Albrecht *et al.*, Phys. Rev. Lett. **76**, 3506 (1996).
- [142] I. Vitev and B.-W. Zhang, Phys. Lett. **B669**, 337 (2008), 0804.3805.
- [143] I. A. Golutvin *et al.*, Phys. Part. Nucl. Lett. **5**, 447 (2008).
- [144] [http://www.phenix.bnl.gov/phenix/WWW/docs/upgrades/ncc/PHENIX\\_NCC\\_march2006.pdf](http://www.phenix.bnl.gov/phenix/WWW/docs/upgrades/ncc/PHENIX_NCC_march2006.pdf).
- [145] S. Frixione and W. Vogelsang, Nucl. Phys. **B568**, 60 (2000), hep-ph/9908387.

# Data Tables

$p_{T,t}$ [GeV]	$p_{T,a}$ [GeV]	Yield	Stat	Sys.(low)	Sys(high)
5-7	1-2	0.01407	0.01110	0.05737	0.05737
	2-3	0.02228	0.00542	0.01751	0.01751
	3-5	0.00630	0.00196	0.00504	0.00504
	5-10	0.00067	0.00043	0.00063	0.00063
7-9	1-2	0.01565	0.01839	0.03938	0.03938
	2-3	-0.00542	0.01016	0.01655	0.01655
	3-5	0.01024	0.00381	0.00445	0.00445
	5-10	0.00049	0.00091	0.00065	0.00065
9-12	1-2	0.07701	0.02569	0.02856	0.02856
	2-3	0.00140	0.01508	0.01308	0.01308
	3-5	0.00555	0.00576	0.00402	0.00402
	5-10	-0.00019	0.00150	0.00062	0.00062
12-15	1-2	0.06552	0.05967	0.06286	0.06286
	2-3	-0.02884	0.02446	0.01879	0.01879
	3-5	-0.04321	0.01216	0.01057	0.01057
	5-10	-0.00176	0.00314	0.00024	0.00024

Table 1: Near-side direct  $\gamma$ -h yields for p + p collisions

$p_{T,t}$ [GeV]	$p_{T,a}$ [GeV]	Yield	Stat	Sys.(low)	Sys(high)
5-7	1-2	0.12230	0.00907	0.03301	0.03301
	2-3	0.02783	0.00482	0.01165	0.01165
	3-5	0.01230	0.00179	0.00300	0.00300
	5-10	0.00100	0.00042	0.00048	0.00048
7-9	1-2	0.14860	0.01651	0.02772	0.02772
	2-3	0.05129	0.00973	0.01085	0.01085
	3-5	0.01844	0.00384	0.00346	0.00346
	5-10	0.00141	0.00096	0.00065	0.00065
9-12	1-2	0.23709	0.02623	0.02291	0.02291
	2-3	0.07264	0.01519	0.00919	0.00919
	3-5	0.01506	0.00620	0.00362	0.00362
	5-10	0.00472	0.00176	0.00066	0.00066
12-15	1-2	0.17050	0.04697	0.06633	0.06633
	2-3	0.11703	0.02724	0.01917	0.01917
	3-5	0.02886	0.01326	0.01116	0.01116
	5-10	0.00173	0.00316	0.00175	0.00175

Table 2: Away-side direct  $\gamma$ -h yields for p + p collisions

$p_{T,t}$ [GeV]	$p_{T,a}$ [GeV]	Yield	Stat	Sys.(low)	Sys(high)
5-7	1-2	0.04153	0.04107	0.09507	0.09507
	2-3	-0.01110	0.01145	0.03868	0.03868
	3-5	-0.00130	0.00207	0.01299	0.01299
	5-10	0.00044	0.00039	0.00149	0.00149
7-9	1-2	0.06900	0.07238	0.11339	0.11339
	2-3	0.02702	0.02040	0.02938	0.02938
	3-5	0.00736	0.00401	0.00869	0.00869
	5-10	0.00095	0.00083	0.00127	0.00127
9-12	1-2	0.04843	0.11346	0.12543	0.12543
	2-3	-0.00071	0.03202	0.03224	0.03224
	3-5	-0.00689	0.00599	0.01203	0.01203
	5-10	0.00100	0.00139	0.00186	0.00186
12-15	1-2	-0.00833	0.20753	0.27619	0.27619
	2-3	0.08008	0.06257	0.04669	0.04669
	3-5	0.00537	0.01415	0.01064	0.01064
	5-10	-0.01291	0.01052	0.00888	0.00888

Table 3: Near-side direct  $\gamma$ -h yields for Au + Au collisions

$p_{T,t}$ [GeV]	$p_{T,a}$ [GeV]	Yield	Stat	Sys.(low)	Sys(high)
5-7	1-2	0.07950	0.04284	0.03167	0.03167
	2-3	0.03083	0.01160	0.00402	0.00402
	3-5	0.00373	0.00191	0.00098	0.00098
	5-10	0.00003	0.00035	0.00021	0.00021
7-9	1-2	0.09175	0.07582	0.04456	0.04456
	2-3	0.03496	0.02101	0.00664	0.00664
	3-5	0.00802	0.00366	0.00097	0.00097
	5-10	0.00074	0.00074	0.00019	0.00019
9-12	1-2	0.08369	0.11957	0.05662	0.05662
	2-3	0.05643	0.03396	0.00868	0.00868
	3-5	-0.00145	0.00571	0.00176	0.00176
	5-10	0.00155	0.00130	0.00016	0.00016
12-15	1-2	0.44819	0.22307	0.11094	0.11094
	2-3	0.06242	0.06395	0.01363	0.01363
	3-5	0.02052	0.01347	0.00098	0.00098
	5-10	-0.07468	0.09284	0.01815	0.01815

Table 4: Away-side direct  $\gamma$ -h yields for Au + Au collisions

$p_{T,t}$ [GeV]	$p_{T,a}$ [GeV]	Yield	Stat	Sys.(low)	Sys(high)
5-7	1-2	0.11563	0.00642	0.01484	0.01484
	2-3	0.04581	0.00448	0.00429	0.00429
	3-5	0.02061	0.00273	0.00177	0.00177
	5-10	0.00055	0.00115	0.00109	0.00109
7-9	1-2	0.15371	0.01110	0.00972	0.00972
	2-3	0.06292	0.00786	0.00354	0.00354
	3-5	0.03498	0.00539	0.00162	0.00162
	5-10	0.00469	0.00248	0.00078	0.00078
9-12	1-2	0.25864	0.01983	0.00717	0.00717
	2-3	0.07806	0.01212	0.00361	0.00361
	3-5	0.04887	0.00877	0.00156	0.00156
	5-10	0.00499	0.00407	0.00097	0.00097
12-15	1-2	0.23389	0.03423	0.01531	0.01531
	2-3	0.11000	0.02412	0.00780	0.00780
	3-5	0.08213	0.01966	0.00377	0.00377
	5-10	0.00395	0.03509	0.01108	0.01108

Table 5: Away-side direct  $\gamma$ -h yields for p + p collisions in the isolation method

$p_{T,t}$ [GeV]	$x_E$	Yield	Stat
5.270	0.220	1.627	0.020
	0.260	1.078	0.016
	0.300	0.731	0.013
	0.340	0.528	0.011
	0.380	0.393	0.009
	0.420	0.289	0.008
	0.460	0.209	0.007
	0.500	0.163	0.006
	0.540	0.129	0.005
	0.580	0.104	0.005
	0.620	0.077	0.004
	0.660	0.065	0.003
	0.700	0.050	0.003
	0.740	0.037	0.003
	0.780	0.033	0.002
	0.820	0.022	0.002
6.410	0.180	2.344	0.042
	0.220	1.531	0.033
	0.260	1.019	0.026
	0.300	0.659	0.021
	0.340	0.523	0.018
	0.380	0.393	0.016
	0.420	0.283	0.013
	0.460	0.209	0.011
	0.500	0.173	0.010
	0.540	0.134	0.009
	0.580	0.080	0.007
	0.620	0.084	0.007
	0.660	0.047	0.005
	0.700	0.040	0.004
7.430	0.180	2.313	0.065
	0.220	1.412	0.049
	0.260	0.983	0.040
	0.300	0.677	0.033
	0.340	0.534	0.029
	0.380	0.368	0.024
	0.420	0.264	0.020
	0.460	0.227	0.018
	0.500	0.174	0.015
	0.540	0.112	0.012
	0.580	0.098	0.011
	0.620	0.053	0.008
8.450	0.140	3.941	0.132
	0.180	2.227	0.095
	0.220	1.459	0.076
	0.260	0.978	0.061
	0.300	0.798	0.054
	0.340	0.505	0.042
	0.380	0.399	0.037
	0.420	0.252	0.029
	0.460	0.208	0.025
	0.500	0.122	0.019
	0.540	0.129	0.019
10.100	0.140	3.766	0.136
	0.180	2.372	0.105
	0.220	1.540	0.083
	0.260	1.015	0.065
	0.300	0.739	0.055
	0.340	0.490	0.044
	0.380	0.361	0.037
13.000	0.100	6.750	0.495
	0.140	3.115	0.318
	0.180	2.350	0.271
	0.220	1.454	0.206
	0.260	1.046	0.170
	0.300	0.854	0.149

Table 6:  $\pi^0$   $x_E$  distributions from p + p collisions

$p_{T,t}$ [GeV]	$x_E$	Yield	Stat	Sys.(low)	Sys(high)
5.27	0.200	1.349	0.062	0.082	0.102
	0.280	0.745	0.042	0.042	0.059
	0.360	0.318	0.027	0.019	0.033
	0.440	0.182	0.019	0.010	0.022
	0.520	0.094	0.014	0.006	0.015
	0.600	0.066	0.011	0.003	0.011
	0.680	0.044	0.008	0.002	0.008
	0.760	0.027	0.006	0.001	0.006
6.41	0.200	1.591	0.088	0.059	0.106
	0.280	0.704	0.055	0.024	0.060
	0.360	0.344	0.037	0.012	0.039
	0.440	0.174	0.026	0.006	0.027
	0.520	0.079	0.019	0.004	0.019
	0.600	0.045	0.012	0.002	0.013
	0.680	0.033	0.009	0.001	0.009
7.43	0.200	1.468	0.112	0.040	0.119
	0.280	0.574	0.067	0.016	0.068
	0.360	0.306	0.048	0.009	0.048
	0.440	0.211	0.037	0.005	0.038
	0.520	0.077	0.023	0.002	0.023
	0.600	0.055	0.016	0.001	0.016
8.45	0.200	1.606	0.148	0.030	0.151
	0.280	0.562	0.087	0.013	0.088
	0.360	0.238	0.057	0.007	0.057
	0.440	0.204	0.046	0.003	0.046
	0.520	0.073	0.026	0.001	0.026
10.10	0.120	3.177	0.260	0.084	0.273
	0.200	1.088	0.151	0.043	0.157
	0.280	0.427	0.093	0.020	0.095
	0.360	0.277	0.065	0.007	0.066
13.00	0.120	3.841	0.546	0.251	0.601
	0.200	1.191	0.279	0.087	0.292
	0.280	0.588	0.181	0.037	0.185

Table 7: Isolated direct photon  $x_E$  distributions from p + p collisions

$p_{T,t}$ [GeV]	$p_{OUT}$ [GeV]	Yield	Stat
5.27	0.125	0.827	0.009
	0.375	0.756	0.008
	0.625	0.654	0.008
	0.875	0.574	0.009
	1.125	0.485	0.009
	1.375	0.254	0.007
	1.625	0.138	0.005
	1.875	0.072	0.004
	2.125	0.044	0.003
	2.375	0.023	0.002
	2.625	0.014	0.002
	2.875	0.010	0.001
	3.125	0.005	0.001
	3.375	0.003	0.001
	3.625	0.002	0.001
	3.875	0.002	0.001
	4.125	0.001	0.000
	4.375	0.000	0.000
6.41	0.125	1.046	0.017
	0.375	0.912	0.016
	0.625	0.772	0.015
	0.875	0.652	0.015
	1.125	0.511	0.016
	1.375	0.302	0.012
	1.625	0.151	0.009
	1.875	0.074	0.006
	2.125	0.050	0.005
	2.375	0.028	0.004
	2.625	0.016	0.003
	2.875	0.010	0.002
	3.125	0.007	0.002
	3.375	0.004	0.001
	3.625	0.002	0.001
	3.875	0.002	0.001
	4.125	0.001	0.001
	4.375	0.001	0.001
7.43	0.125	1.293	0.030
	0.375	1.083	0.027
	0.625	0.916	0.026
	0.875	0.762	0.027
	1.125	0.546	0.026
	1.375	0.294	0.019
	1.625	0.155	0.013
	1.875	0.112	0.012
	2.125	0.050	0.008
	2.375	0.038	0.007
	2.625	0.023	0.005
	2.875	0.008	0.003
	3.125	0.009	0.003
	3.375	0.007	0.003
	3.625	0.002	0.002
	4.375	0.001	0.001
	4.625	0.002	0.002

Table 8:  $\pi^0$   $p_{OUT}$  distributions from p + p collisions

$p_{T,t}$ [GeV]	$p_{OUT}$ [GeV]	Yield	Stat
8.45	0.125	1.610	0.051
	0.375	1.340	0.046
	0.625	0.903	0.039
	0.875	0.794	0.041
	1.125	0.589	0.042
	1.375	0.332	0.031
	1.625	0.158	0.020
	1.875	0.120	0.018
	2.125	0.069	0.014
	2.375	0.058	0.014
	2.625	0.006	0.003
	2.875	0.005	0.003
	3.125	0.007	0.004
	3.625	0.006	0.004
	4.375	0.003	0.003
10.10	0.125	1.969	0.061
	0.375	1.621	0.055
	0.625	1.160	0.048
	0.875	0.861	0.046
	1.125	0.705	0.050
	1.375	0.374	0.035
	1.625	0.197	0.024
	1.875	0.110	0.018
	2.125	0.055	0.013
	2.375	0.038	0.012
	2.625	0.037	0.013
	2.875	0.016	0.007
	3.125	0.006	0.003
	3.375	0.005	0.005
	3.625	0.007	0.004
13.00	0.125	2.373	0.177
	0.375	2.050	0.165
	0.625	1.415	0.142
	0.875	1.271	0.155
	1.125	0.561	0.113
	1.375	0.356	0.098
	1.625	0.178	0.065
	1.875	0.102	0.045
	2.125	0.024	0.017
	2.375	0.106	0.065
	2.625	0.071	0.041
	2.875	0.018	0.018
	3.125	0.022	0.022
	3.875	0.026	0.026

Table 9:  $\pi^0$   $p_{OUT}$  distributions from p + p collisions (continued)

$p_{T,t}$ [GeV]	$p_{OUT}$	Yield	Stat.	Sys(low)	Sys(high)
5.27	0.250	0.500	0.039	0.086	0.072
	0.750	0.470	0.041	0.062	0.057
	1.250	0.333	0.042	0.035	0.035
	1.750	0.079	0.021	0.011	0.010
	2.250	0.026	0.012	0.003	0.003
	2.750	0.012	0.007	0.001	0.001
	3.250	0.002	0.004	0.001	0.001
	3.750	0.003	0.003	0.000	0.001
	4.250	-0.000	0.001	0.000	0.000
	4.750	0.001	0.001	0.000	0.000
6.41	0.250	0.687	0.044	0.040	0.039
	0.750	0.482	0.042	0.033	0.031
	1.250	0.321	0.042	0.019	0.019
	1.750	0.140	0.024	0.006	0.006
	2.250	0.037	0.013	0.002	0.002
	2.750	0.020	0.009	0.001	0.001
	3.250	0.015	0.007	0.001	0.001
	3.750	-0.002	0.001	0.000	0.000
	4.250	-0.001	0.000	0.000	0.000
	4.750	0.000	0.000	0.000	0.000
7.43	0.250	0.866	0.055	0.026	0.026
	0.750	0.585	0.050	0.020	0.019
	1.250	0.344	0.050	0.012	0.011
	1.750	0.066	0.022	0.004	0.004
	2.250	0.054	0.018	0.001	0.001
	2.750	0.022	0.011	0.001	0.001
	3.250	0.017	0.009	0.001	0.001
	3.750	0.001	0.002	0.000	0.000
	4.250	-0.001	0.001	0.000	0.000
	4.750	0.003	0.003	0.000	0.000
8.45	0.250	0.999	0.071	0.020	0.019
	0.750	0.665	0.064	0.012	0.012
	1.250	0.394	0.059	0.007	0.007
	1.750	0.134	0.033	0.002	0.002
	2.250	0.051	0.022	0.001	0.001
	2.750	0.012	0.007	0.000	0.000
	3.250	0.002	0.003	0.000	0.000
	3.750	-0.001	0.001	0.000	0.000
	4.250	-0.001	0.001	0.000	0.000
	4.750	0.008	0.008	0.000	0.000
10.10	0.250	1.010	0.093	0.039	0.036
	0.750	0.881	0.090	0.021	0.021
	1.250	0.555	0.084	0.011	0.012
	1.750	0.108	0.039	0.003	0.003
	2.250	0.054	0.033	0.002	0.002
	2.750	-0.001	0.005	0.000	0.000
	3.250	0.008	0.008	0.000	0.000
	3.750	-0.002	0.001	0.000	0.000
	4.250	-0.000	0.000	0.000	0.000
	4.750	0.000	0.000	0.000	0.000
13.00	0.250	1.340	0.193	0.089	0.086
	0.750	1.159	0.189	0.057	0.056
	1.250	0.358	0.133	0.022	0.021
	1.750	0.244	0.122	0.007	0.008
	2.250	0.087	0.054	0.003	0.003
	2.750	0.025	0.017	0.001	0.001
	3.250	-0.013	0.012	0.003	0.003
	3.750	-0.001	0.001	0.000	0.000

Table 10: Isolated direct photon  $p_{OUT}$  distributions from p + p collisions